Passive and Active Waveguide Systems for Solar Concentrators

Zur Erlangung des akademischen Grades eines Doktors der Ingenieurwissenschaften (Dr.-Ing.) genehmigte

Dissertation von

M. Sc. Maik Meudt

in der Fakultät 6 - Elektrotechnik,
Informationstechnik und Medientechnik
an der Bergischen Universität Wuppertal

Eingereicht am: 09.05.2022
Mündliche Prüfung am: 06.07.2022

Referenten
Prof. Dr.-Ing. Patrick Görrn
Prof. Dr. rer. nat. Thomas Riedl

2023

Acknowledgments

The scientific results presented in this thesis were obtained under the funding from the European Research Council (ERC), the Ministerium für Wirtschaft, Innovation, Digitalisierung und Energie des Landes Nordrhein-Westfalen (EFRE), and Photonik Forschung Deutschland (BMBF). This thesis was written at the Lehrstuhl für Großflächige Optoelektronik (LGOE), Faculty 6 of the University of Wuppertal.

First, I want to thank my supervisor Prof. Dr.-Ing. Patrick Görrn who enabled me to pursue my doctorate at the LGOE. His scientific guidance and inexhaustible commitment to my supervision was greatly helpful to make this thesis a success. Thank you.

Second, I thank Prof. Dr. rer. nat. Thomas Riedl to take the position of the second assessor of my thesis.

Furthermore, I want to thank all co-workers who work and have worked at the LGOE and the Lehrstuhl für Elektronische Bauelemente (LFEB). Herein, I want to mention Prof. Dr.-Ing. Hella-Christin Scheer, Dr.-Ing. Ralf Heiderhoff, Dr.-Ing. Detlef Theirich, Karsten Brennecke, Kai Oliver Brinkmann, Tobias Haeger, Tim Hasselmann, Manuel Runkel, Manuel Theisen, Christian Tückmantel, Florian Zimmermann, Dr.-Ing. Andreas Behrendt, Dr.-Ing. Sara Trost, Dr.-Ing. André Räupke, Dr.-Ing. Lukas Hoffmann, Dr.-Ing. Neda Pourdavoud, Dr.-Ing. Tobias Gahlmann, Dr.-Ing. André Mayer, Dr.-Ing. Marc Papenheim, Dr.-Ing. Christian Steinberg, Dr.-Ing. Si Wang, Johannes Staabs, Miriam Schröer and Johannes Rond for many scientific talks, an exciting working atmosphere and seven unforgettable years, which we shared together.

A special thanks goes to Maximilian Buchmüller, Andreas Henkel, Ivan Shutsko, Christopher Knoth and Sven Oliver Schumacher for countless helpful talks and support in hard times. We started our journey as colleagues and we part ways as friends.

Moreover, I want to thank all the student workers at our Chair and the students who carried out their Bachelor and Master thesis under my supervision. Herein, I would like to mention Kevin Wrobel, Leies Albus, Daniel Kluger, Milad Cheraghi, Christopher Knoth, Sven Oliver Schumacher, Fabian Kröber, Chakan Bogiadzi, Tobias Müller, Maximillian

Buchmüller, Robin Sander, Jason Littig and Kai Buchholz.

Last, I am deeply thankful to my wife Cleo, to my parents Helga and Michael, to my brother and his wife Steve and Katja, to my grandfather Rolf, to my parents-in-law Ina and Meudt, to my brothers-in-law Kjelle and Jan, to their partners Anne and Jean, and to all my friends and other family members for their support and understanding throughout my doctorate.

Contents

Chapter 1

Introduction

In the face of the climate change [1–4], establishing renewable, climate neutral, and local sources of energy is one, if not the one key challenge of our generation, and upcoming generations [5, 6]. This challenge is called the 'energy transition' [7]. Although the energy transition has been set as a top priority in politics (see for example the 'Climate Agreement of Paris' [8] from 2015), it has turned out that its local progress is of strongly varying pace [9]. Altogether, humanity lags behind the initial goal of limiting the global warming to an average temperature increase of 2.0°C in the time span from the begin of the industrialization to the year 2100 [9]. Further reducing the costs of renewable energies via technological innovation is, thus, an important key step to master the energy transition [10, 11].

1.1 Why Solar Concentrators?

Currently, there are several promising sources of renewable energy which are capable of facing global warming. Biochemical energy is based on producing energy from biomass and biofuels [12–15]. It is challenging to make use of biochemical energy due to low energy densities in biomass [16]. Furthermore, the use of biomass and biofuels for energy production causes secondary emissions of greenhouse gases. These greenhouse gases need to be isolated from the environment and safely stored to make biochemical energy environment friendly [17]. Wind and water energy are based on converting the kinetic energy of wind and water into electric energy [18–21]. Geothermal energy utilizes the earth's internal heat either for its direct use for heating applications or for electricity generation [22–25]. All of these energy sources mentioned above have the potential to replace fossil energy sources but are not realistically available everywhere (e.g. in urban environments) [26].

Solar energy can fill this gap and stands in front of a promising future for successfully integrating renewable energies as it can be easily harvested in urban environments [6, 9], and on empty, wind-still areas [27]. However, the average solar irradiance above the earth's atmosphere, called 'solar constant', is only approximately 1.3 kW/m^2 [6]. The effective solar irradiance on the earth's surface normal is significantly smaller due to the absorption and reflection by the atmosphere. Moreover, depending on the location on earth, a tilted incident angle of the solar irradiation with respect to the earth's surface can further reduce the solar irradiance. Therefore, very large areas have to be covered to collect useful amounts of solar energy [6]. As a consequence, an appropriate solar energy technology must exhibit low production and maintenance costs, high rates of production, and low primary and secondary emissions of greenhouse gases per area [6, 11, 28–31].

Today, two solar energy technologies dominate the market: solarthermics and photovoltaics. Solarthermics are based on converting solar energy to heat energy which is then either directly used (e.g. to heat buildings [32–34]), stored [34–36] or converted to electrical energy [34, 35, 37, 38]. In their simplest form, solarthermics devices consist of a surface, which absorbs light and infrared radiation, and a heat conductor or heat conducting medium which transports the heat to a desired location [35, 39, 40].

Photovoltaics are based on directly converting solar energy to electrical energy and have emerged as a key technology [6, 27, 28, 41]. Since 2008, the costs per Watt of silicon based photovoltaics has been drastically reduced as a result of the upscaling of production lines, and the reduction of silicon prices [11, 42]. As a result, photovoltaics emerged as a competitive technology against fossil energy technologies. At the moment, only around 2% of the world's electricity production are covered by photovoltaics [43]. However, the production rate and generated electrical power of silicon-based photovoltaics increases rapidly [9, 42, 44]. In addition, very recent next generation photovoltaics based on perovskites might reduce the costs and increase the production rate of photovoltaics even further [45, 46]. Due to these developments, it is predicted that, in the year 2050, a significant portion of the world's electricity production will be highly likely realized by photovoltaics [42, 44, 47, 48]. It is further expected that, due to other renewable energy sources, the use of fossil energy sources could be drastically reduced [9, 11, 49]. These circumstances provide an optimistic prospect for the climate's future. Nonetheless, it is crucial to question how these trends can be further boosted and whether there are ways to reduce the amount of materials and industrial processes which harm the environment.

Indeed, there is one way to boost both solarthermics and photovoltaics: the concentration of solar power via low-cost, environment-friendly solar concentrators [50, 51]. By concentrating the incident solar power from a large area A_{in} to a small focus spot area A_{spot} via solar concentrators, the power density can be increased by a maximum factor

of $C = A_{in}/A_{spot}$ [50].

Concerning solarthermics, an absorptive material exhibits significantly larger temperatures through concentration [52]. As it is known from the Carnot limit from thermodynamics [53], a larger relative temperature increases the efficiency of a heat engine [54]. The kinetic energy produced by a heat engine can then be converted into electrical energy [52]. In total, the concentration of light increases the conversion efficiency from solar energy into electrical energy. This concept is commonly used for solar thermal power plants (CSPs) and has been established as viable alternative to fossil energy sources [52, 55].

Concerning photovoltaics, the concentration of light can be regarded as a reduction of the area size of a solar cell by a factor of $1/C$, whereby approximately the same amount of energy per area is harvested. This method is called 'concentrated photovoltaics' (CPV) [56–59]. Hereby, concentrated photovoltaics can reach larger energy conversion efficiencies than conventional photovoltaics under appropriate thermal management. For instance, it is stated in current reports that the use of multijunction solar cells combined with concentrated light enables record energy conversion efficiencies [60]. For single junction solar cells, concentrated light can lead to increased energy conversion efficiencies as a result of larger open-circuit voltages [56, 61]. This renders CPV as an interesting route to follow. Assuming that a solar concentrator can be fast produced at low costs, it seems possible to either reduce the necessary solar cell area by a factor of $1/C$, or increase the production rate by a factor C, and increase the total energy conversion efficiency per area by using high efficiency solar cells of small area sizes. Hereby, excess heat can be further utilized in thermoelectrics [62–64] or in similar ways as for conventional solarthermics [65].

However, these advantages and promises of solar concentrators only account for a static light source: in fact, the Sun's azimuth and angle of elevation are constantly changing throughout the day and season. Now considering a light concentrator (e.g. a conventional Fresnel lens) under the moving Sun, the position of the spot of concentrated Sun-light constantly shifts depending on the daytime and date. From a naive point of view, it might be suspected that a well-engineered concentrator design could compensate this shifting. Unfortunately, here comes a fundamental limit of solar concentrators into play: the second law of thermodynamics forbids that the concentration exceeds a value of [66]

$$C_{lim,2D} = \frac{n_c'^2}{\sin \Delta\theta_{LS}{}^2}, \tag{1.1}$$

whereby n_c' is a light concentrator's refractive index and $\Delta\theta_{LS}$ is the half-opening angle of a light source (e.g. the Sun). Hereby, it is assumed that the angular distribution of the light source is disk-shaped, so that its solid angle Ω is approximated by θ_{LS}^2. For the concrete example of the Sun, $\Delta\theta_{LS}$ is approximately 0.26°, so that the maximum

concentration in air is $C_{lim,2D} \approx 48562$ [66]. For reasons of reciprocity, $\Delta\theta_{LS}$ is also the 'static acceptance angle' of the concentrator with respect to a fixed spot position [66]. In other words, a passive light concentrator of high concentration will only focus light onto a receiver (the solar cell or absorber) for a short duration of time throughout the day and the time-averaged collection efficiency is small. In reverse, a concentrator which focuses light onto the receiver for a longer amount of time cannot provide high concentration.

To elevate the time-averaged efficiency, the system of concentrator and receiver must be constantly adapted to the Sun's azimuth and angle of elevation. Such an adaption is called 'Sun-tracking' and is aimed to obtain an increased 'dynamic acceptance angle' [66, 67]. For instance, both the concentrator and receiver can be mounted on a goniometric stage, which follows the Sun's position at the sky [66, 68]. At the first sight, in a world full of automated technology, Sun-tracking does not seem like a hard challenge. In fact, the requirements on active trackers are challenging to say the least. They must be long-lived, accurately controllable, easily programmable, reliable, cost-efficient on the investment and maintenance level, ideally light-weight, and robust to environmental influences (e.g. wind loads, large temperature changes, rough weather conditions, dust, sand, corrosion, etc.) [69, 70]. Taking all these requirements together, the realization of CPV has turned out significantly more expensive than conventional photovoltaics [70]. In addition, CPV systems are often too heavy to be installed on roof-tops. In consequence, CPV almost completely disappeared from the market and is currently considered as a dead field [70].

Why then should anybody care about CPV nowadays? The answer is simply that the promises of CPV still hold true when cost-efficient Sun-tracking could be realized. First of all, it is important to recognize that there have been many technological innovations since CPV has been mostly abandoned by the industry [70]. These innovations will be elaborated in the next Section.

1.2 Existing Solar Concentrators and Tracking Technologies

The first generations of solar concentrators are based on the same principle: first, a solar concentrator with a desired static acceptance angle is designed using the principles of geometric optics. For instance, the most common designs of such concentrators are largely dimensioned parabolic through concentrators (PTC) [71,72], parabolic dish concentrators (PDC) [73–75], compound parabolic concentrators (CPC) [76–78], heliostat mirror arrays (HMA) [52, 79], and Fresnel lenses [80–82] or mirrors [83, 84]. Depending on the type of concentrator, direct incident Sun-light is concentrated on a focal line or focal point. To

compensate the movement of the Sun at the sky, 1-axis or 2-axis trackers are combined with the solar concentrators [68,85–89]. Herein, the complexity of a tracker system largely depends on the solar-concentrators' acceptance angle [68, 85–89].

The next generation of solar concentrators, whatsoever, relies on different approaches which come along with several advantages. One development to mention is solar concentrators in combination with micro tracking. Instead of largely dimensioned single concentrators, the concentration of light is realized within a panel of many individual concentrators and Sun-tracking is realized by the small mechanical movements of internal parts. For instance, free form optics [90] or arrays of Fresnel lenses (with or without secondary optics) are used [91–95]. Herein, the tracking is typically realized via a translational movement of a receiver plate within a plane [91–95]. This way, the complicated mechanics (goniometric stages with high-load joints) of two-axis trackers could be reduced to a technologically much simpler mechanics (linear translation stages). On the lab-scale, micro tracking has been demonstrated to show time-averaged efficiencies of around 30% using a GaAs micro-solar cell [96].

Another development is the use of planar waveguides. Using the phenomenon of total internal reflection, it is aimed to trap Sun-light within a waveguide and to subsequently guide it to solar cells which are, for example, placed at the waveguide's outer facets [97–104]. This way, the large three-dimensional distances between the concentrator and its focal line (or focal spot) of first-generation concentrators are converted to lateral dimensions within the waveguide. Most existing concepts of waveguide concentrators are based on the use of an array of focusing elements (e.g. micro lens arrays), and small-sized light coupling elements [91,101,105–108]. This way, the probability that light is scattered out on its way to the waveguide's facet is minimized so that the achievable concentration is maximized. Herein, many waveguide based solar concentrators can benefit from micro tracking as well [91, 101, 105–108].

The advantages of next-generation solar concentrators and micro tracking in comparison to first generation solar concentrators and trackers are mostly given by their reduced bulkiness [109]. Reduced bulkiness ultimately renders CPV and CSP as feasible for roof-top installations, comes along with reduced issues with respect to shadowing, and potentially decreases the overall investment and maintenance costs [70, 109].

Nonetheless, it is obvious that the best way to further improve next-generation solar concentrators and trackers is to either get rid of any moving mechanical parts or largely simplify their mechanical complexity. Very recently, there have been interesting new concepts to tackle these challenges. Two novel concepts are the use of smart materials [110, 111] or simplistic mechanics and artificial intelligence (AI) [112–115] to revive first generation solar concentrators and trackers. For instance, start-up projects have been showing

convincing evidence that concentrated solarthermics with low-cost heliostat mirror arrays controlled by AI reach comparable time-averaged efficiencies as for conventionally controlled high-cost heliostat mirror arrays. Electrical beam steerers based on tunable liquid-liquid interfaces promise to enable Sun-tracking by steering the Sun-light onto a fixed conventional solar concentrator [109, 116, 117]. Another concept is to make use of dynamical systems: there exist several reports for waveguide based solar concentrators, which exhibit dynamical light coupler elements. Such dynamical light coupler elements automatically adapt to the Sun's position in the sky without any need of control systems and have been realized via micro actuators [118, 119], phase-change materials [120], light-sensitive colloidal solutions [121] and thermally induced bubble generation [122]. However, so far, the experimentally obtained time-averaged efficiencies of systems with dynamical light coupler elements are rather small. To solve these challenges, new concepts for future solar concentrators and trackers without the necessity of moving mechanical parts are currently sought. In a nutshell, an efficient future generation solar concentrator with mechanics-free Sun-tracking could indeed deliver a new boost for CPV and perhaps for CSP as well.

1.3 Scope of the thesis

In this thesis, waveguide-based systems and other optical systems are investigated and put in the context of existing solar energy technologies. First, a theoretical basis on waveguides, plasmonics, and periodic structures (gratings) will be given. Second, experimental techniques as well as fabrication methods will be explained. Experimental results on various structured waveguides and optical systems for broadband light coupling and long distance propagation of light will be demonstrated. Third and last, a strategy to actively control the coupling of light into and out of waveguides without the use of moving mechanical parts will be provided in theory and experiment. This strategy will be discussed with respect to its potential significance as a fundament for future solar concentrators and trackers.

Chapter 2

Electromagnetic Theory of Waveguides and Structured Systems

Over the course of this chapter, the fundamental physics to understand the behavior of electromagnetic waves in planar and structured geometries will be given. Subsequently, important measures of interest will be defined with the help of some simple examples. These examples cover the eigenmodes of optical slab waveguides, the properties of plasmons, and the eigenmodes of waveguide gratings. With this knowledge, the physics of more complicated geometries as discussed in our scientific publications as well as in Chapter 4 can be understood more intuitively.

2.1 Maxwell equations

The fundament of the physical behavior of optical systems is given by a set of a few fundamental equation, namely the Maxwell equations and the material equations [123]. For the treatment of steady-state electromagnetic waves (including light), the time-harmonic Maxwell equations with the time-phasor $e^{-j\omega t}$ have to be considered. They are given by [123, 124]

$$\vec{\nabla} \cdot \vec{D} = \rho \tag{2.1}$$

$$\vec{\nabla} \times \vec{E} = j\omega\mu\vec{H} \tag{2.2}$$

$$\vec{\nabla} \cdot \vec{B} = 0 \tag{2.3}$$

$$\vec{\nabla} \times \vec{H} = \vec{J} - j\omega\varepsilon(\omega)\vec{E} \tag{2.4}$$

with

$$\vec{\nabla} = \begin{pmatrix} \partial/\partial x \\ \partial/\partial y \\ \partial/\partial z \end{pmatrix} \tag{2.5}$$

as the 'Nabla operator', ρ as the volume density of external electric charges and $\vec{J}$ as the density of external electric currents [123, 124]. Importantly, the Maxwell equations are a system of coupled linear differential equations and, thus, the electromagnetic fields underlie the principle of superposition ($\vec{E}_{tot} = \sum_i \vec{E}_i, \vec{H}_{tot} = \sum_i \vec{H}_i$) [123, 124].

The material equations are given by [123]

$$\vec{D} = \varepsilon_0\vec{E} + \vec{P} = \varepsilon\vec{E} = \varepsilon_0\varepsilon_r\vec{E}. \tag{2.6}$$

$$\vec{B} = \mu\vec{H} = \mu_0\mu_r\vec{H}. \tag{2.7}$$

with $\vec{P}$ as the polarization density. Herein, ε_0 and μ_0 are the natural constants of the electric permittivity (termed electric constant) and the magnetic permeability. ε_r and μ_r take into account all material related effects [123, 124]. As a side note, all materials considered in this thesis are either para- or diamagnetic, so that μ_r can be set to 1 in very good approximation. ε_r, whatsoever, strongly varies as a function of space (ε_r=$\varepsilon_r(x, y, z)$). Furthermore, the relative permittivity can be a complex-valued quantity $\varepsilon_r = \varepsilon_r' + j \cdot \varepsilon_r''$. Materials with loss or gain exhibit positive or negative values of ε_r'', respectively [123, 124].

In the absence of external charges and currents ($\rho = 0, \vec{J} = 0$), the Maxwell Equations can be used to derive the wave equations

$$\frac{1}{c^2}\frac{\partial^2\vec{E}}{\partial t^2} - \vec{\nabla}^2\vec{E} = 0 \tag{2.8}$$

$$\frac{1}{c^2}\frac{\partial^2\vec{H}}{\partial t^2} - \vec{\nabla}^2\vec{H} = 0 \tag{2.9}$$

with the 'Laplace operator' $\vec{\nabla}^2$, and

$$c = \frac{1}{\sqrt{\varepsilon\mu}} = \frac{1}{\sqrt{\varepsilon_0\mu_0}}\frac{1}{\sqrt{\varepsilon_r\mu_r}} = \frac{c_{vac}}{n}, \tag{2.10}$$

whereby $c_{vac} = 1/\sqrt{\varepsilon_0\mu_0}$ is the vacuum speed of light and $n = \sqrt{\varepsilon_r\mu_r}$ is the refractive index $n = n' + j \cdot n''$ [123–125]. The solutions of these differential equations are electromagnetic waves, including light with wavelengths in the visible range between 380 nm and 780 nm [123].

The task of concentrating light can be understood as the task to guide the power flow of electromagnetic fields into small spatial dimensions. This power flow needs to be defined. Following Poynting's theorem [123], the net change of the electromagnetic energy W per time in a given volume V can be generally expressed by [123]

$$\frac{\partial W}{\partial t} = \frac{\partial}{\partial t}\int_V w \,\mathrm{d}V = \frac{\partial}{\partial t}\int_V \frac{1}{2}(\varepsilon|\vec{E}|^2) + \mu|\vec{H}|^2)\,\mathrm{d}V = -\oint_{\partial V}(\vec{E}\times\vec{H})\,\mathrm{d}\vec{A} - \int_V \vec{J}_{ind}\vec{E}\,\mathrm{d}V \tag{2.11}$$

with $\vec{J}_{ind} = \varepsilon''\omega\vec{E}$. The left side of the equation introduces the energy density w of the electromagnetic field. On the ride side of the equation, the first term of the equation describes the net power flow out through the closed surface ∂V of V, whereby $\vec{S} = \vec{E}\times\vec{H}$ defines the Poynting Vector $\vec{S}$ [123]. The second term describes losses into any other forms of energy than electromagnetic fields (into thermal energy via Ohmic losses) [123].

With the integrated time-averaged Poynting vector [123]

$$\oint_{\partial V}\langle\vec{S}\rangle\,\mathrm{d}\vec{A} = \frac{1}{2}\oint_{\partial V}\mathrm{Re}(\vec{E}\times\vec{H}^*)\,\mathrm{d}\vec{A} \tag{2.12}$$

and the power loss [123]

$$P_{loss} = \frac{1}{2}\int_V \mathrm{Re}(\vec{J}_{ind}\vec{E}^*)\,\mathrm{d}\vec{V} \tag{2.13}$$

the net power flow (in the absence of external charges and currents) can be interpreted as a multi-port described by

$$\oint_{\vec{A}}\langle\vec{S}\rangle\,\mathrm{d}\vec{A} = -P_{in} + P_{out} + P_{loss} = 0 \tag{2.14}$$

as it is visualized in Fig. 2.1. P_{in} and P_{out} are the total incoming and outgoing powers, respectively. The normalized power loss

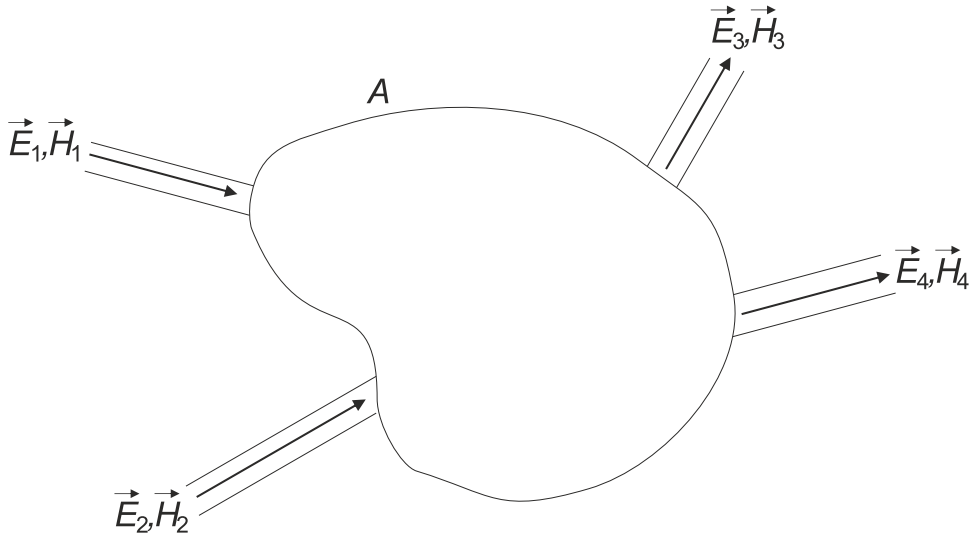

Figure 2.1: Multiport of electromagnetic waves

$$A = \frac{P_{loss}}{P_{in}} \tag{2.15}$$

is called the 'absorption' A [123].

As a side note, this separation of the surface integral into a sum of powers is not trivial as the Poynting-vector is inherently non-linear. Here, it can be applied as long as the incoming and outgoing waves can be expressed by propagating plane-waves [123, 124].

2.1.1 Plane-Wave-Spectrum, General Coupling Coefficients and Reciprocity

At a given frequency ω, a majority of the solutions of equations 2.8 and 2.9 can be expressed by a plane-wave spectrum [123, 124, 126]

$$\vec{E}(\vec{r},\omega,t) = \int \hat{\vec{E}}(\vec{k},\omega) e^{j\vec{k}\vec{r}} e^{-j\omega t}\,\mathrm{d}^3\vec{k} \tag{2.16}$$

with $\hat{\vec{E}}$ as the spatial Fourier transform of $\vec{E}$, which is given by [123, 124, 126]

$$\hat{\vec{E}}(\vec{k},\omega) = \frac{1}{(2\pi)^3} \int \vec{E}(\vec{r},\omega,t) e^{-j\vec{k}\vec{r}} e^{-j\omega t}\,\mathrm{d}^3\vec{r}. \tag{2.17}$$

Importantly, any distribution of incident waves (e.g. a Gaussian beam, a beam of homogeneous intensity, sun-light) can be expressed by Eq. 2.16.

With this decomposition into plane-waves, it is possible to link the ingoing and outgoing

electric fields of a given multi-port by using a coupling matrix

$$\vec{E}_{0,j}(\vec{k}_j) = \underline{C}\vec{E}_{0,i}(\vec{k}_i). \tag{2.18}$$

Once all elements of $\underline{C}$ are known and an incident plane-wave spectrum is known, all outgoing plane-waves can be calculated. These elements are called 'coupling coefficients'. For example, a mirror would contain elements of $\underline{C}$, which flip the sign of the component of $\vec{k}$ of a plane-wave parallel to the mirror's surface normal.

In the case of time-invariant, linear and isotropic materials, it can be shown that the principle of reciprocity must be fulfilled [127]

$$\oint_{\partial V} (\vec{E}_{0,i} \times \vec{H}_{0,j}) - (\vec{E}_{0,j} \times \vec{H}_{0,i}) \, \mathrm{d}\vec{A} = 0 \tag{2.19}$$

Reciprocity can be understood in a way that a light source and a detector can switch places and the received signals remain the same [127]. Reciprocity thus allows to predict the scattering behavior of waves by reversing the arrow of time for a known field solution. For example, if a lens focuses a parallel beam to a distinct spot size at its focal plane, the reverse process of parallelizing a spot source of light using the same lens will work as well.

At this point, the given mathematical expressions treat the multi-port as a black box. As a matter of course, the spatial information of ε_r dictates the elements of $\underline{C}$ and the majority of this thesis deals with the exploration of distinct configurations of ε_r.

Further practical meaning of the plane-wave spectrum, coupling coefficients and reciprocity will become clear when concrete examples are explained in the upcoming sections.

2.1.2 Boundary Conditions

In its integral form (assuming finite field strengths), the Maxwell equations imply certain conditions concerning the behavior of the tangential (indexed as E_t) and normal (indexed as D_n) components of the electric and magnetic fields at an interface between materials of different values of $\varepsilon_{r,1}$ and $\varepsilon_{r,2}$. These conditions are [123]

$$E_{t,1} = E_{t,2} \qquad \text{and} \qquad D_{n,1} = D_{n,2} \tag{2.20}$$

for the electric field strength and electric flux density [123]. Concerning the magnetic

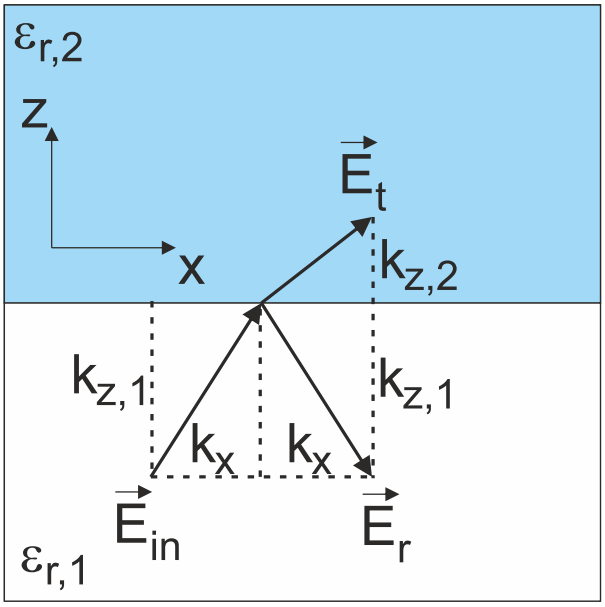

Figure 2.2: reflection and transmission at a planar interface between two materials of relative permittivities $\varepsilon_{r,1}$ and $\varepsilon_{r,2}$. According to ref. [123].

field strength and flux density, both are analogously given by [123]

$$H_{t,1} = H_{t,2} \qquad \text{and} \qquad B_{n,1} = B_{n,2}, \tag{2.21}$$

since all materials are assumed to be non-magnetic ($\mu_{r,1} = \mu_{r,2} = 1$).

One basic phenomenon attributed to this interface is the occurrence of reflection and transmission (see Fig. 2.2). Plane waves in the form of

$$\vec{E}_1 = \vec{E}_{in} \cdot e^{j(k_x x + k_{z,1} z)} e^{-j\omega t} + \vec{E}_r \cdot e^{j(k_x x - k_{z,1} z)} e^{-j\omega t} \tag{2.22}$$

and

$$\vec{E}_2 = \vec{E}_t \cdot e^{j(k_x x + k_{z,2} z)} e^{-j\omega t} \tag{2.23}$$

are assumed using the relations $k_{z,j} = \sqrt{\varepsilon_{r,j} k_0^2 - k_x^2}$, $k_0 = 2\pi/\lambda$ and $\omega = c_{vac} k_0$ [123]. Herein, it is anticipated that both wavevector components can be complex in general

$$k_x = k_x' + j k_x'' \tag{2.24}$$

$$k_{z,j} = k_{z,j}' + j k_{z,j}'', \tag{2.25}$$

whereby k_x' is called the 'lateral momentum' [123, 124].

The continuity of the electromagnetic fields (Eqs. 2.20 and 2.21) leads to the Fresnel equations [123]. Considering s-polarized light (TE) with $E_y = |\vec{E}|, E_x = E_z = 0$ and $H_y = 0$, they read [123, 124]

$$r = r_{1,2} = \frac{k_{z,1} - k_{z,2}}{k_{z,1} + k_{z,2}} \tag{2.26}$$

and [123, 124]

$$t = t_{1,2} = \frac{2k_{z,1}}{k_{z,1} + k_{z,2}}. \tag{2.27}$$

r and t are called 'reflection coefficient' and 'transmission coefficient' [123, 124]. A comparison with Eq. 2.18 shows that r_{12} and t_{12} are the coupling coefficients of the coupling matrix attributed to the single interface. They set the reflected and transmitted fields E_r and E_t in relation to the incident field E_{in}.

For p-polarized light (TM) with $E_y = 0$ and $H_y = |\vec{H}|, H_x = H_z = 0$, analogous considerations lead to the expressions [123]

$$r = r_{1,2} = \frac{\varepsilon_{r,2}k_{z,1} - \varepsilon_{r,1}k_{z,2}}{\varepsilon_{r,2}k_{z,1} + \varepsilon_{r,1}k_{z,2}} \tag{2.28}$$

and [123]

$$t = t_{1,2} = \frac{2\varepsilon_{r,2}k_{z,1}}{\varepsilon_{r,2}k_{z,1} + \varepsilon_{r,1}k_{z,2}}. \tag{2.29}$$

Normalizing P_{in} to 1, the evaluation of the power balance leads to [123]

$$1 = R + T + A, \tag{2.30}$$

whereby R and T are termed as 'reflectance' and 'transmittance' and are given by [123]

$$R = |r|^2 \tag{2.31}$$

and [123]

$$T = \mathrm{Re}(\frac{k_{z,2}}{k_{z,1}})|t|^2. \tag{2.32}$$

In general, Eqs. 2.31 and 2.32 can be applied on any planar geometry including multiple interfaces, whereby r and t then describe the reflected and transmitted fields outside

of the geometry [123]. In the next section, an example in the form of a planar optical waveguide will be provided.

2.2 Planar optical waveguides

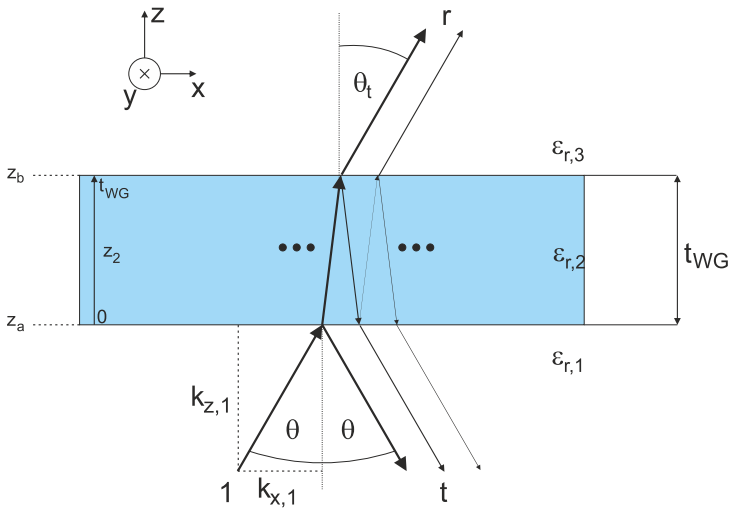

Figure 2.3: The definition of a homogeneous planar waveguide.

A symmetric slab waveguide [123, 124, 128] defined by a substrate, a loss-free dielectric layer and a superstrate with

$$\varepsilon_r(z) = \begin{cases} \varepsilon_{r,1} = n_s^2 & (z < z_a), \\ \varepsilon_{r,2} = n_f^2 & (z_a \leq z \leq z_b), \\ \varepsilon_{r,3} = n_s^2 & (z > z_b) \end{cases} \tag{2.33}$$

with $n_s < n_f$ will be considered in the following lines (see Fig. 2.3). As this geometry is translationally invariant with respect to both the x- and y direction, the x-z-plane is arbitrarily chosen as the plane of incidence for mathematical simplicity. As in Section 2.1, a plane wave ansatz of the form

$$\vec{E} = \vec{E_0} \cdot e^{j(k_x x + k_z z)} e^{-j\omega t} \tag{2.34}$$

and

$$\vec{H} = \vec{H_0} \cdot e^{j(k_x x + k_z z)} e^{-j\omega t} \tag{2.35}$$

is used.

First, the boundary conditions of the waveguide are solved for TE polarized waves. Assuming a wave of amplitude 1 incident from $z < z_a$ and no incident waves else, the electric

field for each region can be expressed by

$$E_t(x,z,t) = \begin{cases} (1 \cdot e^{jk_{z,1}z_1} + g_1 \cdot e^{-jk_{z,1}z_1}) \cdot e^{jk_x x} & (z < z_a), \\ (f_2 \cdot e^{jk_{z,2}z_2} + g_2 \cdot e^{jk_{z,2}(t_{WG}-z_2)}) \cdot e^{jk_x x} & (z_a \leq z \leq z_b), \\ f_3 \cdot e^{jk_{z,3}z_3} \cdot e^{jk_x x} & (z > z_b) \end{cases} \tag{2.36}$$

using $t_{WG} = z_b - z_a$ and local coordinates $z_1 = z$, $0 \leq z_2 \leq t_{WG}$ and $z_3 = z - t_{WG}$ [129]. These local coordinates can be understood as follows: a value of $z_1 = 0$ corresponds to $z = z_a$, values of z_2 in between 0 and t_{WG} correspond to values of z in between z_a and z_b, and a value of $z_3 = 0$ corresponds to $z = z_b$. The reason for using these local coordinates is that additional layers can be easily added to the waveguide as it will be explained in Section 2.4. This way, f_j are the amplitudes of plane waves entering a layer (indexed by 'j') at $z_j = 0$ and g_j are the amplitudes of reflected plane waves reflected at $z_j = t_j$. For the substrate and superstrate, t_j is set to a value of zero. The positive and negative values of $k_{z,j}$ represent forward and backward propagating waves with respect to the z-direction. As side note, the unit of the electric field (V/m) is neglected for simplifying the calculation. Further Note that the notation of amplitudes in Eq. 2.36 was chosen to simplify the expressions for periodically structured layers later on.

The boundary conditions of the tangential field components in Eqs. 2.20 and 2.21 demand that the electric field strength must be a continuously differentiable function with respect to the z-direction and allow to determine all amplitudes g_1, f_2, g_2 and f_3.

A comparison of Eqs. 2.36 with the coupling matrix in Eq. 2.18 immediately shows the relation between these amplitudes and the coupling coefficients: Here, the inputs and outputs of the input-output-network are the incident plane wave of amplitude 1 and the reflected and transmitted plane waves of amplitudes g_1 and f_3, respectively. In other words, the coupling coefficients for this example are the reflection and transmission coefficients r and t of the slab waveguide, which can be identified by

$$r = g_1 = \frac{r_{1,2} - r_{1,2}e^{-2j\Phi}}{1 - r_{1,2}^2 e^{-2j\Phi}} \tag{2.37}$$

and

$$t = f_3 = \frac{t_{1,2}t_{2,3}e^{-j\Phi}}{1 - r_{1,2}^2 e^{-2j\Phi}} \tag{2.38}$$

using the round-trip phase $2\Phi = 2k_{z,2}t_{WG}$ as well as the reflection and transmission coefficients $r_{i,j}$ and $t_{i,j}$ at each interface as described in Section 2.1 [128].

Concerning k_x, there exist the two cases $|k_x| < n_s k_0$ and $n_s k_0 \leq |k_x| \leq n_f k_0$. For the

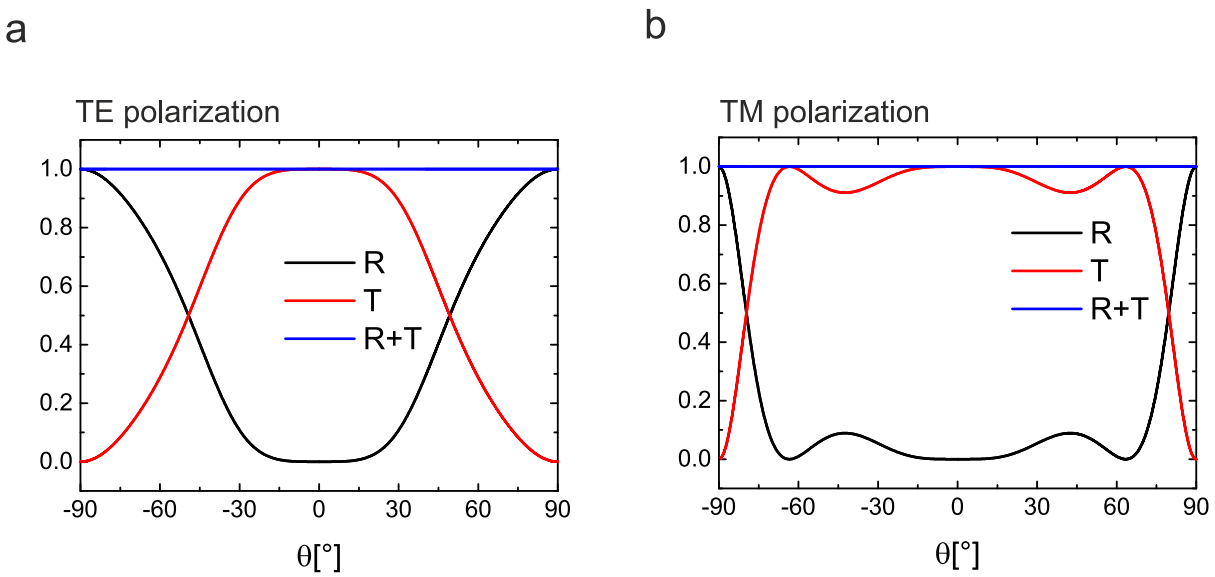

Figure 2.4: a,b) The transmittance T and reflectance R for TE and TM polarized light incidence.

first case, each $k_{z,i}$ is real-valued, displaying plane-waves, which fall onto the waveguide coming from infinity and subsequently reflect from or transmit through it [128, 129]. An exemplary plot of R and T with the parameters $\lambda = 500$ nm, $t_{WG} = 500$nm, $n_s = 1.0$ and $n_f = 2.0$ as a function of $\sin\theta = \arcsin(k'_x/k_0)$ is shown in Fig. 2.4.

It has to be mentioned that $|g_2|$ and $|f_2|$ may occupy values above 1. This is due to the fact that photons remain in the resonator for a distinct period of time t_R. This time period is proportional to the number of round-trips Q (also termed as Q-factor), which photons statistically undergo before they leave the resonator again. As a result, energy is stored inside the resonator and only a portion of $1/Q$ per time interval contributes again to the net power flow [124, 128, 129]. Coming back to the amplitudes f_2 and g_2 later on again, this capability of storing energy will become of particular importance for structured waveguides (see Section 2.16).

For the second case $n_s k_0 \leq |k'_x| \leq n_f k_0$, $k_{z,1}$ and $k_{z,3}$ become purely imaginary numbers, indicating exponentially decaying and growing terms of E_y in the substrate and superstrate. Furthermore, the reflection coefficient can be written as $r_{1,2} = 1 \cdot e^{j\Phi_{r_{1,2}}}$, whereby the amplitude of 1 indicates total internal reflection [124]. To prevent exponentially growing terms, the amplitude of the incident wave must be chosen to zero. Non-trivial solutions of the boundary conditions then only occur at the poles of r and t (see Eqs. 2.37 and 2.38) [129]. These poles are defined by the vanishing of their denominators [128, 129]

$$1 - r_{1,2}^2 e^{-2j\Phi} = 1 - 1 \cdot e^{-j(2\Phi - 2\Phi_{r_{1,2}})} = 0 \tag{2.39}$$

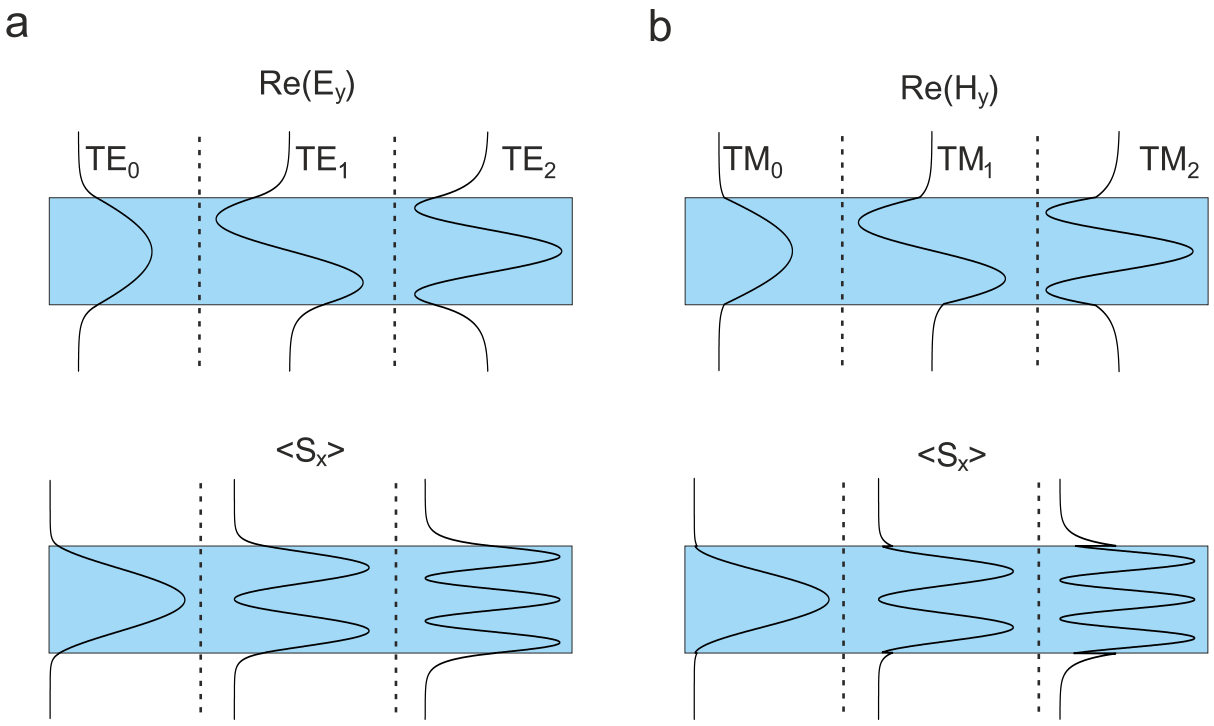

Figure 2.5: a,b) Field distributions and x-components $\langle S_x \rangle$ of the time-averaged Poynting vector $\langle \vec{S} \rangle$ for the first three Eigenmodes (TE_l and TM_l) of the geometry shown in Fig. 2.4.

The solutions for this equation are given by [128, 129]

$$2\Phi - 2\Phi_{r_{1,2}} = l \cdot 2\pi, l \in \mathbb{Z} \tag{2.40}$$

Eq. 2.40 is also known as the characteristic equation. The l^{th} solution of the characteristic equation is called a 'TE_l eigenmode'. For each eigenmode, an effective refractive index $k_x = n_{eff} k_0$ can be attributed [125]. These eigenmodes can be found for $n_s < |n'_{eff}| < n_f$. Geometrically interpreted, n'_{eff} defines the angle $\theta_{int} = \arcsin(n'_{eff}/n_f)$ under which plane-waves propagate inside the layer. Fig. 2.5a shows both the normalized real part of the tangential field E_y and the x-component of the time-averaged Poynting vector $\langle \vec{S} \rangle$ of the first three TE modes as a function of z for $t_{WG} = \lambda$, $n_s = 1.0$ and $n_f = 2.0$. Inside the layer, E_y is characterized by a standing-wave with l nodes (with respect to the z-direction). Outside the layer, both E_y and $\vec{H}$ decay exponentially. For this reason, the electromagnetic fields outside the layer are called 'evanescent fields'. $\langle \vec{S} \rangle$ has only a positive x-component. Therefore, the power flow into the substrate and superstrate is zero. It is confined in an eigenmode and the electromagnetic waves are guided by the waveguide [128, 129].

For TM polarization, analog considerations can be done, leading to the formation of TM_l modes [128, 129]. Using the same parameters, the first three TM modes are shown in Fig.

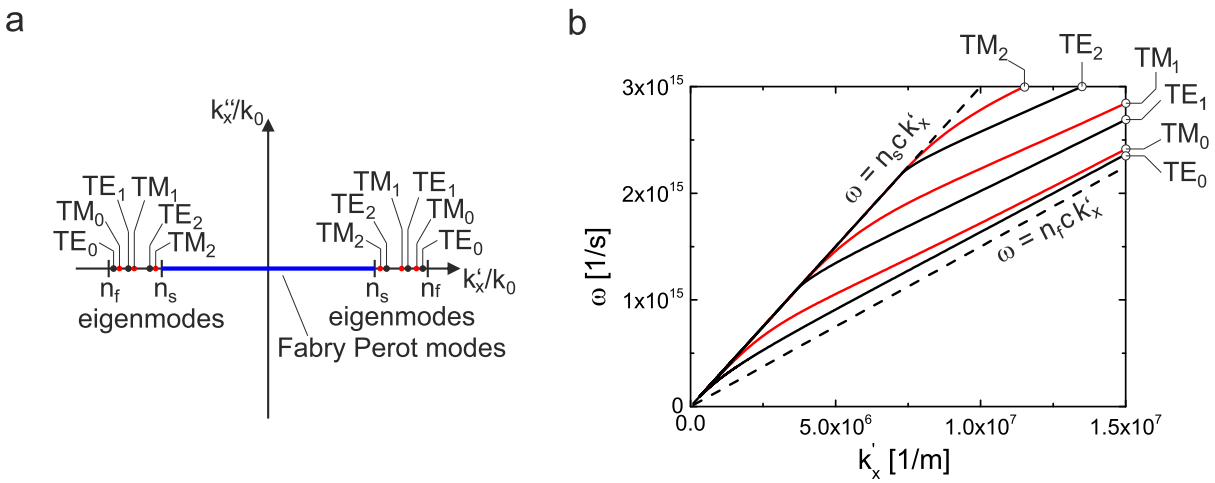

Figure 2.6: a) Complex plane of $k_x = k'_x + j \cdot k''_x$ including the modes in Figs. 2.4 and 2.5. b) Dispersion relation of a symmetric slab waveguide. Visualization according to ref. [123].

2.5b

Fig. 2.6a shows an overview of the phenomena explained above as function of $k_x = k'_x + j \cdot k''_x$ in the complex plane [128]. The so-called dispersion relation of an eigenmode $k'_x(\omega) = n'_{eff}(\omega)\frac{\omega}{c_{vac}}$ (with $k''_x = 0$) is displayed in Fig. 2.6b. Here, as a result of the waveguide's mirror symmetry with respect to the z-axis, it can be observed that the TE_0 and TM_0 eigenmodes can exist for arbitrarily small values of ω [128]. In contrast, each eigenmode of higher orders cannot exist below its characteristic cut-off frequency [128]. Over the course of this thesis, both the complex plane as well as dispersion relations will be used to characterize waveguides.

Another important type of diagram is the two-dimensional k-space diagram, in which data are plotted as a function of k'_x and k'_y [130]. For instance, it can be considered that a rotation of the waveguide at hand around the z-axis does not change the observed dispersion relations. Therefore, the sectional plane of k'_x and k'_y with the eigenmode's dispersion relations build circles of radii $n'_{eff}k_0$ (see. Fig. 2.7) [128].

2.3 Fundamentals of Plasmonics

Over the course of this thesis, several geometries using plasmonics will be discussed. To provide a basic body of knowledge to understand these phenomena, the fundamental properties of plasmons will be provided. Herein, the explanation of these properties will begin with bulk plasmons (3D), move to surface plasmons (2D), briefly explain plasmon waveguides (1D) and end with localized surface plasmons (0D).

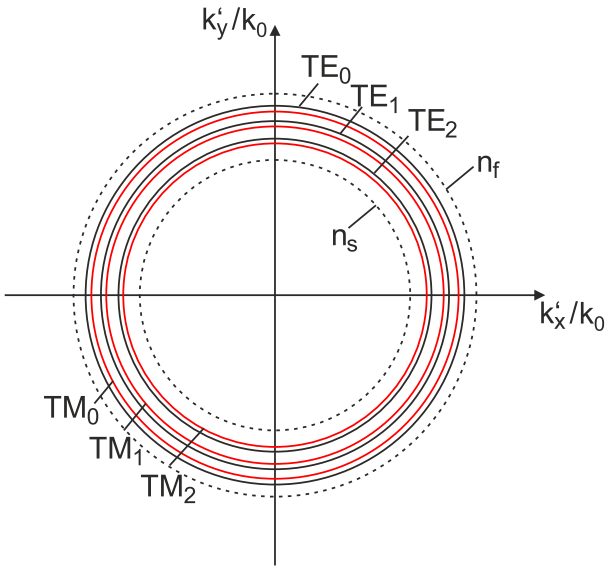

Figure 2.7: Schematic visualization of similar eigenmodes to the waveguide from Fig. 2.3 in the k'_x-k'_y plane (two-dimensional k-space diagram).

2.3.1 Bulk Plasmons (3D)

Bulk plasmons are charge oscillations inside a volume conductor. Their properties can be approximated considering a volume of a conductive material which is exposed to an external electric field of frequency ω. Herein, the charge carriers are assumed to move freely and form a so-called 'free electron gas' [131]. Two mechanisms describe the response of the free electron gas to the external electric field: first, the external field enforces an oscillation of the electrons of charge $-e$ due to the force $-e\vec{E}$. Second, the movement of the electrons inside the volume conductor is dampened (e.g. by Ohmic losses) with a dampening rate Γ. Both mechanisms can be expressed via the differential equation [131]

$$m_e\ddot{\vec{r}} + m_e\Gamma\dot{\vec{r}} = -e\vec{E}(t). \tag{2.41}$$

with m_e as the electron mass.

Solving this equation to $\vec{r}$ and taking the volumetric number density of charge carriers N_c into account, the polarization density is given by $\vec{P} = -N_c e\vec{r}$. Inserting this solution into Eq. 2.6 leads to the relation [131]

$$\varepsilon_r(\omega) = 1 - \frac{\omega_p^2}{\omega^2 + j\Gamma\omega} \tag{2.42}$$

with $\omega_p = \sqrt{N_c e^2/(\varepsilon_0 m_e)}$ as the 'plasma frequency' [131]. Note that the real values of ε may significantly deviate from an Eq. 2.42 as result of band structure effects [131]. For all calculations including metals in this thesis, the experimental data provided in ref. [132]

are used to obtain more realistic results.

2.3.2 Surface Plasmons (2D)

In Section 2.2, it was mentioned that the electric field strength has to be continuously differentiable for TE polarization. For TM polarization, the Maxwell equations do not demand this restriction. Here, H_y has only to be continuous and the electric field strength may even be discontinuous at interfaces [133].

This circumstance allows a special kind of eigenmode solution to exist, which only consists of evanescently decaying fields at one single interface. Using the same principles as in Section 2.2, this eigenmode can be identified by finding e.g. the pole of the reflection coefficient at an interface (see Section 2.1). Using, Eq. 2.28, a pole of r is then present when the characteristic equation [133]

$$\varepsilon_{r,1} k_{z,2} + \varepsilon_{r,2} k_{z,1} = 0 \tag{2.43}$$

is fulfilled, indicating that the real parts of $\varepsilon_{r,1}$ and $\varepsilon_{r,2}$ must have opposite signs (for $k_{z,1}, k_{z,2} > 0$). Such opposite signs occur at the interface of a metal and a dielectric material. The solution of the characteristic equation is called a 'surface plasmon' [133].

The dispersion relation of a surface plasmon can be expressed by [133]

$$k_x = \frac{\omega}{c_{vac}} \sqrt{\frac{\varepsilon_1 \varepsilon_2}{\varepsilon_1 + \varepsilon_2}} = k_0 \cdot n_{eff} \tag{2.44}$$

In contrast to the modes in Section 2.2, the effective index $n_{eff} = k_x/k_0 = n'_{eff} + i \cdot n''_{eff}$ is typically complex-valued for surface plasmons. Therefore, as both H_y, E_x and E_z contain the factor $e^{ik_x x}$, the time-averaged x component $\langle S_x(x) \rangle$ of the Poynting vector can be expressed by

$$\langle S_x(x) \rangle = \langle S_x(0) \rangle \cdot e^{-2k_0 n''_{eff} x} \tag{2.45}$$

and thus decays over to the fraction $1/e$ of its initial value over the 'propagation length' $L_{prop} = \frac{4\pi n''_{eff}}{\lambda}$ as the result of Ohmic loss [133].

Silver is an important metal for optical applications of surface plasmons in the visible range of wavelengths as it enables long propagation lengths. For instance, at a vacuum wavelength of $\lambda = 532$ nm, its dielectric constant exhibits a value of $\varepsilon_m \approx -16 + j0.4$ [132].

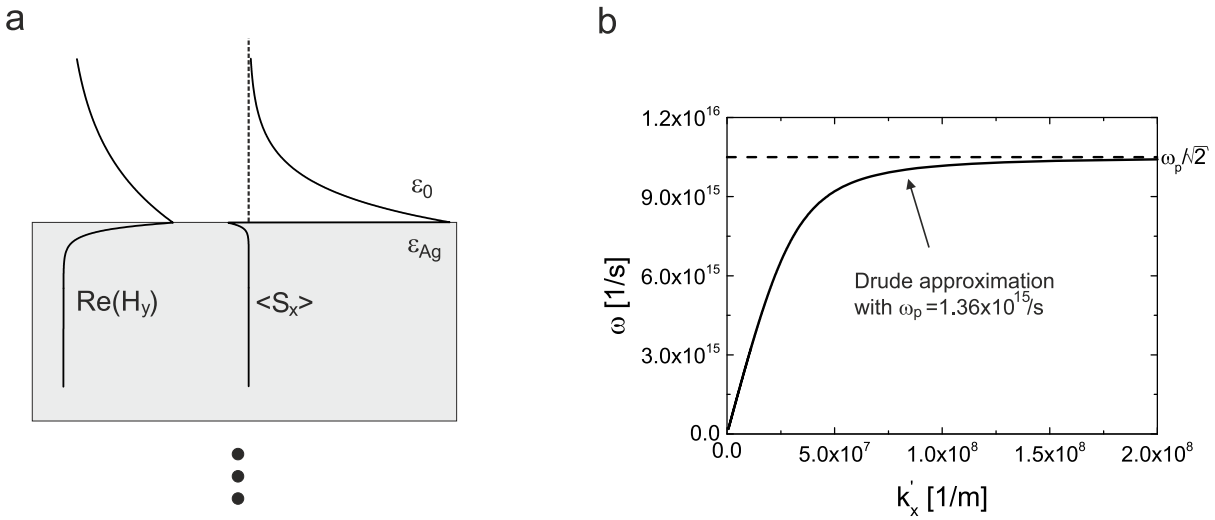

Figure 2.8: a) Magnetic field strength and x-component of the time-averaged Poynting vector of an SPP. b) Dispersion relation of silver under the assumption of an ideal Drude metal with $\omega_p = 1.36 \cdot 10^{16}$. According to ref. [133].

Similar values (large negative real part, small positive imaginary part) are present over the entire visible range [132]. As a result, typical propagation lengths of SPPs at silver-air-interfaces are in the order of several ten microns.

Fig. 2.8a shows the distributions of the real part of H_y and the x component of the time-averaged Poynting vector $\langle \vec{S} \rangle_x$ for a metal-air-interface. It can be observed that surface plasmon eigenmodes are strongly confined with respect to the z-direction. As an example, the dispersion relation of the surface plasmon calculated via an ideal Drude metal ($\Gamma = 0$) with [131]

$$\varepsilon_{Ag} = 1 - \frac{\omega_p^2}{\omega^2} \tag{2.46}$$

and $\omega_p = 1.36 \cdot 10^{16}$ is shown in Fig. 2.8b.

Here, toward infinitely large values of k_x', the dispersion relation converges to a value of $\omega_{sp} = \omega_p/\sqrt{2}$. In general, supposing that the dielectric is loss-free and represented by $\varepsilon_{r,1}$, the dispersion relation converges to [133]

$$\omega_{sp} = \frac{\omega_p}{\sqrt{1 + \varepsilon_{r,1}}} \tag{2.47}$$

in the limit of infinitely large values of k_x'.

2.3.2.1 Long-range (LR-) and short-range (SR-SPPs)

For a thin silver layer (see Fig. 2.9) the evanescent fields of both SPPs on each interface may overlap with each other. As a result, these SPPs couple with each other. This

coupling leads to the formation of a symmetric and antisymmetric eigenmode. The specialist terms such a phenomenon 'hybridization' [134]. In the field of plasmonics, the symmetric and antisymmetric eigenmodes are termed 'long-range SPP' (LR-SPP) and 'short range-SPP' (SR-SPP), respectively [134]. These names originate from the fact that the LR-SPP exhibits less electric-field penetration inside the metal and therefore less Ohmic losses, resulting in a longer propagation length than for pure SPPs. The opposite is the case for the SR-SPP [134]. A sketch of the corresponding magnetic field strengths and dispersion relations is shown in Fig. 2.9

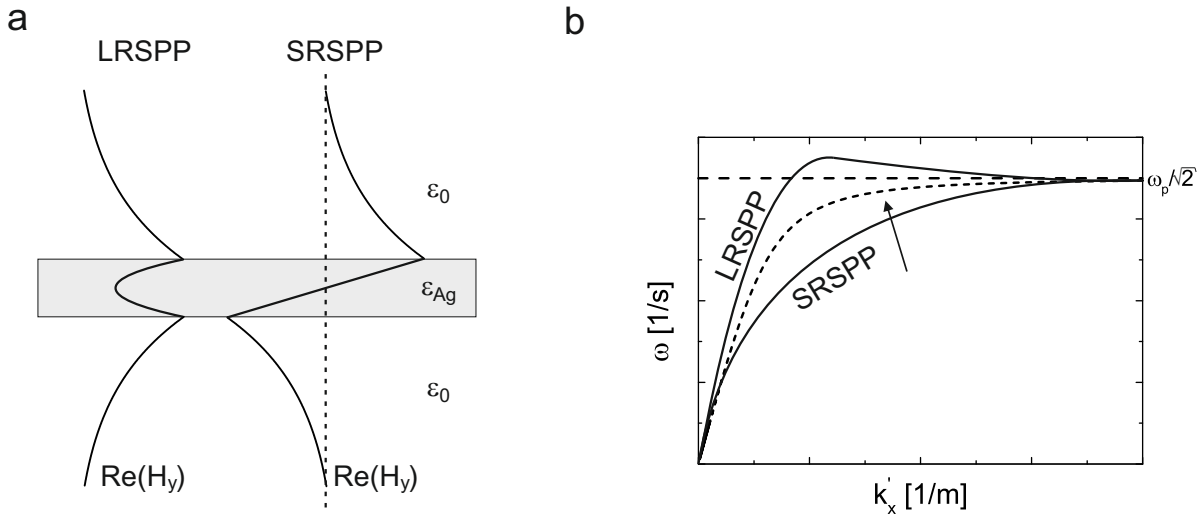

Figure 2.9: a) Magnetic field strengths of a LR-SPP and a SR-SPP. b) Qualitative sketch of the dispersion relations of LR-SPPs and SR-SPPs. According to ref. [133].

For wavelengths near to the visible range, the hybridization of SPPs into LR-SPPs and SR-SPPs become important for silver film thicknesses below approximately 100 nm [133].

2.3.3 Plasmons in 1D geometries

Geometries, which are elongated into one direction and small in all other direction perpendicular to this elongated direction, are considered as one-dimensional (1D). Applying similar principles as for hybridized surface plasmons, such geometries can be used to form plasmonic waveguides. In the simplest case, they consist of conductive stripes of rectangular or circular cross-section [135]. As a side note, although they are not of particular importance for this thesis, plasmonic waveguides have drawn remarkable attention in the recent years as a tool to realize sub-wavelength circuits [131, 135]. An intermediate step towards 0D plasmonic geometries are waveguides consisting of lines of conductive nanoparticles lines (nanoparticle waveguides). The power transfer in nanoparticle waveguides can be understood as the coupling of many individual localized surface plasmons [131]. Such localized surface plasmons will be explained in the next Section.

2.3.4 Localized Surface Plasmons (0D)

Historically, the research field of plasmonics arose from the investigation of glasses containing nanoscopic metallic nano particles [136]. Depending on the diameter and shapes of these particles, it could be observed that the scattering and absorption properties of light can be influenced over broad spectral ranges. These properties are present due to the excitation of localized surface plasmons (LSPs) [137]. As visualized in Fig. 2.10a, LSPs are charge oscillations localized at a metal sphere (e.g. a silver nanoparticle). The LSPs of small spherical particles ($d << \lambda$) are governed by the equations [138]

$$\sigma_{ext} = \frac{18\pi(\epsilon_1')^{3/2}V}{\lambda} \frac{\varepsilon_2''}{(\varepsilon_2' + 2\varepsilon_1')^2 + (\varepsilon_2'')^2} \tag{2.48}$$

$$\sigma_{sca} = \frac{32\pi^4(\varepsilon_1')^2V^2}{\lambda^4} \frac{(\varepsilon_2' - \varepsilon_1')^2 + (\varepsilon_2'')^2}{(\varepsilon_2' + 2\varepsilon_1')^2 + (\varepsilon_2'')^2} \tag{2.49}$$

for the extinction and scattering cross section σ_{ext} and σ_{sca}. Hereby, ε_1 and ε_2 are the relative permittivities of a host material and the metal, respectively. The LSPs of larger spherical particles obey Mie's Theory [139].

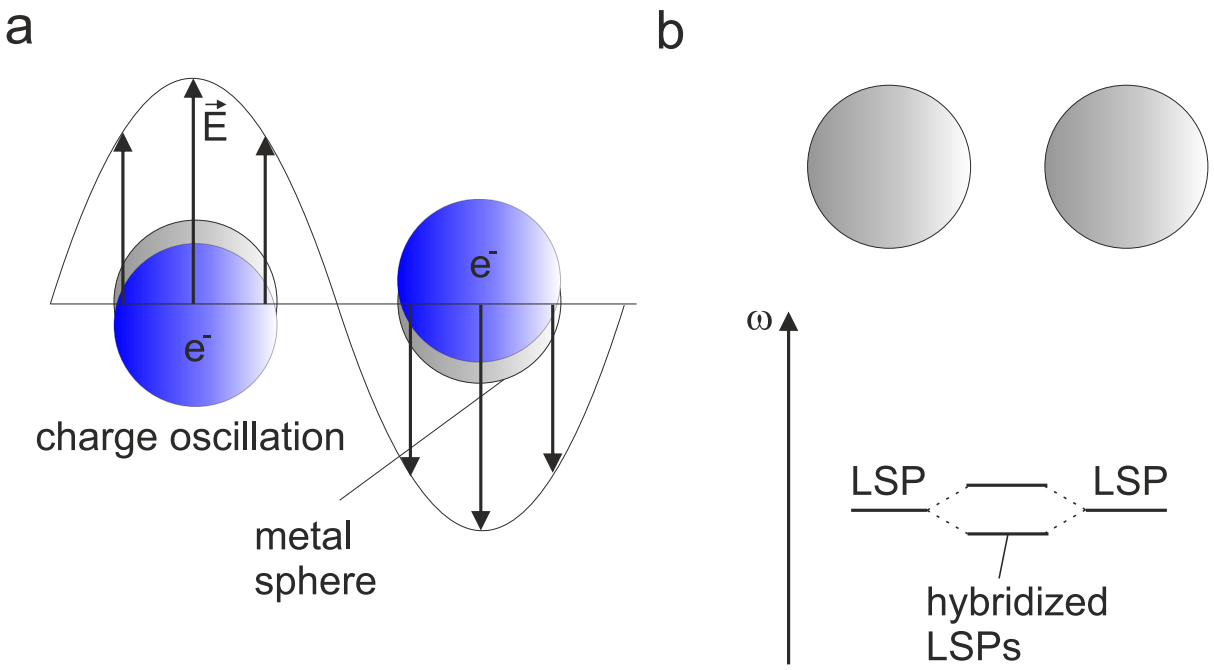

Figure 2.10: a) Sketch of a localized surface plasmon (LSP) of a metallic nanosphere according to ref. [137]. b) Hybridization of LSPs for a dimer of metallic nanospheres. According to refs. [140, 141].

In contrast to surface plasmons, LSPs can be excited without additional structures and, their excitation in an isotropic environment does not depend on the angle of incidence of an incident wave [138, 140, 141]. For large inter-particle distances $d >> \lambda$, the LSPs of AgNPs of the same diameter do not interact with each other. In this case, the extinction

of a light beam's intensity I propagating through a medium containing AgNPs is dictated by the Beer-Lambert-law [138, 142]

$$I = I_0 e^{-N_p \sigma_{ext} x} \tag{2.50}$$

with N_p as the volumetric number density of AgNPs and the extinction cross section $\sigma_{ext} = \sigma_{abs} + \sigma_{sca}$ of a single AgNP.

Interesting phenomena occur when the inter-particle distance is reduced so that LSPs may interact with each other and their field overlap is significantly large. Following Naomi Halas' report about the analogy between discrete electron states of single atoms and LSPs as discrete single AgNP states, and in a similar way as for the formation of LR-SPPs and SR-SPPs, this interaction of LSPs can be understood as the hybridization of LSPs (Fig. 2.10b) [140, 141]). This hybridization enables more energy levels in comparison to non-interacting AgNPs and σ_{ext} can be strongly altered. It will be of importance for some of the phenomena explained in Chapter 4.

2.4 Periodic layers for light coupling

In this section, a generalization from the examples given in Section 2.2 is considered. As a result of this generalization, a geometry now includes multiple layers as well as periodically structured layers of a period Λ in x-direction, termed grating layer. A sketch of such generalized geometry is shown in Fig. 2.11.

The method of rigorous coupled wave analysis (RCWA) will be shortly outlined using the explanations given in ref. [129]. In addition to these explanations, practically applicable formulations of some equations will be provided. The advantages and limitations of the method will be discussed later on.

All layers are counted via an index j. The relative permittivity and its reciprocal values in a grating layer of index $j = p$ can be expressed by [129]

$$\varepsilon_{r,p}(x) = \varepsilon_{r,p}(x + \Lambda) = \sum_{\nu=-\infty}^{\infty} p_\nu e^{j(2\pi\nu x/\Lambda)} \tag{2.51}$$

and [129]

$$1/\varepsilon_{r,p}(x) = 1/\varepsilon_{r,p}(x + \Lambda) = \sum_{\nu=-\infty}^{\infty} s_\nu e^{j(2\pi\nu x/\Lambda)} \tag{2.52}$$

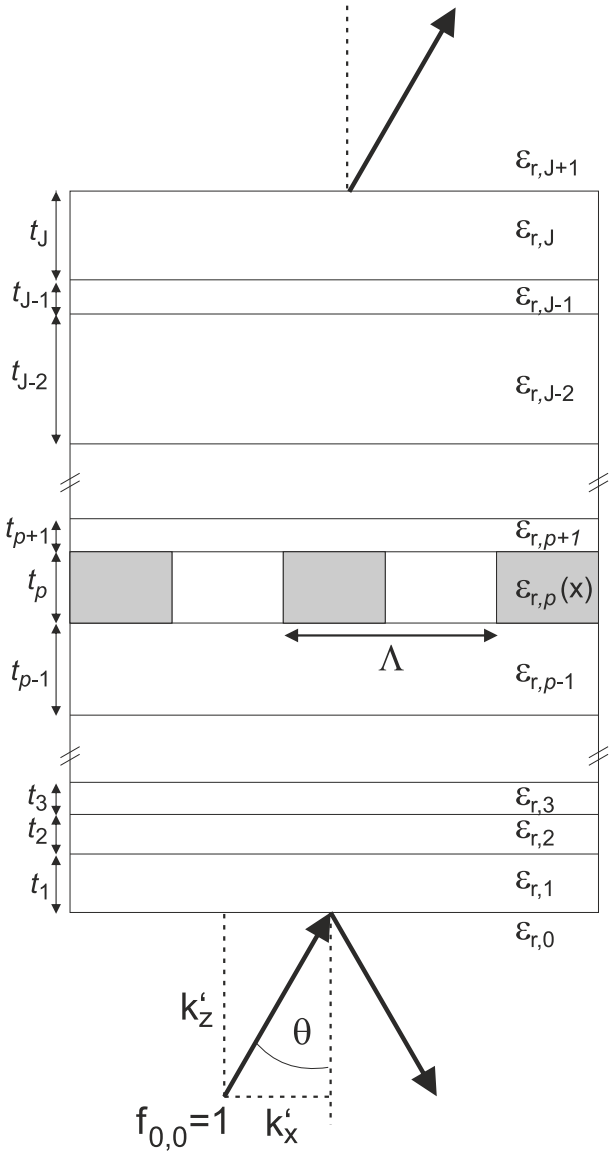

Figure 2.11: Schematic geometry including period layers. From ref. [129].

Herein, ν indexes all diffraction orders. The Floquet theorem tells us that, in a similar way, the electric and magnetic fields can be expressed with periodic functions [129]. It is assumed that plane waves of a lateral momentum k'_x fall onto the geometry from the substrate (see Fig. 2.11) [129]. By inserting an ansatz for the tangential field components of $\vec{E}$ and $\vec{H}$ in the form of [129]

$$E_{t,j} = \sum_{\nu=-\infty}^{\infty} E_{t,j,\nu}(z) e^{jk_{x,\nu}x} \text{ and } H_{t,j} = \sum_{\nu=-\infty}^{\infty} H_{t,j,\nu}(z) e^{jk_{x,\nu}x} \tag{2.53}$$

into the Maxwell equations, using

$$k_{x,\nu} = k'_{x,\nu} + j \cdot k''_x, \quad k'_{x,\nu} = k'_x + \nu \cdot 2\pi/\Lambda, \tag{2.54}$$

a linear differential equation system of second order is obtained. Using again local coordinates, and

$$k_{z,j,\nu} = \sqrt{\varepsilon_{r,j} {k_0}^2 - k_{x,\nu}^2}, \tag{2.55}$$

as well as

$$y_{j,\nu} = \begin{cases} k_{z,j,\nu}/\omega\mu_0 & \text{for TE polarization} \\ \omega\varepsilon_{r,j}/k_{z,j,\nu} & \text{for TM polarization,} \end{cases} \tag{2.56}$$

its solution for all homogeneous layers ($j \neq p$) reads [129]

$$\vec{E}_{t,j} = \sum_{\nu=-\infty}^{\infty} \{f_{j,\nu} e^{jk_{z,j,\nu} z_j} + g_{j,\nu} e^{jk_{z,j,\nu}(t_j - z_j)}\} \cdot e^{jk_{x,\nu} x} \tag{2.57}$$

$$\vec{H}_{t,j} = \sum_{\nu=-\infty}^{\infty} y_{j,\nu} \{f_{j,\nu} e^{jk_{z,j,\nu} z_j} - g_{j,\nu} e^{jk_{z,j,\nu}(t_j - z_j)}\} \cdot e^{jk_{x,\nu} x}, \tag{2.58}$$

whereby selection of the square-roots of $k_{z,j,\nu}$ is defined by $k'_{z,j,\nu} > 0$ for $|k'_{x,\nu}| \leq \mathrm{Re}(k_0\sqrt{\varepsilon_{r,j}})$ or $k''_{z,j,\nu} > 0$ for all other cases [129]. This set of equations can be understood as a set of plane-waves, which propagate through the geometry independently from each other. For a grating layer ($j = p$), the corresponding solution reads [129]

$$\vec{E}_p = \sum_{m=-\infty}^{\infty} \{f_{p,m} e^{jk_{z,p,m} z_p} + g_{p,m} e^{jk_{z,p,m}(t_p - z_p)}\} \times \sum_{\nu=-\infty}^{\infty} a_{m,\nu} e^{jk_{x,\nu} x} \tag{2.59}$$

$$\vec{H}_p = \sum_{m=-\infty}^{\infty} y_{p,m} \{f_{p,m} e^{jk_{z,p,m} z_p} - g_{p,m} e^{jk_{z,p,m}(t_p - z_p)}\} \times \sum_{\nu=-\infty}^{\infty} b_{m,\nu} e^{jk_{x,\nu} x} \tag{2.60}$$

with [129]

$$y_{p,m} = \begin{cases} k_{z,p,m}/\omega\mu_0 & \text{(TE)}, \\ \omega\varepsilon_0/k_{z,p,m}\gamma_p & \text{(TM)} \end{cases} \tag{2.61}$$

whereby γ_p is the average of $1/\varepsilon_r(x)$ taken over one period. The geometry and relative permittivity of the grating is encoded in the matrices [129, 143]

$$\underline{A} = \begin{pmatrix} \ddots & \vdots & \vdots & \vdots & \iddots \\ \dots & a_{-1,-1} & a_{0,-1} & a_{1,-1} & \dots \\ \dots & a_{-1,0} & a_{0,0} & a_{1,0} & \dots \\ \dots & a_{-1,1} & a_{0,1} & a_{1,1} & \dots \\ \iddots & \vdots & \vdots & \vdots & \ddots \end{pmatrix} \quad \text{and} \quad \underline{B} = \begin{pmatrix} \ddots & \vdots & \vdots & \vdots & \iddots \\ \dots & b_{-1,-1} & b_{0,-1} & b_{1,-1} & \dots \\ \dots & b_{-1,0} & b_{0,0} & b_{1,0} & \dots \\ \dots & b_{-1,1} & b_{0,1} & b_{1,1} & \dots \\ \iddots & \vdots & \vdots & \vdots & \ddots \end{pmatrix} \tag{2.62}$$

as well as in $k_{z,p,m}$. Both matrices can be derived from the fundamental matrix [129, 143]

$$\underline{P} = \begin{cases} k_0^2 \underline{\mathcal{E}} - \underline{K_x} & \text{for TE polarization} \\ \underline{\mathcal{Y}}^{-1}(k_0^2 \underline{\mathbb{1}} - \underline{K_x}\underline{\mathcal{E}}^{-1}\underline{K_x}) & \text{for TM polarization} \end{cases} \tag{2.63}$$

of the linear differential equation system, using the definitions below [129, 143]

$$p_\nu = \frac{1}{\Lambda} \int_0^\Lambda \varepsilon_{r,p}(x) e^{j(2\pi\nu x/\Lambda)} \, \mathrm{d}x \tag{2.64}$$

$$s_\nu = \frac{1}{\Lambda} \int_0^\Lambda \frac{1}{\varepsilon_{r,p}(x)} e^{j(2\pi\nu x/\Lambda)} \, \mathrm{d}x \tag{2.65}$$

$$\underline{\mathcal{E}}_{m,\nu} = p_{m-\nu} \tag{2.66}$$

$$\underline{\mathcal{Y}}_{m,\nu} = s_{m-\nu} \tag{2.67}$$

$$\underline{K_x}_{m,\nu} = \delta_{m,\nu} k_{x,\nu} \tag{2.68}$$

As a side note, the expression for $\underline{P}$ in the TM case has been debated about over the course of many publications in the literature: similar to non-commutating mathematical operators, a different expression of $\underline{P}$ occurs when the Fourier-space representations of $\varepsilon_r(x)$ and $1/\varepsilon_r(x)$ are introduced before all necessary algebraic manipulations of the Maxwell equations have been done. Following the work in ref. [144] and an own derivation of $\underline{P}$, it has been confirmed that the expression provided here is correct. Wrong expressions lead to unstable behaviors and slow convergences when a finite number of Fourier orders is calculated (see Section 2.5).

The eigenvalues of $\underline{P}$ are $k_{z,p,m}^2$ and $k_{z,p,m}$ itself is obtained from the positive square root of $k_{z,p,m}^2$. The eigenvectors $\vec{c}_m$ of $\underline{P}$ define a matrix [129]

$$\underline{C}_{eig} = [\dots : \vec{c}_{-1} : \vec{c}_0 : \vec{c}_1 : \dots] \tag{2.69}$$

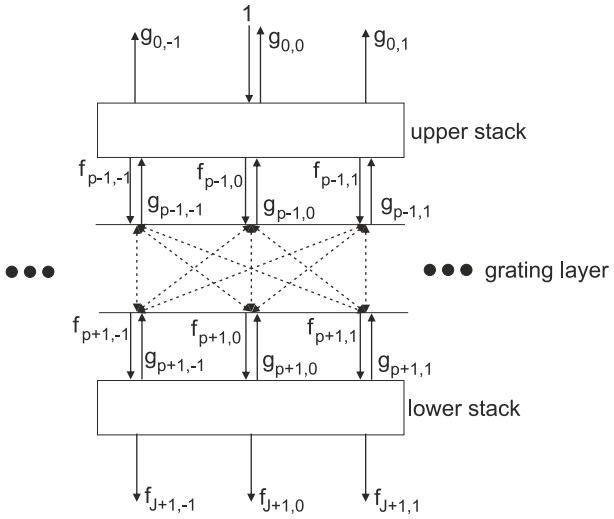

Figure 2.12: Graphical representation of RCWA

Finally, the matrices $\underline{A}$ and $\underline{B}$ can be identified by [129]

$$\begin{cases} \underline{A} = \underline{B} = \underline{C}_{eig} & \text{for TE polarization} \\ \underline{A} = 1/\gamma_p \underline{\mathcal{Y}} \underline{B} \text{ and } \underline{B} = \underline{C}_{eig} & \text{for TM polarization} \end{cases} \tag{2.70}$$

For each layer, the boundary conditions (Eqs. 2.20 and 2.21) of the tangential field components must be fulfilled. As only one plane wave falls onto the geometry from the 0^{th} diffraction order ($\nu = 0$) with the lateral momentum k'_x, the amplitudes in the substrate and superstrate are defined by $f_{0,0} = 1$, $f_{0,\nu} = 0$ for $\nu \neq 0$ and $g_{J+1,\nu} = 0$ [129]. As a result, all amplitudes $g_{j,\nu}$ and $f_{j,\nu}$ can be unambiguously determined [129].

A graphical representation of RCWA is shown in Fig. 2.12. As mentioned above, in all homogeneous layers, plane-waves propagate independently from each other. A grating layer then functions as a coupling element between these plane-waves. Thus, a geometry exhibiting grating layer can be regarded as a resonator with multiple interacting channels, giving rise to interesting resonant phenomena [129].

Concerning the interpretation of the amplitudes $g_{0,\nu}$ and $f_{J+1,\nu}$, they can be identified as the coupling coefficients between the incident wave and diffracted waves. In the literature, the coupling coefficients between different diffraction orders ν are often referred to as diffraction coefficients [145]. For an incident plane-wave coming from the substrate ($j = 0$), the conservation of energy can be expressed by [145]

$$\sum_{\nu} \left[\mathrm{Re}(|g_{0,\nu}|^2 \frac{k_{z,0,\nu}}{k_{z,0,0}}) + \mathrm{Re}(|f_{J+1,\nu}|^2 \frac{k_{z,J+1,\nu}}{k_{z,0,0}}) \right] + A = 1, \tag{2.71}$$

whereby $k_{z,0,\nu}/k_{z,0,0}$ and $k_{z,J+1,\nu}/k_{z,0,0}$ are geometrical correction factors to take into account cross-sectional intensity changes as a result of tilted propagation angles. The reflectance R and the transmittance T are defined by [145]

$$R = |g_{0,0}|^2 \text{ and } T = |f_{J+1,0}|^2 \frac{k_{z,J+1,0}}{k_{z,0,0}}, \tag{2.72}$$

The diffraction efficiencies $D_{R,\nu}$ and $D_{T,\nu}$ are given by [145]

$$D_{R,\nu} = |g_{0,\nu}|^2 \frac{k_{z,0,\nu}}{k_{z,0,0}} \text{ and } D_{T,\nu} = |f_{J+1,\nu}|^2 \frac{k_{z,J+1,\nu}}{k_{z,0,0}}, \quad n \neq 0 \tag{2.73}$$

Before moving on to the physical behavior of planar waveguides including gratings, details on the computation using RCWA will be provided.

2.5 Computation of RCWA

In this section, explanations on the computation of geometries with periodic layers with the equations provided in section 2.4 will be given.

2.5.1 Truncation of Fourier orders and an exemplary rectangular grating

The expressions for both the electric and magnetic fields contain an infinite number of Fourier orders. It is obvious that their practical calculation can only be realized using approximate methods. Instead of an infinite number of Fourier orders, only $-N < \nu < N$ Fourier orders are calculated. This procedure is termed 'truncation' [129]. The number N strongly depends on the parameters of a periodic layer. As rule of thumb, large spatial variations of $\varepsilon_{r,p}(x)$ and large layer thicknesses tend to require a larger value of N to obtain trustworthy results. Furthermore, smaller values of N are required for TE polarization than for TM polarization [129].

Convergence is reached, when the relative error of a simulated quantity X (e.g. the transmittance T, reflectance R, L_{prop}, etc.) becomes smaller than a desired accuracy δ_E. If not stated otherwise, $\delta_E < 10^{-3}$ is chosen. In practice, the maximum number of N can be then found by applying a convergence criterium

$$\frac{|X(N+1) - X(N)|}{|X(N)|} < \delta_E \tag{2.74}$$

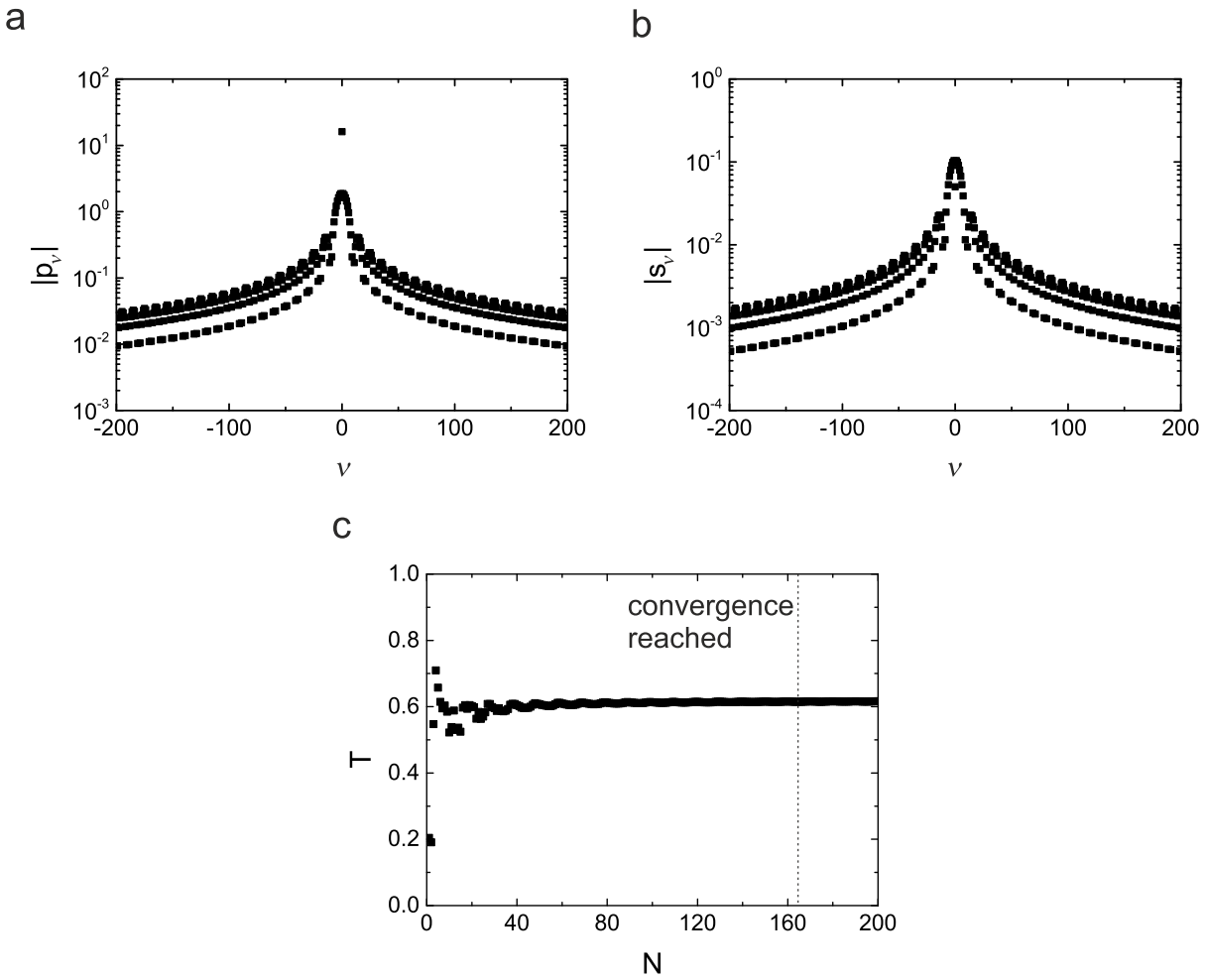

Figure 2.13: a,b) Convergence of $|p_\nu|$ and $|s_\nu|$ for an increasing number of diffraction orders ν. c) Convergence of the transmission T for increasing values of N.

To provide an example, the calculation of a rectangular metal-air grating with increasing values of N will be discussed in the following and compared with reference results from the literature [146].

For a rectangular grating, the dielectric function reads.

$$\varepsilon_{r,p}(x) = \begin{cases} \varepsilon_{r,p1} & (0 \leq x \leq \mathrm{D} \cdot \Lambda), \\ \varepsilon_{r,p2} & (\mathrm{D} \cdot \Lambda < x < \Lambda) \end{cases} \tag{2.75}$$

Inserting 2.75 into 2.64 and 2.65 yields

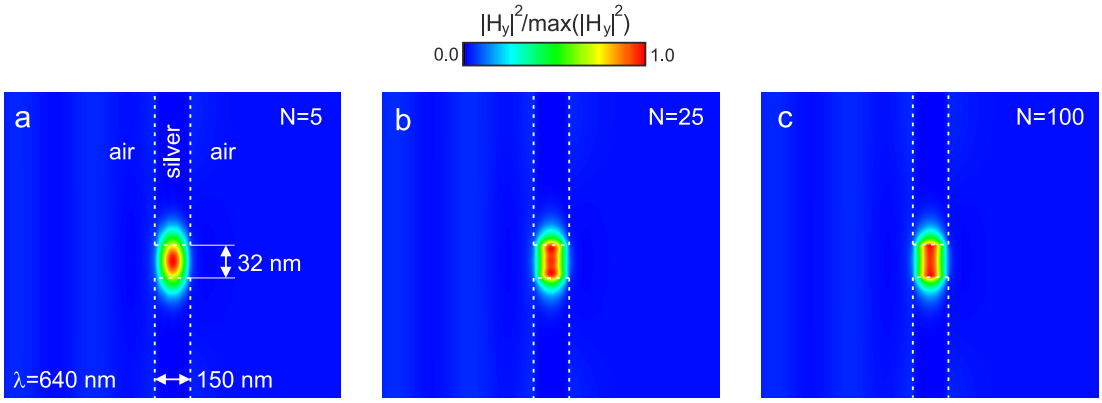

Figure 2.14: Convergence of $|H_y|^2$ for an increasing number of Fourier orders. See ref. [146] for an exact result.

$$p_\nu = \frac{1}{2j\pi\nu}\left[\varepsilon_{r,p1}(e^{j2\pi\nu\mathrm{D}} - 1) + \varepsilon_{r,p2}(e^{j2\pi\nu} - e^{j2\pi\nu\mathrm{D}})\right] \tag{2.76}$$

$$= e^{j\pi\nu\mathrm{D}}\left[\varepsilon_{r,p1}\frac{\sin(n\pi\mathrm{D})}{\nu\pi} + \varepsilon_{r,p2}e^{j\pi\nu}\frac{\sin(\nu\pi(1-\mathrm{D}))}{\nu\pi}\right] \tag{2.77}$$

and

$$s_\nu = \frac{1}{2j\pi\nu}\left[\frac{1}{\varepsilon_{r,p1}}(e^{j2\pi\nu\mathrm{D}} - 1) + \frac{1}{\varepsilon_{r,p2}}(e^{j2\pi\nu} - e^{j2\pi\nu\mathrm{D}})\right] \tag{2.78}$$

$$= e^{j\pi\nu\mathrm{D}}\left[\frac{1}{\varepsilon_{r,p1}}\frac{\sin(\nu\pi\mathrm{D})}{\nu\pi} + \frac{1}{\varepsilon_{r,p2}}e^{j\pi\nu}\frac{\sin(\nu\pi(1-\mathrm{D}))}{\nu\pi}\right] \tag{2.79}$$

The geometry is defined by the parameters $\varepsilon_{r,p1} = 1.0$, $\varepsilon_{r,p2} = \varepsilon_{Ag}$ with ε_{Ag} as the dielectric constant of silver [132], $\mathrm{D} = 0.1$, $t_g = 150$ nm and $\Lambda = 320$ nm. TM polarized light at a wavelength of $\lambda = 640$ nm under perpendicular incidence ($k'_x = 0$) is considered [146]. Note that this geometry represents an extreme example of very small spatial dimensions in the x-direction. It exhibits large discontinuous jumps of $\varepsilon_{r,p}(x)$, and, for a metal, large grating layer thicknesses far above its penetration depth. It is thus ideal to test and investigate the stability and convergence of the implemented RCWA algorithm.

$|p_\nu|$ and $|s_\nu|$ are shown in Figs. 2.13a and b. Toward large values of ν, both functions tend towards zero. Thus, the impact of the Fourier orders on a calculated measure of interest ($X = \vec{E}$,$\vec{H}$,T,R, etc.) becomes smaller for increasing values of ν. This observation means that all measures of interest converge, justifying the method of truncation. In accordance, the transmittance T converges to a distinct value with increasing N (Fig. 2.13c). Here, convergence is reached at the dashed line ($N = 163$). Similar arguments hold for the magnetic field distribution H_y (Fig. 2.14), which looks near identical to the reference distribution for $N \geq 100$ (see Fig. 10a in ref. [146]).

When smaller values of N are used, the field distributions may exhibit artifacts since the truncation acts like a low-pass-filter on the spatial harmonics of H_y.

2.5.2 Slicing

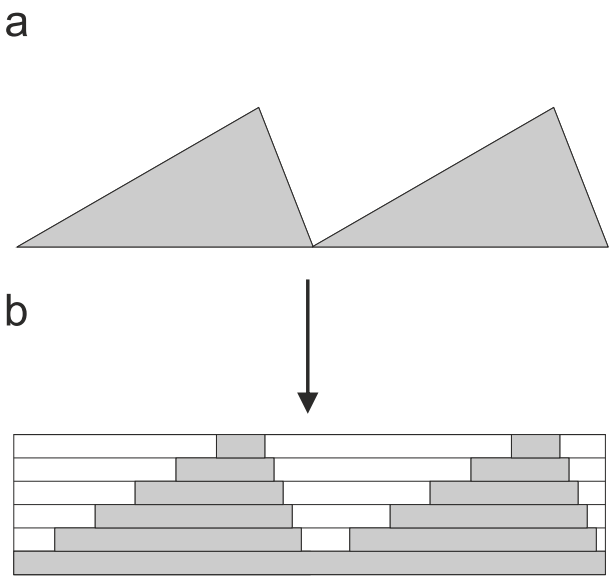

Figure 2.15: Approximation of a grating with curved surface profile (a) by slicing it into multiple layers of rectangular gratings (b). According to ref. [143].

To model a more complicated grating geometry such as a grating with curved interfaces ($\varepsilon_{r,p} = \varepsilon_{r,p}(x, z)$), it can be approximated by slicing it into a stack of one dimensional rectangular grating layers [143]. Such procedure of slicing is visualized in Fig. 2.15. The grating layer is sliced into K sublayers of height t_g/K, each consisting of rectangular grating. For large values of K, the results of an exact calculation are asymptotically approximated.

With increasing grating thickness and complexity (i.e. high spatial frequencies), the calculation time drastically increases as more and more Fourier orders are necessary to model the grating. There exist two ways to circumvent this problem. The first way is to use the C-method, named after a work of Chandezon et al., when the grating can be described by a continuously differentiable surface profile function and the boundary conditions can be solved via a coordinate transformation [147]. The other way is to use numerical methods such as the finite element method (FEM) [148] or finite difference time domain (FDTD) [149]. For complicated grating geometries, a hybrid approach can combine the advantages of these methods: first, the grating's response to an incoming plane-wave can be converted into effective values of p_n and s_n using either the C-Method or numerics. Second, these calculated values can be inserted again into the RCWA algorithm. For the geometries presented in this thesis, pure RCWA and slicing is used

as the grating geometries are neither complicated nor thick and typically converge below $N = 100$ and $K = 50$.

2.5.3 Conservation of Energy

Once convergence is confirmed, it is of crucial importance to check that Eq. 2.71 is accurately true. For example, very large layer thicknesses in the order of $10^3\lambda$ may exhibit exponential terms in the expressions of the electric and magnetic fields, which are too large or too small to be represented by a 32-bit or 64-bit digit. The appearance of these exponential terms reflect in a non-conserved energy balance or discontinuous jumps of simulated values. Here, the implemented algorithm using RCWA was tested up to optical layer thicknesses of approximately 80 μm. Improving this limit is one of the outlooks of this thesis. Nonetheless, energy conservation is confirmed for all geometries presented in this thesis as they are thin enough.

In the next section, using the computation methods explained above, the behavior of an exemplary waveguide grating will be demonstrated and explained.

2.6 Phenomena of an Exemplary Waveguide Grating

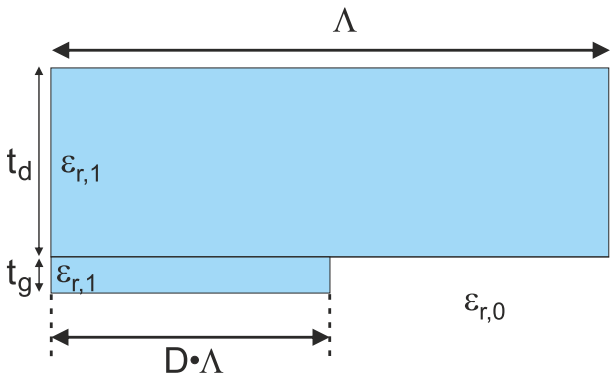

Figure 2.16: Geometry of a simple waveguide grating.

The characteristics of a waveguide grating as defined in Fig. 2.16 will be discussed in this section. It consists of a dielectric layer with a thickness of $t_d = 500$ nm, and one adjacent rectangular grating with $\varepsilon_{r,0} = n_0^2 = 1.0$ and $\varepsilon_{r,1} = n_1^2 = 2.0^2$, a thickness of $t_g = 50$ nm, a period of $\Lambda = 500$ nm and a duty cycle of D = 0.5. The entire waveguide thickness is $t_{WG} = 550$ nm.

Although this geometry is rather simple, it shows a plethora of interesting effects with respect to R, T, $D_{R,\nu}$ and $D_{T,\nu}$ as a function of the incidence angle θ (see Fig. 2.17).

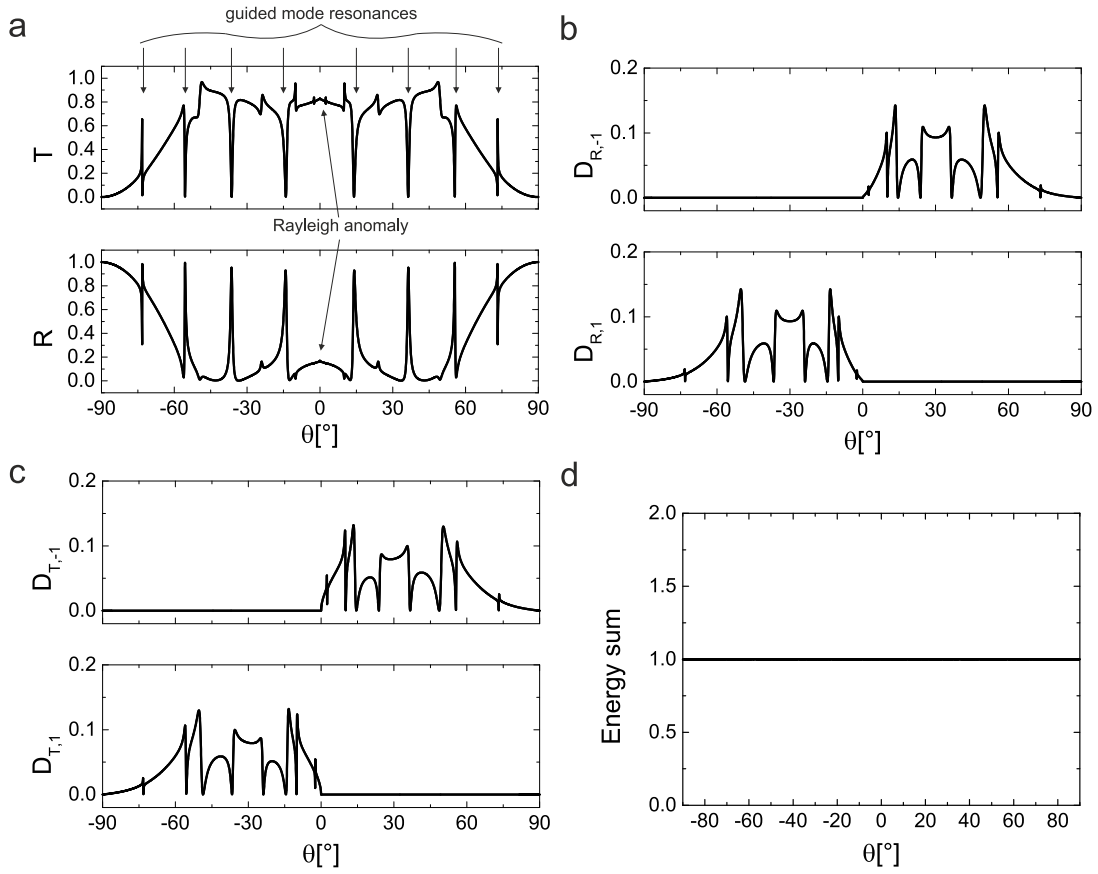

Figure 2.17: Characteristics of the waveguide grating for $\lambda = 500$ nm. a) The transmittance T and reflectance R in the 0^{th} order. b,c) The diffraction efficiencies $D_{R,-1}$, $D_{R,1}$, $D_{T,-1}$, and $D_{T,1}$. d) Calculated values of Eq. 2.71. A value of 1 indicates energy conservation (here, A is zero).

The various values of $k'_{x,\nu}$ (see Section 2.4) appear as diffracted plane-waves at the diffraction angles $\theta_{d,n}$ according to the equation

$$k_0 \cdot n_0 \sin(\theta_\nu) = k_0 n_0 \sin(\theta) + \nu \cdot 2\pi/\Lambda \tag{2.80}$$

At distinct incidence angles θ and in contrast to a non-structured Fabry-Perot resonator (see Section 2.2), both T and R show several sharp additional features (see the arrows in Fig. 2.17a). For example, T and R are not continuously differentiable at $\theta = 0$. This behavior occurs as the wave-vector components $k_{z,j,\nu}$ of the diffracted waves in the substrate and superstrate flip between purely imaginary and purely real numbers. It is called a 'Rayleigh anomaly' named after its discoverer Lord Rayleigh. The remaining sharp features (e.g. at $\theta \approx 56°$) are called 'guided mode resonances' [151]. The origin of these guided mode resonances can be understood by taking a closer look at the reflection coefficients $r = g_{0,0}$. In a similar way as for non-structured geometries, it can be expressed in the form of [129]

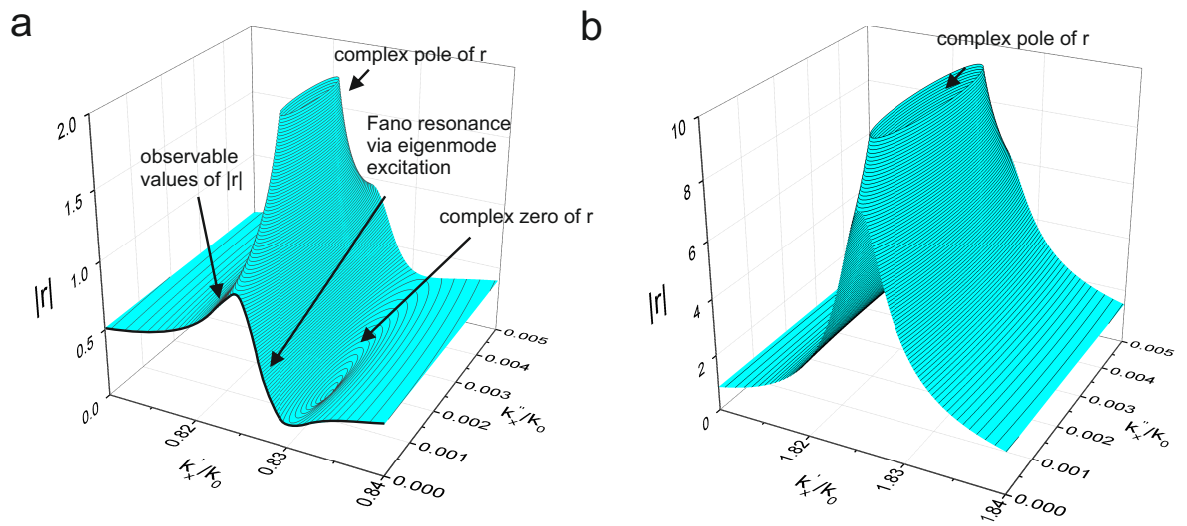

Figure 2.18: a) $|r|$ as a function of $k_x = (k_x' + jk_x'')$. Its cut along $k_x'' = 0$ displays the observable values of $|r|$ under plane-wave incidence from the substrate. Due to the vicinity of a complex zero-pole pair, a guided mode resonance with a Fano curve [150] shape appears. b) The appearance of a second pole under a shifted lateral $k_x' + 2\pi/\Lambda$.

$$r = g_{0,0} \propto \det((\underline{\mathbb{1}} - \underline{R})^{-1}) \tag{2.81}$$

whereby $\underline{R}$ is an effective matrix including all internal reflections and phase shifts of the waveguide grating. A pole of $g_{0,0}$ is then present, when the determinant $\det(\underline{\mathbb{1}} - \underline{R})$ is zero [129]. Fig. 2.18a shows $|r|$ as a function of $k_x = (k_x' + jk_x'')$ near to $\theta = 56°$.

It can be observed that the pole is complex with a positive value of k_x'' although no losses are present in the geometry. Another pole with the same value of k_x'' is present at $k_x' + 2\pi/\Lambda$. This second pole has almost the same real part $k_x' \approx 1.82$ as the TE_1 eigenmode of a homogeneous waveguide for which the grating is replaced with a layer of an effective relative permittivity $1/2 \cdot (\varepsilon_{r,1} + \varepsilon_{r,2})$ (see Fig. 2.18b).

As discussed in Section 2.3, a pole with $k_x''>0$ can be interpreted as a mode with a decaying intensity along the x-direction. A plot of the electric field distribution E_y as well as $\langle S_x \rangle$ shows that power is transferred from the mode to plane-waves in the substrate and superstrate (see Fig. 2.19). The positive value of k_x'' thus occurs due to radiation from the eigenmode into plane-waves in the substrate and superstrate. Applying the principle of reciprocity, an incident plane-wave from the substrate can excite this eigenmode. As a part of the excited energy in the mode couples back to the plane-waves in the substrate and superstrate, interference with the incident plane wave occurs and can be observed as a guided mode resonance of the reflection coefficient r [151]. The curve shape of such guided mode resonance can be understood as a cut of r along the real axis in Fig. 2.18a and is composed of the tails of the pole and an adjacent zero of r (see the black line).

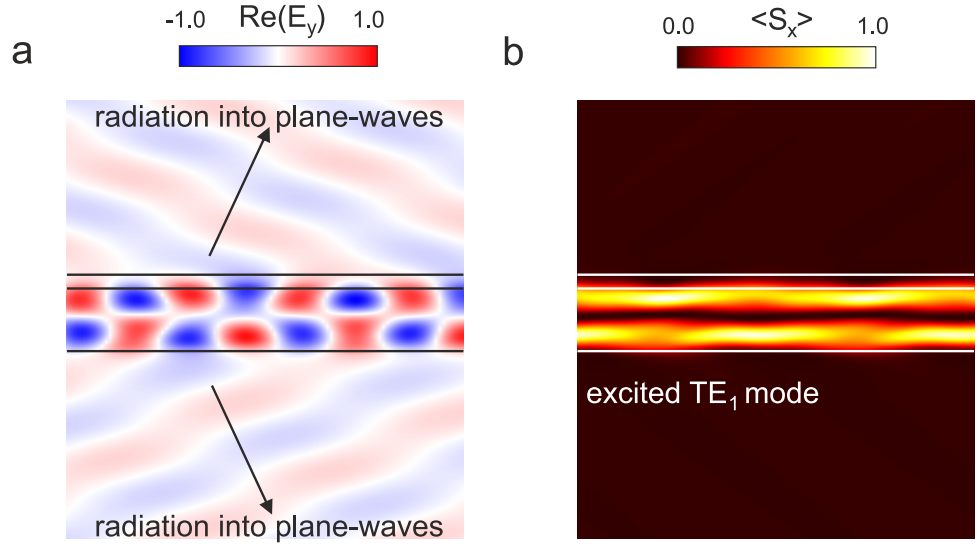

Figure 2.19: a,b) $\mathrm{Re}(E_y)$ and $\langle S_x \rangle$ corresponding to the pole displayed in Fig. 2.18a.

From this geometric interpretation, it follows that larger values of k_x'' lead to resonances of broader full width half maximum $\Delta\theta$ [152]. The relation between $\Delta\theta$ and k_x'' can be derived from Heisenberg's uncertainty principle ($\Delta x \cdot \Delta p_x \geq h$). Identifying $\Delta x = L_{prop}$ and $\Delta p_x = h \cdot \Delta k_x' = h k_0 n_s \cos(\theta) \Delta\theta$, it reads [152]

$$\Delta\theta = \frac{2k_x''}{k_0 n_0 \cos(\theta)} \tag{2.82}$$

From analog considerations, using the energy-time uncertainty, the spectral width of the guided mode resonance can be expressed by

$$Q = \frac{\omega_0}{\Delta\omega} = \frac{\mathrm{Re}(n_{eff})}{2\mathrm{Im}(n_{eff})}, \tag{2.83}$$

whereby the right side of the equation is only valid for waveguides with an attributed propagation length. In contrast, the expression $Q = \omega/\Delta\omega$ is valid for all kinds of optical resonators [124].

A plot of R reveals the dispersion relations of eigenmodes in the form of guided mode resonances and underlines this interpretation of mode excitation (Fig. 2.20). They can be interpreted as a photonic band structure. The word band-structure is chosen based on its similarity with the band-structure of electronic states in solid-state materials [153]. This similarity is the reason why periodically structured photonic geometries are often referred to as 'photonic crystals' [154].

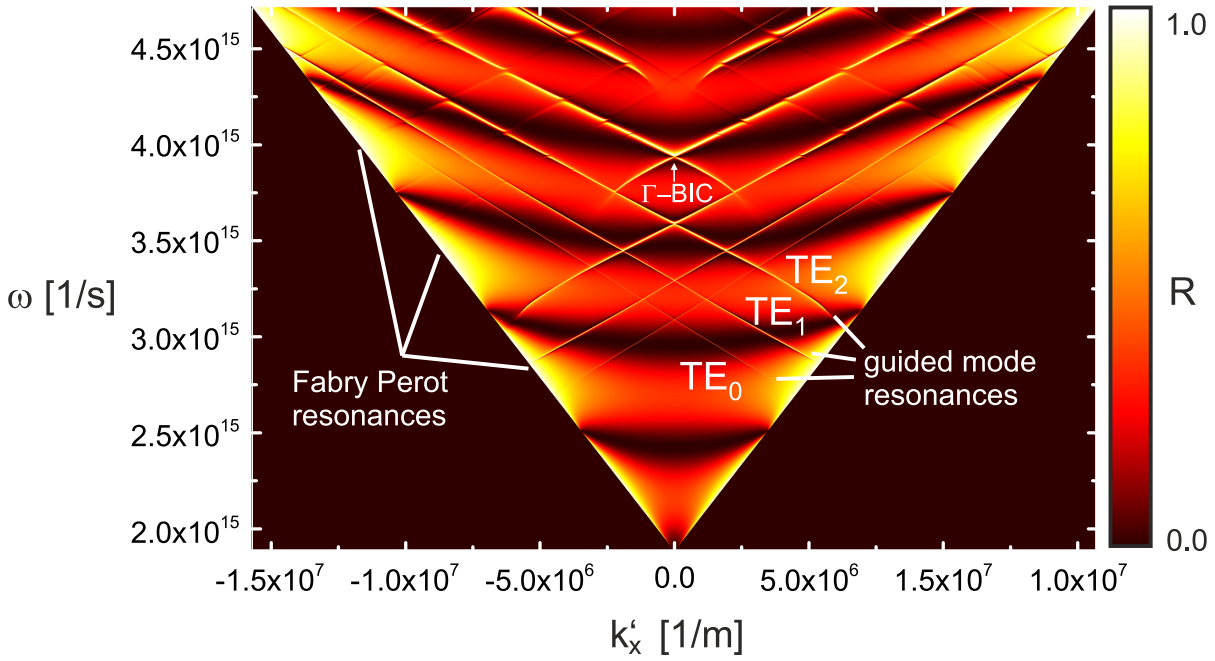

Figure 2.20: Reflectance R as a function of k'_x and ω.

2.6.1 Bound States in the Continuum (BIC)

Taking a closer look at the crossing point between the dispersion relations of two counter-propagating modes in Fig. 2.20 toward $k'_x = 0$, they form two eigenmodes: A symmetric eigenmode and an antisymmetric eigenmode of zero group velocity $\partial\omega(k'_x)/\partial k'_x$ (standing waves) [128, 129]. Here, the words 'symmetric' and antisymmetric' are referred to the electric field's symmetry with respect to the x-direction. Herein, the symmetric eigenmode can couple to plane-waves in the substrate and superstrate [155]. In contrast, the antisymmetric eigenmode is incompatible with the symmetry of plane waves in the substrate and superstrate at $k'_x = 0$. As result, an excited eigenmode cannot couple to these plane plane waves and vice versa. This circumstance is the reason why, toward $k'_x = 0$ the spectral width of the antisymmetric eigenmode asymptotically converges to zero and indicates divergence of Q ($k''_x = 0$). As the divergence of Q occurs on a continuous dispersion relation characterized by $k''_x > 0$ for all values of k'_x except zero, it is called a 'Γ-BIC' or 'Symmetry-Protected BIC' [155, 156].

Another type of BIC, called Friedrich-Wintgen BIC (FW-BIC) can occur as the result of an avoided crossing of the dispersion relations of coupled eigenmodes [156]. This type of BIC will be discussed in detail in Chapter 4 in the context of the discussion of a photonic-plasmonic hybrid waveguide grating.

2.7 Out- and Incoupling Efficiency and Concentration

So far, the behavior of waveguide gratings has been elaborated assuming infinitely extended plane-waves. Of course, real light sources are finite with respect to their spatial dimensions. This section will provide a step-by-step transition from plane-waves and infinitely large geometries to finite light sources. These steps follow the methods provided in ref. [157]. In the context of these steps, the concentration attributed to the eigenmode of a waveguide grating will be defined.

It is considered that no incident plane-wave from the substrate or superstrate is present. Instead, a mode with a total input power per unit length in y-direction P_{in}/l_y at $x = 0$ is assumed, which propagates in the positive x-direction. As for the former example of SPPs (see Section 2.3), the time-averaged Poynting vector attributed to the eigenmode obeys the equation [157]

$$\langle S_x(x)\rangle = \langle S_x(0)\rangle \cdot e^{-2k_0 n''_{eff} x}, \tag{2.84}$$

whereby it is measured at some z-position inside the waveguide. n''_{eff} takes into account both radiation into the substrate and superstrate and all forms of loss (e.g. Ohmic loss). The propagation length can then be composed via [157]

$$L_{prop} = (\frac{1}{L_{prop,rad}} + \frac{1}{L_{prop,loss}})^{-1} \tag{2.85}$$

In the limit $x \to \infty$, $\langle S_x(x)\rangle$ becomes zero. Therefore, all of the initial power in the eigenmode P_{in} is distributed into a radiation part P_{rad} and a loss part P_{loss}. The intensity of light radiated away from the waveguide grating shows an exponentially decaying profile as well (see Fig. 2.21). Herein, it is important to recognize that the light outside the waveguide grating propagates undisturbed, so that all diffraction orders separate from each other in the far field. This circumstance enables to neglect the interference of waves radiating into the substrate and superstrate and to assign the time averaged Poynting vectors [157]

$$\langle \vec{S}_{\xi,\nu}\rangle = \frac{1}{2}\vec{E}_{\xi,\nu} \times \vec{H}^*_{\xi,\nu} \tag{2.86}$$

to them, whereby $\xi \in \{-,+\}$ is used to differentiate between radiation into the substrate ('$-$') and the superstrate ('$+$'). The corresponding expressions for $\vec{E}_{\xi,\nu}$ and $\vec{H}^*_{\xi,\nu}$ are defined via the individual summands in Eqs. 2.57 and 2.58. Every pair of numbers given up by ξ, ν is called a 'radiation channel'. Eq. 2.86 then allows to calculate the power in

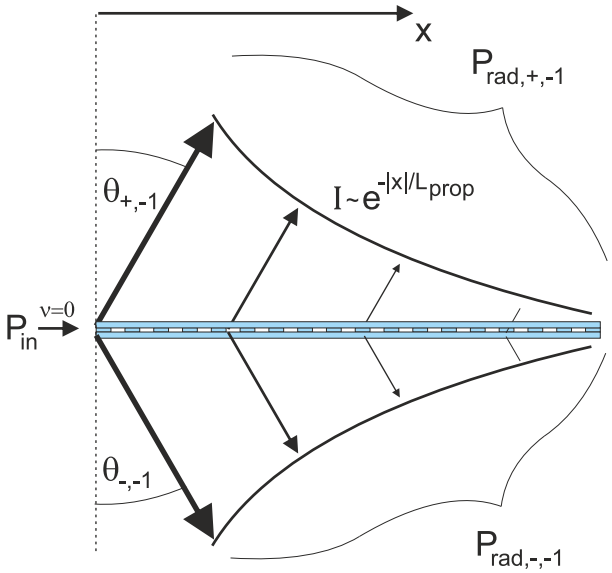

Figure 2.21: Decay of an excited mode ($\nu = 0$) into radiation (two radiation channels with $\nu = -1$) and absorption losses. According to refs. [157, 158]

each radiation channel via [157]

$$P_{rad,\xi,\nu}/l_y = |\int_0^\infty \langle \vec{S}_{\xi,\nu} \rangle \vec{e}_z \mathrm{d}x|, \tag{2.87}$$

whereby the integral is calculated at some position of z outside the waveguide grating.

The indexing of $P_{rad,\xi,\nu}$ can be understood in the same way as for Eq. 2.86. Using Eq. 2.87, and defining the coupling efficiency per radiation channel [157]

$$\eta_{\xi,\nu} = \frac{P_{rad,\xi,\nu}}{P_{in}}, \tag{2.88}$$

the conservation of energy can then be written in the form [157]

$$\sum_{\xi,\nu} \eta_{\xi,\nu} + A = 1, \tag{2.89}$$

whereby the sum of all coupling efficiencies per radiation channel (the left summand in Eq. 2.89) is called 'outcoupling efficiency'. Furthermore, the process of the transferring power from an eigenmode into the radiation channels is termed 'outcoupling'.

Importantly, the equations above exhibit information about the concentration of light. $\langle \vec{S}_{\xi,\nu} \rangle$ can be interpreted as the intensity $I_{\xi,\nu}(x)$ of light radiated into one radiation channel. From Eqs. 2.84-2.87, it can be derived that the average of this intensity is given

by

$$\overline{I_{\xi,\nu}} = \frac{\eta_{\xi,\nu} P_{in}}{L_{prop} \cos\theta_{\xi,\nu} l_y} \tag{2.90}$$

with $\theta_{\xi,\nu}$ as the mean diffraction angle attributed to a radiation channel (see Fig. 2.21).

Considering the initial intensity I_{in} attributed to the eigenmode, it can be calculated via the effective mode thickness $t_{mode} = t_{WG} + t_{e,1} + t_{e,2}$ and P_{in} via [128]

$$I_{in} = \frac{P_{in}}{t_{mode} l_y} \tag{2.91}$$

Hereby, $t_{e,1} = 1/\mathrm{Im}(k_{z,0,0})$ and $t_{e,2} = 1/\mathrm{Im}(k_{z,J+1,0})$ are the penetration depths of the evanescent fields in the substrate and superstrate. When the optical thickness $t_{WG}\overline{n'}$ of a waveguide grating of an average refractive index n' is larger than $\lambda/2$, the initial intensity can be approximated to $I_{in} \approx P_{in}/(t_{WG} l_y)$. Comparing both $\overline{I}_{\xi,\nu}$ and I_{in} with each other, the intensity in the radiation channel is thus reduced by a factor [157]

$$\frac{\overline{I}_{\xi,\nu}}{I_{in}} = \eta_{\xi,\nu} \frac{t_{WG}}{L_{prop} \cos\theta_{\xi,\nu}} = \eta_{\xi,\nu} \frac{1}{C_{geo}} \tag{2.92}$$

with the geometric concentration factor

$$C_{geo} = \frac{L_{prop}}{t_{WG}} \cos\theta_{\xi,\nu} \tag{2.93}$$

Now, the principle of reciprocity is applied: after the entire power P_{in} is radiated away and absorbed, reversing the time must result in the excitation of the mode via the radiation channels [157]. Therefore, a waveguide grating can concentrate light with a maximum concentration factor of C_{geo}. Hereby, maximum concentration is reached in the absence of loss and an exponentially increasing intensity profile with respect to the negative x-direction. To elaborate this explanation, a mirror symmetric waveguide grating with two radiation channels is assumed (see Fig. 2.22a). As no losses are present ($A = 0$), $\eta_{\xi,\nu} = 0.5$ must hold true. Applying reciprocity, the eigenmode is excited with 100% incoupling efficiency (η_{tot}) when the waves in both radiation channels are used as incident waves by reversing time (see Fig. 2.22b). When only one radiation channel is used to excite the eigenmode, the eigenmode can only be excited with 50% incoupling efficiency (see Fig. 2.22c). The same argumentation accounts for the presence of loss, whereby the incoupling efficiency is always smaller than 100% [157]. It is important to note that the principle of reciprocity must be applied to the electromagnetic fields, so that all phase relations of the electromagnetic fields are correctly taken into account. For instance, considering a TE_1 eigenmode for the same symmetric waveguide grating, the relative phase between

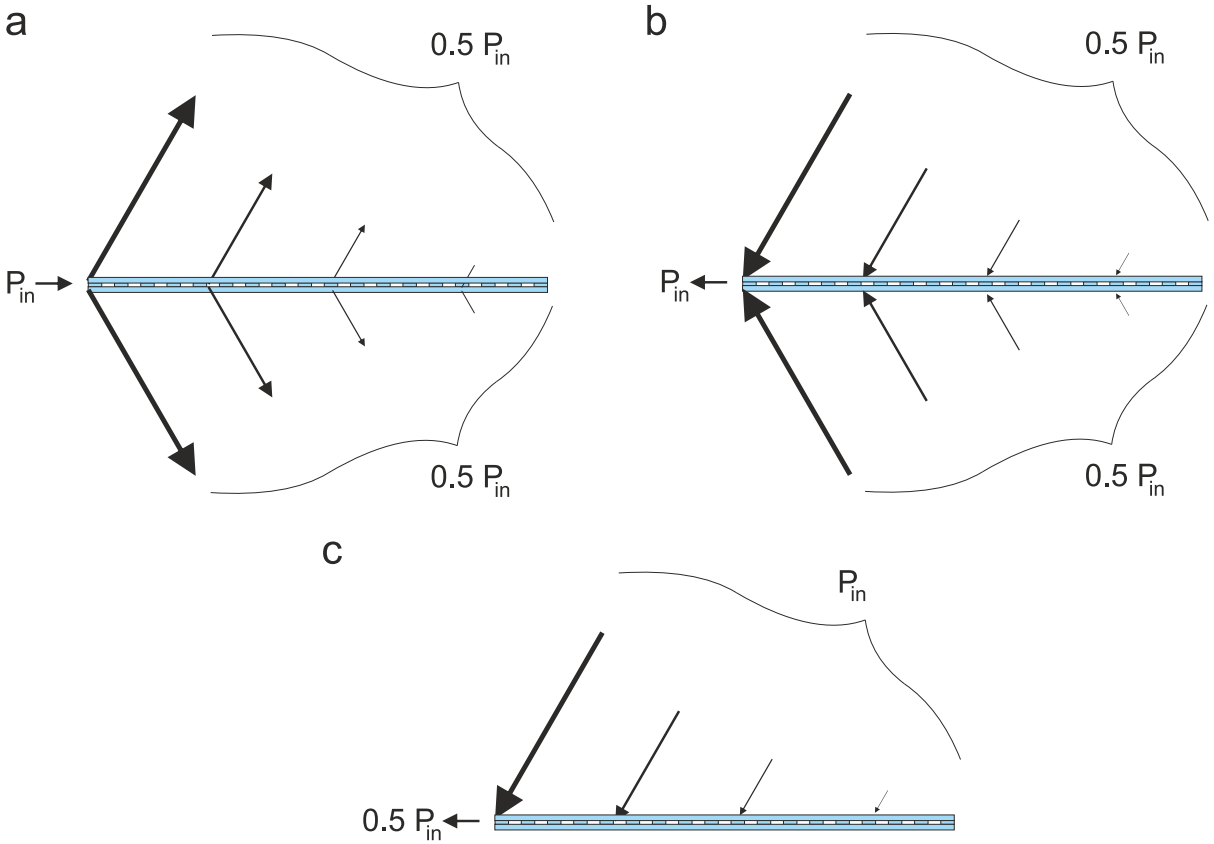

Figure 2.22: Mirror symmetric waveguide grating with two radiation channels under $A = 0$. a) The outcoupling efficiency is 100%. b) Via reciprocal excitation, the eigenmode can be with an incoupling efficiency of 100%. c) The incoupling efficiency decreases to 50% when only one beam falls onto the waveguide grating. According to refs. [157]

the fields in both radiation channels is π. Two incident waves with a relative phase of zero would not excite a TE_1 mode. In contrast, a TE_0 eigenmode is symmetric and can be excited with 100% incoupling efficiency by two incident waves with a relative phase of zero [157]. Such considerations will be of importance in Chapter 5.

There is another important point to consider. In reality, incident light is commonly not governed by an exponentially increasing intensity profile, but rather by a homogeneous (e.g. the sun), or a Gaussian one (e.g. a laser) [159]. Considering that the incoming waves excite the eigenmode via a distinct radiation channel ξ, ν, then the incoupling efficiency per radiation channel $\eta_{in,+/-,\nu}$ can be expressed via the overlap integral between the ideal (time-reversed) field distribution $\vec{F}_{rad,\xi,\nu}$ and the field distribution of incident waves $\vec{F}_{in,\xi,\nu}$ [152, 157]

$$\eta_{in,\xi,\nu} = \eta_{\xi,\nu} \frac{|\int_A \vec{F}^*_{in,\xi,\nu} \vec{F}_{rad,\xi,\nu} \, \mathrm{d}\vec{A}|^2}{\int_A |\vec{F}_{in,\xi,\nu}|^2 \, \mathrm{d}\vec{A}| \int_A |\vec{F}_{rad,\xi,\nu}|^2 \, \mathrm{d}\vec{A}}, \tag{2.94}$$

whereby $\vec{F}_{in,\xi,\nu}$ and $\vec{F}_{rad,\xi,\nu}$ refer to the electric field for TE polarization, and to the

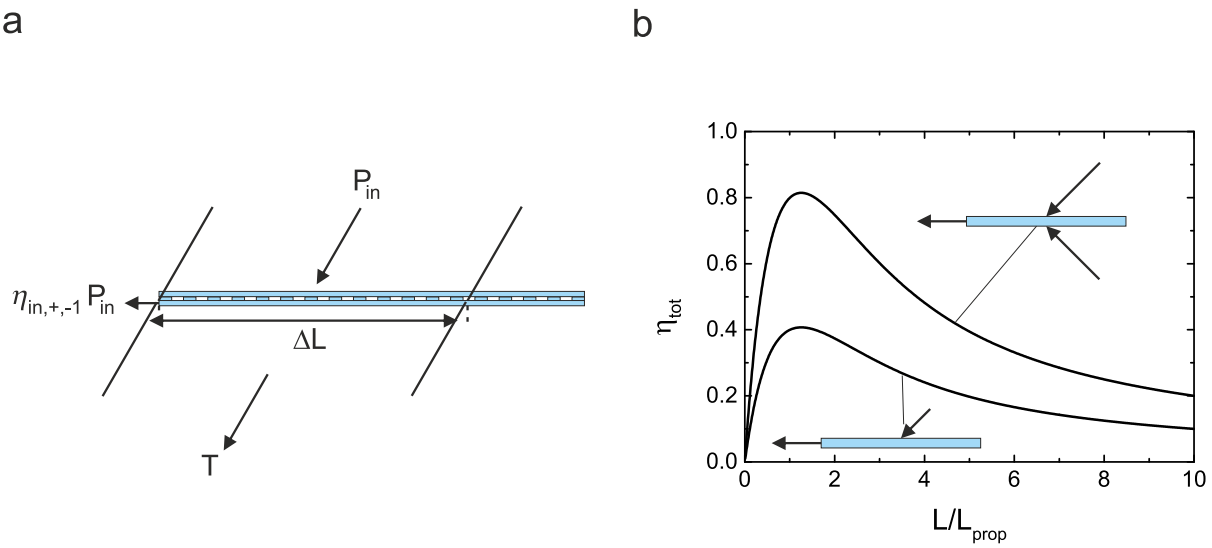

Figure 2.23: a) Excitation of an eigenmode by incoming waves of extent ΔL of homogeneous intensity. b) Corresponding efficiency under the assumption of mirror symmetry to the z-direction. Maximum incoupling efficiency occurs at $L \approx L_{prop}$. The incoupling efficiency is doubled for two incident beams. According to refs. [152, 157].

magnetic field for TM polarization. Note that the integral in Eq. 2.94 must be calculated over an x-y plane in the substrate or superstrate (depending on ξ). For translational invariance in the y-direction, it reduces to an integral over one dimension.

Using Eq. 2.94, the incoupling efficiency can be finally expressed by [152, 157]

$$\eta_{tot} = \sum_{\xi,\nu} \eta_{in,\xi,\nu} \leq 1 \tag{2.95}$$

This theory chapter will be closed with an example of the incoupling efficiency of a homogeneous beam with a spatial extent L with respect to the x-direction, which falls onto a waveguide grating with equal coupling coefficients for both z-directions (Fig. 2.23a). It is further assumed that an investigated eigenmode only radiates into a single diffraction order, so that there is one radiation channel in the substrate and one radiation channel in the superstrate. The incoupling efficiency becomes zero for $\lim_{L\to 0}$ and $\lim_{L\to\infty}$ (Fig. 2.23b) [152, 157]. This behavior can be understood as follows. For small widths $\Delta L << L_{prop}$, only a restricted number of grating slits is illuminated. Due to Heisenberg's uncertainty principle, the angular divergence of diffracted waves becomes large and most of the diffracted angles do not match the internal angle of the eigenmode. From the mathematical point of view, an incident beam of small spatial dimension is represented by a broad plane-wave spectrum. The plane-wave spectrum of an eigenmode is significantly smaller in comparison to the one of the incident beam. Both arguments explain why the overlap integral and the incoupling efficiency become small. For large widths $L >> L_{prop}$,

only photons within a range of a few L_{prop} have a large probability to reach $x = 0$. All other photons have a large probability of being diffracted out of the waveguide and, thus, the incoupling efficiency becomes small. In between these two limits, for $\Delta L \approx L_{prop}$, an optimum of the incoupling efficiency of $\eta_{tot} \approx 0.41$ is observed. This value occurs as the symmetry limits the incoupling efficiency to 0.5 when only one incident beam on one side of the waveguide is present. The reduction from 0.5 to 0.41 results from the mismatch between the homogeneous beam profile of the incident waves and the exponential beam profile corresponding to the ideal field distribution. Two homogeneous beams could thus reach a maximum efficiency of 0.82 [152, 157].

The same considerations can be applied to more complicated beam profiles (such as Gaussian beams) as well by expressing its plane-wave spectrum via a spatial Fourier transform (see. Eq. 2.16).

2.8 Short Summary

With the methods and characteristics explained in the last sections, the fundament to understand the publications presented in Chapters 4 and 5 is established. If needed, additional elaborations on these methods will be given over the course of the thesis.

Chapter 3

Experimental Methods

In the previous chapter, the theoretical characteristics of waveguide gratings have been analyzed. The assumptions for calculating these characteristics are perfectly homogeneous, and flat dielectric films as well as perfect structures. It is obvious that real layers and structures differ from these assumptions. In fact, it is challenging to achieve precisely produced films and structures of low surface roughness, low densities of undesired light scattering defects, and large areas. On top of that, their implementation for solar applications inherently demands the use of inexpensive processes (e.g. roll-to-roll fabrication). In addition, the optical characteristics of samples need to be measured and analyzed. In this chapter, both methods to fabricate and characterize waveguide gratings as well as other geometries will be discussed.

3.1 Fabrication methods

Two exemplary geometries are anticipated, which will be discussed in our publications in Chapters 4 and 5: A symmetric hybrid waveguide grating geometries consisting of dielectric layers and silver gratings, and plasmonic geometries consisting of a silver layer and silver nanoparticles (AgNPs). Exemplary visualizations of both geometries are shown in Figs. 3.1a and b.

Methods to fabricate such geometries are introduced in the following sections. They can be separated into two categories:

1. The fabrication and lamination of dielectric layers.
2. The fabrication of dielectric and metallic structures.

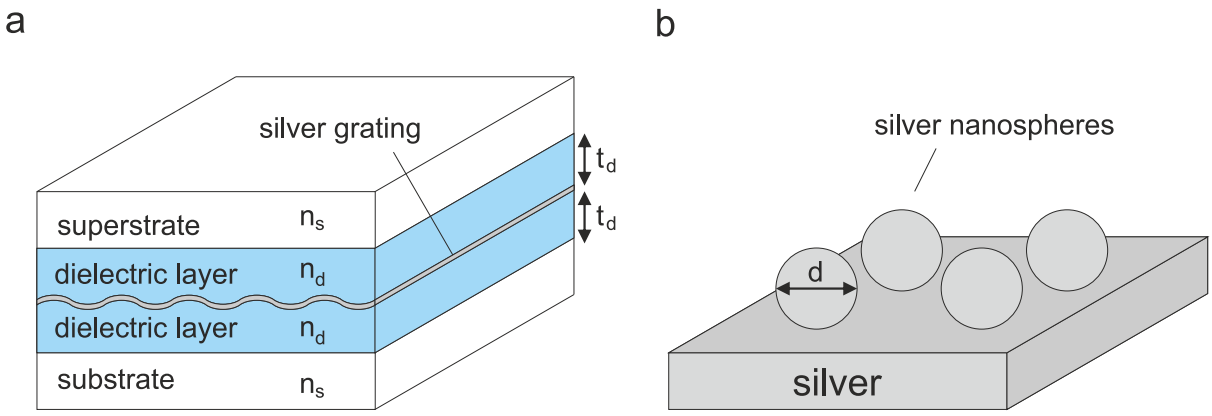

Figure 3.1: Exemplary geometries which are challenging to fabricate. a) A waveguide with symmetric dielectric layers and a point-symmetric silver grating with a period of $\Lambda \approx \lambda$ in the visible range. b) Silver nanospheres of small diameter $d << \lambda$ on top of a planar silver layer.

3.1.1 Fabrication and Lamination of Dielectric layers

In the existing body of literature, there are various reports on the fabrication of dielectric layers. For instance, polymer waveguides, e.g. consisting of polystyrene (PS) or polymethyl metacrylate (PMMA), can be coated from the liquid phase [160], are cost-efficient and large-scale compatible, and can be plastically deformed with ease above their glass temperature to form structures. Thanks to these properties, polymers can be coated and structured in high throughput roll-to-roll processes [161–163]. Moreover, polymer layers can be deposited on top of each other using orthogonal solvents [164, 165] or cross-linking [166].

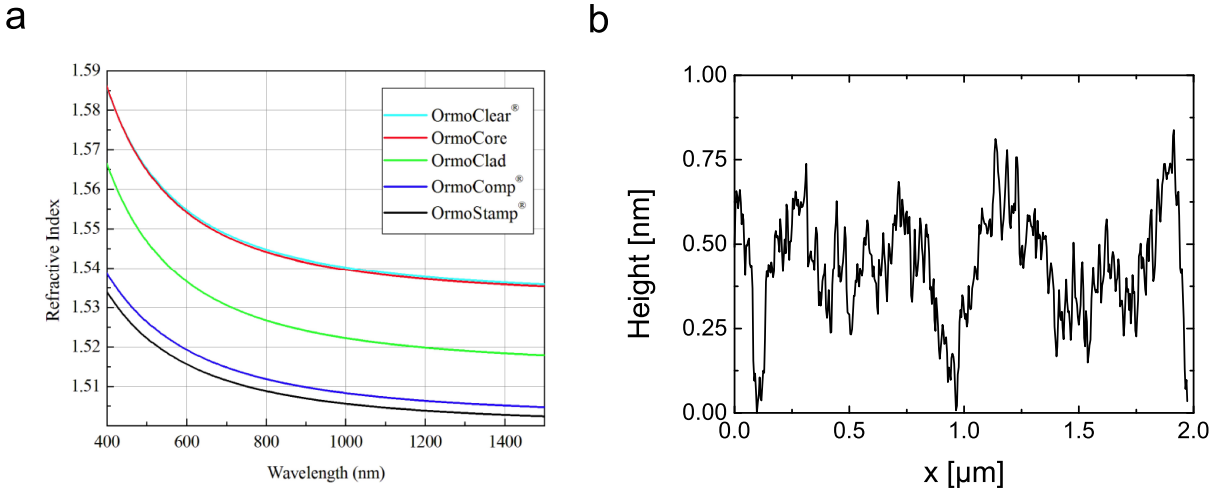

Figure 3.2: a) Refractive index of various OrmoCERs including OrmoCore and OrmoClad. From [167]. b) Typical surface profile of a spin-coated and cross-linked OrmoCore film with a surface roughness of $\sigma_{RMS} < 1$ nm (obtained via atomic force microscopy [168]).

In this thesis, the polymers 'OrmoCore' and 'OrmoClad' are used [167, 169]. OrmoCore and OrmoClad exhibit relatively large refractive indices (Fig. 3.2a), can be deposited from the liquid phase and contain photo-initiator groups so that they can be cross-linked into a rigid layer via illumination with UV-light. They exhibit a small surface roughness of $\sigma_{RMS} = 0.3...1.0$ nm (Fig. 3.2b) after deposition and are highly transparent over the entire visible and near-infrared range of wavelengths (see Section 3.2 for further details).

In the following, a standard procedure to obtain dielectric layers and symmetric waveguides is provided. First, a clean transparent substrate is pre-treated by a heating step of 120° (Fig. 3.3a) and a subsequent UV-light irradiation step (Fig. 3.3b) at $\lambda = 172$ nm at a dose of approximately 10 J/m^2 to increase its surface energy [170]. This increased surface energy of the substrate energetically favors a wetting of its surface by an OrmoCore film [171].

Afterwards, an OrmoCore layer is deposited via spin-coating. To do so, a solution of OrmoCore and propylene glycol methyl ether acetate (PGMEA) [172] is cast onto the substrate (Figs. 3.3c and d). Subsequently, the substrate is put into rotation with a defined rotation frequency profile $\omega_R(t)$. The rotation frequency profile typically consists of a linear ramp-up with $\omega_R(t_0) = 0$ and $\omega_R(t_1) = \omega_F$ with $\omega_F \approx 300$/s and $t_1 = 5$ s. The ramp-up is followed by a plateau of a constant frequency ω_F until the rotation is stopped at $t_2 = 30$ s. In the beginning of the ramp-up, the solution spreads over the substrate as a result of centrifugal forces [173]. With further increasing rotation frequency, excess solution moves toward the substrate's edge and is eventually hurled away. The remaining solution is dominated by three processes [173]. The first one is the ongoing presence of centrifugal forces. The second one are viscous forces, which are directed towards the center of rotation. The third one is linked to an increase of viscosity as the film becomes gradually thinner and, simultaneously, experiences solvent evaporation. These processes then lead to a thickness dependence $h(t)$ of [173]

$$h(t) = \frac{h_0}{\sqrt{1 + h_0^2 \omega_F^2 a_L(t) t}} \approx A_{0,S} \frac{c_S}{\sqrt{\omega_F}} \tag{3.1}$$

during the plateau. Hereby, h_0 is the initial film thickness immediately after the ramp-up ($t = t_1$), and a_L is a solution specific parameter including the solution's viscosity. The approximation on the right side displays a practically more useful relation including a constant $A_{0,S}$, and the mass concentration c_S of OrmoCore in the solution. In consequence, the thickness of the film can be controlled via controlling c_S and ω_F [174].

Subsequently, residual solvents are evaporated via a post-baking step at 120°C (Fig. 3.3e), or alternatively via a vacuum step at an air pressure of below 1 mbar (below the vapor pressure of PGMEA of 3.6 mbar [172]) for 10 minutes, respectively.

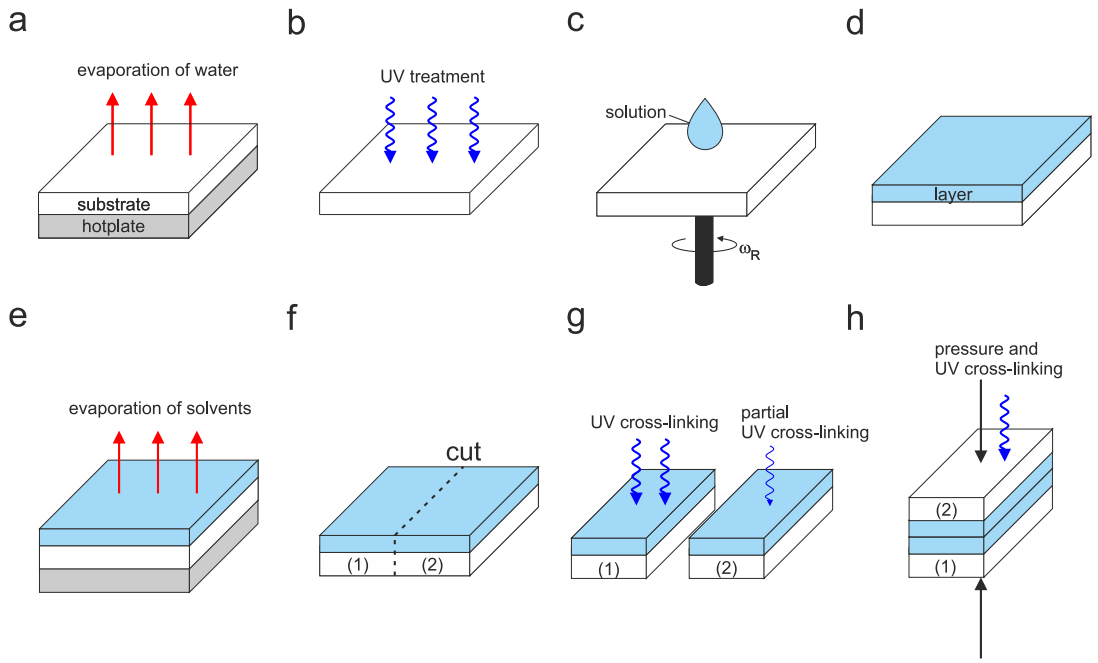

Figure 3.3: Deposition and lamination of OrmoCore layers for the fabrication of symmetric waveguides. a,b) Pre-treatment of a substrate via heating and UV light. c,d) Spin-Coating of a layer of OrmoCore from solution. e) Post-treatment to evaporate solvents. f) Separation of the coated substrate into two Pieces (1) and (2). g) Cross-linking of Piece (1) and partial cross-linking of Piece (2). h) Lamination of both pieces by mechanical pressure and simultaneous UV cross-linking.

Now, the layer could be cross-linked and more layers could be added to build a waveguide. As a matter of course, such approach underlies systematic and statistic variations of the layer thickness which may result from the spin-coating process. As they render the fabrication of a mirror symmetric waveguide grating by stacking difficult, the contributions to these variations will be explained. First, only parts of the substrate's surface which are far away from its edges obey Eq. 3.1. Toward the substrate's edges, residual excess material leads to a systematic increase of the OrmoCore thickness [173]. Second, away from the edges, solution flow instabilities, inhomogeneous evaporation, e.g. due turbulences in the gas above the substrate, and inhomogeneous substrates or solutions can lead to statistical thickness variations around the average thickness [173]. Third, the environmental conditions, surface characteristics of the substrate, and viscosity of the solution may slightly vary between subsequent spin-coating processes. This means that slightly different average thicknesses may occur for subsequently spin-coated films which are fabricated under nominally the same conditions.

Concerning the first contribution, larger substrates enable larger regions of homogeneous layer thicknesses. For the second contribution, an optimization of all parameters of the process can be done to minimize statistical variations. This optimization has been performed by spin-coating OrmoCore films under a controlled temperature and air humidity

in a clean room, whereby the spin-coater exhibits a pump system to ensure a laminar nitrogen gas flow above the substrate's surface. Moreover, by ensuring a sufficiently long mixing time of the solution of at least 24 hours, fresh and unexposed OrmoCore (>2 months before the expiration date), thoroughly cleaned substrate surfaces via subsequent supersonic acetone and isopropanol baths following a nitrogen dry blow, the use of solution filters with a pore size smaller than 200 nm, a solution concentration below 40%, and a complete solution coverage of the substrate before starting the ramp-up, the local statistical thickness variations have been optimized to relative values of below 1.0%.

For the third contribution, whatsoever, it has been observed that it cannot be easily tackled by simply controlling all parameters. Instead, a different method, called 'lamination' is chosen. Lamination will be explained with the following example.

A substrate with a non cross-linked, spin-coated OrmoCore layer is mechanically separated into two pieces (1) and (2) (Fig. 3.3f). The OrmoCore layer on piece (1) is fully cross-linked with a UV-dose of 2.0 J/cm^2 at wavelength of $\lambda = 365$ nm. In contrast, the OrmoCore layer on piece (2) is only partially cross-linked with a corresponding dose of 0.23 J/cm^2 (Fig. 3.3g). This way, the OrmoCore film on piece (2) is not viscous anymore, but still plastically deformable. It is then possible to mechanically press piece (1) and piece (2) together at a mechanical pressure of 100 bar and cross-link the OrmoCore film on piece (2) through its corresponding substrate with another UV-dose of 2.0J/cm^2 (Fig. 3.3h). This last step is called 'lamination'. Using lamination, a symmetric substrate/OrmoCore/OrmoCore/substrate-waveguide with identical OrmoCore average layer thicknesses can be created.

It is important to note that lamination can be extended to include structured layers in between both OrmoCore layers. For instance, additional structuring and metallization steps of piece (1) prior to the lamination lead to the geometry shown in Fig. 3.1. Explanations on how layers can be structured follow in the next section.

3.1.2 Structuring Methods

The structured dielectric layers used in this thesis are fabricated with the help of replication of a master stamp and subsequent UV-nano-imprint lithography (UV-NIL) [175,176]. This procedure is cost-efficient and compatible with large-area processing by step-and-repeat [177] or roll-to-roll imprint [161]. As a matter of course, an initial master stamp must be produced by a structuring process such as electron-beam-lithography (EBL) [178] and reactive ion etching (RIE) [179], laser interference lithography (LIE) [180], conventional photo lithography [181] or mechanical ruling [182]. For this thesis, commercially available master stamps are used.

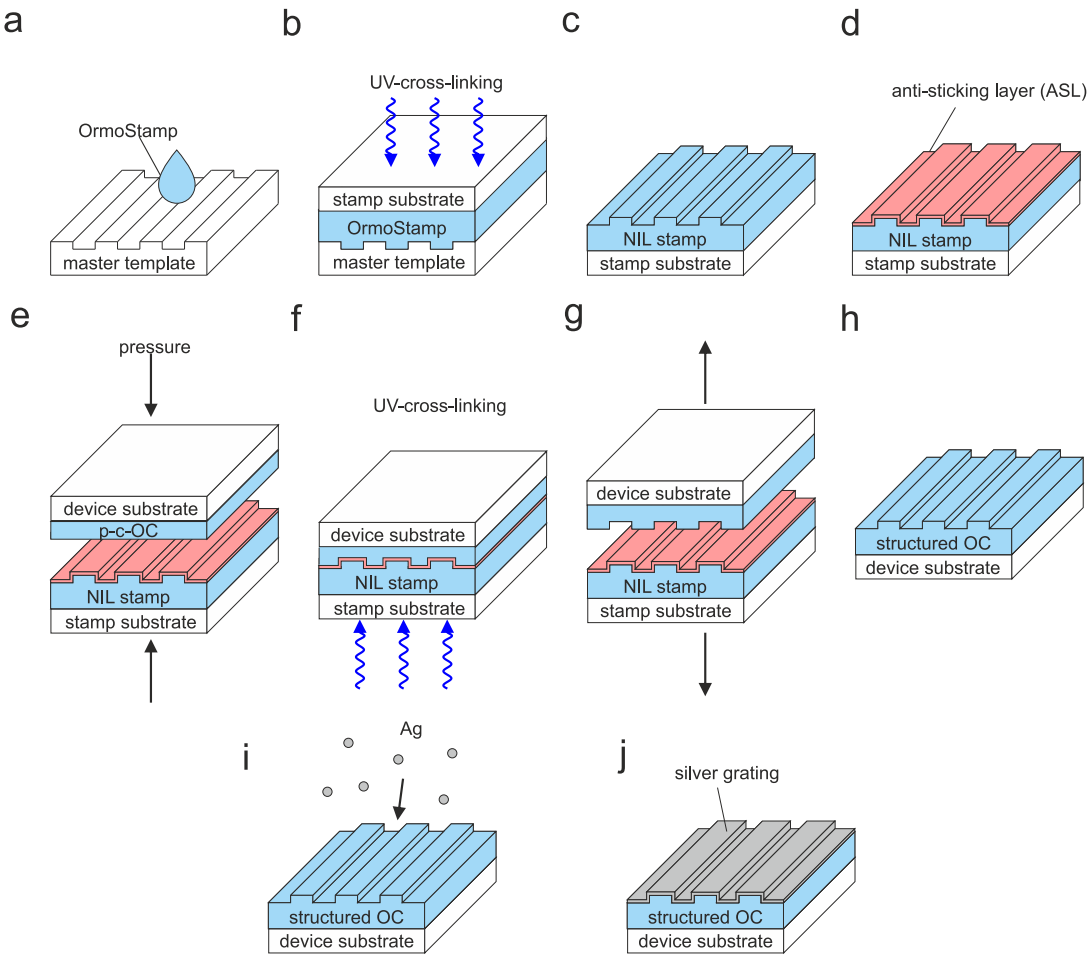

Figure 3.4: Replication of structured master templates and UV-NIL of partially cross-linked OrmoCore (p-c-OC). a) Casting of OrmoStamp onto a master template. b,c) Bringing a transparent 'stamp substrate' into contact with the OrmoStamp, subsequent UV-cross-linking and release of the master template. d) Deposition of an anti-sticking layer (ASL). e) Imprinting of the stamp's negative surface profile into a partially cross-linked OrmoCore layer. f) Cross-linking through the stamp. g) Release of the stamp. h) A structured OrmoCore layer on a device substrate is obtained i,h) Optional metallization steps via physical vapor deposition (PVD) to achieve a structured metal layer.

The replication procedure is as follows: A master template is coated with a droplet of OrmoStamp [183] (Fig. 3.4a) and brought into contact with a transparent glass substrate ('stamp substrate') under vacuum to avoid defects caused by air inclusions. Capillary and gravitational forces even out the layer thickness of the OrmoStamp to about 30 μm before it is cross-linked using a Xenon-Lamp with a dose of 3 J/cm^2 (Fig. 3.4b). Subsequently, the stamp substrate with the structured OrmoStamp layer is released from the master stamp. This replicate is called a 'NIL-stamp'(Fig. 3.4c). This NIL-stamp is coated with an anti-sticking layer consisting of a monolayer of triflouorosilane [184], which eases the release between the NIL-stamp and a target layer after an imprint and, thus, prevents mechanically induced defects (Fig. 3.4d).

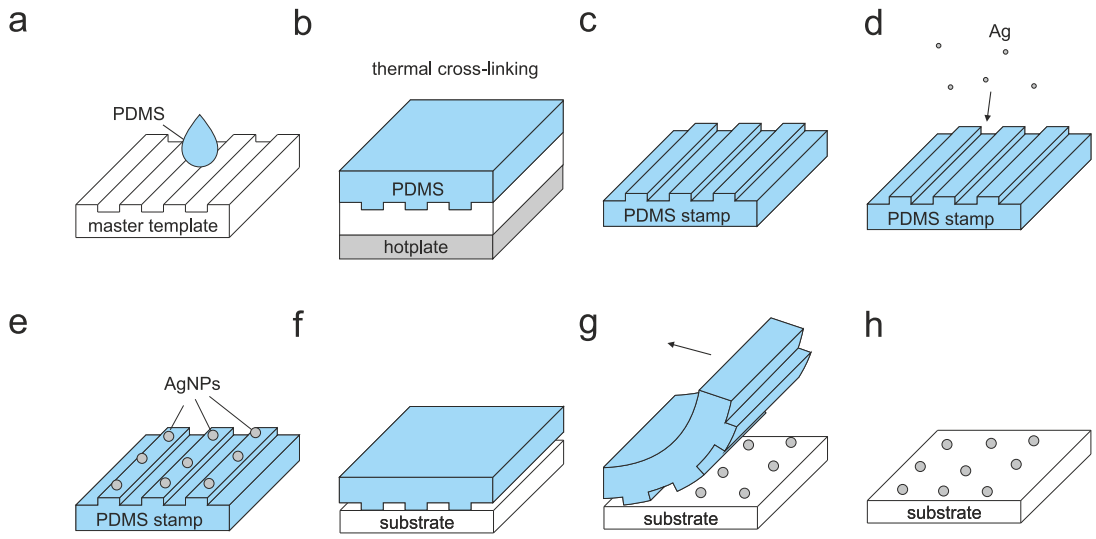

Figure 3.5: Transfer printing of AgNPs [186, 187]. a) Casting of PDMS on a master template. b) Thermal curing and subsequent release to obtain a structured PDMS stamp (c). d,e) Metallization via PVD. The low surface energy of PDMS enables the formation of AgNPs. f,g,h) Transfer of AgNPs onto a substrate via mechanical contact and controlled release.

To structure a partially cross-linked OrmoCore layer (deposited on a 'device substrate') via UV-NIL, it is mechanically pressed together with the NIL-Stamp under a pressure of 100 bar for a period of 10 minutes (Fig. 3.4e). Subsequently, the OrmoCore layer is fully cross-linked through the transparent glass and the replica using UV light with $\lambda = 365$ nm at a dose of 2.0 J/cm^2 (Fig. 3.4f). Afterwards, the replica and the substrate are mechanically separated from each other (Figs. 3.4g and h).

To obtain metallic gratings (Figs. 3.4i and j), a structured OrmoCore film can be subsequently metallized using physical vapor deposition (PVD) [185]. For silver on native cross-linked OrmoCore, closed layers typically occur for nominal thicknesses t_{Ag} above 20 nm.

Another way to obtain structured metal layers is 'transfer-printing' [188]. For transfer-printing, a replicate, called 'PDMS stamp' (Figs. 3.5a-c), is made using thermally cross-linkable polydimethylsiloxane (PDMS) [189]. As PDMS has a low surface energy γ_{PDMS}, PVD coated metals with $\gamma_{PDMS} < \gamma_{metal}$ tend to energetically favor island growth [186]. For instance, silver deposited via PVD on native PDMS typically exhibits a percolation threshold at a nominal thickness of around 40 nm [186, 190]. Below this threshold, silver nanoparticles (AgNPs) form on the surface of the PDMS stamp (Figs. 3.5d and e). The same small surface energy of PDMS then allows to transfer the AgNPs from the PDMS stamp to a target substrate with $\gamma_{PDMS} < \gamma_{substrate}$ (Figs. 3.5f-h).

For larger silver thickness values above the percolation threshold, the same procedure can be used to transfer regions of closed silver layers [187]. The geometry of these regions is

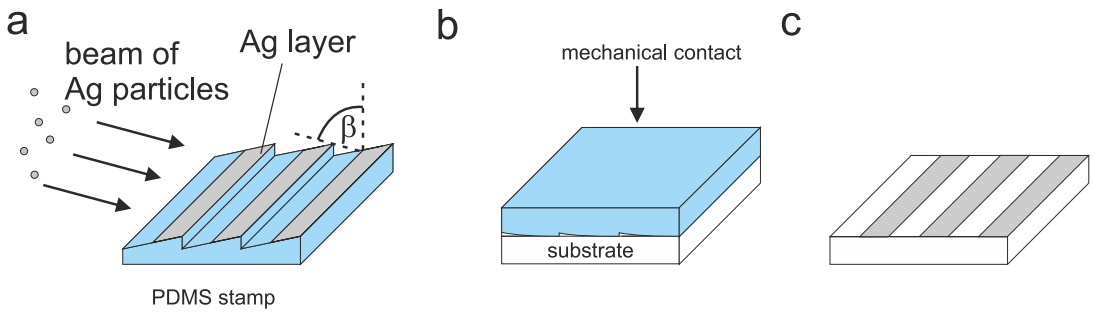

Figure 3.6: Method to obtain binary silver gratings by transfer-printing. a) The surface relief of a PDMS stamp is used as a shadow mask. The duty cycle of the grating can be adjusted with the tilting angle β. b,c) Mechanical contact and subsequent release transfer the grating on a structure. As the stamp is soft, the initial 3-dimensional shape of the silver grating is converted into a binary quasi-2-dimensional shape.

dictated by the geometry of the PDMS stamp. For example, a one-dimensional surface relief grating can be used to transfer print a binary silver layer pattern as shown in Fig. 3.6. Herein, the surface relief of a PDMS stamp can be used as a shadow mask. This way, the duty cycle D of the binary pattern can be controlled via the tilting angle β of the PDMS stamp with respect to the incoming beam.

AgNPs can also be obtained by a chemical process called 'mirror-reaction' [191], or electroless deposition (ELD) [192]. Usually, ELD is used to deposit closed metal films of large thickness in the range of several hundred nanometers. In the first few seconds of a deposition, a metal layer deposited by ELD undergoes a phase in which it consists of nanoparticles only: from the point of view of thermodynamics [193], random agglomerations of silver tend to grow above a critical radius and seeds below this critical radius tend to shrink by releasing free silver ad-atoms onto a substrate's surface. Seeds above the critical radius grow to nanoparticles on the substrate. After a short period of time, the continuous growth of these nanoparticles leads to a closed metal layer [193, 194]. When the ammonia content of the ELD solution is increased, the growth rate can be drastically reduced, opening a window of time during which the growth of nanoparticles can be manipulated [194]. For instance, it is possible to influence the growth positions of AgNPs using external light or surface plasmons as it will be further elaborated in Chapter 4.

All geometries which will be presented in Chapters 4 and 5 can now be understood as the results of combining the fabrication methods explained above (lamination, replication, UV-NIL, PVD, ELD, and transfer-printing).

3.2 Characterization

In this section, a selection of methods to optically characterize waveguides, waveguide gratings and other optical samples are outlined. Other standard characterization methods to obtain film thicknesses and morphological information (e.g. profilometry [195], atomic force microscopy (AFM) [168] and scanning electron microscopy (SEM) [196]) will not be explicitly described as they are well documented in the literature.

3.2.1 RTS and ATR

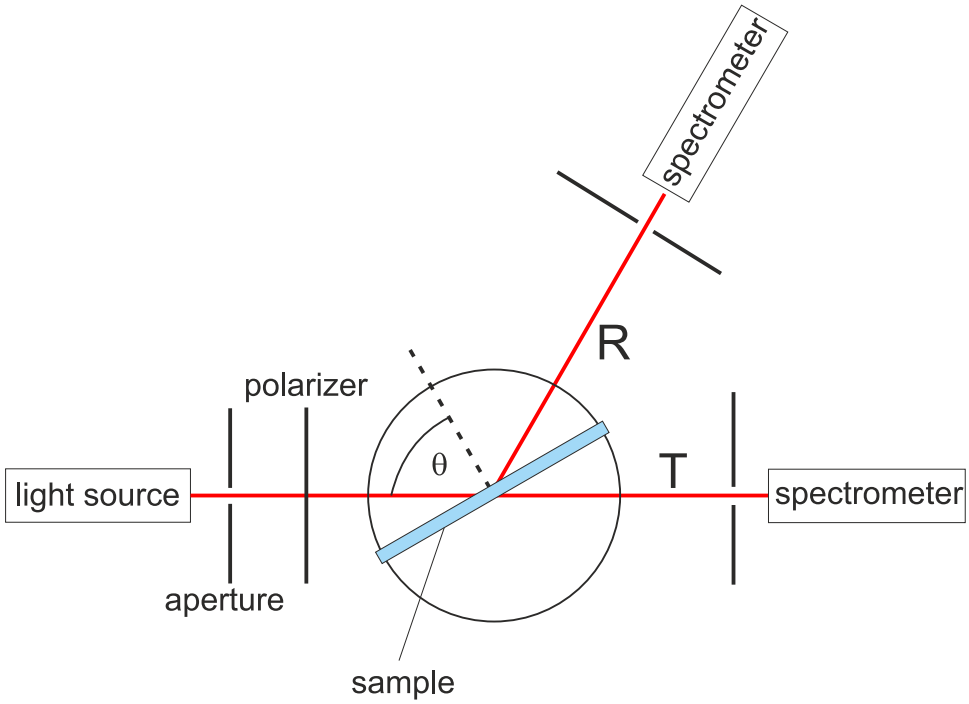

Figure 3.7: Angular resolved reflectance and transmittance spectroscopy (RTS). According to ref. [197].

The most important optical characterization methods used in this thesis are angular resolved reflection and transmission spectroscopy (RTS) [197] and attenuated total reflectance analysis (ATR) [198]. A typical RTS setup is sketched in Fig. 3.7. A parallel and polarized beam of light falls onto a sample under a defined angle θ. Both the spectra of the reflected and transmitted light are measured with spectrometers. By referencing these spectra to the incident light (or a reference sample), the transmittance $T(\lambda, \theta)$ and reflectance $R(\lambda, \theta)$ can be extracted. Importantly, RTS can be used to measure the resonances of a waveguide grating to obtain insights about its eigenmodes (e.g. dispersion relations). Numerous examples of RTS data exhibiting such resonances can be found in Chapters 4 and 5.

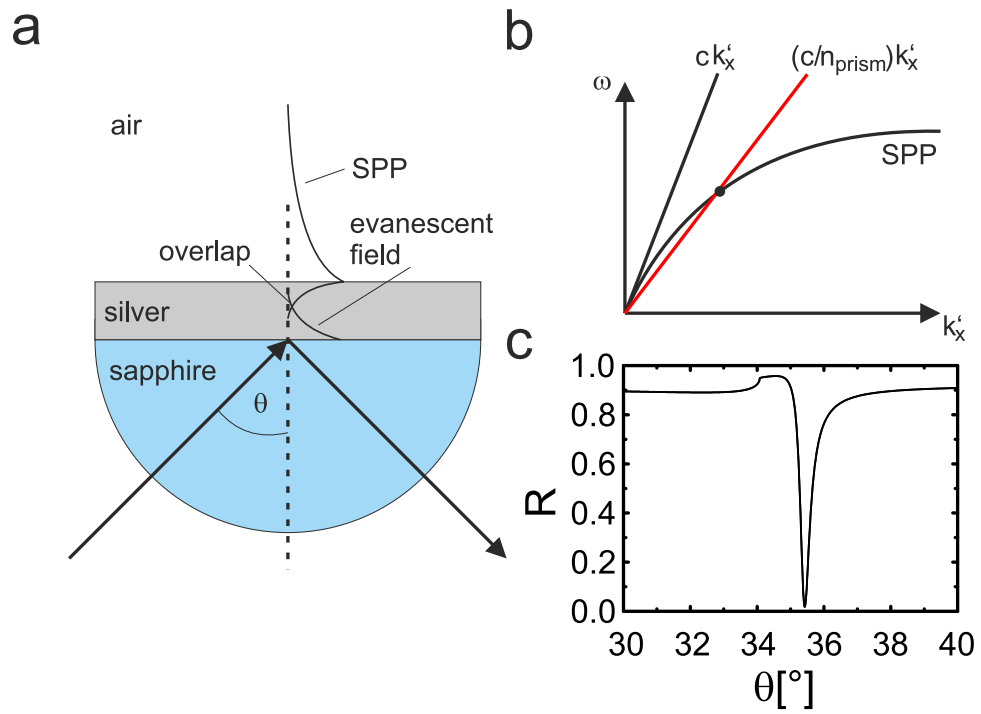

Figure 3.8: Attenuated total reflectance (ATR). a) Kretschmann configuration. b) Qualitative sketch of the corresponding dispersion relation. c) Exemplary reflectance $R(\theta)$ of a 50 nm thick silver film at a wavelength of $\lambda = 632.8$ nm with a prism index of $n_{prism} = 1.7847$. A surface plasmon resonance (SPR) is observable round $\theta = 35.4°$. According to ref. [198].

When no structures are present (e.g. for a planar silver film), it is impossible to excite eigenmodes via RTS. In this case, ATR can be used to gain information about eigenmodes. It is shortly described in the following: light inside a prism of refractive index n_{prism} (Fig. 3.8a) can access larger lateral momenta ($|k'_x| \leq n_{prism} k_0$) than light coming from vacuum and falling onto a planar layer with the prism's refractive index ($|k'_x| \leq k_0$). This increased lateral momentum is enabled by the prism's half-cylindrical shape. When n'_{eff} attributed to a SPP is smaller than n_{prism}, an angle of incidence θ exists for which the condition

$$n'_{eff} \cdot k_0 = n_{prism} \cdot k_0 \cdot \sin\theta \tag{3.2}$$

is fulfilled and the dispersion relations of photons in the prism and surface plasmons cross each other (Fig. 3.8b). Similar as for a guided mode resonance (see Section 2.16), n_{eff} represents a complex pole of $r(k'_x + jk''_x)$. As the photons in the prism can only scan over the real axis ($k'_x = n_{prism} \cdot k_0 \cdot \sin\theta$, $k''_x = 0$), the presence of this pole can be observed as a resonance of $R(\theta) = |r|^2$. This type of resonance is called a 'surface plasmon resonance' (SPR) [198]. An example of a SPR is shown in Fig. 3.8c. As a matter of course, a SPR of measurable width and amplitude only occurs when the field overlap integral between the evanescent field of the waves reflected at the prism base and the field profile of the SPP

is large (see Section 2.23). Typical silver layer thicknesses, for which the field overlap integral is large, are below 100 nm. In the context of this thesis, ATR is of particular importance in Section 4.1.2.

3.2.2 Microscopic Inspection of Edge Emission of Waveguide Modes Excited from High Index Liquid) (MEWEL)

Highly transparent polymers and materials such as OrmoCore and OrmoClad typically exhibit values of n'' in the order of 10^{-7} [199]. A direct measurement of the properties of a waveguide with thickness values t_{WG} of several microns via RTS is challenging: for such small values of n'', the absorption of light per round trip in an OrmoCore or OrmoClad layer is $A = \exp(-2 \cdot 4\pi n'' t_{WG}/\lambda)$. For instance, for a thickness of $t_{WG} = 1$ μm at a wavelength of $\lambda = 632.8$ nm, this absorption is $4 \cdot 10^{-6}$. Under perpendicular incidence and typical refractive index values of around 1.5, the number of round trips is far below 10 [124], so that the absorption $A = 1 - R - T$ exhibits values between $4 \cdot 10^{-6}$ to several 10^{-5}. Simultaneously, R and T exhibit typical values of several 10^{-1}. These values mean that the signal-to-noise ratio of a detector must be at least above 10^4, which is unrealistically high for standard CCD detectors at room temperature [200].

In principle, n'' could be determined by measuring the extinction of light through a large volume filled with the highly transparent material. However, the knowledge of n'' alone does not necessarily mean that a waveguide will exhibit a propagation length as predicted by the theory in Chapter 2. In reality, the waveguide's surface can be rough. During the processing of the waveguide, unwanted light scattering defects or light absorbing particles could be accidentally incorporated. All these effects are additive with respect to n''_{eff} [201] and the propagation length of the eigenmode of a real waveguide is given by

$$\frac{1}{L_{prop}} = \frac{1}{L_{prop,loss}} + \frac{1}{L_{prop,scat}} + \frac{1}{L_{prop,roughness}} \tag{3.3}$$

To accurately characterize the propagation length of a waveguide built from low-loss materials, an eigenmode can be excited and its decay along its direction of propagation can be analyzed.

One method is to directly excite an eigenmode via the waveguide's facet, measure the outcoupled light on the opposing facet, and subsequently shortening the waveguide's length step by step. The change of the outcoupled light's intensity as a function of the waveguide length then enables to calculate the mode's propagation length. This method, when applied to glass fibers, is called 'cut-back method' and has the obvious disadvantage

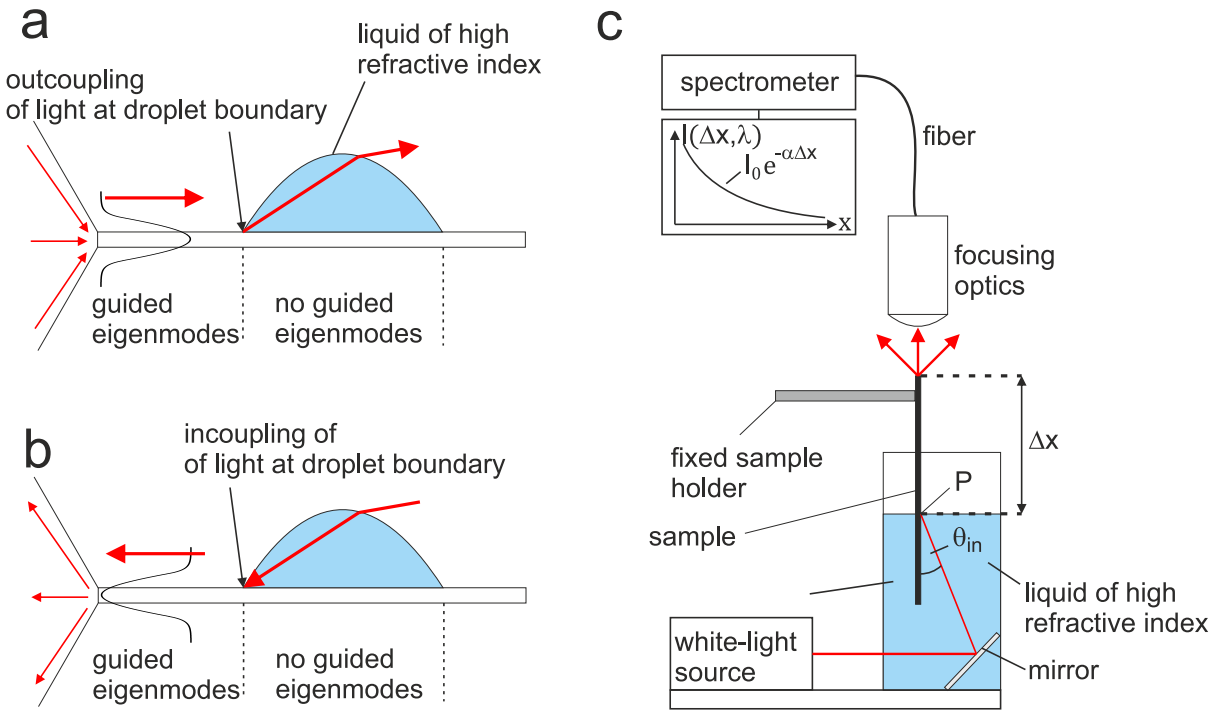

Figure 3.9: Explanation of 'MEWEL' (**M**icroscopic Inspection of **E**dge Emission of **W**aveguide Modes **E**xcited from High Index **L**iquid). a) A droplet of high refractive index leads to the outcoupling of initially guided light propagating via an eigenmode. b) The reciprocal process enables the excitation of eigenmodes. c) Controlled setup based on this phenomenon. White light is coupled into a waveguide at the interface of a liquid of high refractive index. This interface is movable along the waveguide's surface. The spectrally resolved change of intensity with varying distance Δx reveals the extinction coefficient $\alpha(\lambda) = 1/L_{prop}(\lambda)$ of the waveguide. According to ref. [203].

that it destroys the sample [202]. The other and more important disadvantage lies in its inaccuracy since the geometry of the opposing facet may vary with every cut-back step.

Another method is to analyze the intensity distribution of scattered light along the propagation path of an eigenmode [202]. However, to apply this method, the waveguide must exhibit sufficiently large scattering losses.

In this thesis, a different method is used, which is inspired by ref. [204]. Let's suppose there is a droplet of liquid of high refractive index $n_l > n_f$ on top of the waveguide's surface (Fig. 3.9a), whereby n_f is the refractive index of the waveguide core. Beneath this droplet, there is no total internal reflection. Light propagating beneath the droplet via a set of initial eigenmodes must couple out into the droplet. Applying reciprocity, externally incident light can excite eigenmodes at the boundary of the droplet (Fig. 3.9b).

This method to excite eigenmodes is used in the following measurement setup (see its sketch in Fig. 3.9c). A cuvette filled with a high index liquid (e.g. diiodomethane [205] or benzyl benzoate [206]) and a collimated light-source are placed on a movable stage.

The cuvette is equipped with an overflow, so that the level of the liquid does not change when a waveguide is dipped into it. Using a mirror, the light's path is designed in a way that it hits the surface of the liquid under a steep angle θ_{in}. The waveguide to be investigated is fixed with respect to the cuvette so the surface of the liquid can move along the waveguide's surface. This way, the light excites eigenmodes of the waveguide at the meeting point of the liquid-air interface and the waveguide's surface (point P in Fig. 3.9c). Subsequently, the light leaving the waveguide at its upper facet is guided through focusing optics onto a linear spectrometer. This way, the light propagates over a controllable distance Δx through the waveguide. The measured intensity $I(\Delta x, \lambda)$ of the outcoupled light then enables to calculate the propagation length via

$$I(\Delta x, \lambda) = I_0(\Delta x_0, \lambda) \cdot e^{-\Delta x / L_{prop}} \tag{3.4}$$

with Δx_0 as the starting position.

There are some details to consider to practically apply this method: First, a real waveguide is built on top of a substrate of finite thickness. This substrate may support its own eigenmodes (called 'substrate modes'), which disturb the measurement. To avoid substrate modes, a silicon wafer with an oxide layer of 1500 nm thickness is used as a substrate. As silicon strongly absorbs light, the wafer's substrate modes exhibit short propagation lengths compared to the propagation lengths of the waveguide's eigenmodes. Simultaneously, the large thickness of the oxide ensures that the evanescent field of a waveguide's eigenmode decays far enough, so that its propagation length is hardly affected by the absorption of the silicon.

Second, the waveguide may support more than one eigenmode. The MEWEL method cannot differ between multiple eigenmodes and the observed propagation length is composed by the contributions of all eigenmodes. In practice, the observed propagation length can be regarded as a lower bound for the propagation lengths of individual eigenmodes. When the observed propagation length is longer than a value desired for an application, it is fully ensured that the surface roughness, the density of light scattering defects and the raw material's inherent properties meet all requirements for fabricating waveguides of sufficient quality.

Third, the limit of this method is given by the available sample length and accuracy of the spectrometer. For the setup used for this thesis, the lengths of all samples were chosen to 5 cm. This length ensures a detection limit of approximately $L_{prop} = 1$ m.

Fig. 3.10a shows the measured extinction coefficients $\alpha(\lambda) = 1/L_{prop}(\lambda)$ of a waveguide consisting of the mentioned silicon wafer and a layer of OrmoCore with a thickness of 300 nm. The waveguide exhibits propagation lengths around 20 cm in the entire range

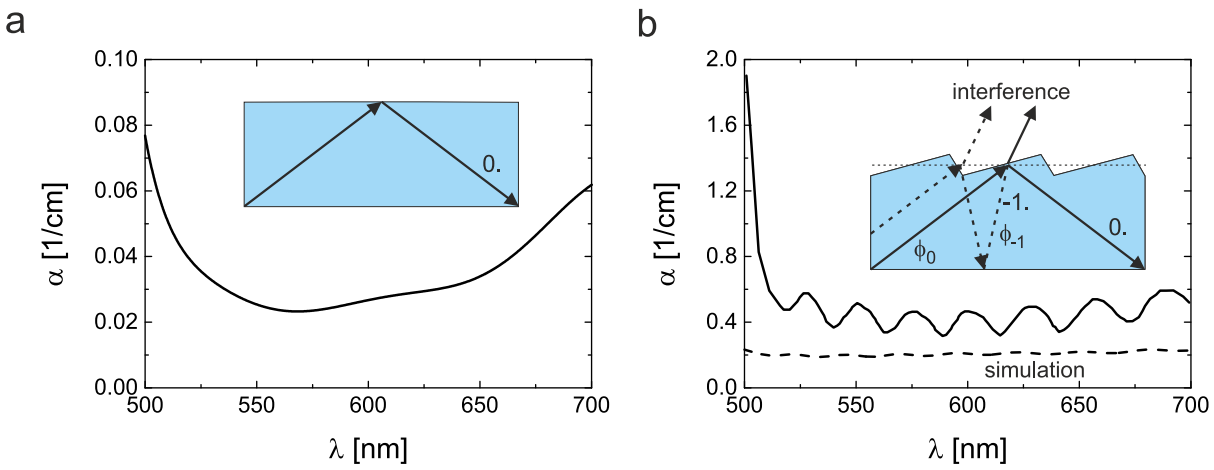

Figure 3.10: Measured extinction coefficients α of two samples by MEWEL. a) Smooth OrmoCore layer of 300 nm thickness on a Si/SiO_2 substrate. b) OrmoCore layer of 5.5 μm with an imprinted blaze grating surface profile (Λ = 555 nm) measured along the direction of the grating vector. The black solid line shows the measurement. The dashed black lines shows the simulation of the TE_0 eigenmode.

between 500 nm and 700 nm, confirming that this waveguide is of sufficient quality for the fabrication of large-area devices.

MEWEL is also helpful to find out whether a structured surface is of high quality. Fig. 3.10b shows the measured propagation lengths of a structured OrmoCore layer of a total thickness of 5500 nm, whereby its surface consists of a blazed surface profile with Λ = 555 nm, a height of 130 nm and a blaze angle of 18°. This waveguide grating is fabricated with the methods explained in Section 3.1. The measured values of α lengths are approximately 0.5/cm between 520 nm and 700 nm. A simulation of the TE_0 eigenmode including the data from Fig. 3.10a results in values of α which are between a factor of 2...3 smaller than these measured data. Considering that the simulation was performed assuming perfect interfaces, this deviation between the measured and simulated values of α can be regarded as small and indicates a high quality of the structured surface.

In addition, $\alpha(\lambda)$ shows an oscillating behavior, which is typical for waveguide gratings and originates from interfering diffraction orders (e.g. the 0th and -1st order). Strikingly, as such interference requires precise phase relations and coupling coefficients, the appearance of this oscillating behavior in a measurement over large distances indicates a high degree of homogeneity of all geometric parameters of the waveguide grating.

Chapter 4

Passive Systems

Waveguide solar concentrators ideally collect sun-light over a broad spectral width and subsequently guide and concentrate light over long distances with minimal scattering losses. In this chapter, three kinds of passive systems will be discussed which tackle these challenges from different directions. First, systems combining different distributions of AgNPs on planar Ag layers (with optional spacer layers) are discussed with respect to their broadband interaction with light. Second, the theoretical properties of symmetric waveguide gratings for achieving large propagation lengths will be elaborated. Last, a method to achieve zero outcoupling with the help of a hybrid waveguide grating will be discussed. Necessary additions to the methods explained in Chapters 2 and 3 will be provided within the context of these discussions.

4.1 Plasmonic Structures for Strong and Broadband Light Coupling

4.1.1 Plasmonic Black Silver by Transfer Printing

As explained in Section 2.3.4, the hybridization of LSPs leads to the formation of additional energy levels. As a result, the absorption spectrum of an ensemble of nanoparticles can be significantly broadened via hybridization [141].

As a matter of course, the absorption of light over a broad spectral range is useful for solar concentrators. For instance, an ideal solar concentrator absorbs the entire incident sun-light and subsequently focuses it to a focal point or line (see Chapter 1). In the case of the hybridized LSPs of AgNPs, the probability is large that photons are thermalized to heat [131, 138] unless they are captured by other devices such as solar cells.

This large probability of thermalization renders the use of AgNPs as particularly useful for solarthermics: as described in Chapter 1, many solarthermics designs are based on strongly absorbing materials in combination with heat conducting materials [207, 208]. As metals like silver inherently exhibit large heat conductivity [209], broadband light absorbing metals can fulfill both of these requirements.

In principle, an almost perfect absorber can be realized by embedding densely packed AgNPs inside a transparent dielectric host material [210]. However, such an absorber would not perform well in solar thermal applications as the host matrix is insulating. To preserve the broadband absorbing properties of interacting LSPs and increase the thermal conductivity, other strategies must be considered. One strategy is to distribute densely-packed AgNPs on pre-structured templates to both minimize reflection losses and form a surface at which moving liquids (e.g. water) can transport the heat away to be used elsewhere [211]. The disadvantage of this method is its restriction to steam generation. Other approaches combine metallic substrates, an insulating spacer layer and metallic nanoparticles to form metal-insulator-metal resonators [212–216]. These existing works in the literature report that most of the heat is created at the locations of the nanoparticles and, thus, the spacer layer hinders the ideal transport of heat.

In the following, a broadband light absorber consisting of a monolayer of AgNPs directly deposited on a silver layer will be presented and explained [190]. This way of arranging the AgNPs has two advantages: first, the silver layer can be regarded as a source for mirror charges, leading to an increased number of resonances right away in comparison to isolated AgNPs [217]. Second, LSPs exhibit enough momentum to excite SPPs [218]. The AgNPs on the silver layer can therefore interact with each other via SPPs to form additional resonances for externally incident light. In contrast to isolated AgNPs, obeying Mie's theory [139], it is complicated to theoretically describe the combination of these processes via analytical models even for small numbers of particles. Instead, the numerical method of Finite Difference Time Domain (FDTD) [219] is used to calculate the absorption spectra of the AgNPs on silver. The goal of this simulation is to gain physical insights by investigating trends of absorption spectra rather than to simulate an entire densely packed network of AgNPs on silver in detail.

As a reference, Fig. 4.1a, shows the electric field intensity of a silver nanosphere of a diameter of 40 nm in vacuum. External light with $\lambda = 360$ nm falls onto the silver nanosphere in negative z-direction and excites an LSP of a dipole-like electric field intensity. The effect of placing the silver nanosphere on the silver layer can be seen in Fig. 4.1b. Herein, the silver layer is assumed to be infinitely thick. The field intensity attributed to a resonance at $\lambda = 363$ nm increases ten-fold near the point of contact of the silver sphere and the silver surface. A comparison of the absorption spectra for

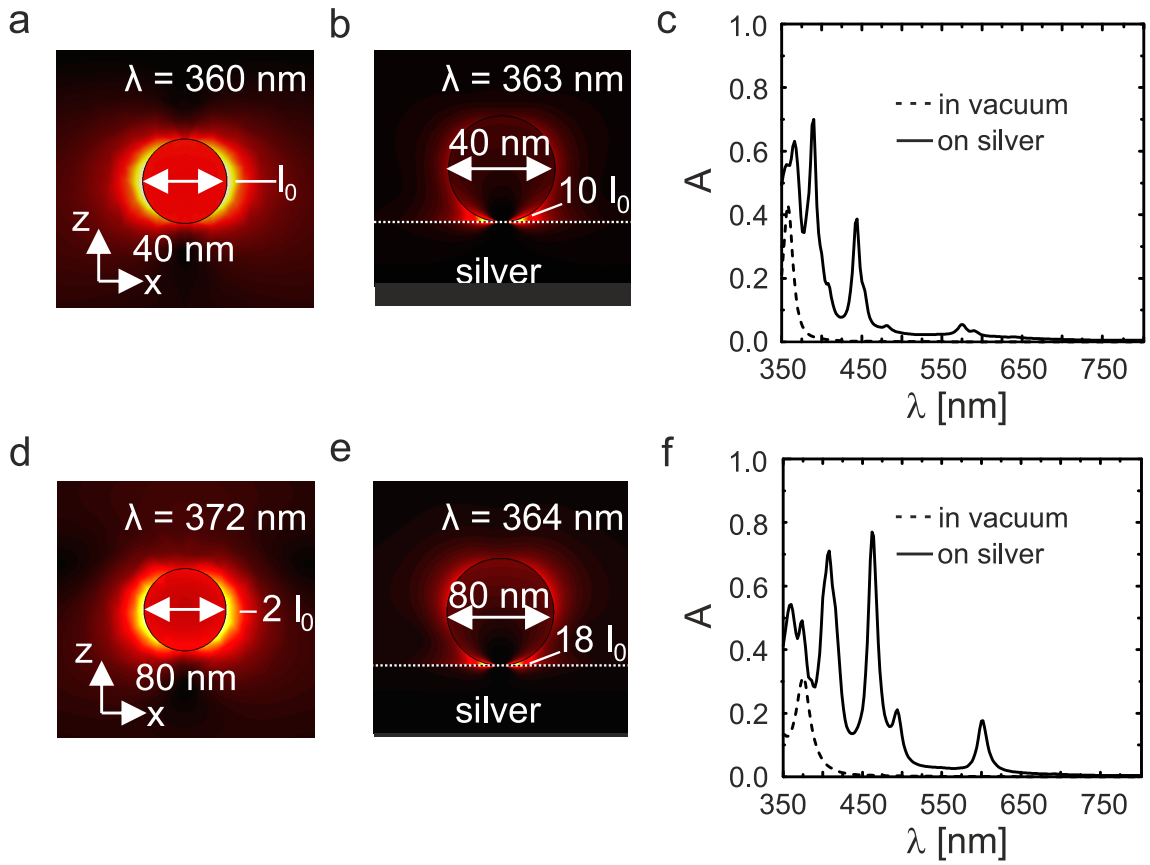

Figure 4.1: FDTD simulations of a silver nanospheres of varying diameters. a) 40 nm sphere isolated in vacuum. b) Contact with a silver layer of infinite thickness. c) Values of the absorption A corresponding to a) (dashed black line) and b) (solid black line). d) 80 nm sphere isolated in vacuum. e) Contact with a silver layer. f) Values of the absorption A corresponding to d) (dashed black line) and e) (solid black line). From ref. [190].

the situations in Fig. 4.1a and Fig. 4.1b is shown in Fig. 4.1c. The dashed black line corresponds to the configuration in Fig. 4.1a and the solid black line to the one in Fig. 4.1b, respectively. The presence of the silver layer strongly increases the average absorption and simultaneously broadens the absorption spectrum. An analogous simulation for a larger particle with a diameter of 80 nm shows similar trends and leads to larger absorption for longer wavelengths (Fig. 4.1d-f).

The next step is to place both particles separated from each other without changing the surface density of nanoparticles Fig. 4.2a. The inter-particle distance is chosen to 150 nm. As a result, the absorption spectrum of these adjacent nanoparticles (solid black line) is dominated by the superposition of their individual absorption spectra (dashed black line), whereby a slight increase of the average absorption is observed (Fig. 4.2b). Now, as shown in Fig. 4.2c, these particles are brought into contact to further increase the number of resonances. It can be observed that, again, the absorption spectrum broadens, and the average absorption further increases as new eigenmodes can exist due to this closely packed arrangement of the nanoparticles (Fig. 4.2d). For instance, a resonance

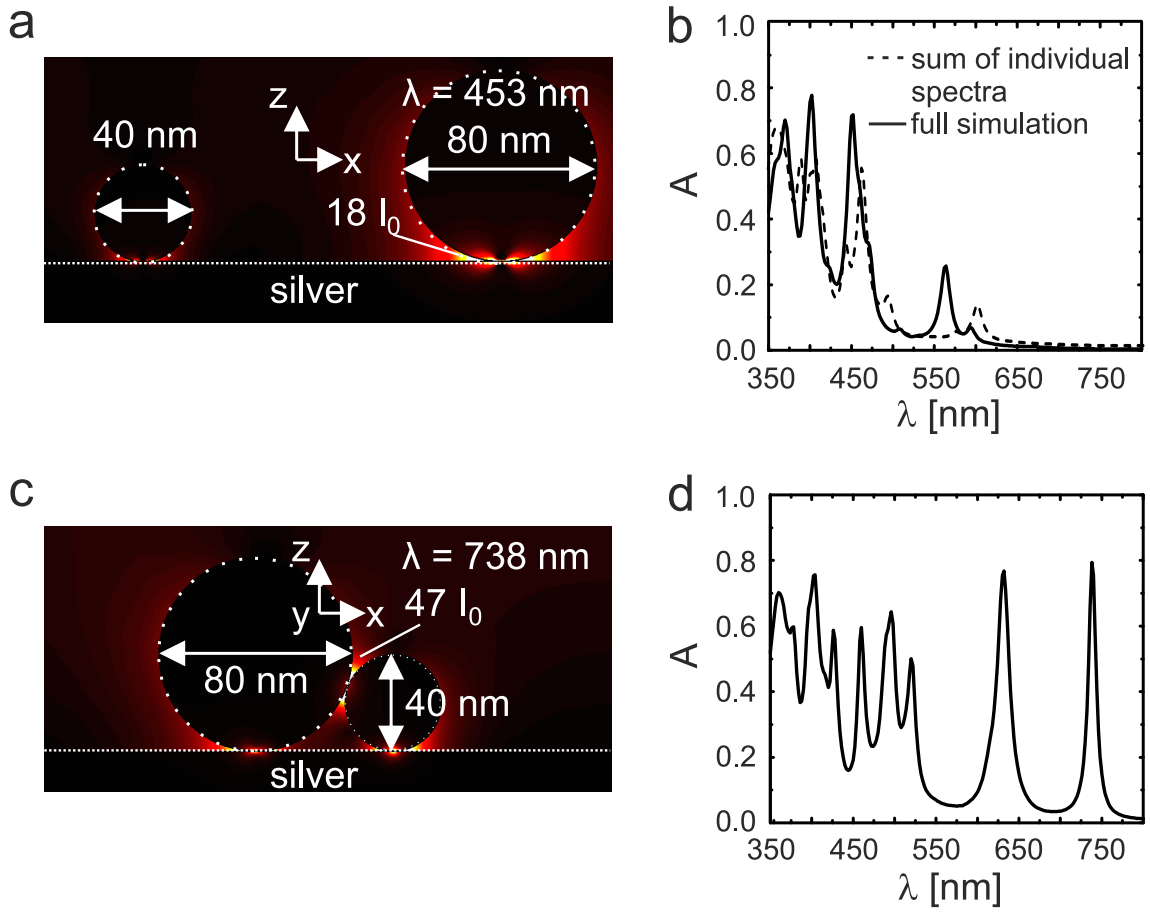

Figure 4.2: FDTD simulations of two silver nanospheres with a diameter of 40 nm and 80 nm, respectively. a) Large inter-particle distance of 150 nm. b) Corresponding absorption spectrum (solid black line). The dashed black line shows the superposition of the individual spectra attributed to Figs. 4.1b and e. c) Touching particles. d) The resulting absorption spectrum $A(\lambda)$ is broadened and shows a significantly larger average value. From ref. [190].

across both particles and the silver layer is present at $\lambda = 738$ nm. These observations suggest that the following logic can be applied: To achieve broadband absorption of light, it is sufficient to build a densely packed layer of nanoparticles of varying diameters to form as many plasmonic resonances as possible.

From the technological point of view, the method of transfer-printing provided in Chapter 3 represents an ideal solution to tackle the challenge of placing round nanoparticles of high particle density on top of a silver layer. Hereby, the variation of particle diameters represents an optimization problem which can be empirically approached. Major parameters are the nominal thickness t_t of silver on a PDMS stamp and the film thickness t_b of the silver layer. Here, both parameters are varied in a combinatorial approach: an unstructured (flat) PDMS stamp and a glass substrate are covered with a film of a linearly increasing thickness gradient $t_t = 0...35$ nm and $t_b = 0...100$ nm, respectively. The PDMS stamp is then placed on the covered glass substrate in a way that both gradients

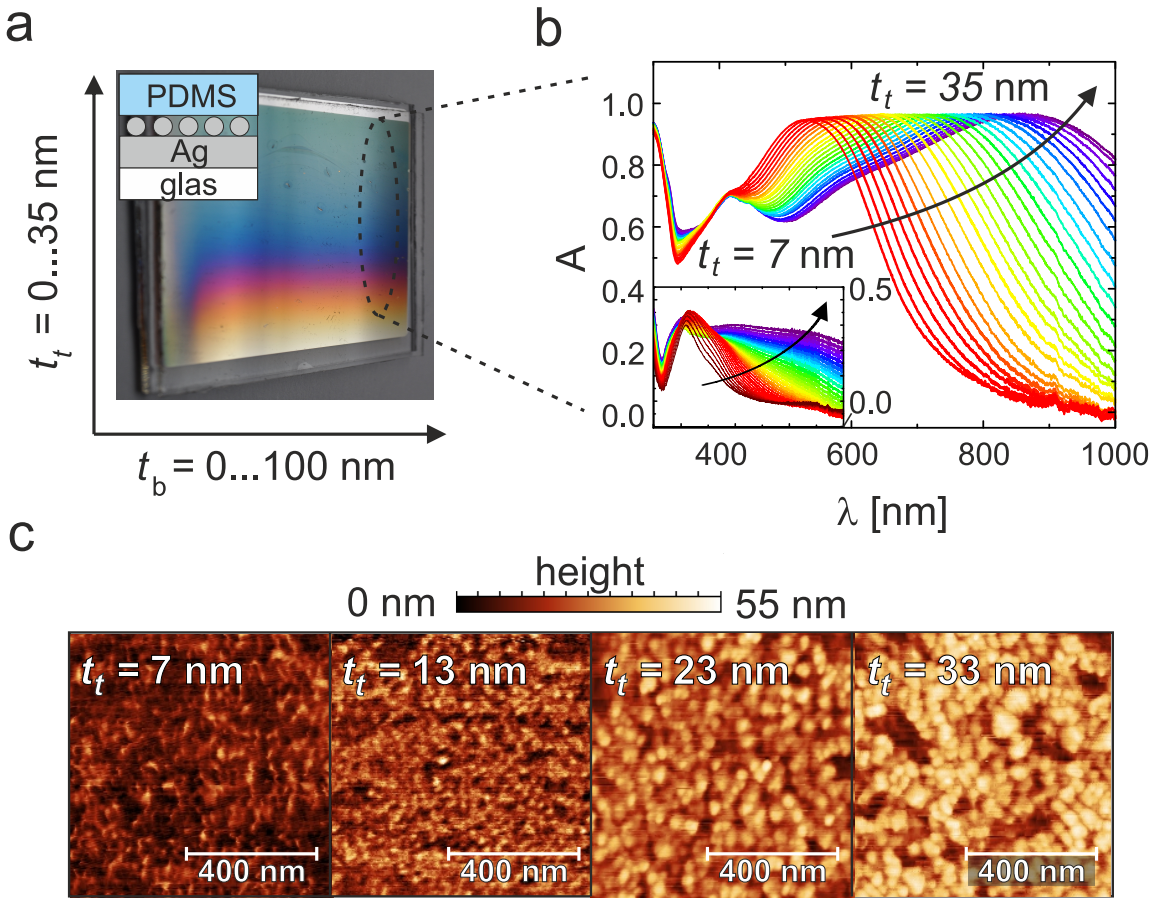

Figure 4.3: Plasmonic absorber fabricated with thicknesses gradients of t_t and t_b from ref. [190]. a) Photograph of the sample. The arrows indicate the directions of both gradients. b) Measured absorption values for t_t = 7...35 nm at t_b = 20 nm. Inset: Measured values of A of the isolated PDMS stamp with AgNPs prior to any contact with the silver layer. c) AFM data of the silver coated PDMS stamp before the transfer-printing at varying values of t_t. From ref. [190].

are aligned perpendicular to each other (see Fig. 4.3a). The corresponding photograph of the sample shows a color gradient with varying t_t, which is almost independent of t_b above a value of 15 nm. The results of RTS measurements under perpendicular incidence show that a significant portion of light is absorbed by the sample (Fig. 4.3b), whereby the wavelength of maximum absorption shifts toward red with increasing values of t_t. In contrast, the absorption values attributed to the isolated PDMS stamp with AgNPs are far below 50% (see the inset in Fig. 4.3b) and indicate that the contact to the silver layer is needed to achieve strong broadband absorption. In addition, it is striking that the measured absorption spectra of the AgNPs in contact with the silver layer are much broader and of higher average values than the simulated ones shown in Fig. 4.2. This strong broadband absorption can be presumably understood by the fact that the AgNPs on the PDMS stamp already form a layer of densely packed nanoparticles and many overlapping plasmonic resonances are present.

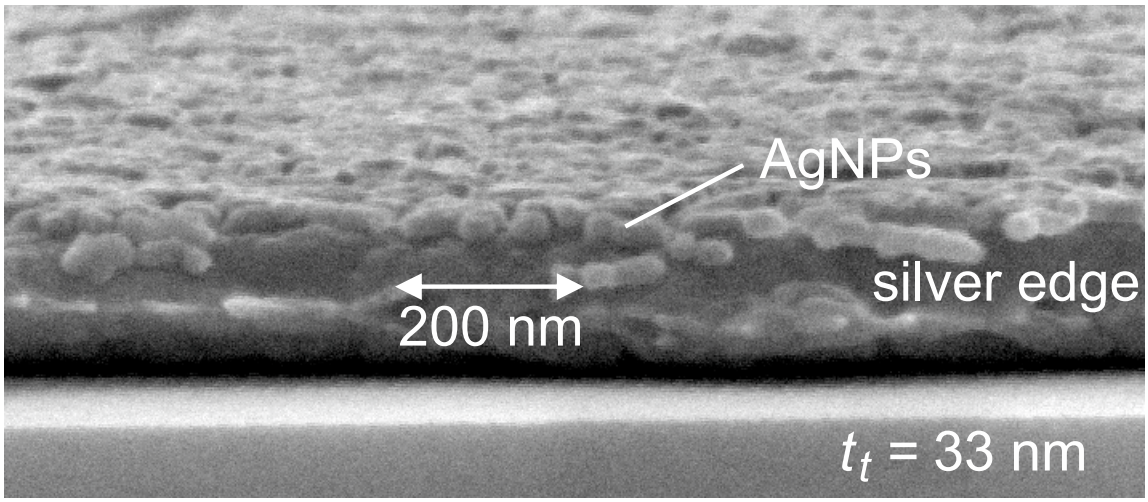

Figure 4.4: SEM micrograph of the sample from Fig. 4.3a after the transfer-printing of AgNPs. From ref. [190].

This presumption of densely packed nanoparticles is confirmed by AFM measurements of the stamp's surface, which were obtained prior the transfer-printing of the AgNP layer (Fig. 4.3c). Above $t_t = 7$ nm, a network of touching AgNPs can be observed. With increasing values of t_t, the average diameters of the particles increases, and, according to the numerical simulation, explains the redshift of the wavelength of maximum absorption. A closer analysis of the AFM data shows that the variation of particle diameters is between 38 nm and 62 nm for $t_t = 33$ nm.

An SEM image of a prepared edge of the sample subsequent to the transfer-printing and removal of the PDMS for $t_t = 33$ nm confirms that the AgNPs indeed form a mono layer of particles, so that the observed absorption cannot be the effect of a three-dimensional distribution of AgNPs (Fig. 4.4).

There is a way to further improve these absorption properties: Considering the observed results of the FDTD simulation, the local variation of particle diameters has to be increased to obtain a broader absorption spectrum and larger average absorption. This task can be addressed by using the morphology of the PDMS stamp as another parameter (see Fig. 4.5). A PDMS stamp fabricated with the help of a sinusoidally structured master template with a period of $\Lambda = 277$ nm and an amplitude of 100 nm is used (Fig. 4.5a). As side note, this small value of the period is chosen to suppress unwanted diffraction.

Now, when silver is evaporated via PVD onto the stamp's surface, the surface is locally tilted with respect to the beam by an angle β. As a consequence, the nominal local mass thickness of the silver layer is reduced by a factor of $\cos\beta$. As the average particle diameter scales with t_t (see Fig. 4.3c), the local variation of the PDMS stamp's surface normal enables a local variation of t_t and, thus, of the local average diameter of the AgNPs (Fig. 4.5b and c). The sinusoidal curvature of the stamp's surface exhibits one elevation

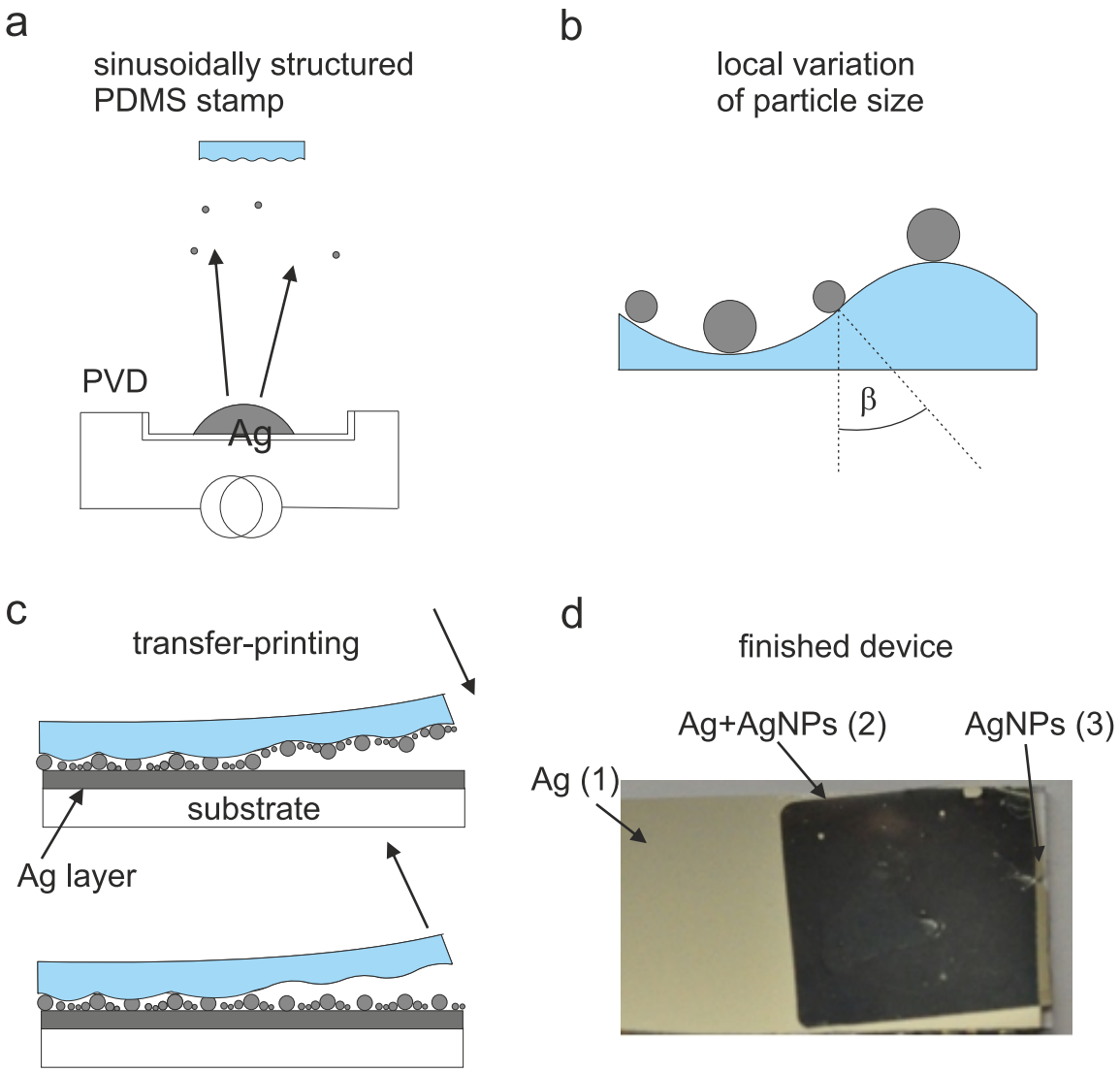

Figure 4.5: Fabrication procedure of optimized plasmonic broadband absorber. a) PVD of silver onto a sinusoidally structured PDMS stamp. b) Sketch of local variation of the particle size. c) Transfer-printing of a AgNPs of strongly varying particle sizes. d) Photograph of a device produced with this fabrication procedure. From ref. [190].

and one sink per period which is characterized by $\beta = 0$. It is therefore expected that, subsequent to the transfer-printing, AgNP particles of large diameters should appear in distances of $\Lambda/2 \approx 139$ nm on the silver layer.

Fig. 4.5d shows a photograph of a sample fabricated with this approach using values of $t_t = 22$ nm and $t_b = 20$ nm. Three regions can be seen, which are marked by region (1), region (2) and region (3). Region (1) only consists of the glass substrate and a flat silver layer and region (2) only consists of the glass substrate and the transfer-printed layer of AgNPs. The deeply black appearing region (3) consists of AgNPs on the silver layer on glass.

Fig. 4.6a shows the AFM data of region (3). Indeed, the diameters of the AgNPs

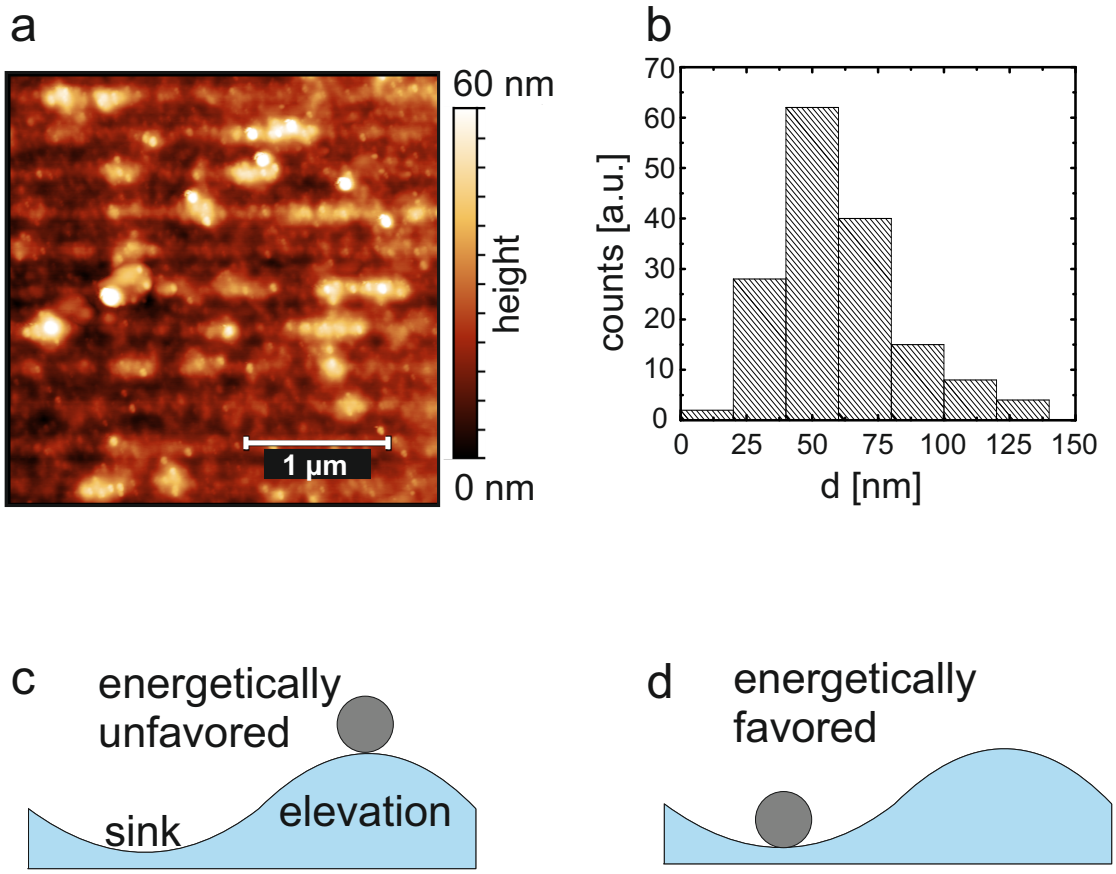

Figure 4.6: a) AFM micrograph of the sample shown in Fig. 4.5d. b) Corresponding statistics of particle diameters. c,d) Energetically favored and unfavored positioning of an AgNP on the PDMS stamp's surface prior to the transfer-printing. The subfigures a) and b) are from ref. [190].

periodically strongly vary along the direction of the PDMS stamp's grating vector. Two observations are surprising. First, the largest particle diameters do not appear every 139 nm along the grating vector, but instead every 277 nm. Second, the statistics of the particle diameters in Fig. 4.6b reveal a variation between values of 20 nm and 120 nm. On the first sight, it appears contradictory that larger particle diameters can appear for the sinusoidally structured stamp at this value of t_t than for the flat stamp at $t_t = 33$ nm. Both the larger distances between large particles as well as the larger particle diameters can be presumably explained as follows: as explained in Section 3.1.2, the surface energy of the PDMS-air interface is significantly smaller than that of the silver-air interface. In consequence, the silver atoms minimize the total surface energy via diffusion [220, 221]. Two extreme situations for the placement of an AgNP can now be considered. The first situation is the placement on an elevation of the PDMS stamp (Fig. 4.6c). This placement is energetically unfavorable as most of the AgNP's surface is exposed to air. The second situation is the placement in a sink of the PDMS stamp (Fig. 4.6d). Here, the total area governed by the silver-air interface is minimized and the area of the PDMS-air interface

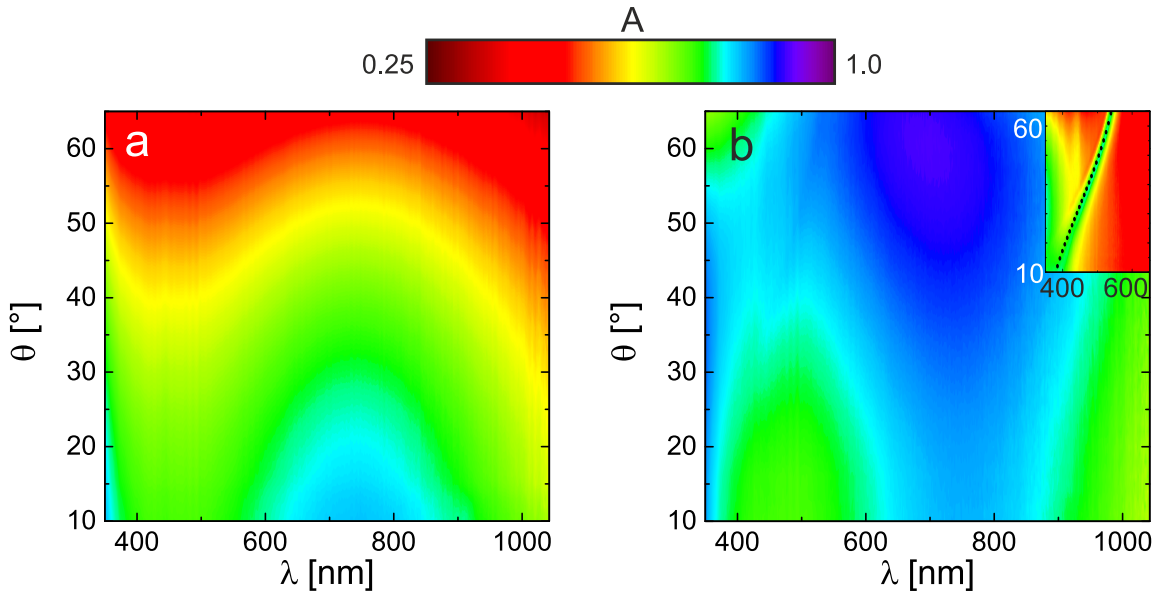

Figure 4.7: RTS data of the sample shown in Fig. 4.5d. a) TE polarization. b) TM polarization (inset: SPP resonance attributed to a closed sinusoidally structured silver layer). From ref. [190].

is maximized. Therefore, the silver tends to diffuse away from the stamp's elevations and towards the PDMS stamp's sinks. This way, larger AgNPs than for a flat PDMS stamp may form. As only one sink per distance Λ is present, particles of large diameters only occur with a periodicity of 277 nm. Such a behavior is called 'curvature driven de-wetting' and has been observed in the literature as well [220, 221].

Fig. 4.7 shows the results of RTS measurements of region (3) with varying angles of incidence and polarizations. Herein, the grating vector and the sample's surface normal define the plane of incidence. For $\theta < 45°$, the absorption between 350 and 1050 nm is above 70% for both TE and TM polarized light. For perpendicular incidence, the largest absorption occurs around $\lambda = 750$ nm. TE polarized light tends to show decreasing absorption with increasing incident angles (Fig. 4.7a). Most of remaining relative power $1 - A$ is present in the reflectance R. This reflectance R loosely follows a similar trend as for standard Fresnel reflection of a lossy dielectric [222]. In contrast, TM polarized light experiences increasing absorption and a broadening of the absorption spectrum with increasing incidence angles (Fig. 4.7b). Again, R behaves similar as for a lossy dielectric, including almost zero reflectance around 57° like for a Brewster angle [222]. Surprisingly, despite the presence of periodicity, no dominant excitation of SPPs at the glass-silver interface is observed. This absence of SPP excitation becomes evident by a comparison with a smooth sinusoidal silver grating, for which significant resonance via SPP excitation occurs along the dotted black line (see the inset in Fig. 4.7b). It can thus be presumed that the absorption is dominated by the localized plasmonic resonances. As a matter of course, such behavior can have multiple microscopic origins, including hybridized LSPs,

and gap plasmons [223]. Due to the complexity of the AgNP layer, it is almost impossible to identify all individual resonances of the sample. Even if all resonances would be known, their number would be so large that it is not straight forward to gain deeper physical insights from them. This problem is similar to many-body problems in physics. Once a physical system gets too complex, it is more useful to summarize all microscopic effects in statistically averaged parameters (e.g. the temperature, the pressure, the relative permittivity, etc.) [224]. Here, in a similar way, the physical behavior of the AgNP layer can be better captured via the attribution of effective relative permittivities. Specialists in plasmonics and photonics term such a statistically averaged layer with sub-wavelength structures a 'metasurface' [225] or 'effective medium' [226]. The AgNP layer is anisotropic because it is densely packed in the x-y plane and a monolayer with respect to the z-direction. Therefore, it can be described as a metasurface with an anisotropic relative permittivity consisting of an in-plane component $\varepsilon_{||}$ in the x-y-plane and an out-of-plane component $\varepsilon_{\perp}$ parallel to the z-direction. Hereby, it is important to mention that the anisotropic relative permittivity is approximated by only two components instead of three components $(\varepsilon_x, \varepsilon_y, \varepsilon_{\perp})$ for the following reason: the reflectance data for both TM and TE polarized light are almost equal toward small angles of incidence. For instance, at $\theta = 10°$, the corresponding values of R only differ by approximately 2%. For such small angles of incidence, the change from TE to TM polarization corresponds to a rotation of the in-plane component of the electric field vector close to 90°. As this rotation does not lead to a significant change of R, the approximation of the anisotropic relative permittivity via $\varepsilon_{||}$ and $\varepsilon_{\perp}$ is considered to be valid.

Using a modified expression of Eq. 2.37 in Section 2.2, it is possible to fit this anisotropic relative permittivity to the measured data of R and T [190]. This modification reads [227, 228]

$$r^{TE/TM} = \frac{r_{0,1}^{TE/TM} - r_{1,2}^{TE/TM} e^{-2jk_1^{TE/TM} d_1}}{1 - r_{1,0}^{TE/TM} r_{1,2}^{TE/TM} e^{-2jk_1^{TE/TM} d_1}} \tag{4.1}$$

with

$$r_{i,j}^{TE} = \frac{k_i^{TE} - k_j^{TE}}{k_i^{TE} + k_j^{TE}} \tag{4.2}$$

$$r_{i,j}^{TM} = \frac{\varepsilon_{j,||} k_i^{TM} - \varepsilon_{i,||} k_j^{TM}}{\varepsilon_{j,||} k_i^{TM} + \varepsilon_{i,||} k_j^{TM}} \tag{4.3}$$

and

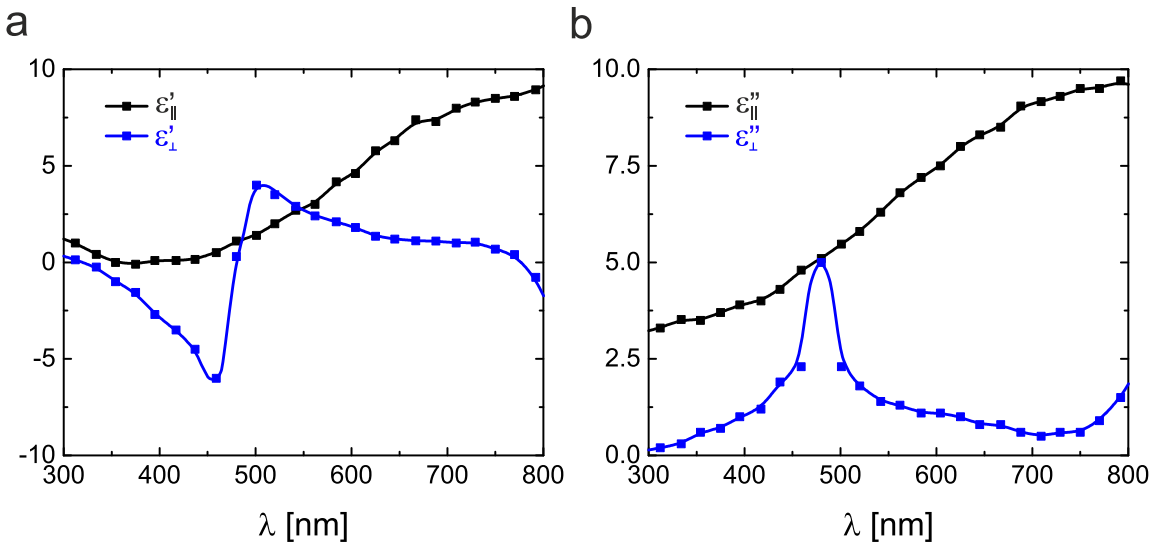

Figure 4.8: Calculated anisotropic dielectric constants of the AgNPs by fitting $R(\lambda, \theta)$ and $T(\lambda, \theta)$ to a modified version of Eq. 2.37. a) Real parts. b) Imaginary parts. From ref. [190].

$$k_i^{TE} = k_0 \sqrt{\varepsilon_{i,||} - \sin(\theta)^2} \tag{4.4}$$

$$k_i^{TM} = k_0 \sqrt{\varepsilon_{i,||} - \frac{\varepsilon_{i,||}}{\varepsilon_{i,\perp}} \sin(\theta)^2} \tag{4.5}$$

The fitting is then performed via the least square method by minimizing the expression

$$\sum_i ((R^{TE}_{measured}(\theta_i) - |r^{TE}(\theta_i)|^2)^2 + (R^{TM}_{measured}(\theta_i) - |r^{TM}(\theta_i)|^2)^2) \tag{4.6}$$

for each wavelength. Hereby, the silver layer is approximated by a semi-infinite volume filled with silver and d_1 is chosen equal to the nominal value of the layer thickness of $t_t = 22$ nm. Note that this choice of d_1 is somewhat arbitrary and, thus, the obtained values of $\varepsilon_{||}$ and $\varepsilon_\perp$ may deviate from the true values with respect to their amplitude. Nonetheless, a variation of d_1 within reasonable limits (larger than the smallest particle diameter and smaller than the largest particle diameter) does not affect the qualitative characteristics of $\varepsilon_{||}$ and $\varepsilon_\perp$.

Their fit results are shown in Fig. 4.8, whereby the symbols are the calculated values and the solid lines are a guide to the eye. $\varepsilon_{||}$ exhibits similar properties to a lossy dielectric layer over the displayed spectral range of 300 nm to 800 nm. In contrast, $\varepsilon_\perp$ exhibits dominant metallic behavior between 300 nm and 470 nm and dominant lossy dielectric characteristics above 470 nm. Similar characteristics are reported in the literature for anisotropic effective media composed of metals and insulators [226]. Note that the fitted

values of $\varepsilon_{||}$ and $\varepsilon_{\perp}$ of the AgNP layer only lead to strong broadband absorption in combination with the silver layer. For instance, the calculated absorption at $\lambda = 730$ nm under perpendicular incidence reduces from around 80% to 34% when the planar silver layer is replaced by PDMS. This reduction of absorption is in well agreement with the measured data of AgNPs on PDMS (see Fig. 4.3b).

The description above showed how a strong broadband absorber of light can be realized by the sole use of electrically conductive materials. Following the Wiedemann-Franz-law [209], a good electrical conductor is also a good thermal conductor and, thus, strong broadband light absorption and large thermal conduction have been combined. Summarizing these results, an interesting concept for solar thermal applications has been demonstrated.

The last part of this discussion revealed a fascinating path of research: Metasurfaces consisting of AgNPs seem to exhibit non-trivial optical properties, when they are brought into close contact with a planar silver layer. In the next section, more of these optical properties are explored for metasurfaces grown by ELD under the influence of coherent light.

4.1.2 Fourier-Space engineering via Plasmon- and Light-induced growth of AgNPs

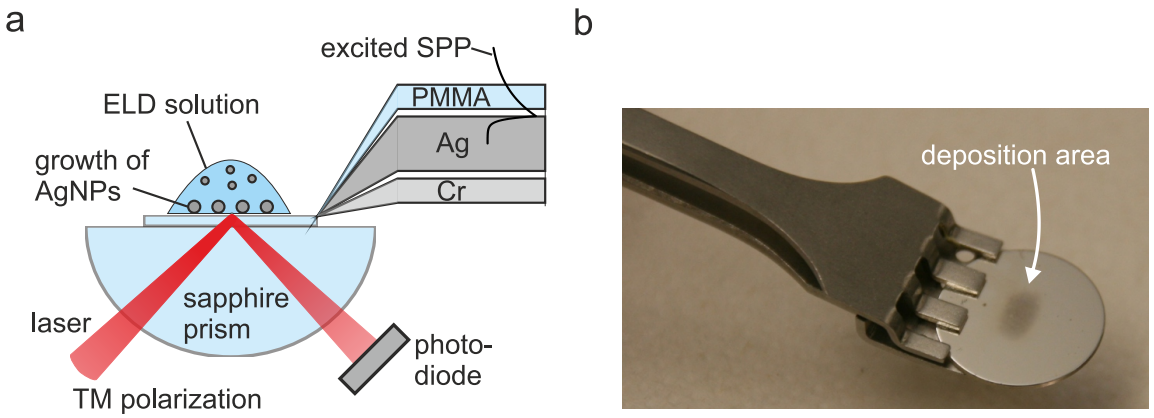

Figure 4.9: a) Experimental setup to obtain surface plasmon induced growth of AgNPs. b) Photograph of a sample after the growth process. From ref. [229].

In this section, metasurfaces grown by ELD under the influence of light will be discussed. A general observation which will arise from this discussion is the ability of AgNP metasurfaces to adapt to an external light source. This behavior enables to obtain complex structures from ELD as cost-efficient bottom-up process. Herein, the fabrication of AgNPs via ELD is based on a distinct process initially developed by Polywka et. al [194]. By increasing the relative content of ammonia in the ELD solution, the growth rate of silver on a substrate's surface is reduced [194]. This, way the growth of silver is more sensitive to other environmental influences such as the irradiation by intense visible light (e.g. a cw-laser). Under such irradiation, light-induced growth of AgNPs can be observed. These AgNPs exhibit structural features which are governed by the properties of the light source, such as its wavelength, angle of incidence and state of polarization [194]. In the following, the concepts of light-induced growth are applied to surface plasmons.

Herefore, instead of a glass substrate, a sapphire substrate coated with a silver layer with a thickness of 54 nm and a PMMA spacer layer of 15 nm is used. As sketched in Section 3.2.1, surface plasmons are excited at the silver-PMMA interface (see Fig. 4.9a) with the help of a half-cylindrical sapphire prism [229].

A coherent laser with $\lambda = 660$ nm excites the SPPs (called 'incident SPPs'). Although it is not yet fully understood, the growth process of the AgNPs is presumed to take place as follows: First, a small number of AgNPs randomly growths and forms seeds for the subsequent growth of other AgNPs. These initial AgNPs can support LSPs above a diameter of approximately 1 nm [230]. Importantly, these LSPs can be excited via the incident SPPs as their electromagnetic fields overlap. Applying reciprocity, LSPs can excite SPPs as well. In good approximation, the AgNPs exhibit rotational symmetry with

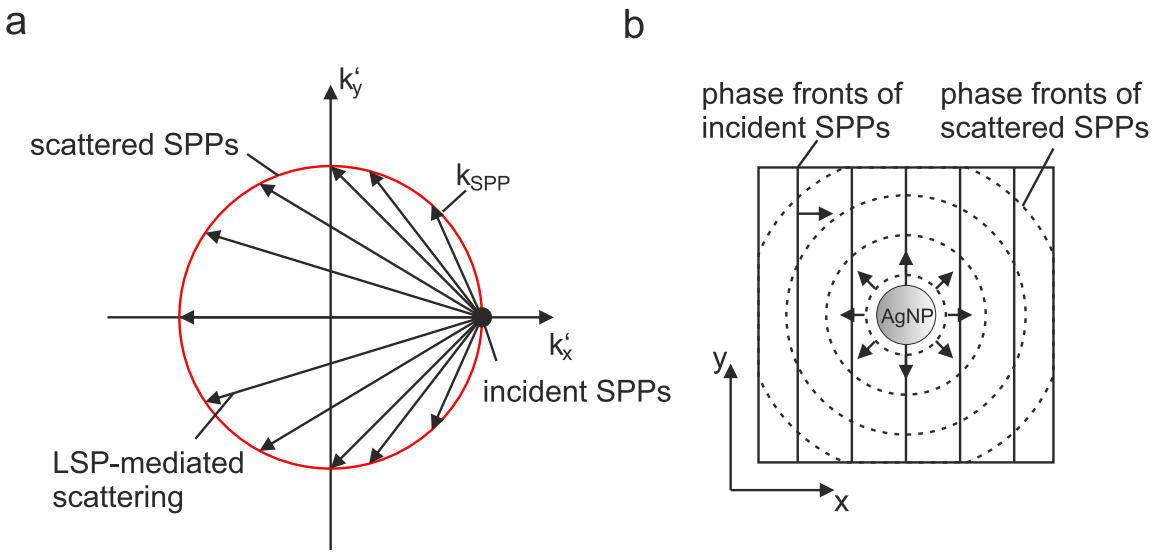

Figure 4.10: Sketch of the formation of a surface plasmon interference pattern. a) Incident SPPs ($k'_x = k_{SPP}$) are converted into scattered SPPs ($k'_{\parallel} = k_{SPP}$) via LSPs. b) The phase fronts of the incident and scattered SPPs.

respect to the z-axis and, thus, the LSPs show no preferred direction for this reciprocal excitation of SPPs. This process is visualized in Fig. 4.10a. It can be understood as an LSP-mediated scattering of the incident SPPs ($k'_x = k_{SPP} = k_0 \cdot n_{eff,SPP}$) into SPPs of any lateral direction ($\sqrt{(k'_x)^2 + (k'_y)^2} = k'_{\parallel} = k_{SPP}$). The latter ones are called 'scattered SPPs'. For the scattered SPPs, it is assumed that no change of the frequency of light occurs and that there exists a fixed phase relation between the incident SPPs and scattered SPPs. As a result, interference may happen and leads to the formation of distinct intensity patterns of the electric field (Fig. 4.10b). To our current understanding, the probability of nucleation is increased for higher electric field intensities and the growth of the subsequent AgNPs is favored at such positions of high intensity [229]. In other words, this interference of SPPs dictates the positions of AgNPs on a microscopic scale, whereby the laser's coherence enables engineered disorder [231] on a macroscopic scale. The meaning of both scales will be elaborated in the following.

Fig. 4.11a and b show SEM images of an AgNP layer subsequent to the growth via plasmon-induced ELD [229]. Seemingly, the AgNPs are randomly distributed. In fact, they show a hidden order which becomes visible in a discrete Fourier transform (FTEM) [232]

$$F(\hat{x}, \hat{y}) = \mathcal{L}(g(x, y)) \tag{4.7}$$

of the SEM data $g(x, y)$ attributed to Fig. 4.11a. Hereby, the results of this Fourier transform are expressed via the spatial frequencies $\hat{x} = k'_x/2\pi$ and $\hat{y} = k'_x/2\pi$. In general,

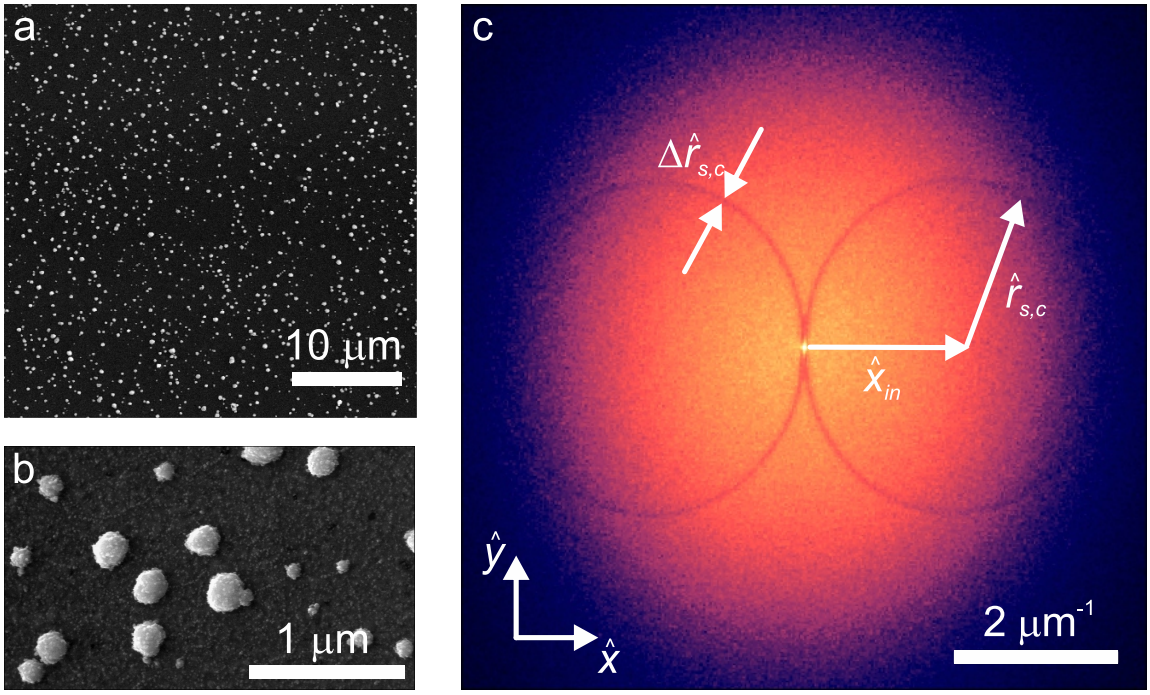

Figure 4.11: a,b) SEM micrographs of the sample from Fig. 4.9b. c) Fourier transformed SEM micrograph (FTEM) attributed to a) and definitions of the values $\hat{r}_{in}$, $\hat{r_{s,c}}$ and $\Delta\hat{r}_{s,c}$. From ref. [229].

all quantities provided via spatial frequencies are marked by a '^' symbol. For instance, the incident SPPs are characterized by the spatial frequency $\hat{x} = n'_{eff,SPP}/\lambda = 1/\lambda_{SPP}$, whereby $n_{eff,SPP}$ is the effective refractive index attributed to an SPP. Fig. 4.11c shows $|F(\hat{x},\hat{y})|$ [229]. It exhibits two 'structure-rings' of a radius [229]

$$\hat{r}_{s,c} = \frac{1}{\lambda_{SPP}}. \tag{4.8}$$

The average width of these structure rings is given by $\Delta\hat{r}_{s,c}$. The center positions of both structure rings are separated from each other by $2\hat{x}_{in} = 2/\lambda_{SPP}$, so that the structure-rings touch each other at $\hat{x} = \hat{y} = 0$. This configuration of structure-rings indicates that the formation of the AgNPs is altered by SPPs. Interestingly, the Fourier amplitude $|F(\hat{x},\hat{y})|$ at the structure-rings is reduced in comparison to the remaining amplitude background visible in the FTEM [229]. As the Fourier amplitude of the AgNP layer is linked to its scattering properties [233], this observation may be interpreted as follows: The AgNPs grow in a way that they inherently minimize the probability of converting an initial SPP into a scattered SPP. To express this interpretation with a simple model, all possible states of scattered SPPs are represented by rings of radius $\hat{r}_w$ and width $\Delta\hat{r}_w$ in the Fourier space. These rings are termed 'wave-rings' [229]. Following this model, the scattering of incident SPPs into scattered SPPs is decreased when the structure-rings perfectly overlap with the wave-rings (Fig. 4.12a). As there is less power lost into

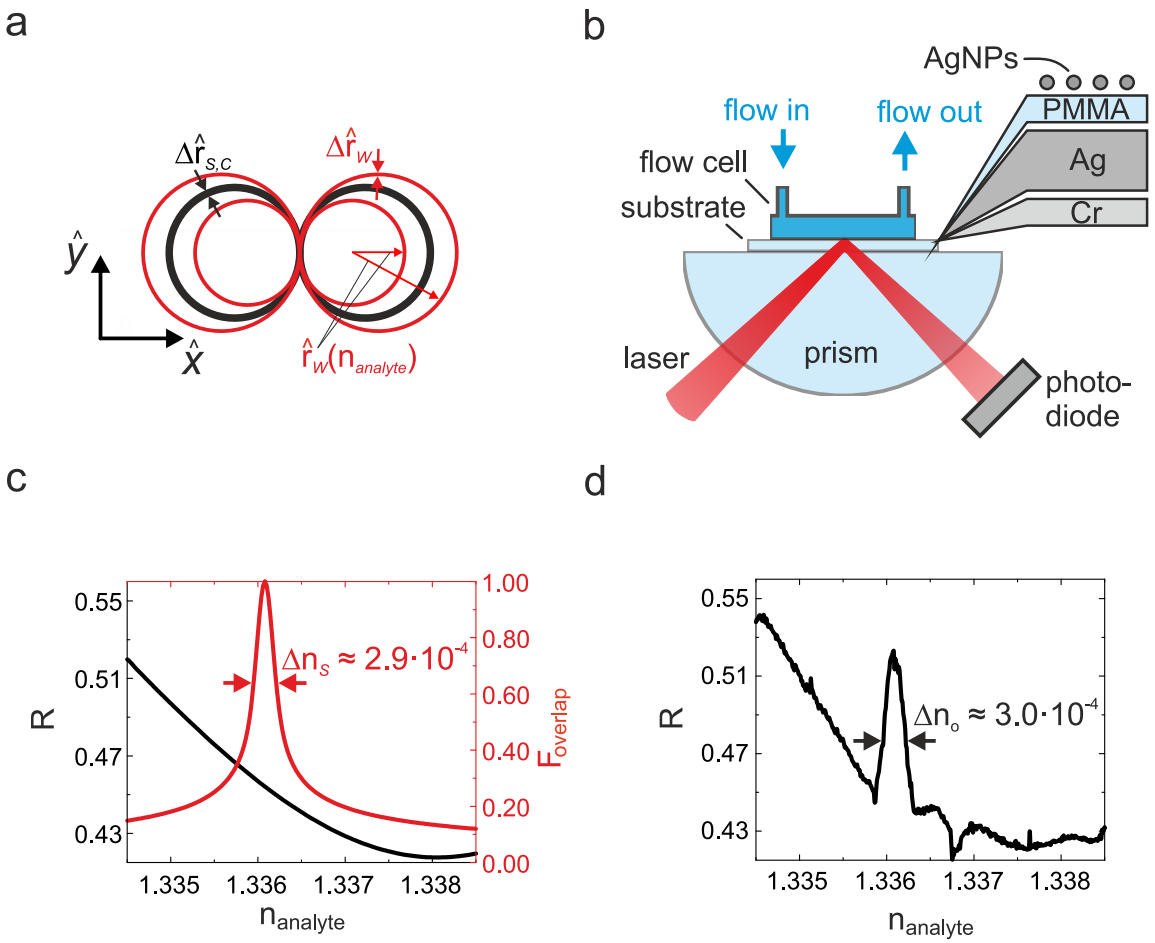

Figure 4.12: Overlap of structure rings and wave rings and application as a sensor. a) Theoretical variation of wave-rings under refractive index variation. b) Experimental setup for a refractive index sensor. c) The simulated reflectance R of the geometry under the simplification of the AgNPs via an effective medium of a thickness of 200 nm and a refractive index $n_{em} = 1.3381 + j0.0051$. SPP The overlap function $F_{overlap}$ between the structure- rings and the wave-rings as a function of $n_{analyte}$. d) Measured values of R as a function of $n_{analyte}$. A peak of R with an extraordinarily small FWHM occurs for $n = n_{ELD}$. From ref. [229].

scattered SPPs, more light is reflected so that R is large. In return, environmental changes or subsequent mechanical misalignments detune the wave-rings with respect to their diameter, position and orientation. In consequence, the overlap between the structure rings and wave-rings may shrink. As a result, the probability of the scattering of incident SPPs into scattered SPPs may increase and less power is reflected from the prism base, so that R decreases. Please note that this overlap must not be confused with the field overlap described in Chapter 2. Instead, it is quantified by an overlap function $F_{overlap}$, which is described in detail in the supporting information of ref. [229]. Its value is 1.0 for perfect overlap and 0.0 for no overlap [229].

This train of thought inspired a refractive index sensor which is designed as visualized in Fig. 4.12b. First, AgNPs are grown as described above. Then, the ELD solution is

replaced by a mixture of chemically passive liquid with a tunable refractive index $n_{analyte}$. Fig. 4.12c shows the simulated reflectance of the geometry under the simplification of the AgNPs via an effective medium. This effective medium is assumed to exhibit a thickness of 200 nm and a refractive index of $n_{em} = 1.3381 + j0.0051$ [229]. The red curve shows the calculated values of $F_{overlap}$ as a function of $n_{analyte}$. $F_{overlap}$ is maximized for $n_{analyte} = n_{ELD}$, whereby n_{ELD} is the refractive index of the ELD solution. The measured values of R in Fig. 4.12d agree with this model: away from n_{ELD}, they are mostly governed by a background of a conventional SPR. Remarkably, toward $n_{analyte} = n_{ELD}$, they exhibit a sharp peak with approximately the same peak center and width as for the overlap function. The maximum of the sensitivity $(1/R)(\partial R/\partial n_{analyte})$ of 968 is comparable to the sensitivity of plasmonic systems structured by electron beam lithography [234]. This observation is remarkable as, except from the PVD evaporation of the silver layer, only solution-based processes have been used. As the growth of AgNPs is a coherent phenomenon, the theoretical limit of this sensitivity is only given by the divergence angle, illumination area and spectral width of the light source [229]. Additional experimental and analytical investigations show that the plasmon-induced growth process of the AgNPs automatically ensures perfect alignment to the incident light source, rendering this sensor advantageous in comparison to sensors built by conventional methods [229].

Another aspect of the light- and plasmon-induced growth of AgNPs is the possibility to create structures which exhibit a distinct type of features in the Fourier space, which is called 'hyperuniformity' [235]. To define and investigate hyperuniformity, it is common to use the 'spectral density' $\chi_s(k'_x, k'_y)$. It can be calculated with the help of Eq. 4.7 via [130]

$$\chi_s(\hat{x}, \hat{y}) = |\mathcal{L}(g(x, y) - \overline{g})|^2 \tag{4.9}$$

with $\overline{g}$ as the average value of $g(x, y)$. From a physical point of view, $\chi_s(\hat{x}, \hat{y})$ provides a measure for the scattering probability of a structure with a lateral momentum transfer of $2\pi\hat{x} + 2\pi\hat{y}$ [130]. Using the angular average $\chi_{s,a}(\hat{r} = \sqrt{\hat{x}^2 + \hat{y}^2})$ of χ_s [235], ideal hyperuniformity can now be defined by

$$\lim_{\hat{r}\to 0} \chi_{s,a}(\hat{r}) = 0 \tag{4.10}$$

To fill this expression with more intuitive insights, one example is given which explains the meaning of hyperuniformity. A hypothetical infinitely large plane covered with nanoparticles of diameters d_p is considered, whereby the average particle diameter is considered to be significantly smaller than the average inter-particle distance. This way, the parti-

cles can be placed in many different configurations. For instance, a completely random positioning of the particles would be characterized by a Poisson distribution. This distribution means that there is a certain probability to find large regions without any particles at all. On the contrary, there is an equally high probability to find densely packed regions. Such a distribution is not hyperuniform as there will be always some local particle configurations which contribute to $\chi_{s,a}(\hat{r})$ no matter how small $\hat{r}$ becomes. A hyperuniform particle distribution, however, is not completely random with respect to the interparticle spacings so that there is a vanishing probability of finding large empty or densely packed regions [235]. For instance, a perfect crystal is hyperuniform as all particles are spaced in well defined distances. For isotropic particle distributions, hyperuniformity indicates the absence of density fluctuations over large distances in all directions [235].

Another phenomenon related to hyperuniformity is the appearance of 'stealthy hyperuniformity'. Stealthy hyperuniformity is defined by [235]

$$\chi_s(\hat{r}) = 0, \quad 0 < \hat{r} \leq \hat{R} \tag{4.11}$$

with $\hat{R}$ as a threshold value of $\hat{r}$. It can appear when an isotropic particle distribution exhibits local short-range order without translational long-range order [231]. As a last definition, any simply connected anisotropic shape in the Fourier space in which the spectral density becomes exactly zero can be attributed to the name 'anisotropic stealthy hyperuniformity' [235].

It is now investigated how hyperuniformity is related to AgNPs grown via ELD. Figs. 4.13a-c show the spectral densities of three AgNP layers grown by ELD with varying deposition times Δt_d of 10, 22, and 25 minutes. The growth took place in darkness. The corresponding values of $\chi_{s,a}(\hat{r})$ are displayed in Fig. 4.13d. Seemingly, according to Eq. 4.10, there is no hyperuniformity present. However, it is important to note that Eq. 4.10 demands a calculation over infinitely large lateral dimensions. In reality, the sample size is always restricted. In consequence, true hyperuniformity cannot be directly observed in experiment [130]. However, it is possible to extrapolate calculated data of $\chi_{s,a}(\hat{r})$ and define a hyperuniformity metric

$$H = \frac{\lim_{\hat{r}\to 0} \chi_{s,a,extrapolated}(\hat{r}) = 0}{\max\left(\chi_s(\hat{r})\right)} \tag{4.12}$$

to estimate whether a distribution of particles is hyperuniform anyway [130]. Smaller values of H indicate a larger degree of hyperuniformity [130]. Here, the three straight lines in Fig. 4.13d labeled by (1), (2), and (3) exemplary show such extrapolation. Following this extrapolation, the corresponding values of H are 0.62, 0.26 and 0.17, respectively

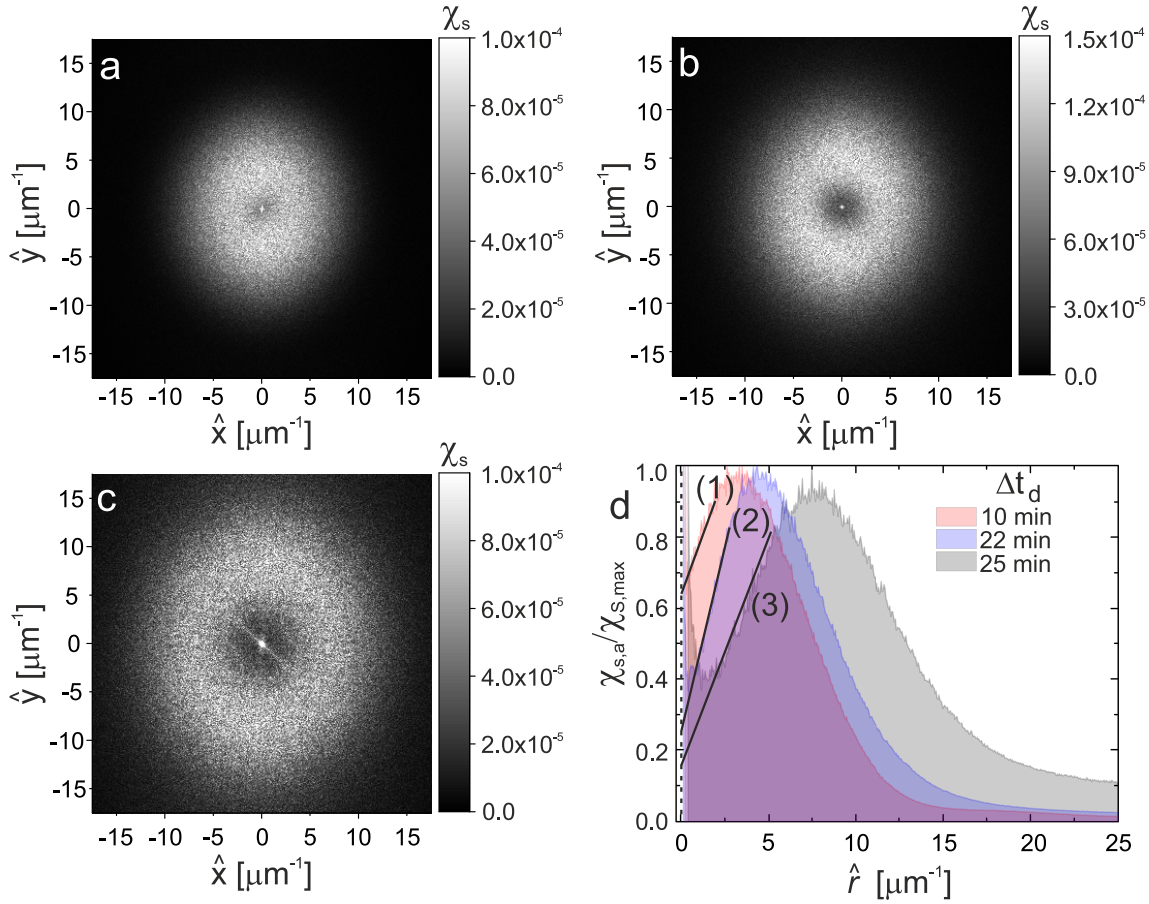

Figure 4.13: Spectral densities of ELD-grown AgNPs on glass under varying deposition times Δt_d. The growth took place in darkness. a) 10 minutes. b) 22 minutes. c) 25 minutes. d) Corresponding normalized and angular averaged spectral densities. The three black solid lines are linear extrapolations to calculate the hyperuniformity metric H. From ref. [130].

[130]. A comparison with the literature reveals that these values are small enough to claim the presence of hyperuniformity [236, 237].

The physical reason for the occurrence of hyperuniformity for ELD grown AgNPs is not understood yet. However, it is highly likely that it is linked to the thermodynamics and chemical processes during the growth. For instance, there is a large probability that at exactly one AgNP growths within a distinct area size after a distinct deposition time. Simultaneously, the probability is small that two AgNPs grow directly adjacent to each other. As a result, the distribution of all AgNPs is not completely random as for a Poisson distribution.

It is further investigated how the influence of external light during growth affects this hyperuniformity. Perpendicular incidence with circularly polarized coherent light is used. Three different wavelengths of $\lambda_l = 405$ nm, 532 nm and 660 nm are used [130]. The spectral densities of all AgNP layers are shown in Fig. 4.14a-c.

Remarkably, all layers apparently show a similar behavior as for stealthy hyperuniformity. This behavior is characterized by the equation [130]

$$\chi_s(\hat{r}) \approx 0, \quad 0 < \hat{r} \leq \hat{R}. \tag{4.13}$$

This equation defines 'quasi stealthy hyperuniformity'. Here, for each wavelength λ, the value of $\hat{R}$ is observed to be [130]

$$\hat{R} = \frac{n_{ELD}}{\lambda} \tag{4.14}$$

with $n_{ELD} = 1.336$. This appearance of quasi stealthy hyperuniformity indicates that the influence of the circularly polarized light on the growth process is highly likely to introduce short-range order in the absence of translational long-range order. As $\hat{R}$ scales with $1/\lambda$, it can be presumed that this short-range order is dictated by the interference between the incident light and light scattered from existing AgNPs. However, there are no deeper insights on the exact growth mechanism leading to the quasi stealthy hyperuniformity yet.

Moreover, for $\hat{r} > \hat{R}$, the spectral density exhibits a doughnut-shaped maximum [130]. Such a characteristic can be understood as an isotropic diffraction grating with only one single diffraction order and is sought in the community of photonic researchers as an ideal Fourier space to form isotropic photonic bandgaps [238].

For plasmon-induced growth of AgNPs, similar phenomena can occur [130]. When the deposition times is reduced with respect to the ones used in Fig. 4.11a, χ_s is characterized by two disks of radii $1/\lambda_{SPP}$. Within these disks χ_s is significantly smaller than outside these disks (see Fig. 4.14d). As this behavior is similar to anisotropic stealthy hyperuniformity, it is termed 'anisotropic quasi stealthy hyperuniformity' [130]. Herein, it is highly likely that the presence of surface plasmons leads to an introduction of near-range order, whereby the direction of the incident surface plasmons along the x-axis causes the anisotropy with respect to the resulting spectral density.

The potential of stealthy hyperuniformity and anisotropic stealthy hyperuniformity for waveguide solar concentrators can be seen by converting the spectral density into a theoretical optical response. Inside a waveguide of a refractive index n', a stealthy hyperuniform structure has a reduced probability of specular light reflection and transmission, and an increased probability of light scattering above a critical angle $\theta_{crit} = \arcsin\left(k'_{\parallel}/(n'K)\right)$. When K is chosen in such a way, that θ_{crit} is equal to the critical angle of total internal reflection of the waveguide, light will be efficiently scattered into the eigenmodes of the waveguide. Thus, stealthy hyperuniform layers could be used as potential light-coupling

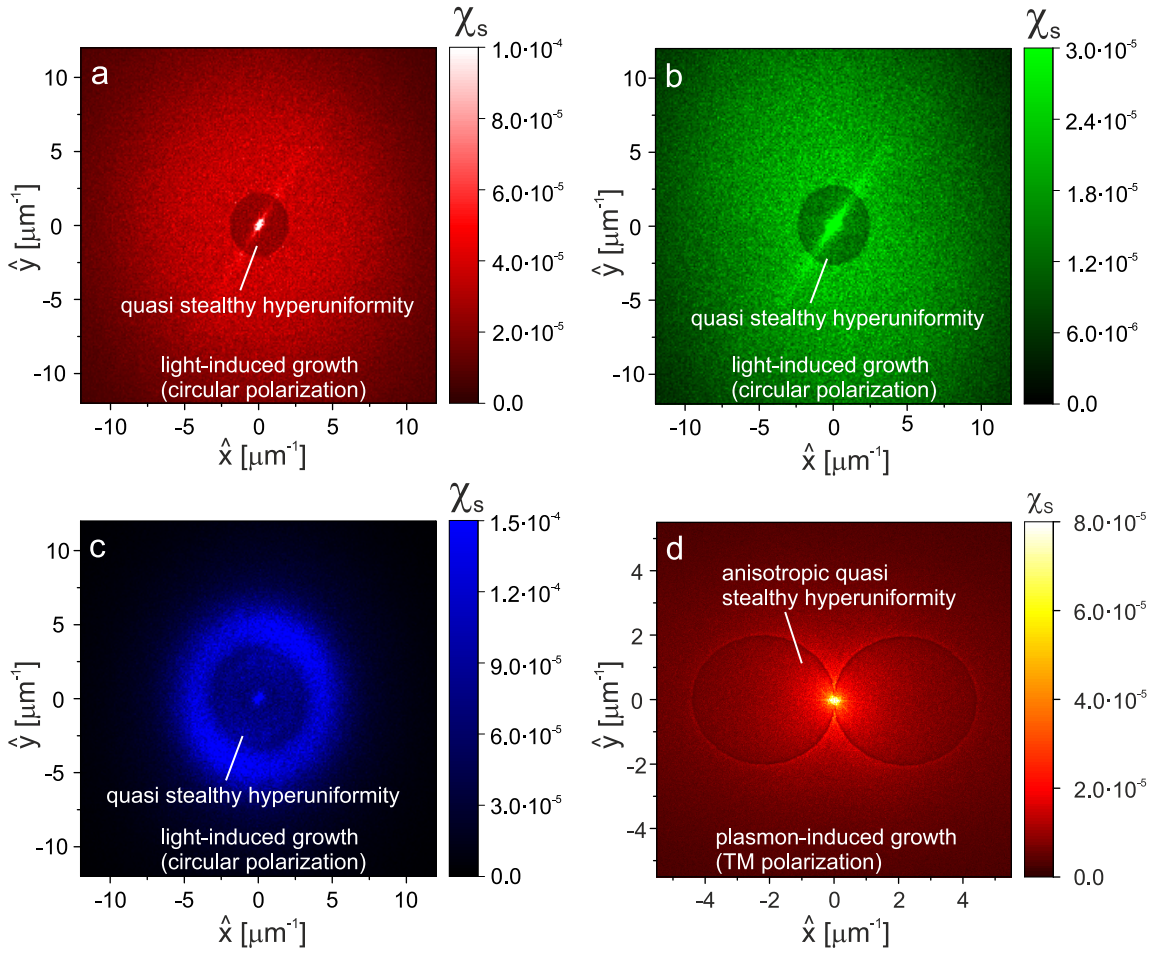

Figure 4.14: a-c) Stealthy hyperuniform spectral densities of ELD-grown AgNPs on glass. The AgNPs were grown under illumination of perpendicular incident, circularly polarized, and coherent light of varying wavelengths. a) $\lambda = 660$ nm. b) $\lambda = 532$ nm. c) $\lambda = 405$ nm. d) Anisotropic stealthy hyperuniform spectral density of an AgNP layer formed by plasmon-induced growth. From ref. [130].

elements for waveguide based solar concentrators. Moreover, they might be useful for photovoltaics enhanced by light trapping [239].

All the results presented above can be summarized as follows. AgNPs grown from ELD show potential for solar concentrators and are worthy to be pursued in future research. As a matter of course, the challenge of all plasmonic systems is to tackle their intrinsic Ohmic losses. On the contrary, loss-free materials inherently enable to build geometries exhibiting long propagation lengths. Such systems of long propagation lengths will be the focus of the next section.

4.2 Long Propagation Lengths utilizing TE Node Modes

In Chapter 2, the concentration attributed to the eigenmode of a waveguide grating was introduced and found to obey the relation

$$C_{geo} \propto \frac{L_{prop}}{t_{WG}} \tag{4.15}$$

with t_{WG} as the thickness of the waveguide grating.

For common waveguide gratings, light in the visible spectrum propagates over typical length scales of several ten microns with waveguide thicknesses in the range of a few λ. Thus, the most common applications of waveguide gratings are grating couplers [240–242] and optical filters [243–248]. However, to achieve large concentration values with waveguide gratings, far longer propagation lengths are desired without increasing the waveguide thickness.

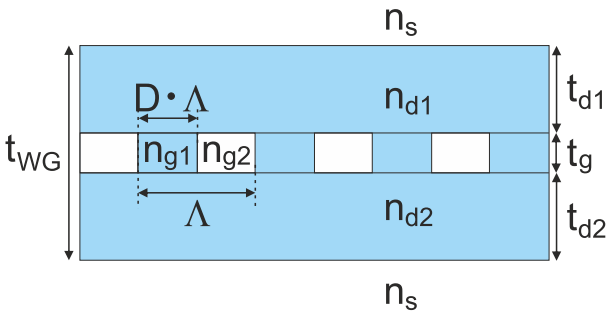

Figure 4.15: Definition of a symmetric waveguide grating. From ref. [249].

However, from a naive point of view, it appears logical that the propagation length of an eigenmode is simply given by the number of interactions between photons and the grating layer. Following this logic, the seemingly only way to increase the propagation length is to increase the waveguide thickness. In fact, this picture is only correct in the limit of geometric optics. As a matter of fact, an eigenmode originates from the interference of plane-waves inside the waveguide grating (see Chapter 2). When this interference is destructive at the position of the grating layer, the effective number of interactions between photons and the grating layer can be strongly decreased. A similar concept has been used to minimize absorptive losses for electric contacts in waveguides [250]. Its extension to waveguide gratings and other structures has been proposed recently [251–253] and the results of concrete simulations [249] for distinct waveguide gratings will be presented in the following.

The geometry parameters of these waveguide gratings are defined in Fig. 4.15. They consist of a substrate and superstrate of a refractive index n_s, two dielectric layers and a rectangular grating layer between these layers. The dielectric layers are characterized by

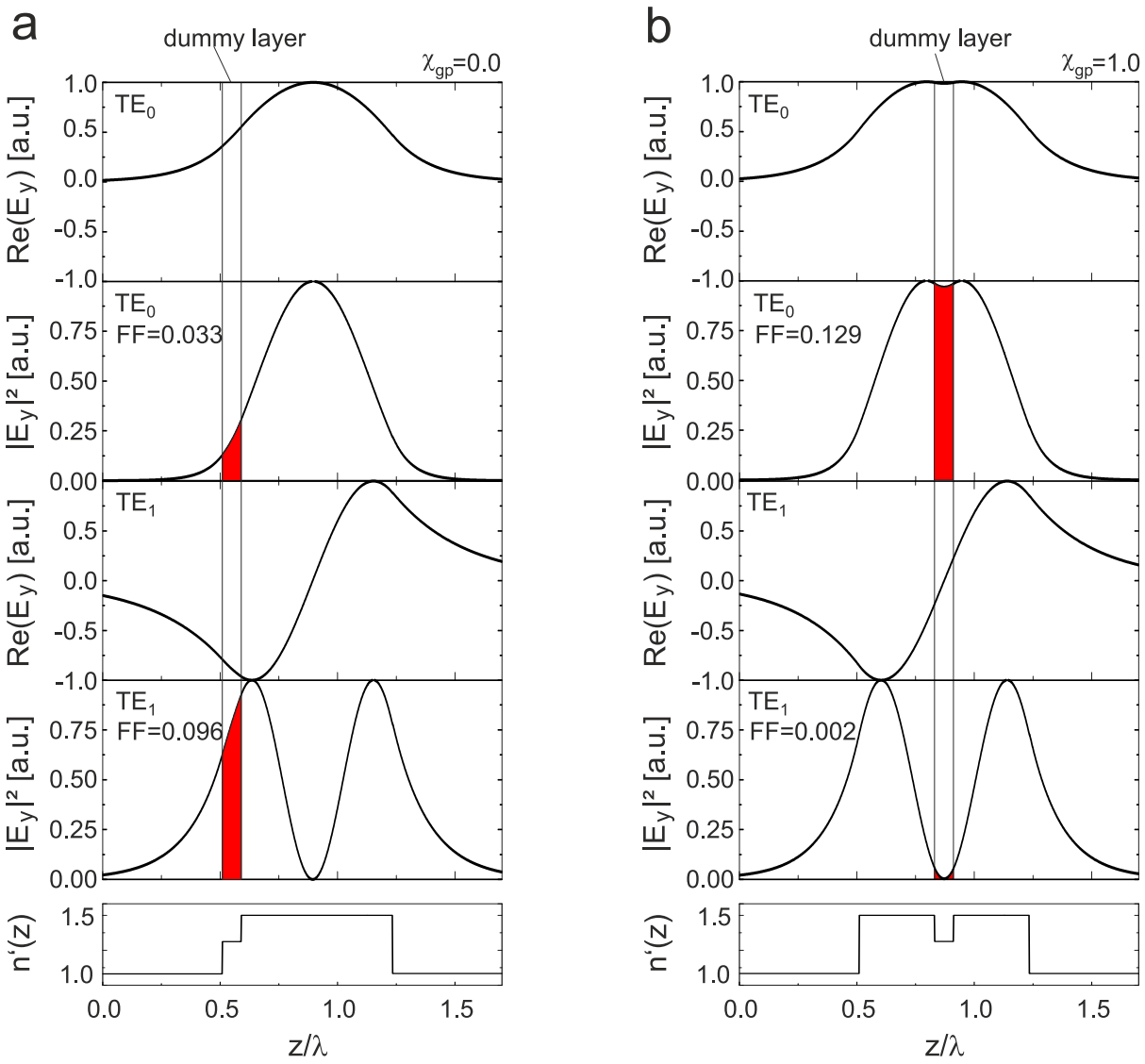

Figure 4.16: Distributions of $\mathrm{Re}(E_y)$ and $|E_y|^2$ of the TE_0 and TE_1 modes with corresponding filling factors FF. a) $\chi_{gp} = 0.0$. b) $\chi_{gp} = 1.0$. The filling factor is the smallest for the TE_1 eigenmode at $\chi_{gp} = 1.0$. From ref. [249].

their thicknesses t_{d1} and t_{d2} as well as their refractive indices n_{d1} and n_{d2}, respectively. The grating is defined by its thickness t_g, the refractive indices n_{g1} and n_{g2}, the duty cycle D, and its period Λ.

The degree of symmetry of the waveguide grating is expressed by the symmetry parameters

$$\chi_{gp} = 1 - \frac{|t_{d1} - t_{d2}|}{t_{d1} + t_{d2}} \tag{4.16}$$

and

$$\chi_n = \frac{n_{d1}}{n_{d2}} \tag{4.17}$$

Perfect symmetry is present for $\chi_{gp} = \chi_n = 1$. The impact of these symmetry parameters

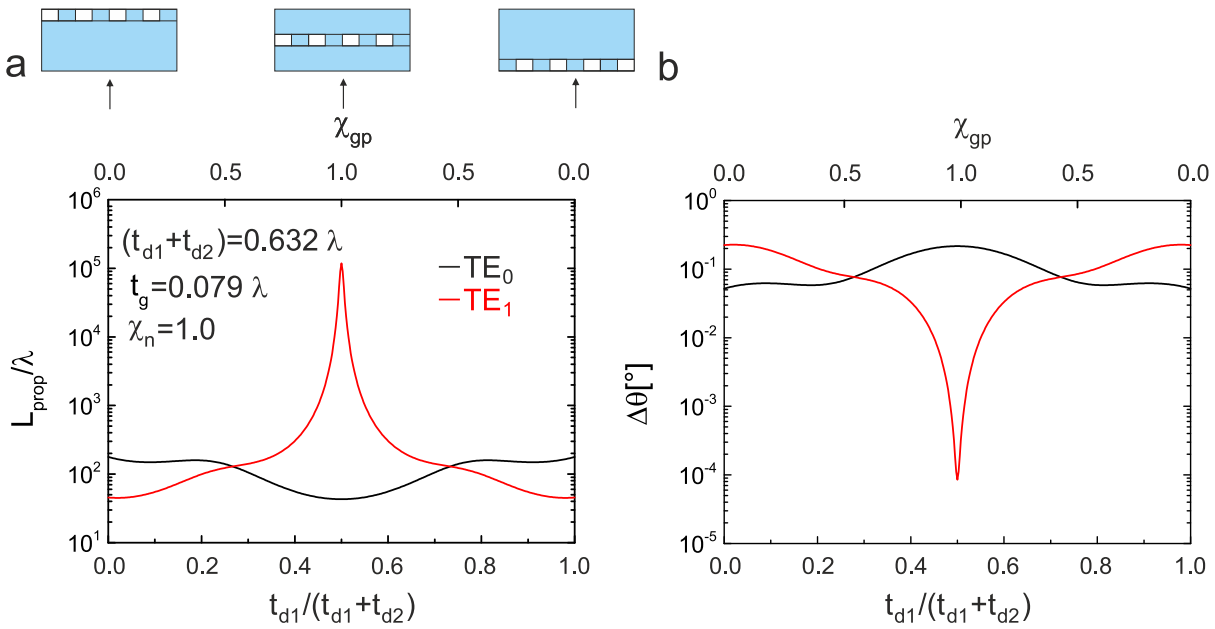

Figure 4.17: Variation of χ_{gp} for a grating layer with $n_{g1} = 1.0$ and $n_{g2} = 1.5$ under a fixed value of $t_{d1} + t_{d2} = 0.632\lambda$. a) Normalized propagation length L_{prop}/λ. The longest propagation length occurs for the TE_1 eigenmode at $\chi_{gp} = 1.0$. b) Attributed divergence angle $\Delta\theta$. From ref. [249].

on the propagation length will be explained in the following lines.

First, the grating is replaced by a homogeneous dummy layer of thickness $t_g = 0.079\lambda$ by setting $n_{g1} = n_{g2} = \sqrt{\frac{1}{2}(1.5^2 + 1.0^2)} = 1.275$. The eigenmodes corresponding to this geometry show evanescently decaying fields in the substrate and superstrate, and allow to define the filling factor [249]

$$FF = \frac{\int_{z_g}^{z_g+t_g} |E_y|^2 \mathrm{d}z}{\int_{-\infty}^{\infty} |E_y|^2 \mathrm{d}z}, \tag{4.18}$$

whereby z_g defines the position of the interface between the grating layer and the bottom dielectric layer (t_{d2}, n_{d2}).

The remaining parameters are $n_s = 1.0$, $n_{d1} = n_{d2} = 1.5$, and $t_{d1} + t_{d2} = 0.632\lambda$. The TE_0 and TE_1 eigenmodes of the waveguide are investigated (see Fig. 4.16). At $\chi_{gp} = 0.0$, the filling factors for the TE_0 and TE_1 eigenmodes are $FF = 0.033$ and $FF = 0.096$, respectively. Concerning $\chi_{gp} = 1.0$, the TE_0 eigenmode exhibits a value of $FF = 0.129$. Remarkably, the filling factor of the TE_1 eigenmode is significantly smaller and exhibits a value of $FF = 0.002$ [249].

To show the meaning of this small filling factor, the parameters of the grating are set to $n_{g1} = 1.0$, $n_{g2} = 1.5$, $D = 0.5$ and $\Lambda = 0.632\lambda$. As explained in Chapter 2, the effective indices n_{eff} of the eigenmodes become complex due to outcoupling. They can

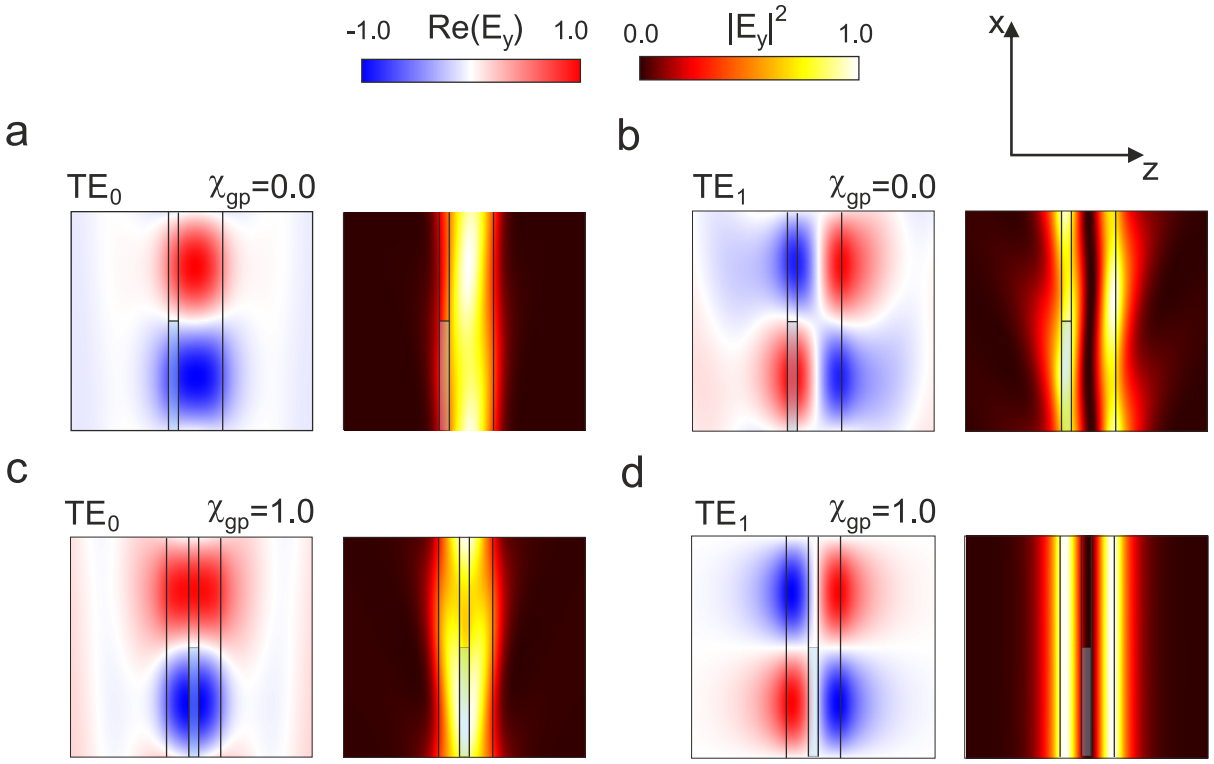

Figure 4.18: Normalized distributions of $\mathrm{Re}(E_y(x,z))$ and $|E_y(x,z)|^2$ of the geometry discussed in Fig. 4.17 for selected parameters. a) TE_0 mode at $\chi_{gp} = 0.0$ b) TE_1 mode at $\chi_{gp} = 0.0$. c) TE_0 mode at $\chi_{gp} = 1.0$. d) TE_1 mode at $\chi_{gp} = 1.0$. From ref. [249].

be attributed to a propagation length L_{prop} and an angular divergence of $\Delta\theta$ according to Eqs. 2.45 and 2.82. Fig. 4.17 shows both their characteristics as a function of χ_{gp}. At $\chi_{gp} = 0.0$, the propagation lengths of the TE_0 and TE_1 eigenmodes are in the order of $L_{prop} = 10^2\lambda$, whereby the attributed divergence angles are around 0.1°. In contrast, for $\chi_{gp} = 1.0$ the TE_1 eigenmode exhibits a 1000-fold longer propagation length of approximately $L_{prop} = 10^5\lambda$ and a divergence angle of $(10^{-4})°$ [249].

Fig. 4.18 shows the electric field distributions attributed to the TE_0 and TE_1 eigenmodes for $\chi_{gp} = 0.0$ and $\chi_{gp} = 1.0$. For the TE_0 eigenmode, the field distributions for both values of χ_{gp} are structured along the x-direction. This is different to the field distributions shown in Fig. 4.16, which are invariant along x. Here, these structures along the x-direction can be interpreted as a result of outcoupling in combination with short propagation lengths (see Chapter 2). Similar observations can be made for the TE_1 mode at $\chi_{gp} = 0.0$. In contrast, the electric field distribution of the TE_1 mode at $\chi_{gp} = 1.0$ looks almost identical to the one in Fig. 4.16d. These observations mean that an excited TE_1 at $\chi_{gp} = 1.0$ eigenmode exhibits a significantly lower probability (per length) of converting the initial power in the eigenmode into radiation channels as a result of the small value of FF [249].

Shortly summarizing, these observations demonstrate that a nearly 1000-fold increase of

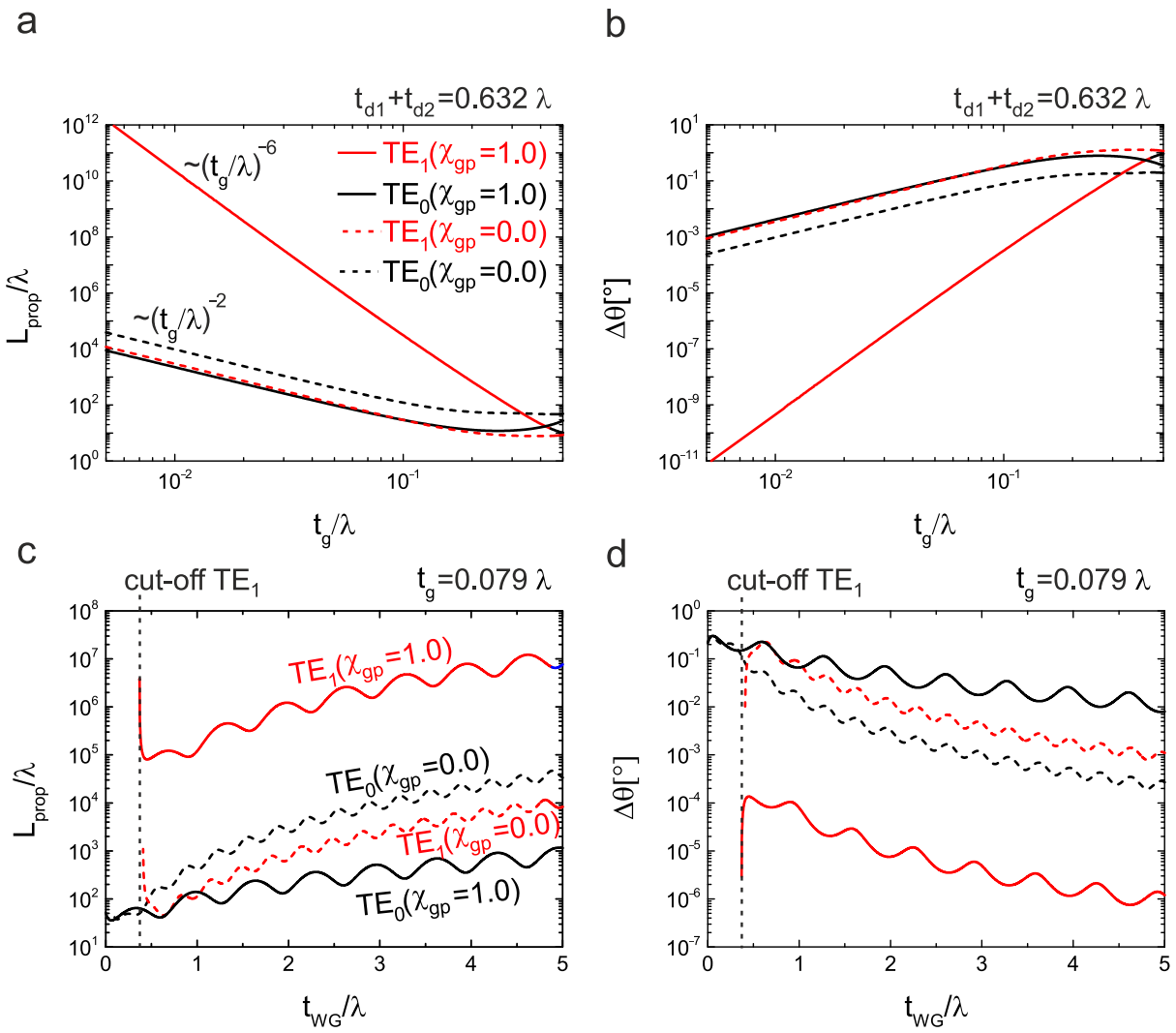

Figure 4.19: Normalized propagation length and divergence angle under the variation of t_g at a fixed value of $t_{d1} + t_{d2} = 0.632\lambda$ (a,b), and under the variation of t_{WG} at a fixed value of $t_g = 0.079\lambda$ (c,d). From ref. [249]

L_{prop} of an eigenmode with respect to a conventional waveguide grating geometry can be achieved without changing t_{WG} or any of the grating parameters. According to Eq. 4.15, the attributed concentration is increased by a factor of around 1000 as well [249].

To demonstrate that the elongated propagation lengths toward $\chi_{gp} = 1.0$ are no coincidence at a distinct set of parameters, but rather a general consequence of a minimized filling factor, the characteristics of the waveguide grating at hand with respect to parameter variations will be shown in the following lines [249].

Fig. 4.19a and b display the behavior of L_{prop} and $\Delta\theta$ under varying grating layer thicknesses and a fixed value of $t_{d1} + t_{d2} = 0.632\lambda$. Increased values of L_{prop} are present for the TE_1 mode at $\chi_{gp} = 1.0$ and for $t_g < 0.4\lambda$. Below this value of t_g, all displayed graphs follow a power law behavior [249]

$$L_{prop} \propto \frac{1}{t_g^p} \tag{4.19}$$

as it can be seen by their linear characteristics in a double-logarithmic plot. The TE_0 eigenmode for both $\chi_{gp} = 0.0$ and $\chi_{gp} = 1.0$ as well as the TE_1 eigenmode for $\chi_{gp} = 0.0$ are characterized by $p = 2$ [249]. This quadratic proportionality is known as 'parabolic region' in the standard theory of waveguide gratings [158]. In contrast, one finds $p = 6$ for the TE_1 eigenmode at $\chi_{gp} = 1.0$ [249]. An explanation for this exponent can be found by taking a closer look at the proportionalities of the filling factor near $\chi_{gp} = 1.0$. A Taylor approximation of the electric field intensity at the center plane z_c of the waveguide grating reads

$$I \propto |E_y(z)|^2 \propto (z - z_c)^2 \tag{4.20}$$

As the filling factor is given by the integral of $|E_y(z)|^2$ around z_c, it obeys the proportionality

$$FF \propto t_g^3 \tag{4.21}$$

From empiric investigations, these findings can be generalized to the relation

$$L_{prop} \propto \frac{1}{t_g^{p_1 \cdot p_2}} \tag{4.22}$$

whereby p_1 is the inherent exponent of any channel (radiative, Ohmic loss, etc.) and p_2 is the exponent provided by $FF \propto t_g^{p_2}$. For instance, the TE_1 mode at $\chi_{gp} = 1.0$ is characterized by $p_1 = 2$ and $p_2 = 3$, and all other displayed cases are approximately characterized by $p_1 = 2$ and $p_2 = 1$.

Figs. 4.19c and d show the behavior of L_{prop} and $\Delta\theta$ under a variation of t_{WG} with a fixed grating layer thickness of $t_g = 0.079\lambda$. These data demonstrate that these increased values of L_{prop} for the TE_1 mode at $\chi_{gp} = 1.0$ persist down to its cut-off [249].

To provide more intuitive insights on these numbers in the visible range, concrete geometry parameters are inserted. Assuming a wavelength of $\lambda = 632.8$ nm, a grating thickness of $t_g = 50$ nm, and a waveguide thickness of $t_{WG} = 450$ nm, a propagation length of $L_{prop} = 7.6$ cm is observed for the TE_1 eigenmode at $\chi_{gp} = 1.0$ and of $L_{prop} = 110\mu$m for the TE_0 eigenmode at $\chi_{gp} = 0.0$. To obtain comparable values of L_{prop} in the range of several centimeters using the TE_0 eigenmode, t_g would have to be reduced to approximately

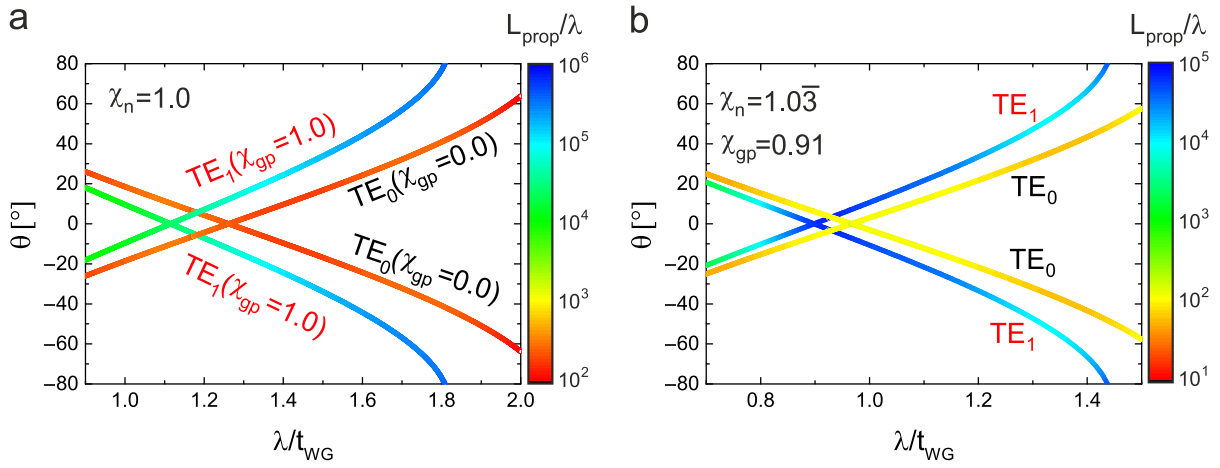

Figure 4.20: a) Normalized propagation length under variation of λ/t_{WG} at fixed ratios of the geometry's parameters (see the text). b) Variation of λ/t_{WG} for a highly asymmetric geometry ($\chi_{gp} = 0.93$,$\chi_n = 1.0\overline{3}$). From ref. [249].

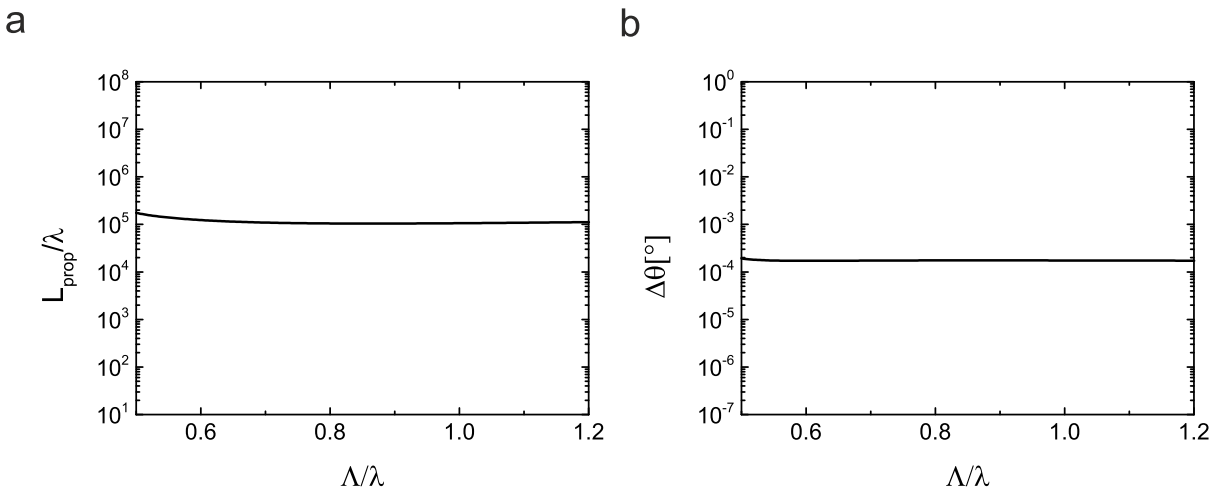

Figure 4.21: Influence of λ on the TE_1 eigenmode at $\chi_{gp} = 1.0$ under otherwise identical parameters as for Fig. 4.17. a) L_{prop}. b) $\Delta\theta$. From ref. [249].

0.8 nm or t_{WG} (at a fixed value of t_g) would have to be increased by an approximate factor of 15 [249].

The elongated values of L_{prop} are present for a variation of the wavelength at otherwise fixed parameter ratios as for Fig. 4.19 at $t_g/(t_{d1} + t_{d2}) = 0.045$ (Fig. 4.20a). Over the displayed range from $\lambda = 0.9\ t_{WG}$ to $\lambda = 1.8\ t_{WG}$, the values of L_{prop}/λ of the TE_1 mode for $\chi_{gp} = 1.0$ are consistently between 10^4 and 10^6. In contrast, the ones of the TE_0 for $\chi_{gp} = 0.0$ stay below a few 10^2 over the entire displayed range. These findings show that, with appropriate choices of materials and grating parameters, the increase of L_{prop} via the minimization of the filling factor is possible over the entire visible and near-IR range of wavelengths for symmetric waveguide gratings. For asymmetric waveguide gratings such as chosen in Fig. 4.20b, the node position of the TE_1 eigenmode shifts with respect to the center position of the grating layer under varying wavelengths. At a

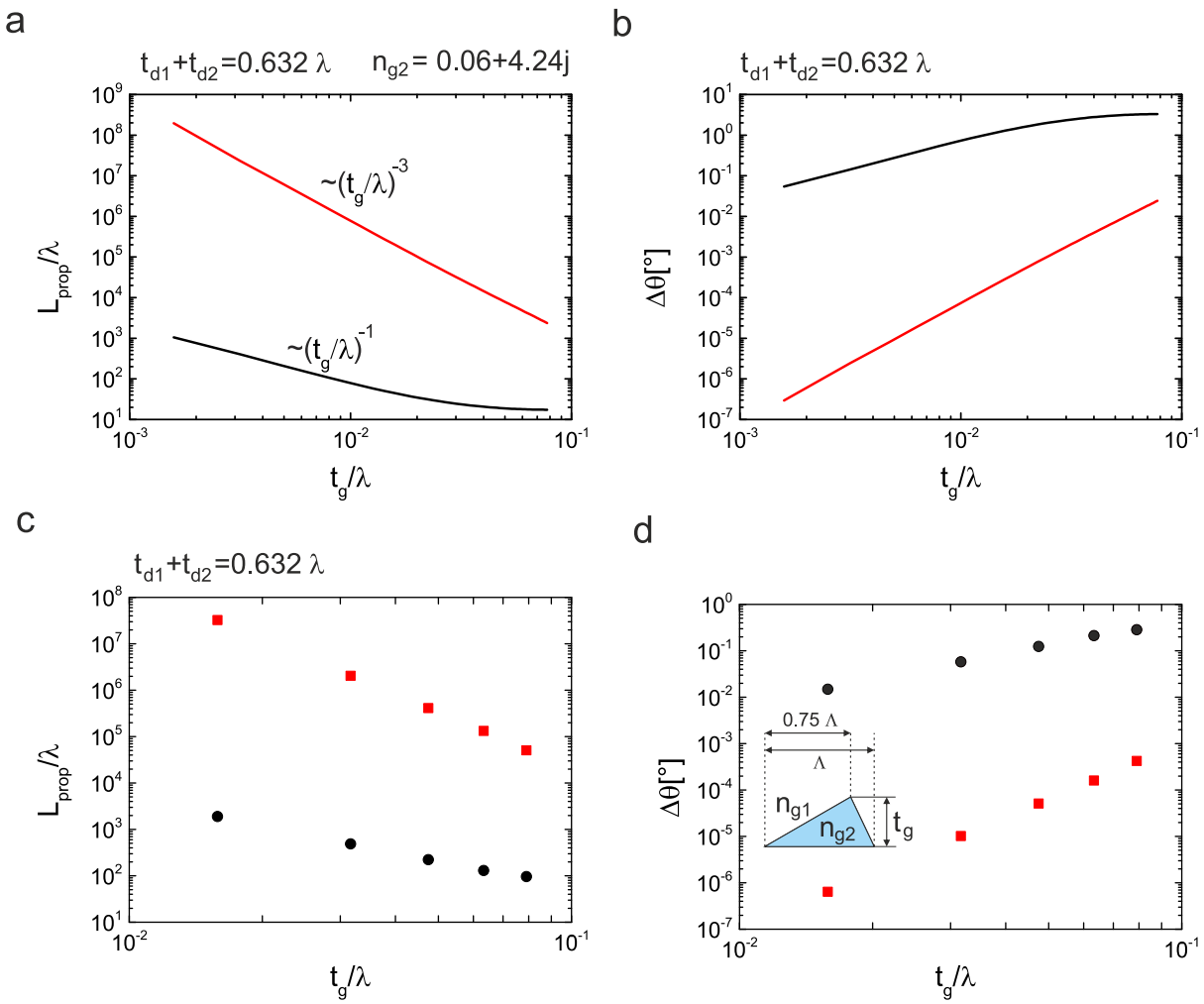

Figure 4.22: a,b) Influence of Ohmic loss on L_{prop} and $\Delta\theta$ for the TE_1 eigenmode (solid red line) and TE_0 eigenmode (solid black line) at $\chi_{gp} = 1.0$. c,d) Influence of an asymmetric grating on L_{prop} and $\Delta\theta$ for the TE_1 eigenmode (red squares) and TE_0 eigenmode (black circles) at $\chi_{gp} = 1.0$. For all four subfigures, aside from the different grating geometry, otherwise identical parameters as for Fig. 4.17 are assumed. From ref. [249].

distinct wavelength, the filling factor is minimized in an analogous way as described for the symmetric waveguide grating, and L_{prop} is maximized at a value of approximately 10^5. Away from this distinct wavelength, the filling factor increases again and L_{prop} decreases down to values between 10^2 and 10^3 [249].

Fig. 4.21 shows the relation of L_{prop} attributed to the TE_1 eigenmode under a variation of Λ under otherwise fixed geometry parameters as discussed in Fig. 4.17 at $\chi_{gp} = 1.0$. It can be observed that no significant change of L_{prop} is present. Therefore, the observed phenomena are not dependent on the grating period, as long as the grating's momentum is large enough to ensure that the TE_1 eigenmode can couple to radiation channels [249].

It could be presumed that the characteristics described above only occur for loss-free gratings, which are mirror symmetric with respect to the z-direction. Concerning the

influence of Ohmic loss, a waveguide grating is simulated for which n_{g2} is set to the refractive index of silver at a wavelength $\lambda = 632.8$ nm ($n_{g2} = 0.06 + j4.24$). The value of χ_{gp} is fixed at 1.0 (see Figs. 4.22a and b). Using otherwise identical parameters as in Fig. 4.19, the grating thickness is varied and all other parameters are fixed. As for loss-free gratings, L_{prop} is significantly larger for the TE_1 eigenmode (solid red line) than for the TE_0 eigenmode (solid black line). The difference to the loss-free grating is as follows: for the TE_0 eigenmode, $p_1 = 1$ and $p_2 = 1$ are present. For the TE_1 eigenmode, $p_1 = 1$ and $p_2 = 3$ can be found. The value of p_1 is observed because the Ohmic losses of the grating layer are proportional to its thickness and dominate over outcoupling [249].

To estimate the effects of an asymmetric grating layer, a geometry containing a triangular grating as shown in Fig. 4.22c and d is simulated, whereby the remaining geometry parameters are chosen as in Fig. 4.19 at $\chi_{gp} = 1.0$. Again the values of L_{prop} for the TE_1 eigenmode (red squares) are significantly larger than for the TE_0 mode (black circles). Here, a value of $p = 4$ is observed for the TE_1 eigenmode and a value of $p = 1.9$ is present for the TE_0 eigenmode [249].

The fact that the elongated values of L_{prop} occur for such large parameter variations confirms that this concept of achieving long propagation lengths can be applied on waveguide gratings in general (under the constraints of thin grating layers as explained above) [249].

Another interesting property of symmetric waveguide gratings using the nodes of TE modes is their sensitivity to asymmetric geometrical or environmental changes. For instance, inducing an asymmetric change of the waveguide grating's refractive index profile ($\chi_n = 1.0 \rightarrow \chi_n \neq 1.0$) drastically reduces L_{prop}. This behavior is visualized in Fig. 4.23 for a waveguide grating with a grating thickness of $t_g = 1.5 \cdot 10^{-3}\lambda$ and otherwise identical parameters as for the geometry discussed in Fig. 4.17. Here, n_{d1} is varied and n_{d2} is fixed at a value of 1.5 and χ_{gp} is fixed at a value of 1.0. A Figure of Merit ($FoM_{L_{prop}}$) to measure the sensitivity can be defined by [249]

$$FoM_{L_{prop}} = \frac{1}{L_{prop}} \frac{\partial L_{prop}}{\partial n_{d1}} \tag{4.23}$$

The values of $FoM_{L_{prop}}$ are strongly pronounced for the TE_1 eigenmode near symmetry and become approximately 10^4. In comparison, the TE_0 eigenmode under the same conditions exhibits values of around 5. In a similar way, the relative change [249]

$$S_{\Delta n} = \frac{L_{prop}(n_{d1} + \Delta n)}{L_{prop}(n_{d1})} \tag{4.24}$$

for a value of $\Delta n = 10^{-4}$ is around $1.5 \cdot 10^6$ for the TE_1 eigenmode near symmetry and around 1 for the TE_0 mode for any value of n_{d1} [249].

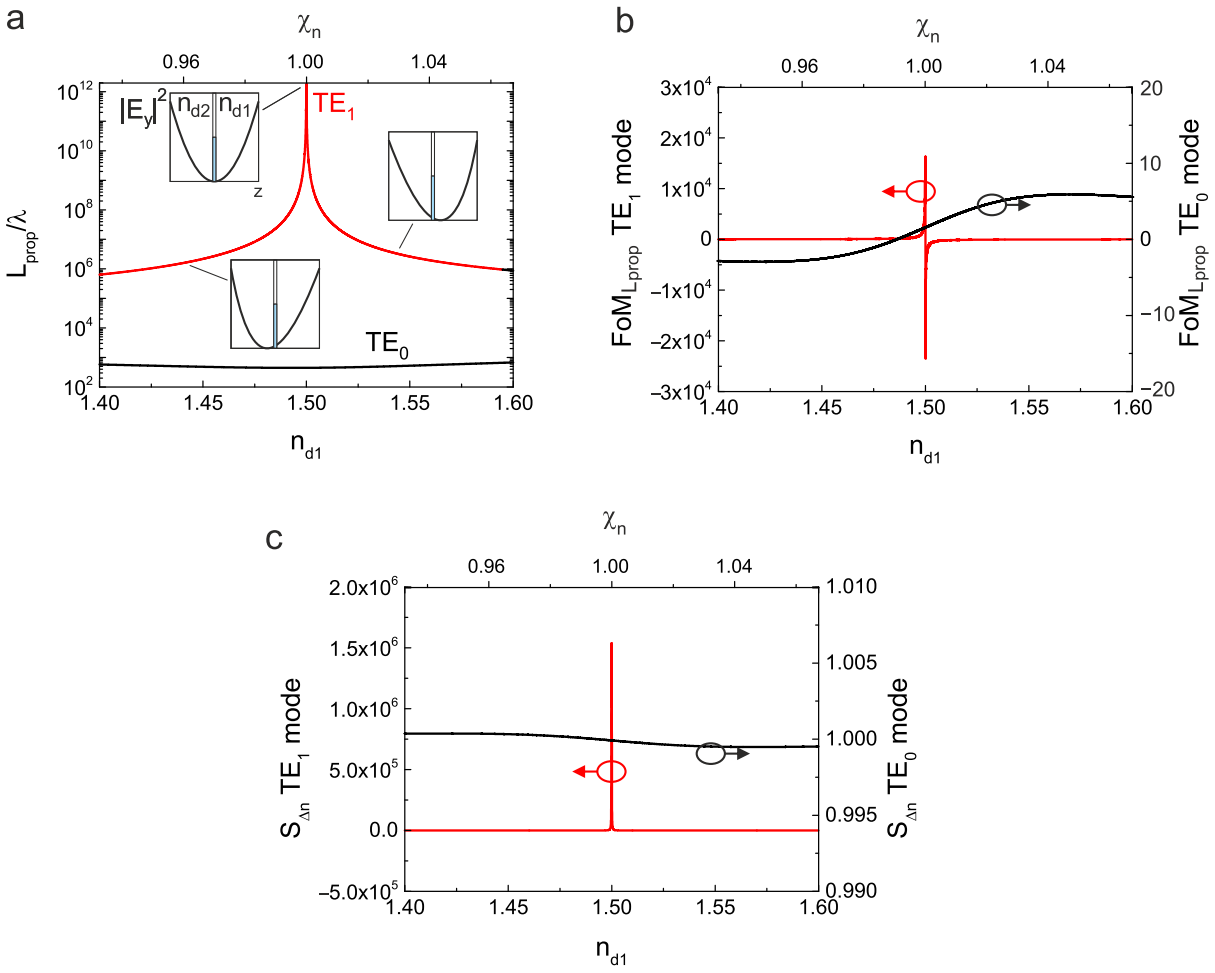

Figure 4.23: Characteristics of a waveguide grating with $t_g = 1.5 \cdot 10^{-3}\lambda$ and otherwise identical parameters as in Fig. 4.17 under a variation of χ_n at $n_{d2} = 1.5$ and $\chi_{gp} = 1.0$. a) Normalized propagation lengths of the TE_0 and TE_1 eigenmodes. b) Figure of Merit $1/L_{prop}(\partial L_{prop}/\partial n_{d1})$. c) Sensitivity $S_{\Delta n}$ to refractive index changes. From ref. [249].

This sensitivity means that the nodes of TE polarized modes in symmetric waveguide gratings can be used to detect even slight asymmetry inducing changes of the geometry or environment [249]. From the reciprocal point of view, controlling the geometry or environment of the waveguide in an asymmetry inducing way enables to control L_{prop} over many orders of magnitude [249]. Besides from potential future advances with respect to existing sensors [254–260] and modulators [261, 262] based on waveguide gratings, these properties can be useful in two ways: first, a highly parallel light-source of controllable divergence angle and local output intensity could be realized. Second, a light concentrator might be realized for which L_{prop} can be matched to the lateral extension of an incoming light beam either through the initial geometry design, e.g. by the selection of distinct layer thicknesses, or through the active adaption of the geometry's layer thicknesses or refractive indices.

However, there is one drawback when solar concentrators are considered. According to

the explanations in Chapter 2, such long propagation lengths demand that both $\Delta\theta$ and $\Delta\lambda = \lambda/Q$ attributed to an eigenmode are small. To collect the spectrum of the sun within its momentary angular range of 0.52° [66], at least $N = 0.52°/\Delta\theta$ waveguide gratings would have to be stacked. As gratings are strongly dispersive, the actual required number of waveguide gratings is substantially higher. Therefore, the advantageous ratio of L_{prop}/t_{WG} for a single eigenmode comes along with the trade-off of a higher number of required eigenmodes to cover the sun's angular range and spectrum. In fact, although preliminary experiments have shown that the stacking of waveguide gratings works in principle, such a high number of eigenmodes would require rather complex geometries. In addition, the collection of light via a waveguide grating, or any other waveguide with homogeneously distributed light-coupling elements, comes along with the unwanted outcoupling of light, which has already been concentrated into the waveguide grating. Both of these challenges will be tackled in the upcoming sections. At first, a method to completely cancel outcoupling for a distinct photonic-plasmonic hybrid waveguide grating will be demonstrated.

4.3 Complete Suppression of Outcoupling with Hybrid Bound States in the Continuum

In the last section, it has been demonstrated that some challenges have to be tackled to make waveguide gratings useful for solar concentrators. One challenge was to find a way to prevent the outcoupling of light after it has been concentrated into a waveguide grating. There exists a curious phenomenon termed 'Bound State in the Continuum' (BIC) which is characterized by a singular eigenmode of zero outcoupling efficiency within a dispersion relation of eigenmodes of non-zero outcoupling efficiency. This phenomenon has drawn remarkably attention in the recent years as it can be used to achieve large quality factors [156], low-threshold lasers [263–265] or vortex lasers [266], higher order harmonic generation [61, 111, 267, 268], and tunable transmittance [269–271]. As briefly outlined in Chapter 2, one way to achieve a BIC is via a symmetry mismatch at $k'_x = 0$ between the field distribution of an eigenmode and the plane-waves in the substrate and superstrate [272]. In the recent years, more ways to achieve BICs in photonic crystals and waveguide gratings at $k'_x \neq 0$ have been demonstrated, ranging from single resonators to coupled systems [156,273]. These BICs originate from a common principle: when multiple internal waves or eigenmodes couple to the same radiation channel (e.g. a diffraction order), and their phase relations as well as amplitudes are chosen in a way that they interfere destructively, outcoupling can be completely canceled [272]. To achieve such destructive interference, the number of internal plane-waves or eigenmodes N_i must be larger than the number of radiation channels N_e [272]. For instance, a BIC for a single eigenmode can occur from the destructive interference of electric and magnetic resonances [273]. As a matter of course, $N_i > N_e$ is only a necessary, but not a sufficient condition for the occurrence of BICs [272]. For instance, asymmetric geometries may exhibit a large number of internal waves or resonances, but their phase and amplitude relations may not exhibit destructive interference for any combination of k'_x and ω, unless a specific set of geometric parameters is chosen. For some occasions, such a specific set of parameters is found by accident and historically led to the name 'accidental BIC' for this type of BIC [274]. However, for symmetric geometries, BICs experience topological protection and exist for all geometric changes which preserve symmetry [156, 264, 266, 272, 275].

Concerning coupled systems, among others [278], there is a type of distinct type of BIC, which is termed 'Friedrich-Wintgen-BIC' (FW-BIC) [279]. For example, a FW-BIC can be achieved by the coupling of two eigenmodes via a grating layer [277, 280, 281]. A simplified model of this coupling is given by the 'Hamiltonian model' [272, 277]. This model is also often referred to as 'coupled mode theory' [282]. In this model, all the amplitudes $g_{j,\nu}$ and $f_{j,\nu}$ of an eigenmode (see Chapter 2) are replaced by a single amplitude a with an attributed complex eigenfrequency $\omega - j\gamma$, whereby the total dampening rate

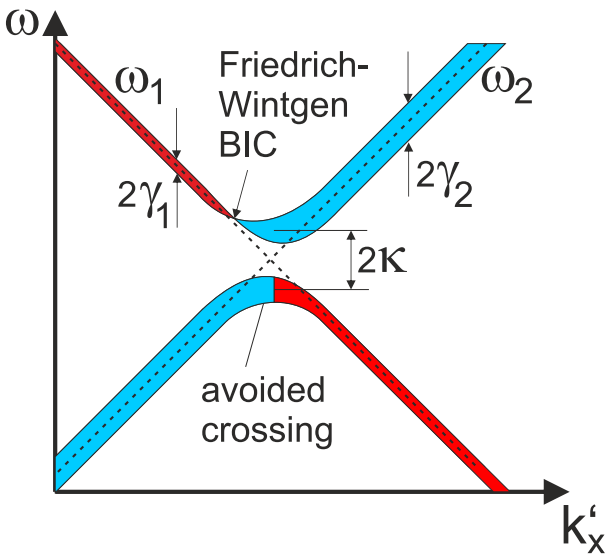

Figure 4.24: Coupling of two resonances in a waveguide grating with one common output channel. For $\kappa > 0$, avoided crossing accompanied by a Friedrich-Wintgen BIC (FW-BIC) can occur. The black dashed lines show the dispersion relations for zero coupling ($\kappa = 0$) for comparison. According to refs. [272, 276, 277].

γ can be derived using the Q-factor by $\gamma = \omega/2Q$. Herein, the Q-factor is composed of a lossy component Q_{loss} and a radiative component Q_r. Both components are linked to Q via [203]

$$\frac{1}{Q} = \frac{1}{Q_r} + \frac{1}{Q_{loss}}. \tag{4.25}$$

Importantly, an outcoupling efficiency of zero is equivalent to an infinitely large Q_r.

Now, two eigenmodes of amplitudes a_1 and a_2, and frequencies $\omega_1 - j\gamma_1$ and $\omega_2 - j\gamma_2$ are considered. The time-evolution of these eigenmodes can then be described by [203]

$$\frac{\partial}{\partial t}\begin{pmatrix} a_1 \\ a_2 \end{pmatrix} = \underline{H}\begin{pmatrix} a_1 \\ a_2 \end{pmatrix} \tag{4.26}$$

$$\underline{H} = \begin{pmatrix} \omega_1 & \kappa \\ \kappa^* & \omega_2 \end{pmatrix} - j\begin{pmatrix} \gamma_1 & \sqrt{\gamma_1\gamma_2} \\ \sqrt{\gamma_1\gamma_2} & \gamma_2 \end{pmatrix} \tag{4.27}$$

The parameters κ and $\sqrt{\gamma_1\gamma_2}$ are the coupling parameters between both eigenmodes. The solutions of this differential equation system is given by the eigenvalues and eigenvectors of $\underline{H}$. Hereby, the eigenvalues obey the equation

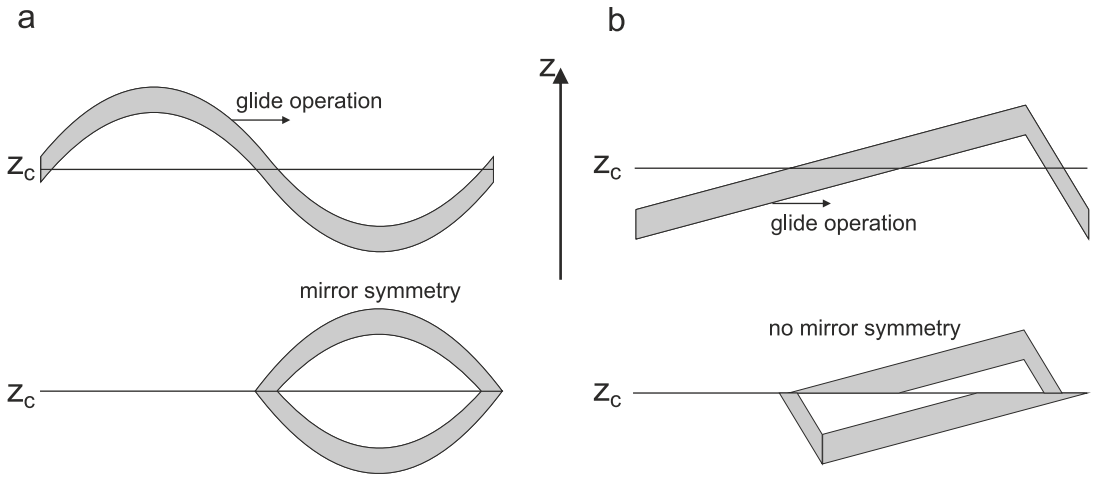

Figure 4.25: Visualization of the meaning of Eq. 4.29. a) A sinusoidal grating exhibits mirror symmetry under glide operations. b) A blaze grating is never mirror symmetric.

$$\omega_{+/-}(k_x') = \frac{1}{2}(\omega_1 + \omega_2) - j\frac{1}{2}(\gamma_1 + \gamma_2) \pm \frac{1}{2}\sqrt{[(\omega_1 - j\gamma_1) - (\omega_2 - j\gamma_2)]^2 + 4(\kappa - j\sqrt{\gamma_1\gamma_2})^2} \tag{4.28}$$

and the eigenvectors are linear combinations of both eigenmodes [277], whereby their amplitude weights and phases are parametrically tuned along their dispersion relations [277]. Such a linear combination is called 'hybrid eigenmode'. As a result of the coupling, the real parts of ω_+ and ω_- show an avoided crossing and the imaginary part of either ω_+ or ω_- becomes zero along one of the dispersion relations of the hybrid eigenmodes [272, 277]. This vanishing imaginary part is the FW-BIC and characterized by an outcoupling efficiency of zero. An exemplary sketch of an avoided crossing accompanied by a FW-BIC is shown in Fig. 4.24.

It is important to note that topologically protected FW-BICs occur when the condition

$$\varepsilon(x + \delta, y, -(z - z_c)) = \varepsilon^*(x, y, (z - z_c)) \tag{4.29}$$

is fulfilled, so that they can always be observed along the hybrid eigenmodes' dispersion relations [274]. Hereby, z_c is the center plane of the grating. This condition describes mirror symmetry with respect to the z-direction under glide operations along the x-direction. For example, a sinusoidal grating can be converted into a perfect mirror symmetric grating via choosing $\delta = \Lambda/2$ (see Fig. 4.25a). In contrast, there is no glide operation which produces mirror symmetry for a blaze-grating (Fig. 4.25b).

In 2018, Azzam et. al [276] theoretically predicted the existence of hybrid photonic-plasmonic FW-BICs (hybrid FW-BICs) when plasmonic eigenmodes (SPP) and photonic

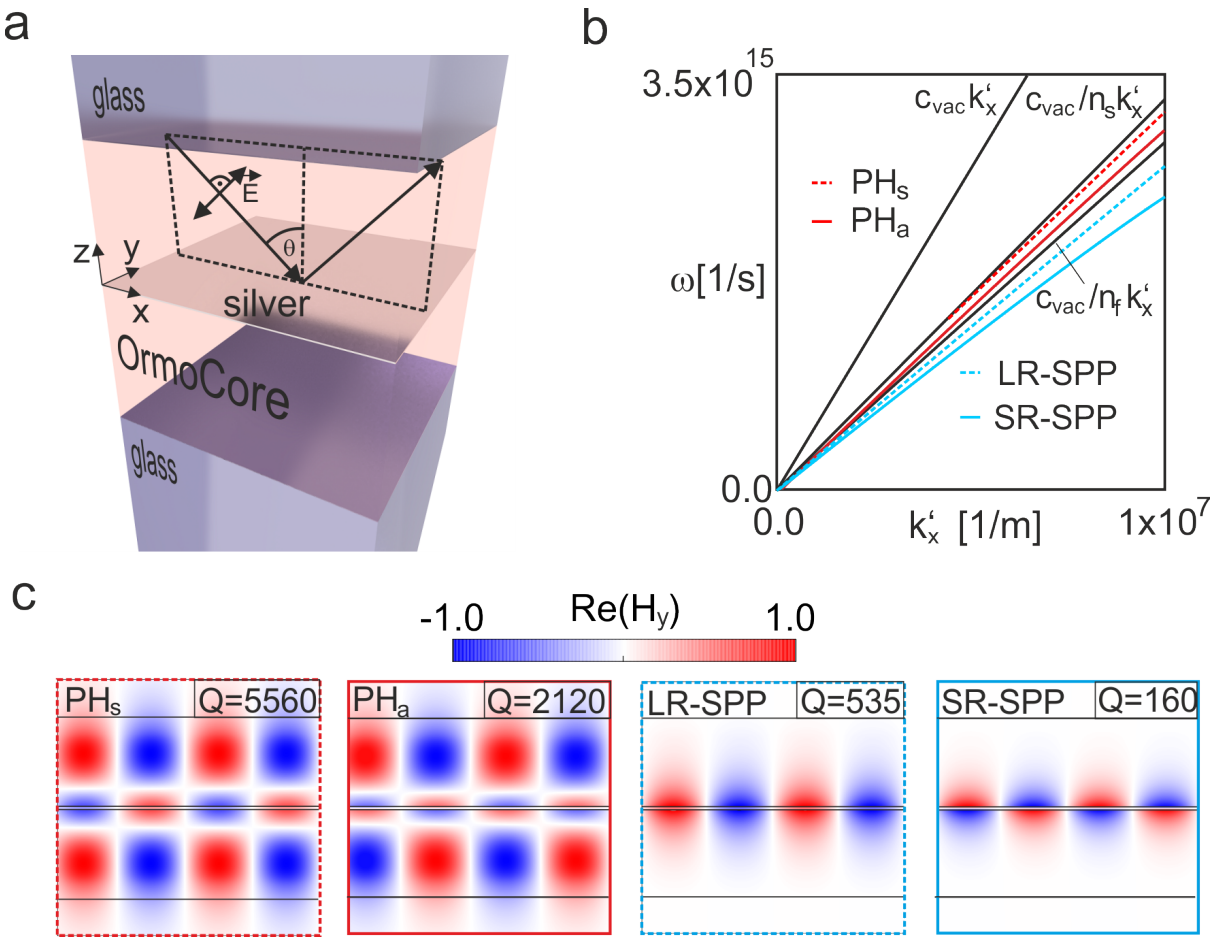

Figure 4.26: a) Planar hybrid waveguide. b) Dispersion relations of the symmetric and antisymmetric photonic (PH_s and PH_s) as well as plasmonic (LR-SPP and SR-SPP) eigenmodes. From ref. [203].

eigenmodes (PH) are coupled with each other via a diffraction grating. Herein, the term 'photonic' means that the majority of the magnetic field strength is distributed within a dielectric layer. As a side note, both $N_i < N_e$ and Eq. 4.29 were fulfilled by treating the entire substrate as a semi-infinite silver layer, acting as a symmetry inducing mirror [276]. This way, all diffraction orders in the substrate were canceled and FW-BICs could be observed via simulations [276].

Here, an experimental demonstration and theoretical considerations on the sensing performance of hybrid FW-BICs will be provided in the following [203].

In a step-by-step explanation, the design of a waveguide grating will be explained which fulfills both $N_i < N_e$ and Eq. 4.29. In a first step, a symmetric waveguide is considered as visualized in Fig. 4.26a. It consists of two OrmoCore layers (refractive index n_{OC}) embedding a thin silver film of a thickness of 60 nm. The superstrate and substrate of this waveguide consist of Borofloat glass of a refractive index n_s [283]. The thickness of both OrmoCore layers is chosen to a value of 1035 nm. For TM polarized light around

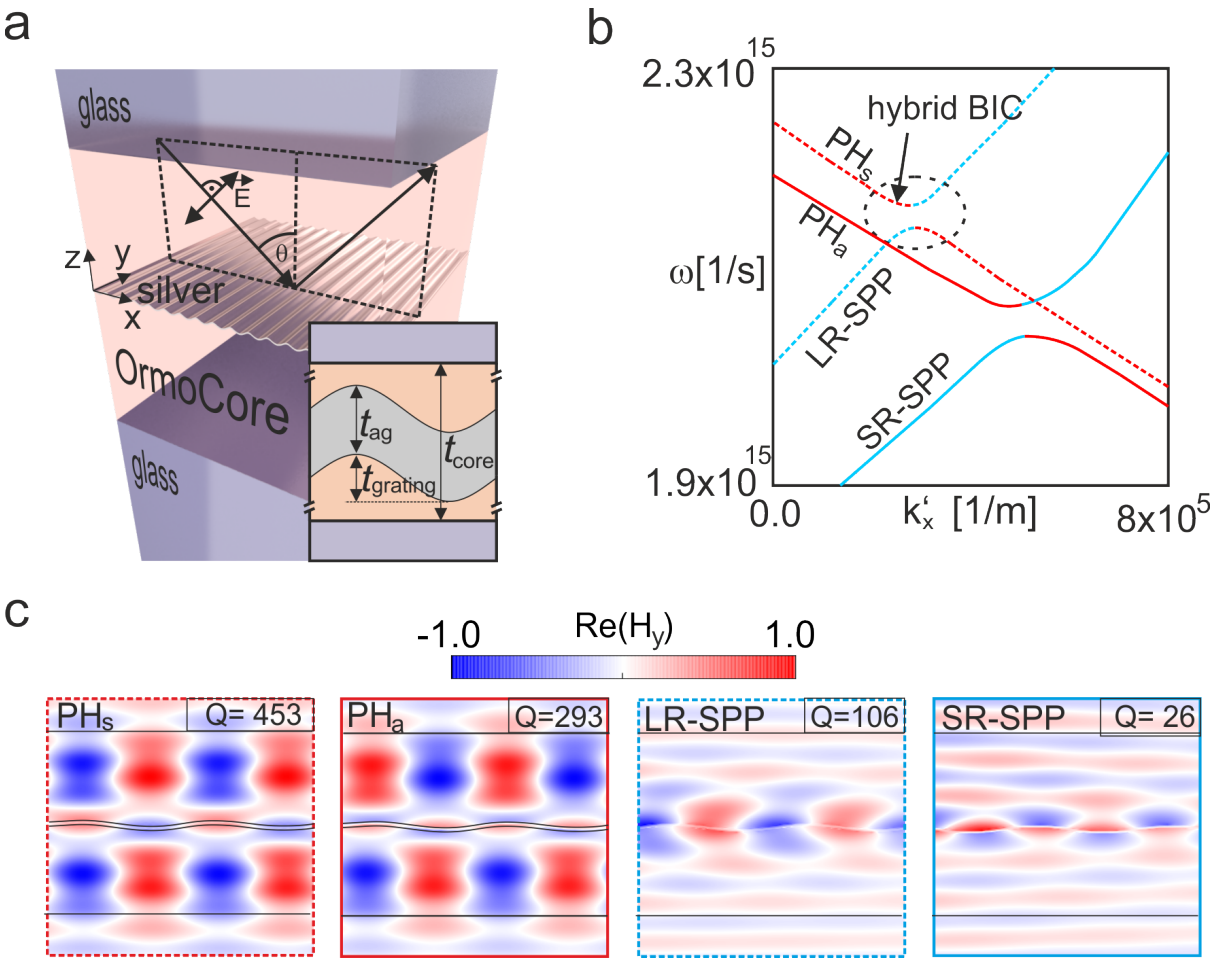

Figure 4.27: a) Hybrid waveguide with a sinusoidally structured silver grating. b) Dispersion relations of the symmetric and antisymmetric photonic (PH_s and PH_s) as well as plasmonic (LR-SPP and SR-SPP) eigenmodes. c) Corresponding normalized magnetic field distributions. From ref. [203].

a wavelength of $\lambda = 860$ nm, this symmetric waveguide supports two photonic eigenmodes and two surface plasmon eigenmodes [203]. The two plasmonic eigenmodes are the (antisymmetric) SR-SPP eigenmode and the (symmetric) LR-SPP eigenmode of the silver layer. The photonic eigenmodes are termed as PH_a and PH_s, whereby the indices 'a' and 's' stand for an antisymmetric and symmetric magnetic field distribution, respectively. The dispersion relations of these eigenmodes are displayed in Fig. 4.26b. Both dispersion relations of the PH_a and PH_s eigenmodes are found between $k'_x = \frac{\omega}{c_{vac}} n_s$ and $k'_x = \frac{\omega}{c_{vac}} n_{OC}$. As the silver film is surrounded by OrmoCore, the SR-SPP and LR-SPP possess larger lateral momenta than $k'_x = \frac{\omega}{c_{vac}} n_{Oc}$ (see Chapter 2). Fig. 4.26c shows the magnetic field distributions of these four eigenmodes together with their corresponding Q-factors. Going from the largest to the smallest Q-factor, the PH_s, PH_a, LR-SPP and SR-SPP exhibit values of 5560, 2120, 535, and 160 [203].

To establish the coupling between these eigenmodes, fulfill Eq. 4.29 , and provide compatibility with the available fabrication procedures, a sinusoidal modulation of the silver

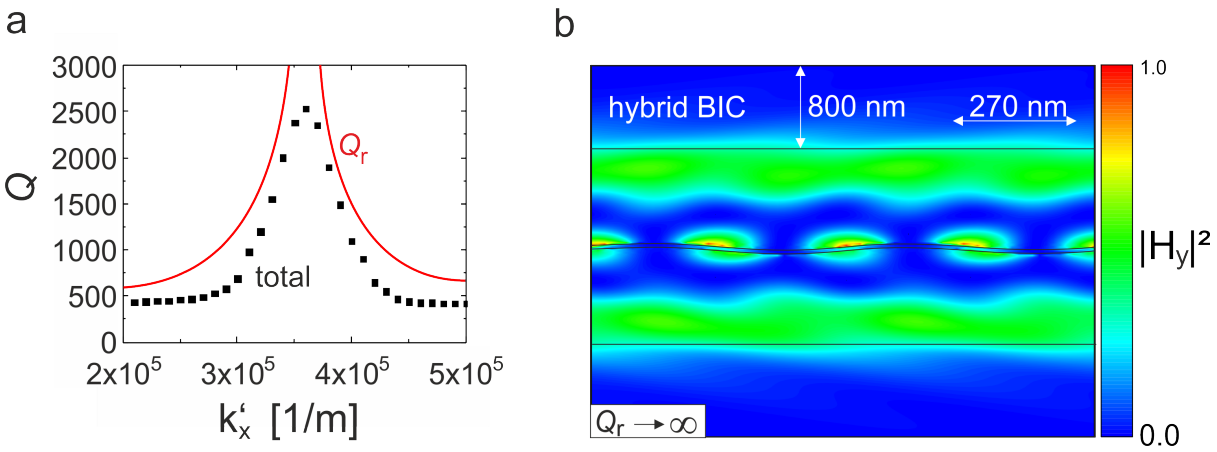

Figure 4.28: a) The Q-factor Q and its radiative component Q_r. The hybrid FW-BIC is characterized by a singularity of Q_r, whereby Q is finite due to Ohmic losses. b) Corresponding distribution of $|H_y|^2$ attributed to the hybrid FW-BIC. The interference pattern near the grating originates from the interference of the counter propagating LR-SPP and PH_s modes. From ref. [203].

film with an amplitude of $t_a = 100$ nm and period of $\Lambda = 555$ nm is introduced (Fig. 4.27a). Due to the formation of a band-structure (see Chapter 2), the dispersion relations of the eigenmodes appear above the light-line, which is defined by $\omega = c_{vac}|k_x|$ (Fig. 4.27b) [203]. No coupling occurs between the PH_s and SR-SPP as well as the PH_a and LR-SPP eigenmodes as their overlap integral vanishes due to their opposing symmetries with respect to the z-direction [203]. In contrast, pair-wise avoided crossing occurs between the PH_s and LR-SPP, as well as between the PH_a and SR-SPP eigenmodes and, thus, indicates their coupling with $\kappa > 0$. The magnetic field distributions of the eigenmodes away from the positions of avoided crossing are shown in Fig. 4.27c. In comparison to the ones shown in Fig. 4.26c, these field distributions are distorted as a consequence of a large outcoupling efficiency [203]. This large outcoupling efficiency decreases the Q-factors by approximately one order of magnitude: the Q-factors of the PH_s and PH_a eigenmodes are 453 and 293 and those of the LR-SPP and SR-SPP are 106 and 26, respectively [203].

Near to the avoided crossing of the LR-SPP and the PH_s eigenmode, there is a significant deviation from these trends. As shown in Fig. 4.28a, the Q-factor of the PH_s eigenmode shows a maximum at a distinct lateral momentum k'_x. This behavior occurs as the radiative component Q_r of the Q-factor diverges to infinity, whereby Q_{loss} stays limited [203]. This observation means that an outcoupling efficiency of zero is present. A cross-sectional plot of $|H_y|^2$ for $Q_r \to \infty$ is shown in Fig. 4.28b. Indeed, the superstrate and substrate are characterized by an evanescently decaying field, independently confirming that an outcoupling efficiency of zero is present [203]. Interestingly, the remaining field distribution inside the waveguide exhibits an interference pattern near to the silver

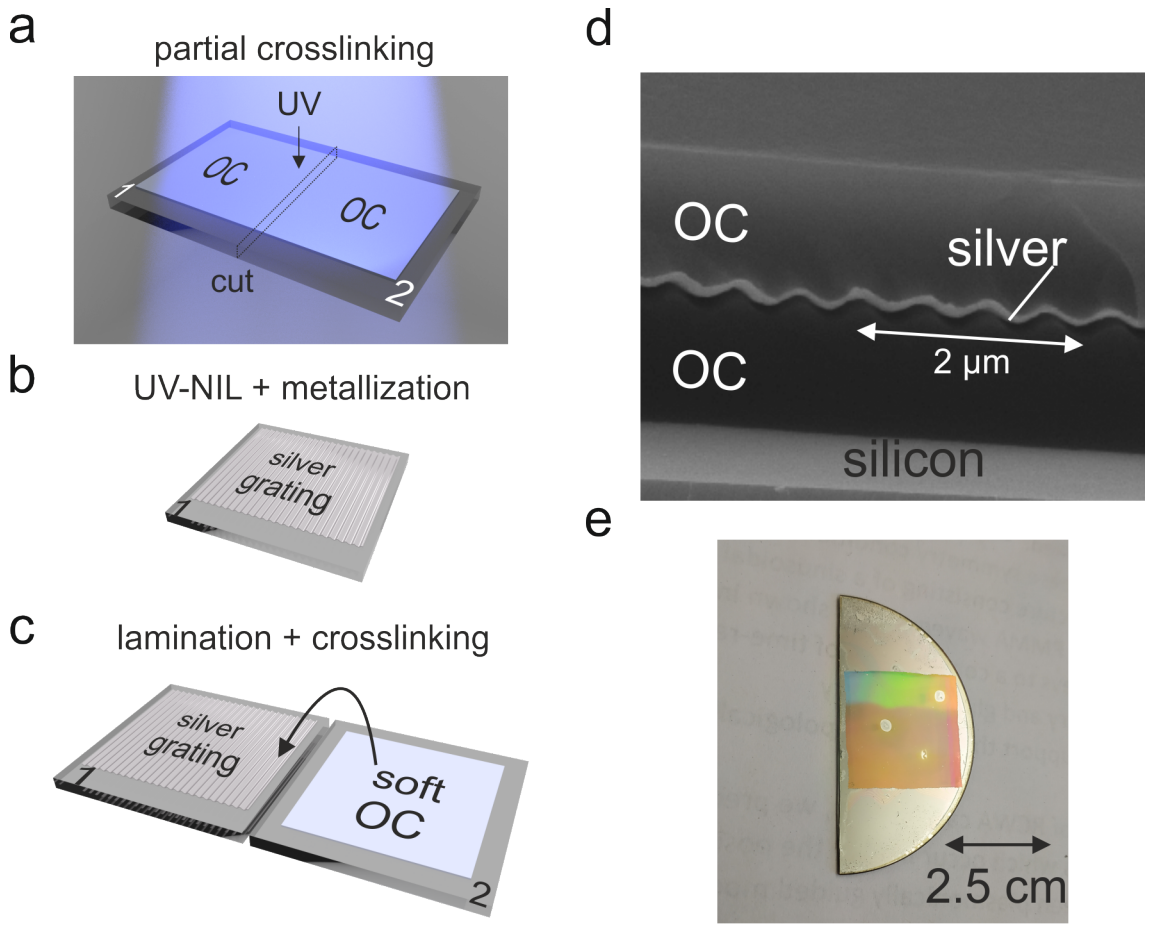

Figure 4.29: a-c) Fabrication procedure of the hybrid waveguide grating using the methods explained in Chapter 3. d) Cross-sectional SEM of laminated OrmoCore layers surrounding a sinusoidal silver grating. e) Photograph of the fabricated sample. From ref. [203]

grating. This interference pattern originates from the opposite directions of propagations of the PH_s and LR-SPP eigenmodes and confirms that the entire field distribution can be understood as a hybrid eigenmode. From this point of view, the occurrence of zero outcoupling efficiency can be interpreted as the destructive interference of radiation emitted by a forward propagating PH_s eigenmode and backward propagating LR-SPP eigenmode into the same diffraction order (with equal amplitudes and opposite phase) [203].

Concerning the experimental demonstration of hybrid FW-BICs, the waveguide grating design from Fig. 4.27a is realized by a combination of UV-NIL, metallization and lamination (Figs. 4.29a-c). A cross-sectional SEM of two OrmoCore layers surrounding a sinusoidal silver grating demonstrates that a high degree of symmetry is achieved with these methods (Fig. 4.29d). To investigate whether the hybrid FW-BICs can be observed, such a stack has been laminated between two one millimeter thick Borofloat layers. A top-view photograph of this stack is shown in Fig. 4.29e [203].

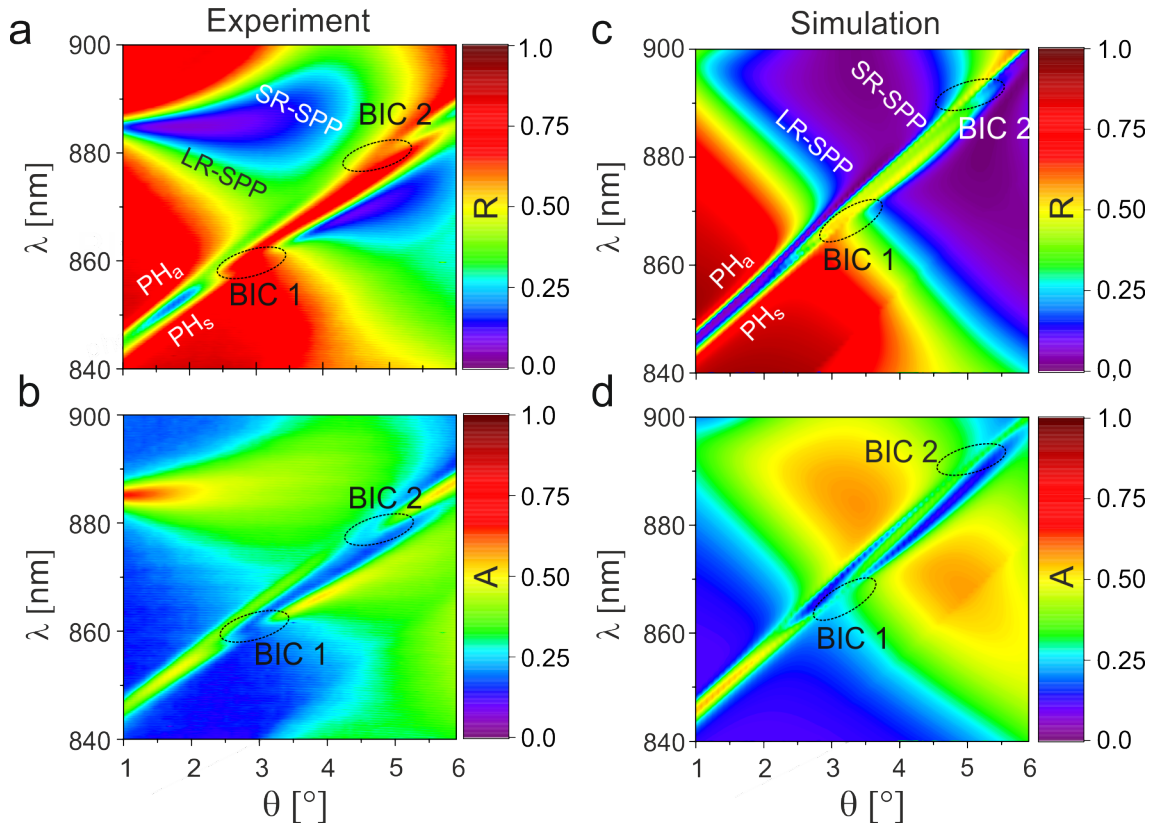

Figure 4.30: The reflectance R and absorption A of the hybrid waveguide grating. a,b) Experimentally obtained values. c,d) Simulated values. From ref. [203]

.

The results of angular resolved RTS measurements of this waveguide grating are shown in Fig. 4.30 [203]. The reflectance R (Fig. 4.30a) shows several distinct features in the displayed parameter range which will be elaborated in the following.

The excitation of the photonic and plasmonic eigenmodes can be observed as dips of R. Herein, the species of eigenmodes can be identified by calculating their attributed values of $\mathrm{Re}(n_{eff})$ (see Chapter 2). For instance, the dip at $\lambda = 843$ nm and $\theta = 1°$ corresponds to $\mathrm{Re}(n_{eff}) = 1.51$. This value lies between n'_s and n'_{OC}, and can therefore be attributed to photonic eigenmodes. The dip at $\lambda = 885$ and $\theta = 1°$ corresponds to $\mathrm{Re}(n_{eff}) \approx 1.6 > n_{OC}$ and can be attributed to plasmonic eigenmodes. As predicted by the simulation, the slopes of the center positions of these dips are of opposite signs, indicating counter-propagating photonic and plasmonic eigenmodes. As a side note, it is not possible to distinguish SR-SPP and LR-SPP resonances from these measurements as their spectral widths are larger than their spectral separation. Nonetheless, their coupling with the photonic eigenmodes can be observed, confirming that all conditions for FW-BICs are fulfilled. Indeed, at a parameter pair near $\lambda = 867$ and $\theta = 2.9°$, one of the dips attributed to the photonic eigenmodes completely vanishes. This vanishing is the result of the existence of a hybrid FW-BIC (BIC 1) attributed to the coupling of the PH$_s$

and LR-SPP eigenmodes. An analogous observation can be made near $\lambda = 878$ nm and $\theta \approx 5.0°$, indicating a hybrid FW-BIC (BIC 2) arising from the coupling of the PH_a and SR-SPP eigenmodes [203].

To exclude that the observed phenomena are not only features of R alone, the absorption $A = 1 - R - T$ is investigated as well (Fig. 4.30b). Here, the excitations of eigenmodes becomes apparent as peaks of A as photons have a higher probability of thermalization under resonance [284]. These peaks vanish at the same wavelength and incidence angles, indicating that no eigenmodes can be excited by the incident light as a result of the presence of the hybrid FW-BICs. These observations are in qualitative agreement with simulated data of R and A (Fig. 4.30c and d), whereby the characteristics attributed to plasmonic eigenmodes shows quantitative differences to the experiment. As the experiment displays an average over many grating periods, this discrepancy presumably originates from local variations of the grating geometry. Apparently, as long as these local variations do not break the local symmetry of the grating, hybrid BICs occur as a result of their topological protection [203]. In comparison, a waveguide grating exhibiting a blaze grating does not fulfill Eq. 4.29 and, thus, shows no occurrence of hybrid FW-BICs (Fig. 4.31) [203].

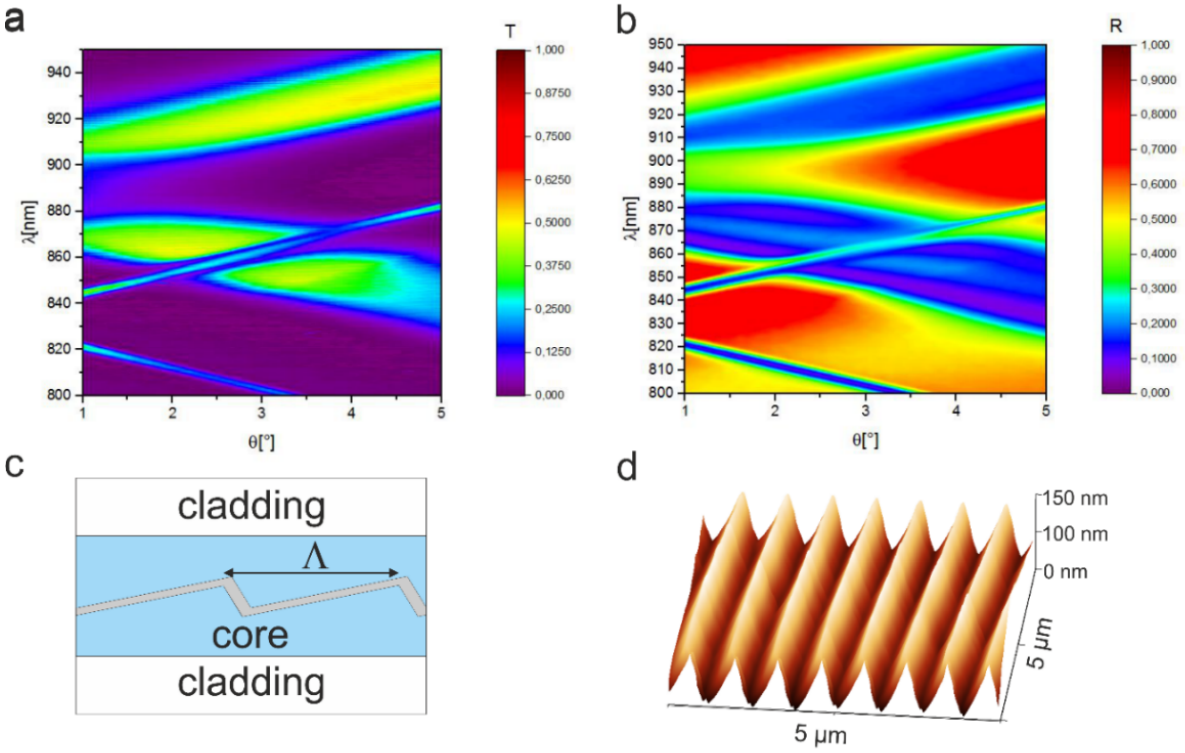

Figure 4.31: a, b) Measured values of R and T for a hybrid waveguide grating containing a blaze grating. c) Sketch of the geometry of the hybrid waveguide grating. d) atomic force micrograph of the blaze grating surface prior to the lamination. From ref. [203].

To provide further experimental evidence for the hybrid FW-BICs, the radiative Q-factors

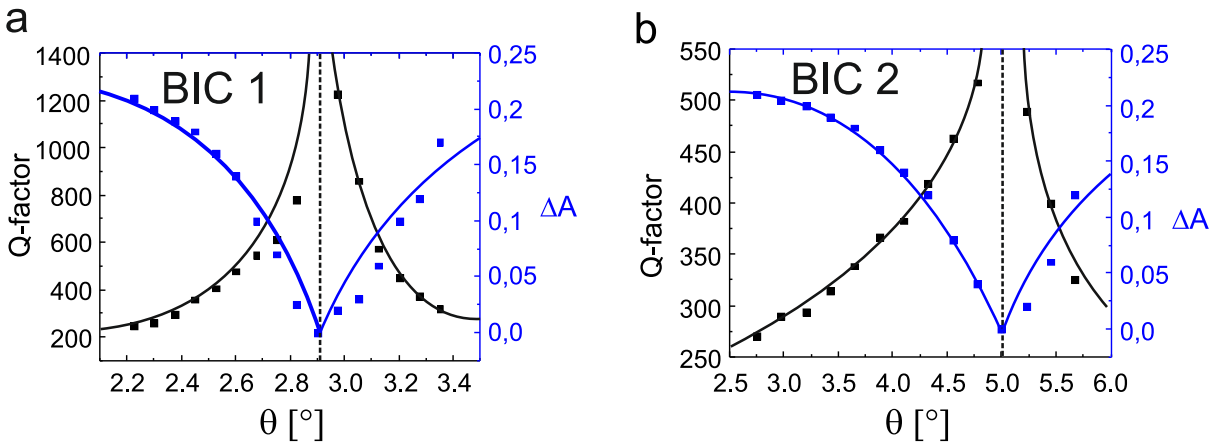

Figure 4.32: Q-factors and absorption amplitudes ΔA obtained from fitting Lorentzian peaks to the measured values of R. a) BIC 1. b) BIC 2. From ref. [203].

($\lambda/\Delta\lambda$) and amplitudes ΔA of the peaks near to the FW-BICs are extracted from the measured data. These extracted values are shown in Fig. 4.32. Towards both hybrid FW-BICs, decreasing peak widths and values of ΔA are observed [203].

All the observations explained above provide convincing experimental evidence for the existence of hybrid FW-BICs. This evidence is the main result of ref. [203] and confirms that outcoupling can be completely suppressed in hybrid waveguide gratings. The consequences for solar applications will be discussed later on. Before this discussion, an investigation about the advantages of hybrid FW-BICs with respect to the sensitivity to refractive index changes will be presented.

To explain the reason why such investigations have not been done before, a typical way to use resonators as sensors will be briefly explained and related to BICs. A common way to build a sensor is to measure the intensity of reflected or transmitted light via a low-cost photo detector and a monochromatic light source. For this case, the performance is usually defined by the intensity related Figure of Merit [285]

$$FoM^* = \frac{1}{I}\frac{\partial I}{\partial n'} \propto S_\lambda Q, \tag{4.30}$$

whereby

$$S_\lambda = \frac{\partial \lambda_{res}}{\partial n'} \tag{4.31}$$

is the sensitivity attributed to a resonance with a center wavelength λ_{res} and n' as a refractive index change.

Naturally, resonators with large values of S_λ and large Q-factors are sought. However, within a given class of resonators (purely dielectric, purely plasmonic), their product remains nearly constant [285–289]. Yu et. al provide an insightful explanation in ref. [290]: the occurrence of a resonance can be understood as the scanning of an eigenmode's

dispersion relation k'_x with a probe (e.g. a prism, a grating, etc.). As a result, both S_λ and $1/Q$ are scaled with the same factor [290].

It is important to note, that the hybridization of one resonator of a large Q factor with another resonator of a large sensitivity S_λ does not provide any improvement of $S_\lambda Q$, when only one of the resonators couples to an output channel (e.g. plane waves in the substrate or superstrate) [285, 291–294]. For instance, the coupling of two resonators, which do not share a common output channel can be modeled via [295]

$$\underline{H} = \begin{pmatrix} \omega_1 & \kappa \\ \kappa^* & \omega_2 \end{pmatrix} - j \begin{pmatrix} \gamma_1 & 0 \\ 0 & \gamma_2 \end{pmatrix} \tag{4.32}$$

In this case, the eigenvalues for $\omega_1 \approx \omega_2$ become

$$\omega_{+/-}(k'_x) = \frac{1}{2}(\omega_1 + \omega_2) - j\frac{1}{2}(\gamma_1 + \gamma_2) \pm \frac{1}{2}\sqrt{4|\kappa|^2 - (\gamma_1 - \gamma_2)^2} \tag{4.33}$$

It can be seen, that the resulting imaginary parts of $\omega_{+/-}$ are always in between γ_1 and γ_2 and the sensitivity is between the sensitivities S_1 and S_2 of the individual resonators [203].

Remarkably, BICs break this relation as S_λ remains constant and Q_r diverges toward a distinct wavelength λ_{BIC} and incident angle θ_{BIC}. Therefore, BICs theoretically enable infinitely large sensing performance. In reality, Q_r is limited due to the presence of residual scattering, finite sample sizes and light sources deviating from ideal plane waves [156, 296, 297]. Nonetheless, various high performance sensors have been demonstrated using BICs [271, 298–300].

However, this high performance only prevails for BICs in the absence of loss ($Q = Q_r$). For the presented hybrid FW-BICs, the resonance amplitude toward λ_{BIC} and θ_{BIC} approaches zero, so that the maximum achievable performance is given by [249]

$$FoM^* = QS/\lambda \tag{4.34}$$

in the limit $Q_r \to \infty$, which is equal or even smaller than the performance of a conventional resonator or a system of coupled resonators [285]. As visualized in Fig. 4.33a-c, this relation can be deduced by considering that the measured signal arises from the interference of incident plane-waves and back-coupled plane waves from an excited eigenmode (see Chapter 2). Toward the hybrid BIC, the amplitude of the signal vanishes, so that the attributed intensity function $I(n')$ is flattened out. From this point of view, it is of no surprise that no reports on the sensing performance of hybrid FW-BICs existed in 2020 [203].

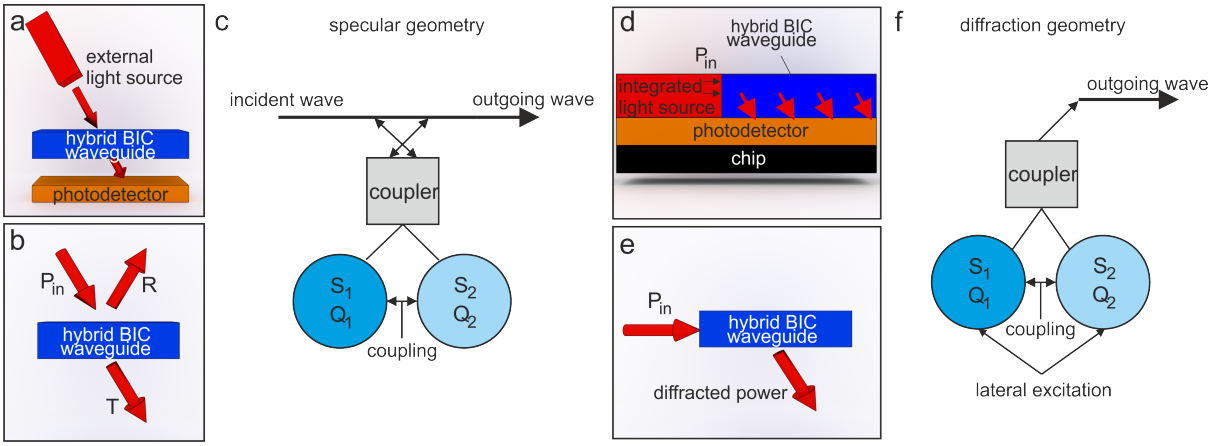

Figure 4.33: a) Sensor setup in specular geometry (S). b) Available detection channels. c) Relation between available detection channels and the resonances of the hybrid waveguide grating. A measured signal is the result of the interference between incoming waves and an excited resonance (see also Chapter 2). d) Sensor setup in diffraction geometry (D). e) The available signals are the intensities attributed to the radiation channels. f) Relation between available detection channels and the resonances of the hybrid waveguide grating. From ref. [203].

The situation is different when no external incidence, but an excited propagating eigenmode under the conditions of a FW-BIC is considered as sketched in Fig. 4.33d-f. Then, the average intensity I of radiated light can be directly derived from Eq. 2.45. This way, the FoM^* is given by [203]

$$FoM^* \approx \frac{1}{\gamma_r}\frac{d\gamma_r}{dn'} \tag{4.35}$$

It is important to note again that the hybrid FW-BIC is located near the avoided crossing of the PH_s and LR-SPP eigenmodes. As visualized in Fig. 4.34, the sensitivity attributed to λ_{BIC} with respect to a change of n is therefore approximately given by the average sensitivity of both eigenmodes, leading to the expression [203]

$$\frac{d\gamma_r}{dn} = \frac{\partial\gamma_r}{\partial(\omega-\omega_{BIC})}\frac{\partial(\omega-\omega_{BIC})}{\partial n'} \approx \frac{\partial\gamma_r}{\partial(\omega-\omega_{BIC})}\frac{1}{2}(S_{\omega_1}+S_{\omega_2}) = \frac{\partial\gamma_r}{\partial(\omega-\omega_{BIC})}\overline{S}_\omega \tag{4.36}$$

with $S_\omega = d\omega_{res}/dn'$. Here, the refractive index of the upper OrmoCore layer is varied. It is empirically found via RCWA calculations, that the first product in the equation can be identified as [203]

$$\frac{1}{\gamma_r}\frac{\partial\gamma_r}{\partial(\omega-\omega_{BIC})} = \frac{Q_r}{\omega}, \tag{4.37}$$

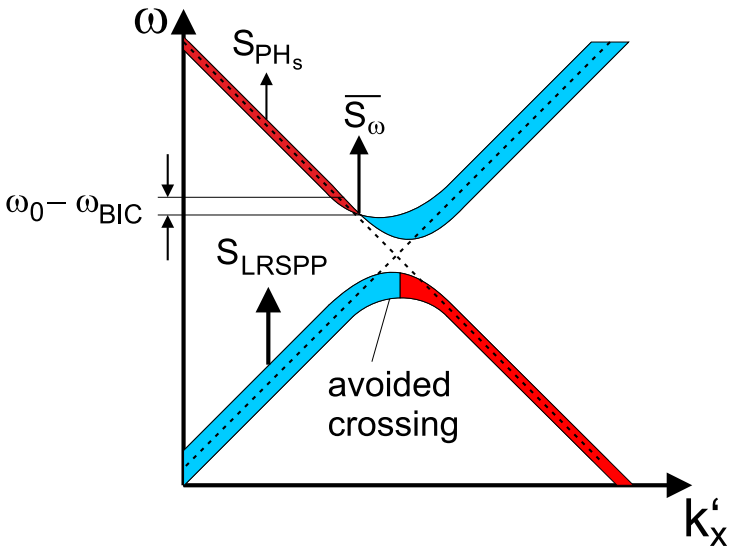

Figure 4.34: Visualization of the sensitivity attributed to a (hybrid) FW-BIC.

so that the entire expression for the FoM^* reads [203]

$$FoM^* = \frac{Q_r}{\omega}\overline{S}_\omega \approx \frac{Q_r}{\lambda}\overline{S}_\lambda \tag{4.38}$$

with $\overline{S}_\lambda = 1/2 \cdot (S_{PH_s} + S_{LRSPP})$. Near the avoided crossing, the values of S_{PH_s} and S_{LRSPP} are 44 nm/RIU and 527 nm/RIU and a value of $\overline{S}_\lambda \approx 285$ nm/RIU is expected. A direct evaluation via RCWA results in $\overline{S}_\lambda \approx 334$ nm/RIU [203].

Fig. 4.35a shows the calculated values of FoM^* via RCWA as a function of λ and θ. Small values of around 1 are present in the absence of resonance. Far away from BIC 1, increased values of the FoM^* are apparent under the excitation of plasmonic ($FoM^* = 2 \cdot 10^2$) and photonic modes ($FoM^* \approx 3 \cdot 10^3$). These values fit well to literature reports of plasmonic and hybrid photonic-plasmonic sensors [285]. Strikingly, toward BIC 1, the FoM^* diverges to infinity as it is typical for BIC based sensors [271, 298–300]. A direct comparison of the calculated FoM^* of a hybrid FW-BIC with a photonic FW-BIC is shown in Fig. 4.35b [203]. Herein, the relative lateral momentum k_{rel} is given by $k_{rel} = k'_x - k_{BIC}$. As predicted, the FoM^* of the hybrid FW-BIC in diffraction geometry (D hybr.) is almost one order of magnitude larger than that of the photonic BIC (D diel.). As a side note, the dashed line shows the FoM^* of the hybrid FW-BIC in specular geometry (S hybr.), which is much smaller as Ohmic losses are present [203].

These results can be understood as follows: for purely photonic eigenmodes, the resulting values of the FoM^* toward a FW-BIC for both the specular geometry and the diffraction geometry are identical. In comparison, the incorporation of plasmonic eigenmodes enhances $\overline{S}_\lambda$ and, thus, the FoM^* by a factor of approximately 8 [203]. As a matter of course, this increase of the sensitivity comes along with Ohmic losses. The consequences

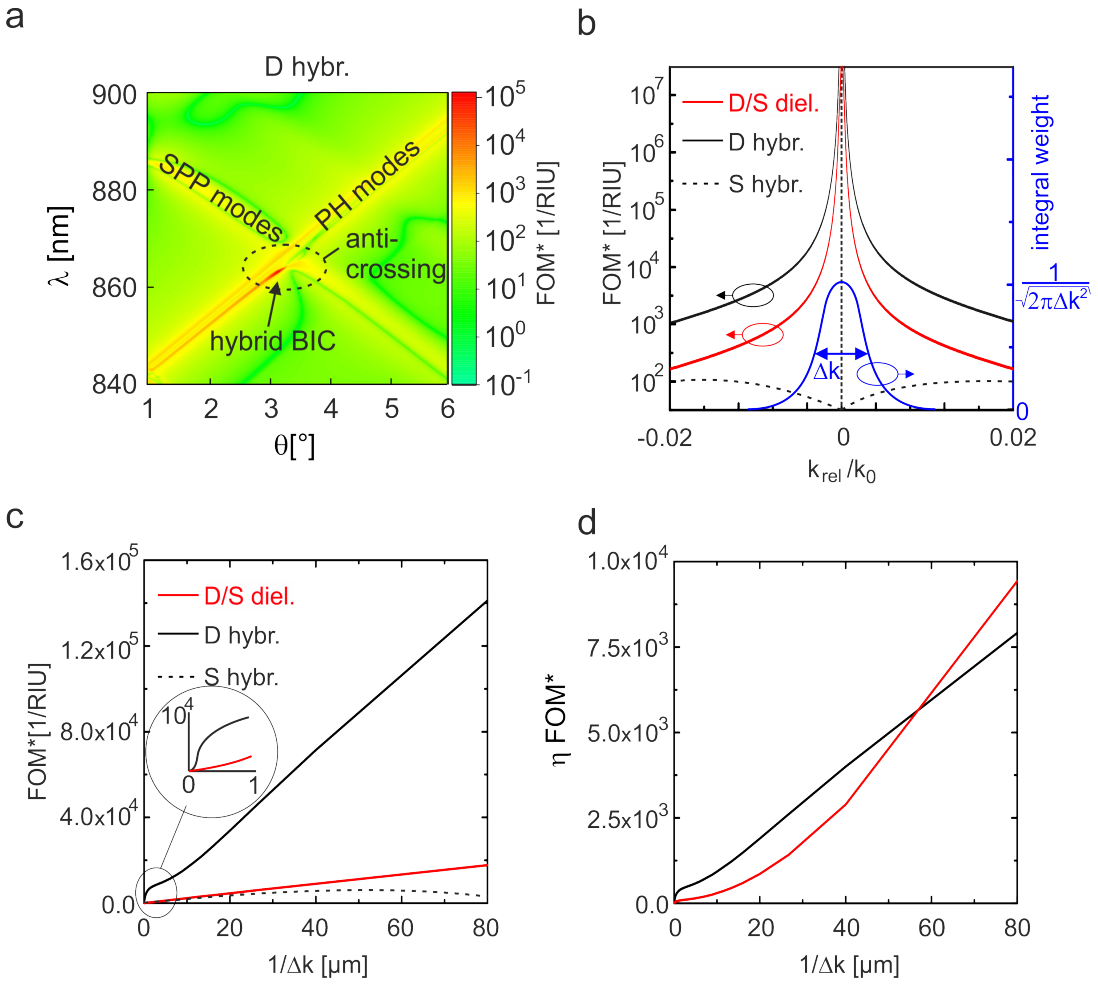

Figure 4.35: a) Simulated values of the FoM^* as a function of λ and θ. Here, θ is the angle under which light is coupled into the substrate and superstrate. b) The FoM^* in the specular geometry (S) and diffraction geometry (D) as a function of $k_{rel} = k'_x - k'_{x,BIC}$. c) Comparison of the FoM^* of BIC 1 and a purely photonic BIC under the assumption of a spread in the k-space $\Delta k'_x$ due to finite beam sizes or finite sample sizes. d) Effective performance $\eta \cdot FoM^*(\Delta k'_x)$ of BIC 1 and a purely dielectric BIC. From ref. [203].

of these Ohmic losses will be discussed later on.

These calculated values of the FoM^* do not yet deliver useful insights on the sensing performance of the waveguide grating under real conditions such as finite sample sizes and beams of finite widths and non-zero divergence angles. To give an estimate for these conditions, the FoM^* is calculated using an averaged intensity obtained over a weighted integral [203]

$$\overline{I}(\Delta k) = \int_{-\infty}^{\infty} G(k_{rel}, \Delta k) I(k_{rel}) \mathrm{d}k_{rel} \tag{4.39}$$

with the weight function [203]

$$G(k_{rel}, \Delta k) = \frac{1}{\sqrt{2\pi\Delta k^2}} e^{-\frac{(k_{rel})^2}{2\Delta k^2}} \tag{4.40}$$

and Δk as the spread of lateral momentum.

The resulting values of $FoM^*(\Delta k)$ are plotted against $1/\Delta k$ in Fig. 4.35c. For small values of $1/\Delta k$ (large values of Δk), the values of $FoM^*(\Delta k)$ tend to zero as only a small portion of the light is modulated by the dynamics of the BIC. Toward larger values of $1/\Delta k$, the values of $FoM^*(\Delta k)$ attributed to the hybrid FW-BIC are consistently larger than these for the photonic BIC [203]. These results show that hybrid FW-BICs are a potential platform for high performance light sensors and modulators. Nonetheless, there are limitations to this concept. As Ohmic losses are present in the waveguide grating, the outcoupling efficiency is limited. To take this efficiency into account, an effective performance $\eta \cdot FoM^*(\Delta k)$ is considered (see Fig. 4.35d). It gives an estimate for a device performance when power consumption is a critical parameter (e.g. for mobile devices). With respect to this effective performance, hybrid FW-BICs are advantageous over photonic BICs below a distinct value of $1/\Delta k$. Here, this value is around 56 μm. In other words, for large sensors, the increase of the FoM^* via the introduction of surface plasmons is paid by a significantly smaller efficiency due to the Ohmic losses [203].

4.4 Short summary

The plasmonic systems presented in Section 4.1, they enable strong broadband interaction with light and are promising for solarthermics well as for the fabrication of high-performance sensors and k-space engineered plasmonic metasurfaces. As a drawback, all of these plasmonic systems suffer from the intrinsic Ohmic losses of metals, which would significantly decrease the efficiency of solar concentrators based on plasmonics.

In Section 4.2, symmetric waveguide gratings supporting long propagation ranges over broad spectral ranges have been demonstrated. In the regime of single eigenmodes, these symmetric waveguide gratings show numerous advantages compared to conventional asymmetric waveguide gratings and could be utilized for highly parallel light sources and sensors. However, to realize solar concentrators with such passive symmetric waveguide gratings, many thousand of them would have to be stacked to capture the opening angle of the Sun. To enable dynamic tracking, even more symmetric waveguide gratings would have to be stacked to enable mode excitation from any angle under any wavelength. Importantly, once light is concentrated into the eigenmodes of a waveguide grating, the subsequent outcoupling cannot be prevented.

Concerning hybrid waveguide gratings, a way to completely cancel outcoupling via hybrid FW-BICs has been experimentally demonstrated. However, the singular nature of BICs means that an outcoupling efficiency of zero can only be achieved for one singular wavelength and outcoupling angle.

In conclusion, all these passive systems show numerous advantages for solar concentrators. However, they do not allow to realize Sun-tracking in an obvious way. In fact, the direction and propagation length of light in a waveguide based solar concentrator needs to be actively switchable on a local level. This task can also be understood as the local active control of outcoupling.

In the following chapter, an active waveguide grating will be presented which enables the local control of outcoupling between zero and, theoretically, 100%.

Chapter 5

Active waveguide systems: Broadband Electrically Controlled Light Trapping

In this chapter, a method to locally control the outcoupling of light inside a waveguide grating will be presented. The core idea of this method can be derived by reconsidering all of the properties of the waveguide gratings from Chapter 4 at the most fundamental level: the maximized propagation lengths for the node eigenmodes in symmetric waveguide gratings are a result of destructive interference at the center plane of the grating. In a similar way, the complete cancellation of outcoupling for hybrid FW-BICs originates from the destructive interference of eigenmodes emitting radiation into the same radiation channels. The reason why this complete cancellation of outcoupling can be reached is that the amplitudes and phases of the eigenmodes can be *parametrically tuned* along their dispersion relations [277,279]. This parametric tuning can be understood as the control of an internal degree of freedom and the actuating variable is λ. This point of view explains why a BIC is of singular nature with respect to λ, whereby it is also singular with respect to θ as a result of dispersion [272]. To obtain broadband cancellation of outcoupling, the actuating variable has to be changed, so that it is independent of λ. One way to realize such change of the actuating variable is provided in the following lines [301, 302].

Consider a thick waveguide which supports a quasi-continuum of eigenmodes ($t_{WG} >> \lambda$). Let's suppose that two beams may propagate inside this waveguide in a zig-zag pattern (Fig. 5.1a). By some physical process, the relative phase $2\Delta\Phi$ between both beams may be adjustable from $0...2\pi$. Now, a thin geometry is placed at the exact center of this waveguide, which is capable of scattering the beams into the substrate and superstrate regions. Using the coupling coefficients $C_{s,1}$ and $C_{s,2}$ of the coupling matrix $\underline{C}$, the electric field vectors $\vec{E}_1$ and $\vec{E}_2$ and wave-vectors $\vec{k}_1$ and $\vec{k}_2$ attributed to the two beams, the intensity I attributed to a scattered plane-wave (indexed by 's') is then given by

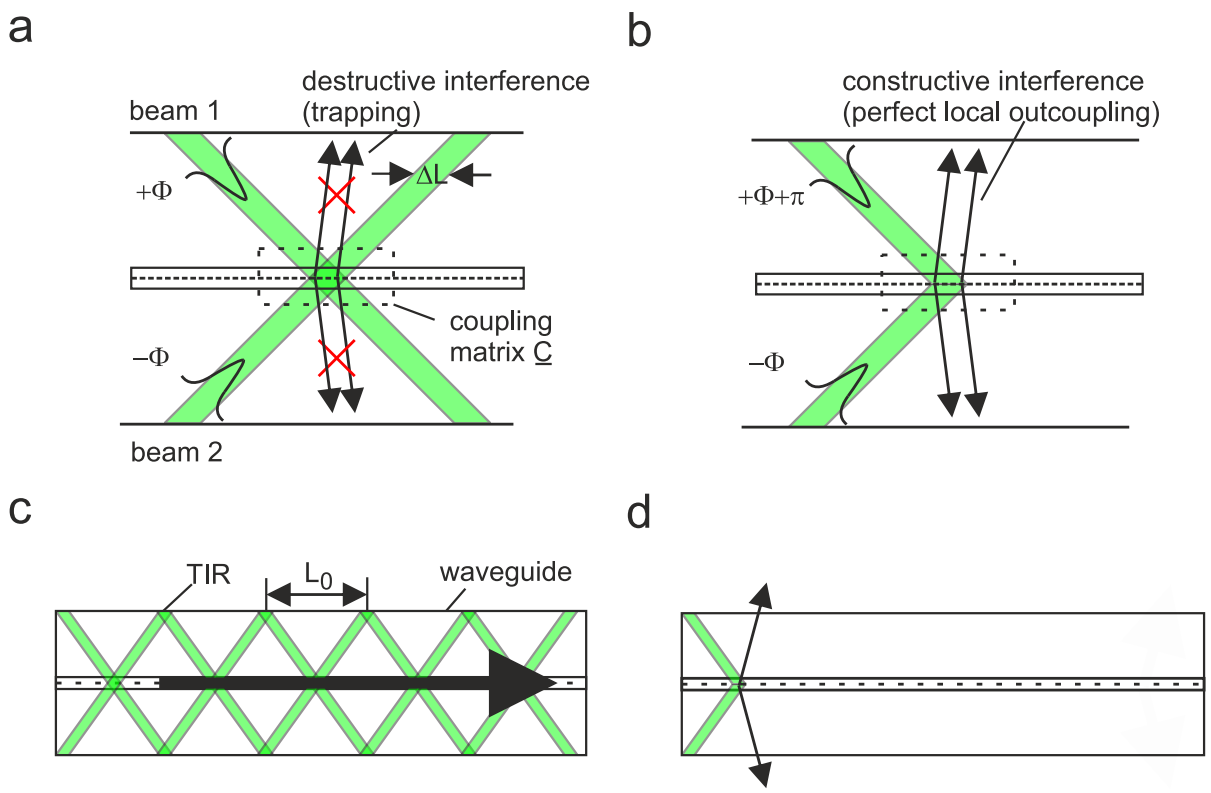

Figure 5.1: Concept of a waveguide with a locally controllable outcoupling efficiency. a) For a distinct relative phase $\Phi - (-\Phi) = 2\Delta\Phi$ between beams, the local outcoupling efficiency becomes zero ('trapping'). b) For another value of the relative phase (e.g. $2\Delta\Phi + \pi$), the local outcoupling efficiency becomes 100% ('perfect local outcoupling'). c) Trapped beams propagate undisturbed as for a homogeneous planar waveguide. d) Under perfect local outcoupling , the beams are immediately redirected into 'local radiation channels' once they hit the thin geometry. According to ref. [301].

$$I \propto |C_{s,1}(\vec{E}_1, \vec{E}_s, \vec{k}_1, \vec{k}_s) \cdot \vec{E}_1 \cdot e^{2j\Delta\Phi} + C_{s,2}(\vec{E}_2, \vec{E}_s, \vec{k}_2, \vec{k}_s) \cdot \vec{E}_2|^2. \tag{5.1}$$

As visualized in Figs. 5.1a and b, the outcoupling efficiency can be locally completely suppressed (or maximized), when the scattered waves are of equal amplitude and the relative phase $2\Delta\Phi$ is chosen in a way that they interfere destructively or constructively (Fig. 5.1b). The relative phase $2\Delta\Phi$ is thus the new actuating variable. Importantly, there is difference to the definition of the outcoupling efficiency from Chapter 2: Here, it is aimed to measure the fraction of the power of the two beams, which is locally coupled out of the waveguide. For this reason, a measure termed 'local outcoupling efficiency' must be introduced. Such a new definition is necessary as any loss-less, infinitely extended waveguide geometry, which exhibits non-zero outcoupling, is automatically of 100% outcoupling efficiency. It is hence obvious that the outcoupling efficiency is not a useful measure to describe phenomena on a local level. The local outcoupling efficiency will be mathematically further elaborated in the next section.

For now, it is sufficient to know that a local outcoupling efficiency of 0% means that the two beams propagate undisturbed in the waveguide (Fig. 5.1c). On the contrary, a local outcoupling efficiency of 100% means that the two beams are locally coupled out of the waveguide and no power remains within the waveguide (Fig. 5.1d). Herein, a local outcoupling efficiency of 0% is referred to as 'trapping'. Beams which propagate under trapping are termed as 'trapped beams'. Any process which sets the beams into a condition of trapping is termed as 'the trapping of beams'. In return, a local outcoupling efficiency of 100% is referred to as 'perfect local coupling'. It is anticipated that, in reality, the local outcoupling efficiency can only be maximized up to a distinct value which depends on the geometry parameters and parameters of the two beams. Such a maximum of the local outcoupling efficiency below 100% is termed 'maximized local outcoupling'. It is further anticipated that a switching between trapping and perfect local outcoupling can be done at any position where the two beams cross the thin geometry. In addition, it is important to note that this procedure can only be applied as long as both beams do not interfere with themselves. This is termed as the 'absence of self-interference'. Absence of self-interference is present when the lateral distance L_0 between the beams is larger than their lateral extent ΔL (see Figs. 5.1a and c).

Until 2022, except for ref. [301] and ref. [302], no such scheme has been reported in the literature yet: concerning the control of the coupling efficiency to radiation channels or to absorption via two beams and a relative phase, there are only reports using free-space beams (without a waveguide) [303–312]. Concerning the guidance or local control of light, integrated photonics [313–318], micro-electro-mechanical systems (MEMS) [319–321], controllable photonic structures [322,323], liquid crystals [324–327] and modulators based on surface-acoustic-waves (SAW) [328] are the current state-of-the-art.

In the following sections, the proposed scheme will be concretely applied to waveguide gratings in theory. Subsequently, these theoretical results will be compared with experimental data and their consequences will be discussed with respect to this state-of-the-art as well as to solar applications.

5.1 Theory of Light Trapping and Perfect Local Outcoupling

For waveguide gratings, the general expression in Eq. 5.1 can be specified. As outlined in Chapter 2, the two beams inside the thick waveguides can be expressed by a plane-wave spectrum. It is assumed that the thin geometry in the center of the waveguide contains one or multiple gratings of period Λ and can be described by RCWA ($\varepsilon(x) = \varepsilon(x + \Lambda)$).

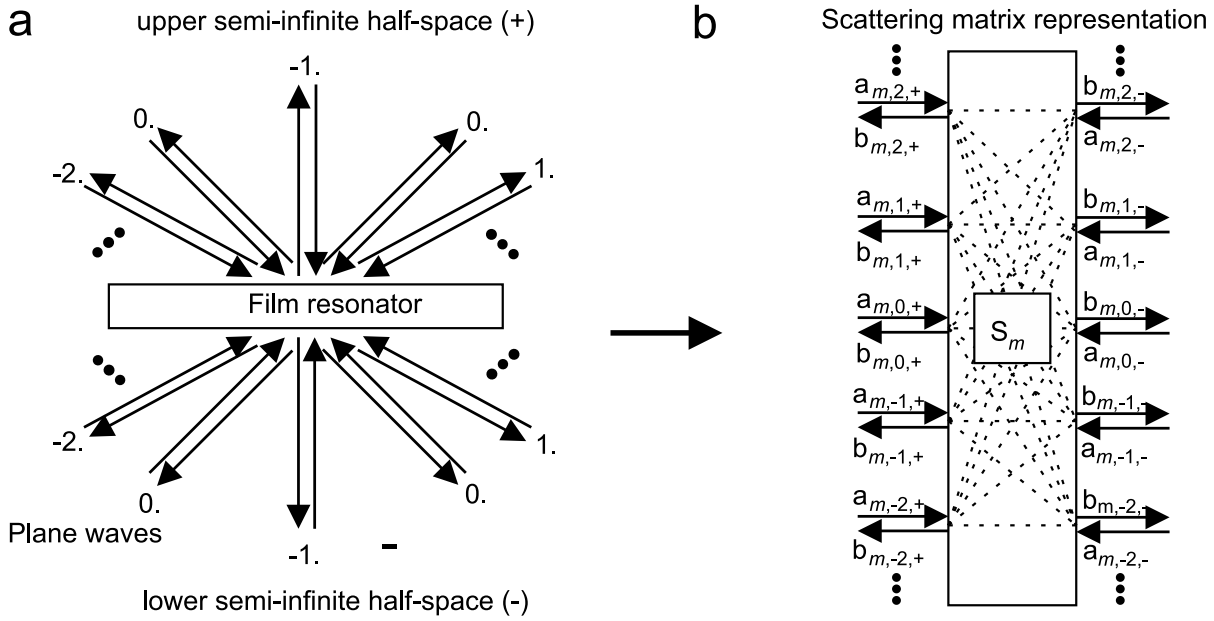

Figure 5.2: a) Plane wave channels of the two beams falling onto and exiting the film resonator. b) Scattering matrix representation of the film resonator under the assumption of semi-infinite half-spaces above and below it. According to ref. [301].

In the following, the thin geometry is termed 'film resonator'. The two beams are further assumed to be mirror symmetric with respect to the center plane of the thick waveguide. This way, every plane-wave component of a beam has a mirrored plane-wave component in the other beam and the response of the film resonator can be fully described by the superposition of the electric and magnetic fields resulting from two incident plane-waves (see Eq. 5.1 and Fig. 5.2a).

As the lateral extent ΔL of the two beams is smaller than the projected lateral path length L_0, there is no self-interference outside the film resonator, so that an RCWA model of the film resonator can be applied under the assumption of an infinitely large waveguide thickness (semi-infinite half-spaces). For each of the two incident plane waves, there exists a set of coupling coefficients to outgoing plane-waves leaving the film resonator into these half-spaces (Fig. 5.2a). As both beams are of the same lateral momentum $k'_{x,0}$, the lateral momenta $k'_{x,\nu}$ of the outgoing plane-waves are pair-wise identical and the electric and magnetic fields of these outgoing plane waves are two-wave superpositions. These two-wave superpositions can be represented by a matrix formalism for which the former notation of the coupling coefficients is modified for reasons of simplicity. This matrix formalism together with its notation is visualized in Fig. 5.2b.

Plane waves which come from and leave into the upper/lower semi-infinite half-space are assigned to a $+/-$ symbol, respectively. The diffraction order is symbolized by 'ν'. The positions at which the two beams interact with the film resonator are termed as 'dots' and counted with an index $m = 1, 2, 3, ...$ To give a few examples, the reflection coefficient of

a plane-wave coming from the upper semi-infinite space is noted as $r_{m,0,+,+}$. The coupling coefficient of a plane wave coming from the upper semi-infinite space and leaving into the first diffraction order in the lower semi-infinite space is noted as $d_{m,0,1,+,-}$. Some more variations to show the notation of the coupling coefficients are shown in Fig. 5.3. In contrast to the definition of the radiation channels in Chapter 2, this indexing signifies that each dot m exhibits both the 0^{th} order for plane-waves, which are guided in the waveguide, and other diffraction orders which form a set of 'local radiation channels'. The meaning of these local radiation channels will become clear over the course of the upcoming explanations.

To obtain the possibility to set boundary conditions and calculate the progression of the plane-wave amplitudes during propagation, the input and output amplitudes $\vec{a}_m$ and $\vec{b}_m$ of each dot are expressed by the equation system

$$\vec{b}_m = \begin{pmatrix} \vec{b}_{m,-N} \\ \vdots \\ \vec{b}_{m,-1} \\ \vec{b}_{m,0} \\ \vec{b}_{m,1} \\ \vdots \\ \vec{b}_{m,N} \end{pmatrix}, \quad \vec{a}_m = \begin{pmatrix} \vec{a}_{m,-N} \\ \vdots \\ \vec{a}_{m,-1} \\ \vec{a}_{m,0} \\ \vec{a}_{m,1} \\ \vdots \\ \vec{a}_{m,N} \end{pmatrix}, \quad \vec{b}_m = \underline{S}_m \vec{a}_m \tag{5.2}$$

with

$$\underline{S}_m = \begin{pmatrix} \underline{R}_{m,-N} & \underline{D}_{m,-N,-N+1} & \cdots & \cdots & \cdots & \underline{D}_{m,-N,N-1} & \underline{D}_{m,-N,N} \\ \underline{D}_{m,-N+1,-N} & \ddots & \vdots & \vdots & \vdots & \iddots & \underline{D}_{m,-N+1,N} \\ \vdots & \cdots & \underline{R}_{m,-1} & \underline{D}_{m,-1,0} & \underline{D}_{m,-1,1} & \cdots & \vdots \\ \vdots & \cdots & \underline{D}_{m,0,-1} & \underline{R}_{m,0} & \underline{D}_{m,0,1} & \cdots & \vdots \\ \vdots & \cdots & \underline{D}_{m,1,-1} & \underline{D}_{m,1,0} & \underline{R}_{m,1} & \cdots & \vdots \\ \underline{D}_{m,N-1,-N} & \iddots & \vdots & \vdots & \vdots & \ddots & \underline{D}_{m,N-1,N} \\ \underline{D}_{m,N,-N} & \underline{D}_{m,N,-N+1} & \cdots & \cdots & \cdots & \underline{D}_{m,N,N-1} & \underline{R}_{m,N} \end{pmatrix} \tag{5.3}$$

Each element of $\vec{b}_m$ and $\vec{a}_m$ is given by

$$\vec{b}_{m,\nu} = \begin{pmatrix} b_{m,\nu,+} \\ b_{m,\nu,-} \end{pmatrix} \tag{5.4}$$

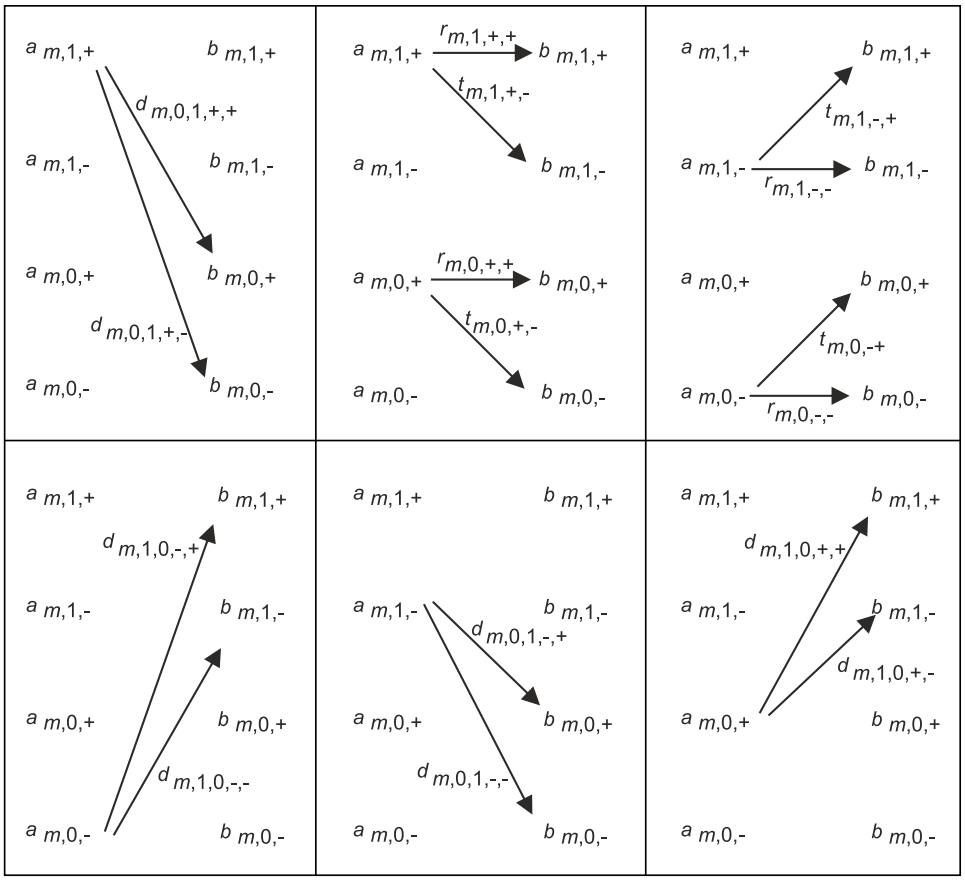

Figure 5.3: Notation of the elements of S_m.

$$\vec{a}_{m,\nu} = \begin{pmatrix} a_{m,\nu,+} \\ a_{m,\nu,-} \end{pmatrix} \tag{5.5}$$

The elements of $\underline{S}_m$ contain all coupling coefficients and read

$$\underline{R}_{m,\nu} = \begin{pmatrix} r_{m,\nu,+,+} & t_{m,\nu,-,+} \\ t_{m,\nu,+,-} & r_{m,\nu,-,-} \end{pmatrix} \tag{5.6}$$

$$\underline{D}_{m,\nu,j} = \begin{pmatrix} d_{m,\nu,j,+,+} & d_{m,\nu,j,-,+} \\ d_{m,\nu,j,+,-} & d_{m,\nu,j,-,-} \end{pmatrix} \tag{5.7}$$

Note that the geometric correction factors in Eq. 2.71 are already included in the coupling coefficients of the matrix $\underline{S}_m$, so that it is unitary in the absence of loss

$$\underline{S}^H \underline{S} = \mathbb{1} \tag{5.8}$$

As the two beams are reflected at the waveguide's outer interfaces, the output and input amplitudes of two dots can be connected via the expression

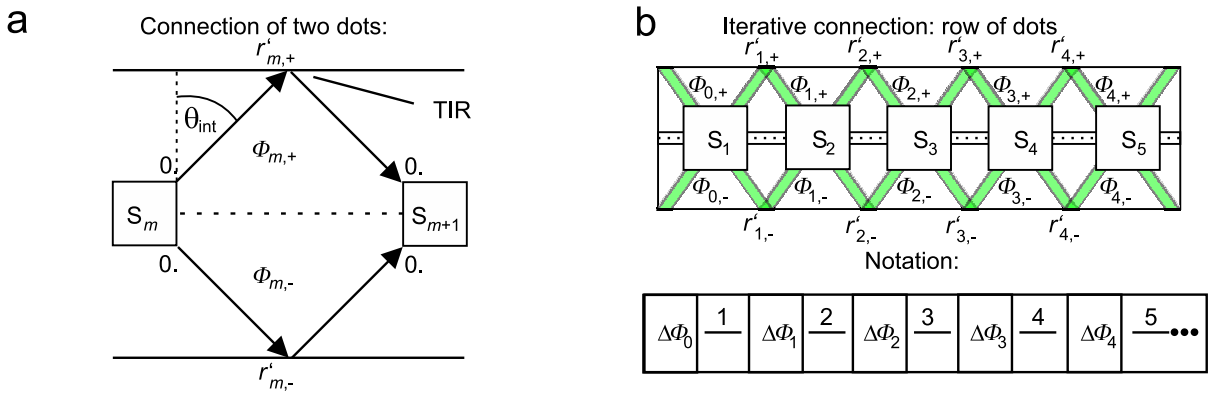

Figure 5.4: Visualization of the connection of dots via Eq. 5.9. According to ref. [301].

$$\vec{a}_{m+1,0} = \begin{pmatrix} r'_{m,+}e^{j\Phi_{m,+}} & 0 \\ 0 & r'_{m,-}e^{j\Phi_{m,-}} \end{pmatrix} \vec{b}_{m,0} = \underline{T}_m \vec{b}_{m,0} \tag{5.9}$$

This relation is visualized in Fig. 5.4. Herein, a change of the relative phase at an $(m+1)^{\text{th}}$ dot is defined via

$$2\Delta\Phi_m = \Phi_{m,+} - \Phi_{m,-} \tag{5.10}$$

As a first boundary condition, it is assumed that only waves from the 0^{th} diffraction order fall onto each dot

$$\vec{a}_{m,\nu} = \begin{pmatrix} 0 \\ 0 \end{pmatrix} \forall \ \nu \neq 0 \tag{5.11}$$

Therefore, Eq. 5.9 simplifies to

$$\vec{a}_{m+1,0} = \underline{T}_m \vec{b}_{m,0} = \underline{T}_m \underline{R}_{m,0} \vec{a}_{m,0} \tag{5.12}$$

The second boundary condition is the definition of input amplitudes at $m = 1$ and reads

$$\vec{a}_{1,0} = \begin{pmatrix} E_+ e^{j\Phi_{0,+}} \\ E_- e^{j\Phi_{0,-}} \end{pmatrix} \tag{5.13}$$

with the normalization

$$|\vec{a}_{1,0}|^2 = 1 \tag{5.14}$$

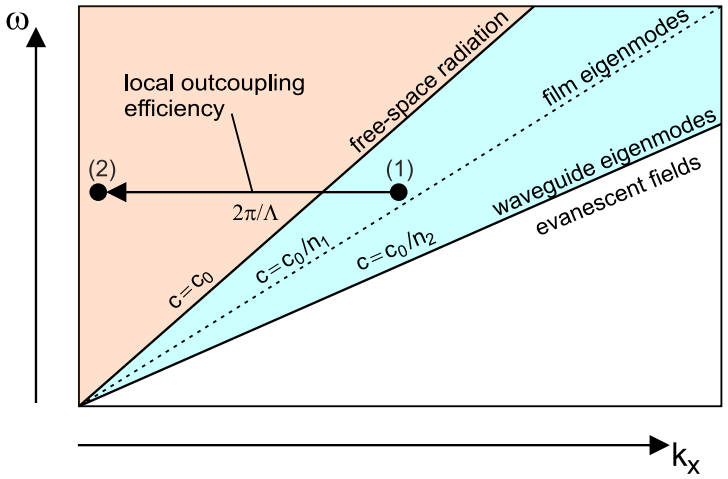

Figure 5.5: Frequency-momentum space visualizing trapping and perfect local outcoupling for one dot. The environment of the waveguide grating is assumed as air. The average refractive index of the film resonator is n_1. The refractive index of the remaining waveguide is n_2. It is assumed that $1 < n_1 < n_2$ is true. Under trapping (1), the two beams occupy a state below the light line. For perfect local outcoupling (2), the two beams occupy a state above the light line. For a local outcoupling efficiency between 0% and 100%, both states are present: one part of the input power is coupled into local radiation channels (2) and the other part remains in the waveguide grating (1).

and E_+, E_- as real-valued input amplitudes. The angle θ_{int} is assumed to be large enough to ensure total internal reflection ($|r_{m,+}| = |r_{m,-}| = 1$). Then, all waves are trapped inside the waveguide when

$$\vec{b}_{m,\nu} = \begin{pmatrix} 0 \\ 0 \end{pmatrix} \forall \ \nu \neq 0 \tag{5.15}$$

is true for all m. With the boundary conditions assumed above, Eq. 5.15 thus describes trapping. Viewed in the frequency-momentum space (see Fig. 5.5), trapping can be regarded as a bound continuum which is decoupled from the radiation continuum (the black dot labeled by (1)). Herein, the two trapped beams form the bound continuum. In this graph, the local radiation channels of one dot are symbolically represent by the -1^{st} diffraction order marked by (2). From this point of view, it can be seen that trapping is different to a BIC in a waveguide grating. This difference between trapping and BICs a direct consequence of the absence of self-interference. Again, a BIC of a given geometry is singular with respect to λ and θ. In contrast, trapping can be found for any specific set of input parameters, coupling coefficients and phases $\Phi_{m,+}, \Phi_{m,-}$. Here, only the coupling coefficients are fixed and the remaining parameters are variable, so that there is no direct restriction of the values of λ and θ for which trapping can occur.

In the following the conditions for trapping will be further elaborated by considering

a film resonator which exhibits translationally invariant coupling coefficients along the x-direction. The translational invariance can be expressed by $\underline{R}_{m+1,i} = \underline{R}_{m,i} = \underline{R}_i$, $\underline{D}_{m+1,\nu,j} = \underline{D}_{m,\nu,j} = \underline{D}_{\nu,j}$, and $\underline{T}_{m+1} = \underline{T}_m = \underline{T}$, whereby $\underline{R}_\nu$, $\underline{D}_{\nu,j}$, and $\underline{T}$ are given by

$$\underline{R}_\nu = \begin{pmatrix} r_{\nu,+,+} & t_{\nu,-,+} \\ t_{\nu,+,-} & r_{\nu,-,-} \end{pmatrix} \tag{5.16}$$

$$\underline{D}_{\nu,j} = \begin{pmatrix} d_{\nu,j,+,+} & d_{\nu,j,-,+} \\ d_{\nu,j,+,-} & d_{\nu,j,-,-} \end{pmatrix} \tag{5.17}$$

$$\underline{T} = \begin{pmatrix} r'_+ e^{j\Phi_+} & 0 \\ 0 & r'_- e^{j\Phi_-} \end{pmatrix} \tag{5.18}$$

Under these assumptions, trapping is present when the condition implied by Eq. 5.15 and

$$\vec{a}_{m+1,0} = \underline{T}\vec{b}_{1,0} = \underline{T}\underline{R_0}\vec{a}_{m,0} = c\vec{a}_{m,0} \tag{5.19}$$

are fulfilled. These conditions can be understood as follows. $|b_{m,\nu,+}|^2$ and $|b_{m,\nu,-}|^2$ are a measure for the local coupling efficiency per local radiation channel (except for $\nu = 0$). As an example, a value of $|b_{1,-1,+}|^2 = |\vec{a}_{1,0}|^2$ means that the plane waves incident on the first dot are coupled to the local radiation channel defined by the -1^{st} diffraction order in the superstrate with 100% local outcoupling efficiency.

When the local outcoupling efficiency at the first dot is zero under distinct input parameters, and the same input parameters are reproduced for the next dot, then the local outcoupling efficiency is zero for all dots. Thereby, c is a complex number representing any amplitude and phase changes, which do not change the phase and amplitude relation between the input parameters. For instance, lossy and loss-free systems are characterized by $|c| < 1$ and $|c| = 1$, respectively. This form of $\underline{T}$ is obviously the case as the entire waveguide grating is assumed to be mirror symmetric.

By using an Euler representation of the coupling coefficients ($x = |x|e^{j\Phi_x}$), and explicitly inserting these conditions in Eq. 5.2

$$\vec{b}_{1,0} = \underline{R}_0\vec{a}_{1,0} = \begin{pmatrix} r_{0,+,+} \cdot E_+ e^{j\Phi_{0,+}} + t_{0,-,+} \cdot E_- e^{j\Phi_{0,-}} \\ t_{0,+,-} \cdot E_+ e^{j\Phi_{0,+}} + r_{0,-,-} \cdot E_- e^{j\Phi_{0,-}} \end{pmatrix} \tag{5.20}$$

$$\vec{b}_{1,\nu} = \underline{D}_{\nu,0}\vec{a}_{1,0} = \begin{pmatrix} d_{\nu,0,+,+} \cdot E_+ e^{j\Phi_{0,+}} + d_{\nu,0,-,+} \cdot E_- e^{j\Phi_{0,-}} \\ d_{\nu,0,+,-} \cdot E_+ e^{j\Phi_{0,+}} + d_{\nu,0,-,-} \cdot E_- e^{j\Phi_{0,-}} \end{pmatrix}, \tag{5.21}$$

it can be shown that the local outcoupling efficiency at the first dot can be zero for the amplitude relation

$$|d_{\nu,0,+,+}||d_{\nu,0,-,-}| = |d_{\nu,0,-,+}||d_{\nu,0,+,-}| \tag{5.22}$$

and the phase relations

$$2\Delta\Phi_0 + \Delta\Phi_{d_+} = \pi(2n+1) \tag{5.23}$$

$$2\Delta\Phi_0 + \Delta\Phi_{d_-} = \pi(2n+1) \tag{5.24}$$

with

$$\Delta\Phi_{d_+} = \Phi_{d_{\nu,0,+,+}} - \Phi_{d_{\nu,0,-,+}} \tag{5.25}$$

$$\Delta\Phi_{d_-} = \Phi_{d_{\nu,0,+,-}} - \Phi_{d_{\nu,0,-,-}} \tag{5.26}$$

General solutions of Eq. 5.19 can be derived with numerical methods. Here, to provide analytically describable physical properties attributed to trapping, a mirror symmetric film resonator with respect to the z-direction and equal input amplitudes

$$E_+ = E_- = \frac{1}{\sqrt{2}} \tag{5.27}$$

is considered. Due to this mirror symmetry, the coupling coefficients read

$$|d_{\nu,0,-,+}| = |d_{\nu,0,+,-}| = |d_{\nu,0,t}| \tag{5.28}$$

$$|d_{\nu,0,+,+}| = |d_{\nu,0,-,-}| = |d_{\nu,0,r}| \tag{5.29}$$

$$|r_{0,+,+}| = |d_{0,-,-}| = |r_0| \tag{5.30}$$

$$|t_{0,+,-}| = |t_{0,-,+}| = |t_0| \tag{5.31}$$

The amplitude relations in Eq. 5.22 therefore simplify to

$$|d_{\nu,0,t}|^2 = |d_{\nu,0,r}|^2 \Leftrightarrow d_{\nu,0,t} = \pm d_{\nu,0,r} = \pm d_\nu \tag{5.32}$$

The conditions on the phase relations for zero local outcoupling efficiency at the first dot are then solved for exactly two cases

- Solution 1: $d_{\nu,0,t} = -d_{\nu,0,r}$, $2\Delta\Phi_0 = 2n\pi$

- Solution 2: $d_{\nu,0,t} = d_{\nu,0,r}$, $2\Delta\Phi_0 = (2n+1)\pi$

with $n \in \mathbb{N}$.

The output amplitudes in the 0^{th} diffraction order (Eq. 5.20) can be rewritten to

$$b_{1,0,+} = \frac{1}{\sqrt{2}} e^{j(\Phi_{0,+}+\Phi_{r_0})} \left[|r_0| + |t_0| e^{j(-2\Delta\Phi_0+\Phi_{t_0}-\Phi_{r_0})} \right] \tag{5.33}$$

$$b_{1,0,-} = \frac{1}{\sqrt{2}} e^{j(\Phi_{0,+}+\Phi_{r_0})} \left[|t_0| e^{j(\Phi_{t_0}-\Phi_{r_0})} + |r_0| e^{2j\Delta\Phi_0} \right] \tag{5.34}$$

Inserting these solutions into Eq. 5.20 leads to

- 1) $b_{1,0,+} = b_{1,0,-}$ for Solution 1.
- 2) $b_{1,0,+} = -b_{1,0,-}$ for Solution 2.

Therefore, the amplitude and phase relation between the input amplitudes of the subsequent dot are identical to those of the first dot. As Eq. 5.19 is true, Solutions 1 and 2 thus represent trapping. In the absence of loss, it can be shown that

$$|b_{1,0,+}|^2 + |b_{1,0,-}|^2 = 1 \tag{5.35}$$

and the entire power is indeed guided within the waveguide with zero local outcoupling efficiency for each dot. Consequently, the outcoupling efficiency for the entire waveguide grating is zero as well. This finding can be interpreted as follows: once the beams are trapped (Solution 1 or 2), they remain trapped for the subsequent dots.

There is another benefit which comes along with $2\Delta\Phi_0$ as a degree of freedom. For

- $d_{\nu,0,t} = -d_{\nu,0,r}$, $2\Delta\Phi_0 = (2n+1)\pi$
- $d_{\nu,0,t} = d_{\nu,0,r}$, $2\Delta\Phi_0 = 2n\pi$

with $n \in \mathbb{N}$, the local outcoupling efficiency is maximized and leads to the expressions

$$|b_{1,0,+}|^2 + |b_{1,0,-}|^2 = 1 - 4\sum_{\nu} |d_\nu|^2 \tag{5.36}$$

$$|b_{1,i,+}|^2 + |b_{1,i,-}|^2 = 4\sum_{\nu} |d_\nu|^2. \tag{5.37}$$

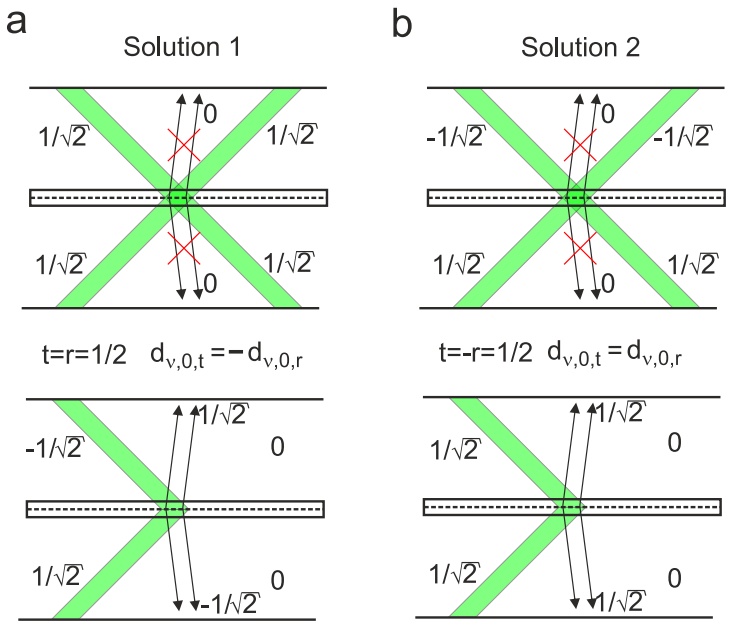

Figure 5.6: Examples of trapping and perfect local outcoupling for a hypothetical mirror symmetric waveguide grating with an ideal scattering matrix. For simplicity, the four black arrows in each subfigure represent the local radiation channels attributed to all diffraction orders. a) Solution 1 with $d_{\nu,0,t} = -d_{\nu,0,r}$ and $t = r = 1/2$. b) Solution 2 with $d_{\nu,0,t} = d_{\nu,0,r}$ and $t = -r = 1/2$.

For $|t_0| = |r_0| = 1/2$ and the absence of loss, these equations become

$$|b_{1,0,+}|^2 + |b_{1,0,-}|^2 = 0 \tag{5.38}$$

$$\sum_{\nu} (|b_{1,\nu,+}|^2 + |b_{1,\nu,-}|^2) = 1 \tag{5.39}$$

and the entire power is coupled to local radiation channels. This behavior displays perfect local outcoupling. Both the occurrence of trapping and perfect local outcoupling mean that the control of $2\Delta\Phi_0$ enables to continuously control the local outcoupling efficiency between 0% and 100% of the power incident on a dot (see Fig. 5.6).

It is important to note, that once trapping is established, any local relative phase shift $2\Delta\Phi_m \neq 0$ would lead to an increase of the local outcoupling efficiency of subsequent dots. This circumstance will be elaborated later on.

As a matter of course, all these considerations above have been done with a series of assumptions, which question whether they are of any practical meaning. In the next Section, concrete and realistic waveguide gratings will be presented which demonstrate the validity of these considerations.

5.2 Exemplary Calculation of a Symmetric Waveguide

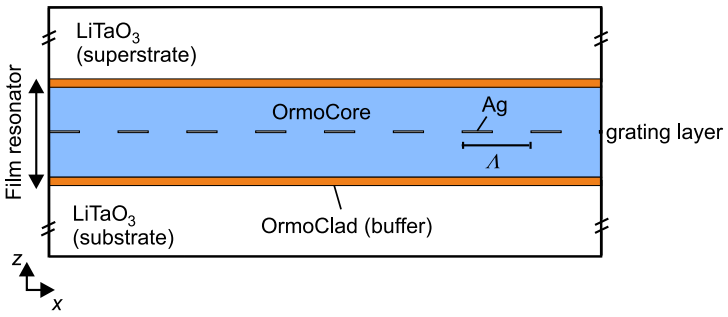

Figure 5.7: Visualization of a mirror symmetric waveguide grating. See the text for further details. From ref. [301].

In this section, the concepts explained in Section 5.1 will be applied to an exemplary waveguide grating. This waveguide grating is visualized in Fig. 5.7. Its outer layers consist of two 500 μm thick lithium tantalate ($LiTaO_3$) layers. Hereby, the c-axises of these layers are of opposite directions with respect to each other. Both c-axises are parallel to the z-direction. This way, the Pockels effect can be used to cause a relative phase shift. This procedure will be elaborated later on and, for the next sections, the phases $2\Delta\Phi_m$ are not yet linked to any physical phenomena to keep the following discussion as general as possible. The film resonator is placed in between the $LiTaO_3$ layers. It consists of two thin cladding layers of OrmoClad with a thickness of 70 nm, two OrmoCore layers with a thickness of 1900 nm, and a rectangular silver-OrmoCore grating of 30 nm thickness, a duty cycle of $D = 0.35$, and period of $\Lambda = 555$ nm. In the linear regime (excluding the Pockels effect), it is thus mirror symmetric with respect to the z-direction. TE polarized light is considered.

First, the response to plane-waves will be investigated. Later on, the response to Gaussian beams will be composed via their plane-wave spectra.

At first, a fixed wavelength of $\lambda = 632.8$ nm is considered. θ_{int} is varied between 42.0° and 43.5° and all the locii of t_0, r_0, $d_{-1,0,r}$ and $d_{-1,0,t}$ are plotted in the complex plane (see Fig. 5.8a). Following the explanations from Section 5.1, it is sought to find a value of θ_{int} for which $d_{-1,0,r} = d_{-1,0,t}$ and $|t_0| = |r_0| = 0.5$ are fulfilled. Concerning the former condition, $d_{-1,0,r}$ and $d_{-1,0,t}$ are almost equal for all values of θ_{int}. At $\theta_{int} = 43.0°$, it can be indeed observed the absolute values of t and r both become 0.5. This is no coincidence, as the film resonator exhibits a resonance attributed to an eigenmode for this incident angle. In contrast to the systems discussed in the previous chapters, this eigenmode can be directly excited from the 0^{th} order because the film resonator is surrounded by a medium of higher refractive index. Due to this higher refractive index, photons of an excited eigenmode have a non-zero probability of tunneling into the lithium tantalate,

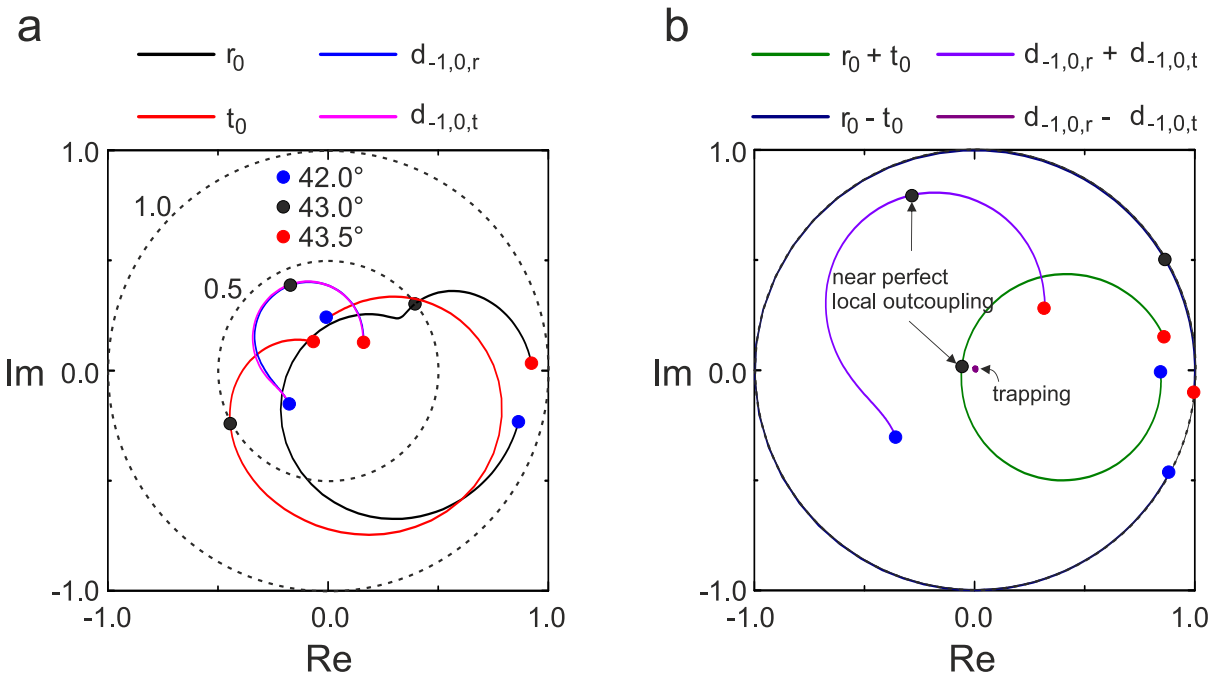

Figure 5.8: Locii of scattering matrix elements of the waveguide grating at $\lambda = 632.8$ nm as a function of θ_{int}. a) single plane wave incidence. Note that $d_{-1,0,r}$ (blue curve) and $d_{-1,0,t}$ (pink curve) are almost equal. b) Incidence with two plane waves. At resonance (43.0°), trapping and near perfect local outcoupling can be achieved.

resulting in a non-zero overlap integral. Such an eigenmode is termed 'leaky eigenmode'.

So far, these values describe the response of one dot to plane waves coming from only one half-space. For two incident plane waves of equal amplitudes, as described in Section 5.1, interesting phenomena can be observed (Fig. 5.8b). Two cases are considered: $2\Delta\Phi_0 = 0$ and $2\Delta\Phi_0 = \pi$. For the first case, one finds $\sqrt{2}b_{1,0,+} = \sqrt{2}b_{1,0,-} = r_0 + t_0$ and $\sqrt{2}b_{1,-1,+} = \sqrt{2}b_{1,-1,-} = d_{-1,0,r} + d_{-1,0,t}$. For the latter case, the outgoing amplitudes read $\sqrt{2}b_{1,0,+} = -\sqrt{2}b_{1,0,-} = r_0 - t_0$ and $\sqrt{2}b_{1,-1,+} = -\sqrt{2}b_{1,-1,-} = d_{-1,0,r} - d_{-1,0,t}$. The locii of these expressions are shown in Fig. 5.8b. Strikingly, their characteristics are close to the behavior of trapping as well as perfect local outcoupling attributed to Solution 2: at $\theta_{int} = 43.0°$ and $2\Delta\Phi_0 = 0$, the local outcoupling efficiency becomes maximized. For $2\Delta\Phi_0 = \pi$, one observes $d_{-1,0,r} - d_{-1,0,t} \approx 0$ and $r - t \approx 1$, indicating that the local outcoupling efficiency is indeed suppressed and that the remaining power stays in the 0^{th} order. This remaining power is termed 'guided power'.

This behavior is further elaborated in Fig. 5.9. $|b_{1,0,+}|^2 + |b_{1,0,-}|^2$ and $|b_{1,-1,+}|^2 + |b_{1,-1,-}|^2$ for $m = 1$ are displayed as a function of $2\Delta\Phi_0$. Herein, for each plane-wave component of a beam, the former expression can be understood as a measure for the guided power in the 0^{th} order and the latter one for the local coupling efficiency into the -1^{st} diffraction order. Indeed, $|b_{1,-1,+}|^2 + |b_{1,-1,-}|^2$ becomes near to zero for $2\Delta\Phi_0 = \pi$ (indicating trapping) and maximized for $2\Delta\Phi_0 = 0$. Remarkably, for $2\Delta\Phi_0 = \pi$, $|b_{1,0,+}|^2 + |b_{1,0,-}|^2$

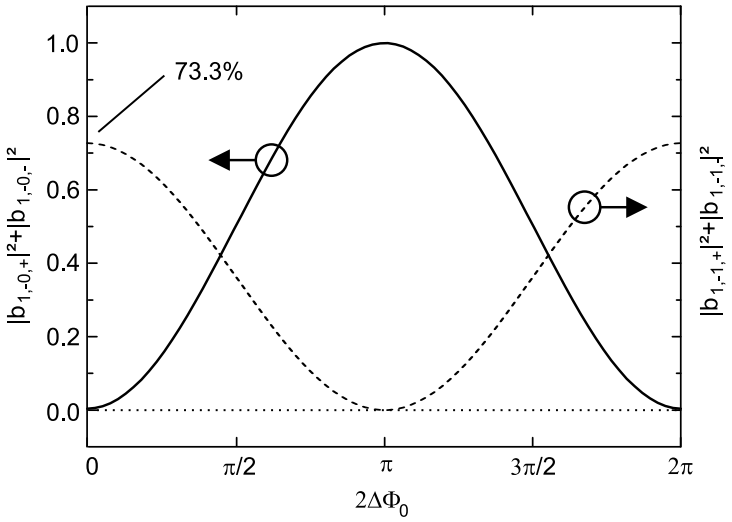

Figure 5.9: $|b_{1,0,+}|^2 + |b_{1,0,-}|^2$ and $|b_{1,-1,+}|^2 + |b_{1,-1,-}|^2$ at $m = 1$ as a function of $\Delta\Phi$.

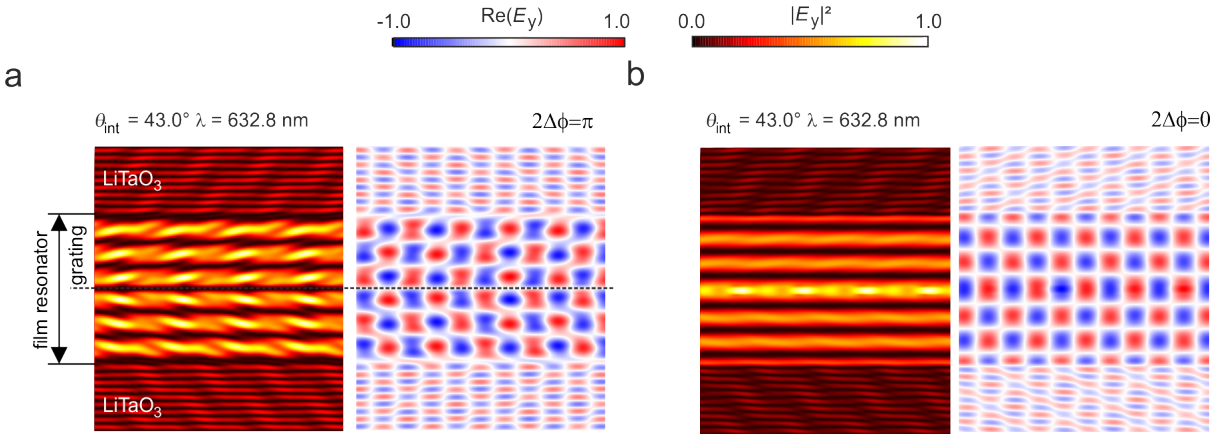

Figure 5.10: Distributions of $\mathrm{Re}(E_y)$ and $|E_y|^2$. The dashed black line marks the film resonator's symmetry plane. a) $2\Delta\Phi_0 = \pi$ b) $2\Delta\Phi_0 = 0$. According to ref. [301].

a value of 99.97% of $|\vec{a}_1|^2$ although the grating consists of a lossy material. For $2\Delta\Phi_0 = 0$, $|b_{1,-1,+}|^2 + |b_{1,-1,-}|^2$ reaches a value of 73.3% of $|\vec{a}_1|^2$, indicating the occurrence of maximized local coupling. The difference to 100% originates from three contributions. The first contribution is the local coupling efficiency into to other diffraction orders of approximately 16.3% , the second contribution are Ohmic losses of around 10%, and the third contributions is residual guided power of 0.4%.

The electric field distributions at $2\Delta\Phi_0 = \pi$ and $2\Delta\Phi_0 = 0$ are displayed in Fig. 5.10a and b, respectively. Herein, it is important to note that the relative phase change $2\Delta\Phi_0$ is assumed to take place before the plane waves fall onto the dot. This way, the film resonator can be assumed to be symmetric as its refractive index profile is dictated by linear optics. For the first case, it can be observed that the field distribution is antisymmetric with respect to the center plane of the waveguide grating and shows vanishing values of $|E_y|^2$ at the grating layer, indicating that the interaction of the grating with

the incident waves is minimized. For the latter case, contrary observations of symmetric field distributions and maximized values of $|E_y|^2$ at the grating layer can be made.

The behavior of the subsequent dots ($m > 1$) is considered in the following lines. When $2\Delta\Phi_0$ is fixed at π, the local outcoupling efficiency of all subsequent dots remain small (Fig. 5.11a). This means that the beams are effectively trapped and remain trapped. At $m = 100$, $|b_{1,0,+}|^2 + |b_{1,0,-}|^2$ decreased to a value of 97% of $|\vec{a}_1|^2$ (identical to 0.9997^{100}), confirming that trapping is preserved for each dot. Thereby, the observed decrease can be attributed to Ohmic losses. Using θ_{int} and the thickness of the $LiTaO_3$ layers to determine L_0, this decrease of the guided power over m can be attributed to a propagation length of $L_{prop} \approx 3$ m. Concerning a fixed value of $2\Delta\Phi_0 = 0$, $|b_{1,0,+}|^2 + |b_{1,0,-}|^2$ is dampened over a short distance due to maximized local outcoupling as well as losses. The resulting attributed propagation length is $L_{prop} \approx 0.3$ mm. It is anticipated that these values are close to the ones for a full calculation using beams of finite size (see Section 5.3).

To express these results in the same language as for the hybrid FW-BICs in Section 4.3, a radiative component of the Q-factor (Q_r) and a total Q-factor is attributed to the waves propagating in the 0^{th} order. Their values are displayed in Fig. 5.11b as function of $2\Delta\Phi_0$.

For the simulated waveguide grating at hand, maxima of Q and Q_r of around $7 \cdot 10^7$ and $8 \cdot 10^9$ are observed, respectively. The corresponding minima of Q and Q_r are $5 \cdot 10^3$ and $1 \cdot 10^4$. For an ideal scattering matrix fulfilling the conditions for Solution 2 and perfect local outcoupling, Q_r would show values between zero and infinity. The observed deviations from an ideal film resonator occur due to slightly imperfect coupling coefficients ($d_{i,0,r} \approx d_{i,0,t}$ and $t_0 \approx -r_0$) and the presence of Ohmic losses.

To show that the control of $|b_{1,0,+}|^2 + |b_{1,0,-}|^2$ and $|b_{1,-1,+}|^2 + |b_{1,-1,-}|^2$ is available on a local level, another result of a simulation is shown for which a fixed value of $2\Delta\Phi_0 = \pi$ (Fig. 5.11c). As described before, the waves propagate with a permanent phase relation of π through the waveguide grating and the beams are trapped. Now, another phase shift of π is introduced at the 50^{th} dot to cause maximized local outcoupling at the 51^{th}. Indeed, maximized local outcoupling analogous to the case of $2\Delta\Phi_0 = 0$ in Fig. 5.9 occurs. Therefore, light can be locally outcoupled from the waveguide by locally controlling the phase $2\Delta\Phi_m$.

So far, only one distinct wavelength λ has been considered. To show that the same phenomena occur at a broad range of incident angles and wavelengths, the contrast

$$C_{PW} = \frac{\max(|b_{-1,0,+}|^2(2\Delta\Phi_0))}{\min(|b_{-1,0,+|}|^2(2\Delta\Phi_0))} \tag{5.40}$$

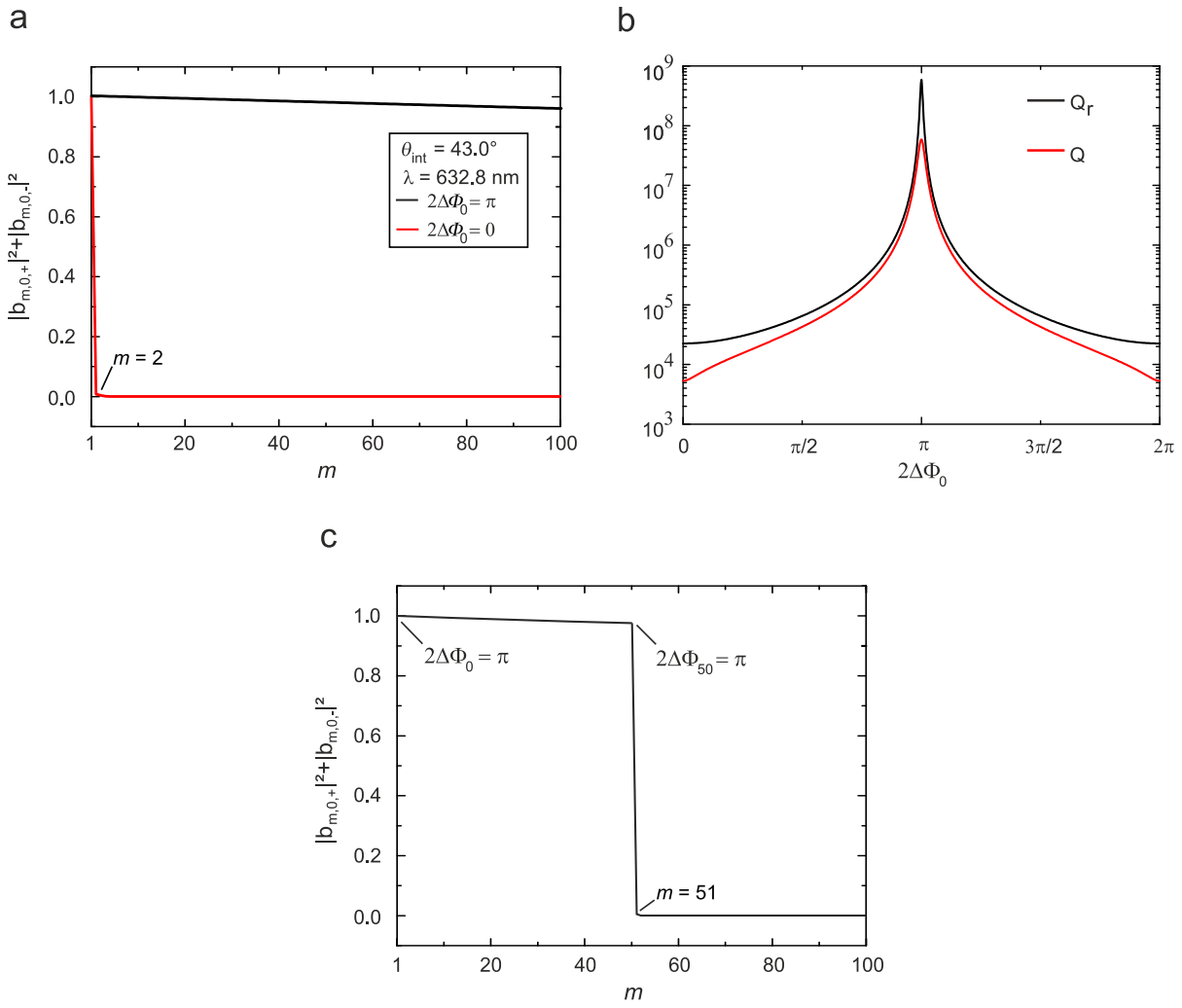

Figure 5.11: a) Relative guided power in the waveguide for $2\Delta\Phi_0 = \pi$ (black line) and $2\Delta\Phi_0 = 0.0$ (red line). b) Radiative and total Q-factors Q_r and Q as a function of $2\Delta\Phi_0$. c) Demonstration of the control of the local outcoupling efficiency by choosing $2\Delta\Phi_0 = \pi$ and $2\Delta\Phi_{50} = \pi$. These conditions mean that trapping is initiated at $m = 1$ and maximized local outcoupling (near perfect local outcoupling) is initiated at $m = 51$.

and the error function

$$F_{error} = (|t_0| - 0.5)^2 + (|r_0| - 0.5)^2 \tag{5.41}$$

are calculated. Infinite contrast values indicate trapping. The error function becomes zero for $|t_0| = |r_0| = 1/2$ and indicates that no power is left in the 0^{th} order after passing the film resonator as a result of perfect local outcoupling (see Section 5.1).

The simulated values of F_{error} and the C_{PW} are displayed in Fig. 5.12a and b, respectively. Note that for later comparisons with experimental data, the outcoupling angle θ_{ext} with respect to air is used. It is linked to θ_{int} via

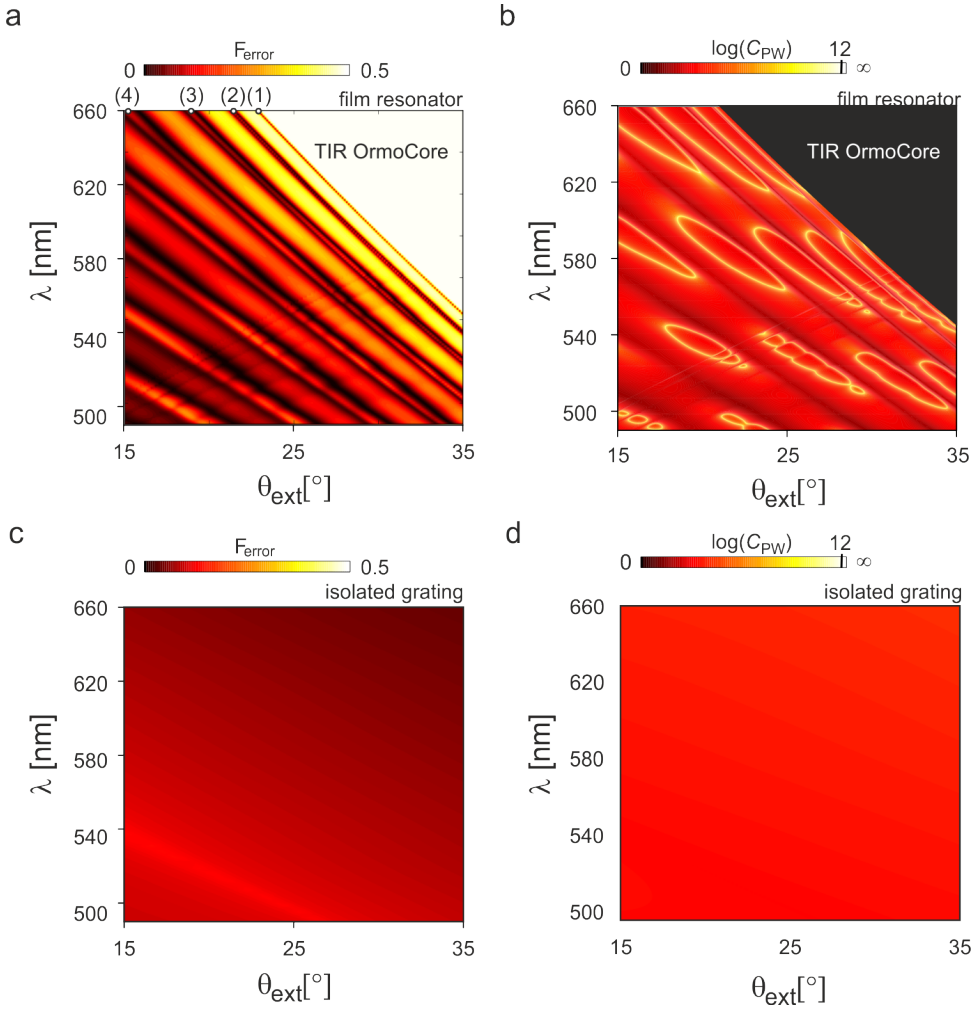

Figure 5.12: Calculated values of the Error function F_{error} from Eq. 5.41 (a) and the contrast C_{PW} from Eq. 5.40 (b) (According to ref. [301].). The simultaneous occurrence of $F_{error} = 0$ and infinite values of C_{PW} correspond to the fulfillment of the conditions for trapping and perfect local outcoupling. The markings (1), (2), (3) and (4) can be attributed to the leaky eigenmode pairs TE_0/TE_1, TE_2/TE_3, TE_4/TE_5, and TE_6/TE_7, respectively. c,d) Corresponding values attributed to an isolated grating.

$$\theta_{ext} = \arcsin\left(n'_{LiTaO_3} \sin\theta_{int} - \frac{\lambda}{\Lambda}\right) \tag{5.42}$$

The F_{error} exhibits values near to zero along the dispersion relations of the leaky eigenmodes. Strikingly, infinite contrast values occur on ellipse-like lines near the dispersion relations of the leaky eigenmodes (Fig. 5.12b). It is thus obvious that the phenomena described in Fig. 5.9 are not singular with respect to λ and θ_{ext} as it would be the case for BICs. Quite the contrary, these infinite contrast values can be found over a vast range of λ and θ_{ext}.

From these observations, it can be concluded that the elements of $\underline{S}_m$ become almost ideal with respect to the conditions mentioned in Section 5.1 as a result of resonance.

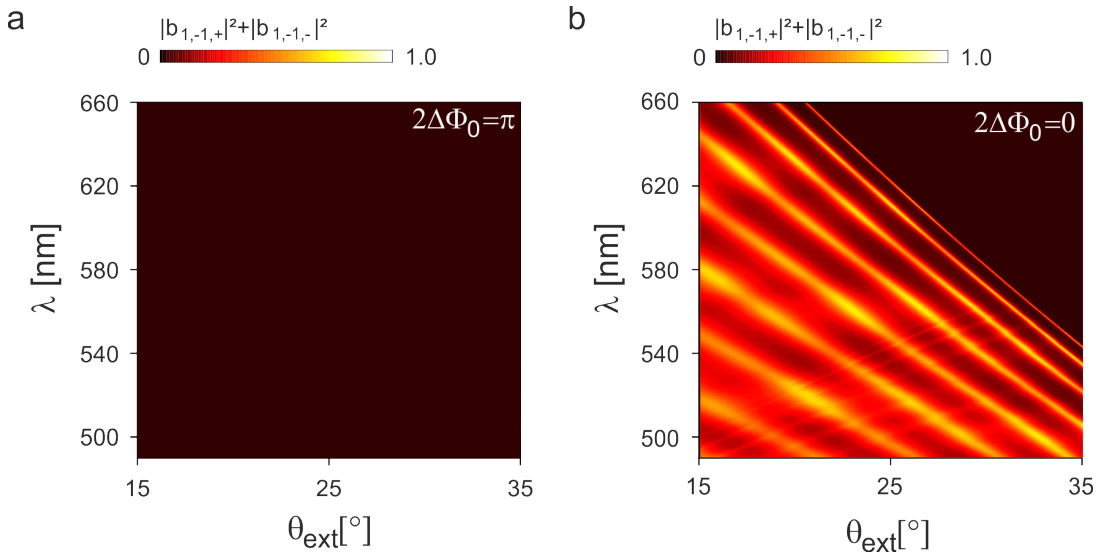

Figure 5.13: Simulated values of $|b_{1,-1,+}|^2 + |b_{1,-1,-}|^2$. These values can be interpreted as the local coupling efficiency into the -1^{st} diffraction order for the first dot ($m = 1$). a) $2\Delta\Phi_0 = \pi$. b) $2\Delta\Phi_0 = 0$.

Thereby, the film resonator's (linear) mirror symmetry with respect to the z-direction enforces the occurrence of trapping and maximized local outcoupling (near perfect local outcoupling) over a broad spectral range.

In comparison, when the film resonator is replaced by an isolated diffraction grating (identical to the one in the film resonator), significantly smaller contrasts as well as values of the error function far above zero occur (Figs. 5.12c and d). These results indirectly confirm the necessity of the film resonator.

A plot of $|b_{1,-1,+}|^2 + |b_{1,-1,-}|^2$ displays the local coupling efficiency into the -1^{st} diffraction order as a function of $2\Delta\Phi_0$ is shown in Fig. 5.13. For $2\Delta\Phi_0 = \pi$, $|b_{1,-1,+}|^2 + |b_{1,-1,-}|^2$ is almost zero in the entire parameter range, whereby the smallest values occur at wavelengths and external angles for which the contrasts in Fig. 5.12a are infinite. On the contrary, for $2\Delta\Phi_0 = 0$, $|b_{1,-1,+}|^2 + |b_{1,-1,-}|^2$ reaches values of around 80% of $|\vec{a}_1|^2$ along the dispersion relations of the eigenmodes.

At this point, the waveguide grating's response to plane-waves is fully characterized. In the next sections, the effects of finite beam sizes, unequal input amplitudes will be considered. Subsequently the theoretical model at hand will be compared with experimentally obtained data, whereby the effects of local inhomogeneities and global asymmetries will be introduced in the context of this comparison.

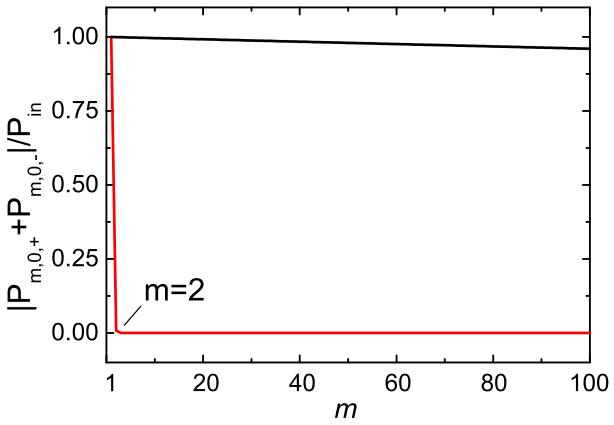

Figure 5.14: Effects of the finite beam size on the beam power $P_{m,0,+} + P_{m,0,-}$ in the 0^{th} order as a function of m (the guided power). It is normalized to the input power P_{in}. The solid black line corresponds to $2\Delta\Phi_0 = \pi$ and the solid red line corresponds to $2\Delta\Phi_0$.

5.3 Effects of Finite Beam Size

In the last section the response of an exemplary waveguide grating to plane waves has been investigated. Although this response already reveals the core characteristics of trapping and perfect local outcoupling, there remains the transition to beams of finite size. To model both beams, they can be decomposed into plane-wave spectra (see Chapter 2). This way, the response of the waveguide grating to the beams can be constructed from the plane-wave responses known from Section 5.2. Due to the large dimensions of the $LiTaO_3$ layers with respect to the z-direction, the power of the beams in the 0^{th} diffraction order as well as in all diffracted beams can be regarded as far field phenomena. Therefore, to evaluate the local outcoupling efficiency or efficiency attributed to the guided power of a dot, the integral can be directly executed over the values of $|b_{m,\nu,+}|^2$ and $|b_{m,\nu,-}|^2$ obtained from the plane-wave response. This method is stated as 'Finite Beam RCWA' (FB-RCWA) in the literature [329]. Hereby, it is important to note that the electromagnetic fields of the beams, including their full amplitude and phase information, are rigorously calculated throughout their propagation in the waveguide.

For the remaining discussion, a Gaussian intensity profile with translational invariance with respect to the y axis is chosen. Beams with such intensity profile are termed 'Gaussian beams'. To provide comparable conditions as for the experiments shown later on, the divergence angle and initial lateral spot size of the Gaussian beams are fixed at values of 0.5 mrad and 0.5 mm. Furthermore, the intensity profile is normalized in a way that both Gaussian beams share an initial power P_{in} per unit length in the y-direction of $P_{1,0,+} + P_{1,0,-} = P_{in}$ with $P_{m,\nu,+}$ and $P_{m,\nu,-}$ as the powers of the beams (per diffraction order) in the upper and lower half-space, respectively. To give an example, $P_{m,0,+}$ and $P_{m,0,-}$ are obtained via integrating over $|b_{m,0,+}|^2$ and $|b_{m,0,-}|^2$ in the k-space [329].

Fig. 5.14 shows an analogous calculation as for Fig. 5.11 with an internal angle of $\theta_{int} = 43.0$ and $\lambda = 632.8$ nm. Strikingly, the introduction of a finite beam size does not seem to affect trapping in an obvious way. A closer look at the data reveals that the guided power behind the first dot for $2\Delta\Phi_0 = \pi$ is now 99.96% of P_{in} instead of 99.97% of $|\vec{a_1}|^2$. This marginal difference originates from small residual local outcoupling efficiency of around $3{\cdot}10^{-5}P_{in}$ introduced by misaligned plane-waves with respect to the parameters for infinite contrast in Fig. 5.12. For $2\Delta\Phi_0 = 0$, the local coupling efficiency into the -1^{st} diffraction order is still 73.3% These values mean that the propagation length for Gaussian beams with a relative phase of π is still in the meter range. These facts can be intuitively understood by taking two considerations into account. The first consideration is, that the divergence angle of the Gaussian beams is small and the spot size is relatively large. Under these conditions, the Gaussian beams are mostly described by a single plane wave component. The second consideration is, that the matrix formalism model in Section 5.1 links the amplitudes and phases of plane waves together as if the plane waves would not overlap with each other. This way, plane waves from separate dots do not affect each other. For these two reasons, calculations using plane waves already represent useful approximations for all beams of small divergence angles (as long as there is no self-interference).

To confirm that the procedure above produces trustworthy results, the response of a dot to two Gaussian beams is calculated via FEM as an independent method, whereby the divergence angle and lateral spot size are chosen to 0.5 mrad and 0.5 mm as well. The results of this calculation are shown in Fig. 5.15. Hereby, it has to be mentioned that the implemented refractive index $LiTaO_3$ in the simulation tool (COMSOL Multiphysics) is given by $n'_{LiTaO3} = 2.17$ at a wavelength of $\lambda = 632.8$ nm. Here, this value is also assumed for calculations via the matrix formalism to enable a valid comparison to the numerical calculations. The power scattered away from the dot is measured via a far field monitor. The scattering angle α is defined in the x-z plane and visualized in Fig. 5.15a. The scattered power for $2\Delta\Phi_0 = 0$ is shown in Fig. 5.15b. The local coupling efficiency into the -1^{st} diffraction order is 71.1% and both Gaussian beams behind the dot are of near zero relative phase. For $2\Delta\Phi_0 = \pi$ (see Fig. 5.15c), the guided power behind the first dot for $2\Delta\Phi_0 = \pi$ is 99.8%, and the residual local outcoupling efficiency is $7.3{\cdot}10^{-5}P_{in}$. Importantly, the relative phase of the beams behind the dots is 0.9991π and, thus, confirms the results obtained via the matrix formalism. Strikingly, the calculated values of $P_{1,\nu,+}$ and $P_{1,\nu,-}$ equal the numerically obtained values within a relative error of 0.7%.

This small error may occur as a result from slight numerical inaccuracies due to the required large mesh density of the grating. Nonetheless, the numerical simulations independently demonstrate the occurrence of trapping and maximized local outcoupling and

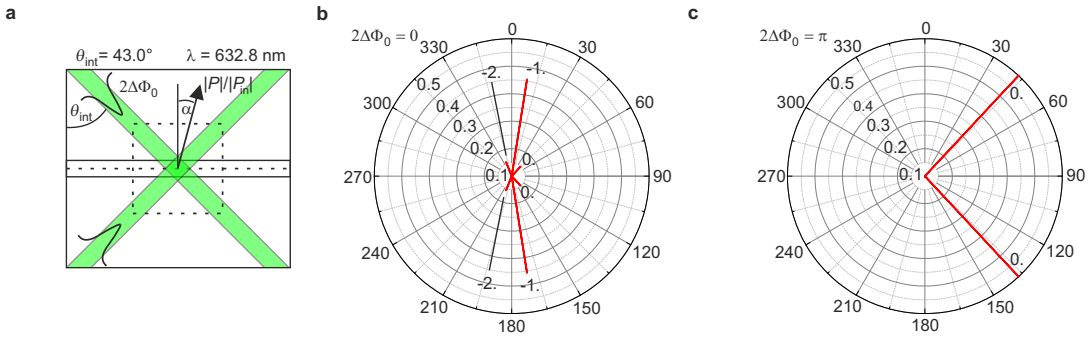

Figure 5.15: Numerical calculation to confirm the results obtained via FW-RCWA. a) Definition of the scattering angle α. b) Far field power under $2\Delta\Phi_0 = 0$. b) Far field power under $2\Delta\Phi_0 = \pi$.

validate the use of FB-RCWA for the following sections.

5.4 Effects of Unequal Beam Powers and Varying Relative Phases

So far, all calculations have been done under the assumption that all plane-waves and Gaussian beams are of equal amplitudes and power values, respectively. In reality, such condition is obviously not always true. Scattering events and inhomogeneities may put the beams out of balance. Second, for a real device, the beams must be somehow coupled into the waveguide grating in the first place so that they might begin their propagation with unbalanced power values right away. So far, it is unclear how such imbalance affects both trapping and perfect local outcoupling.

To discuss this apparent problem, the entries of $\underline{S}_m$ are revisited under plane-wave incidence as described in Section 5.2. It can be recognized that these entries behave in a special way: as the waveguide grating is symmetric and homogeneous, it can be assumed that the amplitude vector of an $(m+1)^{\text{th}}$ dot is related to the input amplitudes of each plane-wave component of the Gaussian beams via

$$\vec{a}_{m+1,0} = \underline{R}_0^m \vec{a}_{0,0} \tag{5.43}$$

Hereby, any phase shifts between the dots which do not change the phase relation between both beams are neglected. For simplicity, an absence of loss and the conditions for Solution 2 are assumed. These assumptions are mathematically expressed by choosing $T = \underline{\mathbb{1}}$. Explicitly inserting r_0 and t_0 into $\underline{R}_0^m$ then leads to the expression

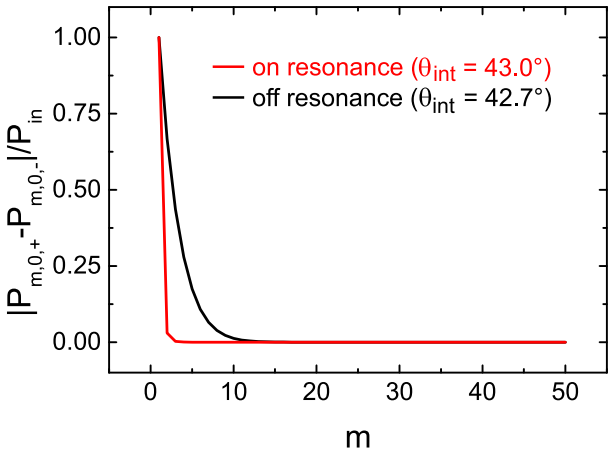

Figure 5.16: The leveling of Gaussian beams for an initial choice of $P_{1,0,+} = P_{in}$ and $P_{1,0,-} = 0$ at $\lambda = 632.8$ nm. The solid red and black lines correspond to $\theta_{int} = 43.0°$ and $\theta_{int} = 42.7°$, respectively. For the former value, resonance is present.

$$\underline{R}_0^m = \begin{pmatrix} (r_0 - t_0)^m + (r_0 + t_0)^m & (r_0 + t_0)^m - (r_0 - t_0)^m \\ (r_0 + t_0)^m - (r_0 - t_0)^m & (r_0 - t_0)^m + (r_0 + t_0)^m \end{pmatrix} \tag{5.44}$$

From the previous Section 5.2 it is known that the waveguide grating exhibits the property $|r_0 + t_0| < |r_0 - t_0|$. Without further proof, this property also prevails for different wavelengths than $\lambda = 632.8$ nm. It is then obvious that $(r_0 + t_0)^m$ becomes smaller than $(r_0 - t_0)^m$ with increasing m and $\underline{R}_0^m$ converges to

$$\lim_{m\to\infty} \underline{R}_0^m = \begin{pmatrix} (r_0 - t_0)^m & -(r_0 - t_0)^m \\ -(r_0 - t_0)^m & (r_0 - t_0)^m \end{pmatrix} \tag{5.45}$$

As this matrix has entries of equal amplitudes and reversing signs, any set of input amplitudes results in equal amplitudes for infinitely large values of m. This phenomenon is called 'leveling'. The results of an exemplary calculation of leveling are shown in Fig. 5.16. The same waveguide grating as in Fig. 5.9 is considered.

A worst case scenario is chosen: The entire input power is in the upper beam and no power is in the lower beam for $m = 1$ ($P_{1,0,+} = P_{in}$). Two sets of parameters are considered: resonant conditions ($\theta_{int} = 43.0°$, $\lambda = 632.8$ nm) and non-resonant conditions ($\theta_{int} = 42.7°$, $\lambda = 632.8$ nm). The normalized difference of the beam powers $|(P_{m,0,+} - P_{m,0,-})|/P_{in}$ is displayed as a function of m. It can be observed, that for both conditions, the power difference of the beams converges to zero, whereby significantly faster convergence occurs at resonance. These observations confirm that leveling takes place under initially unequal beam powers.

It is important to note that this leveling is consistent with the previous descriptions and

includes both trapping and perfect local outcoupling as special cases: In the absence of loss ($r_0 - t_0 = 1$), equal input amplitudes under $2\Delta\Phi_0 = 0$ enforce $\vec{a}_{m+1,0} = 0$ (perfect local outcoupling) and $|\vec{a}_{m+1,0}|$=1 under $2\Delta\Phi_0 = \pi$ (trapping). More general, similar to a tilted polarizer, any set of input parameters can be converted into a basis of a trapping and perfect local outcoupling

$$\begin{pmatrix} a_{0,+} \\ a_{0,-} \end{pmatrix} = \frac{1}{\sqrt{2}} \left[A_0 \begin{pmatrix} -1 \\ 1 \end{pmatrix} + B_0 \begin{pmatrix} 1 \\ 1 \end{pmatrix} \right] \tag{5.46}$$

with $A_0 = (a_{0,+} - a_{0,-})/\sqrt{2}$ and $B_0 = (a_{0,+} + a_{0,-})/\sqrt{2}$. When the conditions for trapping and perfect local outcoupling are fulfilled, the power of an input beam is automatically split up into a trapped part ($P_{trapped}$) and a part which is outcoupled (P_{rad}). Herein, the total power being trapped and being outcoupled is given by a weighted integral over $|A_0|^2(k'_x)$ and $|B_0|^2(k'_x)$, respectively (see Section 5.3). When the beams are dominated by respectively one plane-wave, as for lasers, these integrals become approximately

$$\frac{P_{trapped}}{P_{in}} = |A_0|^2 \tag{5.47}$$

$$\frac{P_{rad}}{P_{in}} = |B_0|^2 \tag{5.48}$$

It is now assumed that both Gaussian beams at $m = 1$ can be represented by a pair of amplitudes $(a_{beam,+}, a_{beam,-})$ and a relative phase $2\Delta\Phi_B$

$$\begin{pmatrix} a_{beam,+} \\ a_{beam,-} \end{pmatrix} = \begin{pmatrix} \cos(\alpha_B) \\ \sin(\alpha_B) \cdot e^{2j\Delta\Phi_B}, \end{pmatrix} \tag{5.49}$$

whereby α_B determines the amplitude ratio between both beams. Then, $P_{trapped}$ reads

$$\begin{aligned} \frac{P_{trapped}}{P_{in}} = & \frac{1}{2}[\sin^2(\alpha_B)\sin^2(2\Delta\Phi_B) + \sin^2(\alpha_B)\cos^2(2\Delta\Phi_B) \\ & - 2\sin\alpha_B\cos\alpha_B\cos(2\Delta\Phi_B) + \cos^2(2\Delta\Phi_B)] \end{aligned} \tag{5.50}$$

To provide some examples of Eq. 5.50, the waveguide grating discussed in Section 5.2 is considered under varying selections of unequal beam powers and relative phases.

In the first example, the entire input power is in the upper beam ($P_{1,0,+} = P_{in}$) and no power is in the lower beam. According to Eq. 5.46, this condition leads to $A_0 = -B_0$. Therefore, approximately one half of the input power should be trapped and the other half should be outcoupled or absorbed via Ohmic losses. Fig. 5.17a shows the behavior

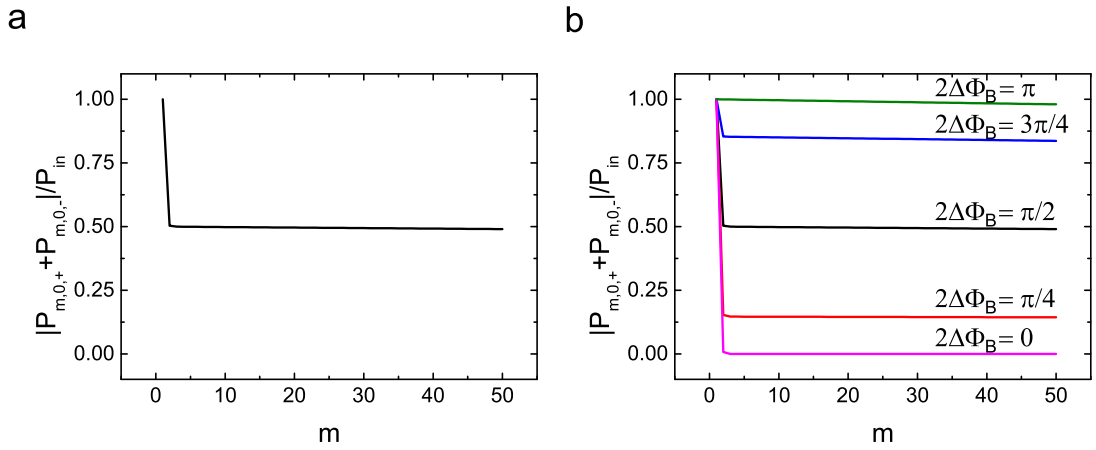

Figure 5.17: Separation of beams of unequal power values and varying relative phases at $\lambda = 632.8$ nm and $\theta_{int} = 43.0°$. a) Evolution of $(P_{m,0,+} + P_{m,0,-})/P_{in}$ for an initial choice of $P_{1,0,+} = P_{in}$. This choice means that only one beam falls onto the first dot. Here, approximately 50% of P_{in} are trapped. b) Evolution of $(P_{m,0,+} + P_{m,0,-})/P_{in}$ for varying values of $2\Delta\Phi_B$. Here, both input beam powers at the first dot are identical. Depending on the values of $2\Delta\Phi_B$, a smaller or larger part of P_{in} is trapped in the waveguide grating. Generally, any initial set of input beam amplitudes and phases can be separated into a trapped part of power $P_{trapped}$ and an outcoupled part of power P_{rad}.

of $(P_{m,0,+} + P_{m,0,-})/P_{in}$ as a function of m. The internal angle of incidence is $\theta_{int} = 43.0°$ and the wavelength is $\lambda = 632.8$ nm, so that resonant conditions are present (see Section 5.2). Indeed, $(P_{m,0,+} + P_{m,0,-})/P_{in}$ rapidly converges to a value of approximately 0.5, indicating that the descriptions above are correct.

In the second example, equal beam powers are chosen ($\alpha_B = 0.25\pi$) and their relative phase is varied (Fig. 5.17b). Here, an evaluation of equation 5.50 leads to the expression

$$\frac{P_{trapped}}{P_{in}} = \frac{1}{2}(1 - \cos(2\Delta\Phi_B)) \tag{5.51}$$

For some selected values of the relative phase, $P_{trapped}/P_{in}$ exhibits values as displayed in Table 5.4

$2\Delta\Phi_B$	$P_{trapped}/P_{in}$
0.0 π	0.0
0.25 π	0.146
0.5 π	0.5
0.75 π	0.853
1.0 π	1.0

It can be observed that the calculated values are close to these expected values, confirming that the splitting of power into a trapped part and an outcoupled part is indeed present.

As a matter of course, for any system with Ohmic and residual scattering losses, $P_{trapped}$ is at least slightly smaller than predicted by equation 5.46. Here, as already mentioned in Section 5.3, the deviation from trapping in the absence of loss and the absence of finite beam sizes is around 0.04% per dot. Nonetheless, this finding means that a small disturbance away from the conditions of a trapping does not lead to a breakdown of trapping. Instead, a small portion of light is radiated away and the remaining light stays trapped in the waveguide grating. This behavior is termed 'self-stabilization'. As a matter of course, local changes of the relative phase (or amplitude corrections) could be introduced to either increase $|A_0|^2$ or $|B_0|^2$. Therefore, the two beams in the waveguide can be switched between trapping and maximized local outcoupling (up to perfect local outcoupling) at any lateral position in the waveguide. Note that equivalent observations can be made for a hypothetical system obeying Solution 1.

An experimental realization of such switching together with other experimental data will be presented in the next section. Throughout this section, other influences like geometrical asymmetries and concrete calculations of the effects of local inhomogeneities will be introduced along with the discussion of these experimental data.

5.5 Comparison to the Experiment

In this section, experimental data of a waveguide grating will be provided and compared to simulation.

These experimental data were obtained with a waveguide grating as displayed in Fig. 5.18a. A laser beam of a radial Gaussian intensity profile (here also referred to as 'Gaussian beam') is coupled into the waveguide grating via a grating coupler (Fig. 5.18b, left). This coupled Gaussian beam crosses the resonator and splits into two beams. After leveling, the phase between the two beams is locally tuned via the Pockels effect using two tip electrodes. Again, the c-axises of the lithium tantalate layers are of opposite direction with respect to each other, whereby both c-axises are parallel to the z-direction. This way, the electric field of the tip electrodes increases the refractive index in one layer and simultaneously decreases it in the other layer. This refractive index difference causes the desired change of the relative phase. Without any phase change, scattering and diffraction of light out of the waveguide grating is observed. This behavior is displayed in the photographs shown in Fig. 5.18c. For a better visibility of these phenomena, zoomed versions of these photographs with inverted colors and an increased gamma value of 1.5 are displayed besides the original photographs. Here, gamma is referred to the gamma value known from standard image processing. Scattered light appears pink. The individual dots can be clearly recognized in these photographs. Strikingly, for a certain applied

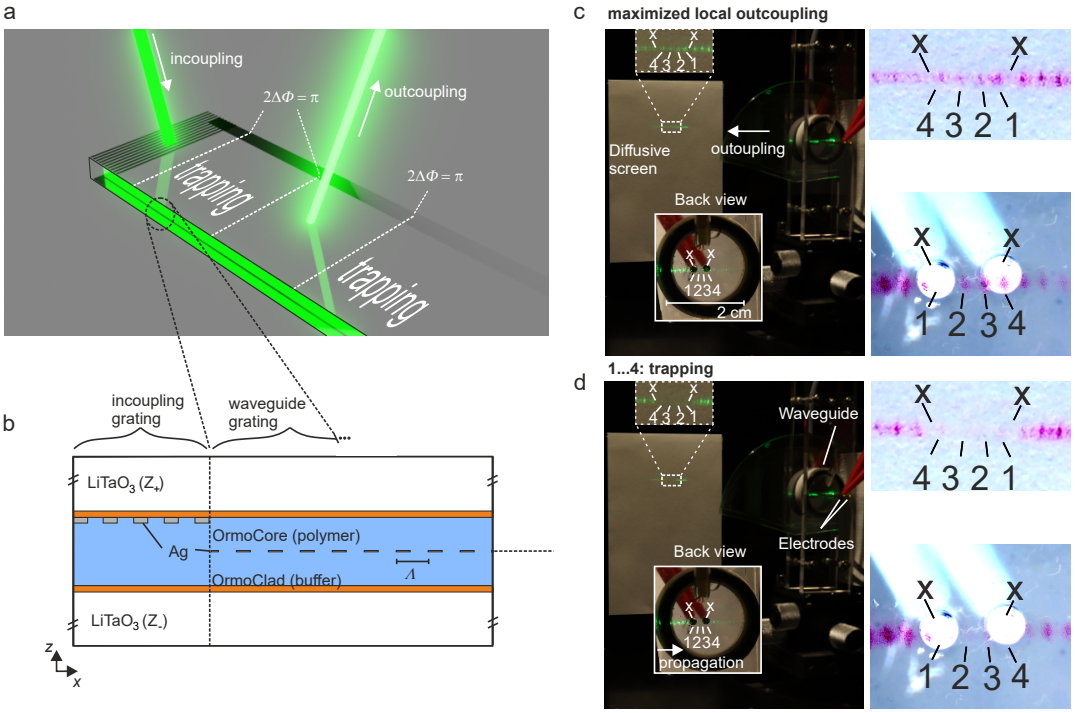

Figure 5.18: a) Rendered illustration of the waveguide grating used in experiment. b) The waveguide grating geometry used for experiments. In addition to the geometry explained in Fig. 5.7, there is a coupler region exhibiting an incoupling grating. c) Photograph of the sample without any applied voltage at the tip electrodes. The enlarged insets show the light which is diffracted and scattered away from the waveguide. For better visibility, color-inverted images are shown on the right side. d) Analogous photographs and enlarged insets of the sample with a tip electrode voltage causing trapping between them. From ref. [301].

voltage, which corresponds to a phase change of π at both positions marked by 'x', it is then observed that scattering and diffraction are suppressed between both electrodes (Fig. 5.18d). This observation indicates the presence of trapping.

To model these experimental conditions and to estimate how the effects explained in the last section affect the broadband behavior of trapping and maximized local outcoupling, Gaussian beams with a divergence angle of 0.5 mrad and an initial spot size of 0.5 mm are used. These values fit well to the data of the laser used for the experiments. To take into account the effect of the incoupling grating, the initial beam powers are chosen to $P_{1,0,+} = P_{in}$. The leveling of the beams is simulated by assuming a propagation over $L = 20$ dots prior to any local phase shift events. Now, a local phase shift of $\Delta\Phi_0$ is considered, whereby the counting of m starts at the 21$^{\text{st}}$ dot. The attributed contrast

$$C_m = \frac{\max(\eta_m(2\Delta\Phi_{m-1}))}{\min(\eta_m(2\Delta\Phi_{m-1}))} \tag{5.52}$$

with the local coupling efficiency into the -1st diffraction order $\eta_m = P_{m,-1,+}$ is shown in

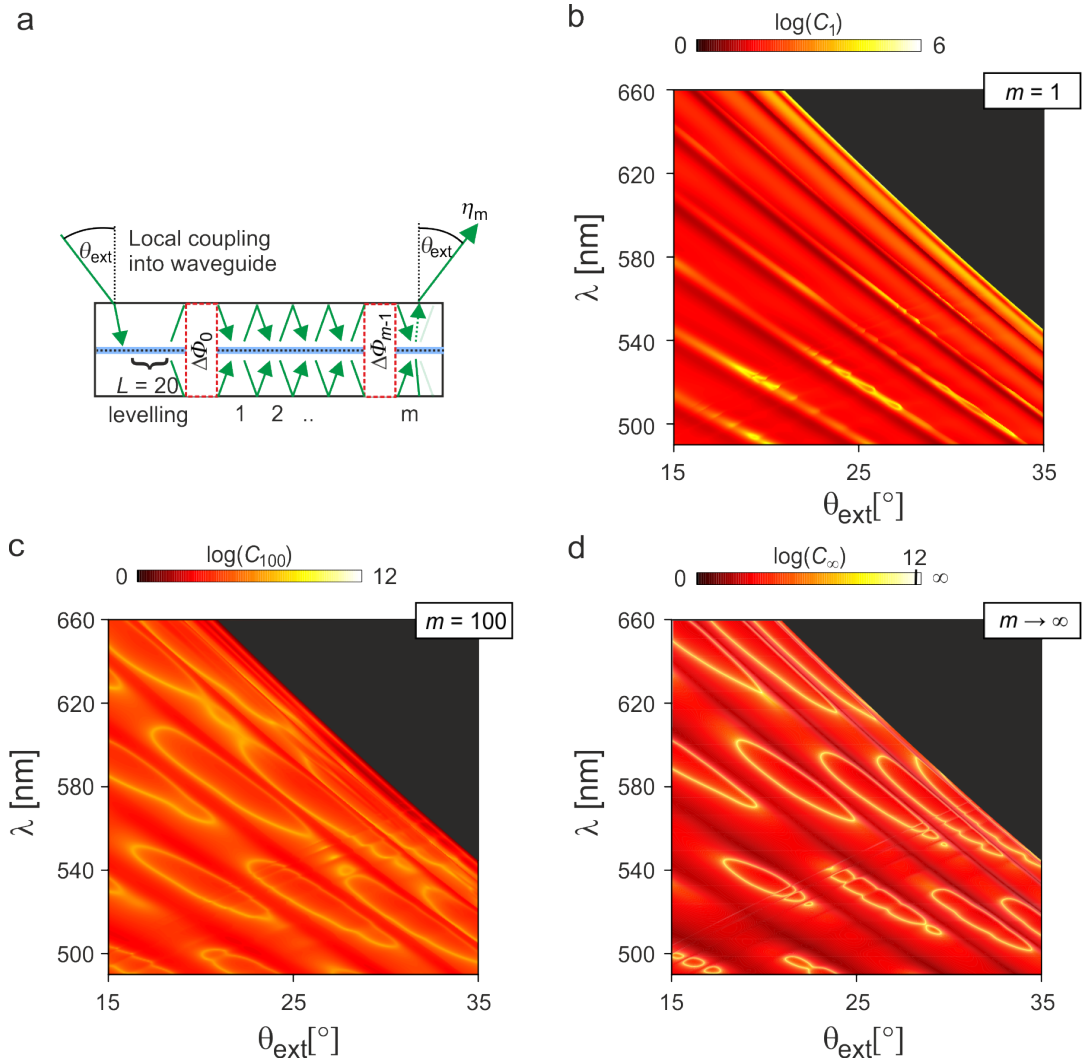

Figure 5.19: a) Simulation setup to mimic the experimental conditions. b) Contrast of Gaussian beams after leveling over $L = 20$ dots ($m = 1$). c) Contrast after propagation over $m = 100$ dots under trapping. d) Contrast toward $m \to \infty$. The subfigure (d) is from ref. [301].

Fig. 5.19.

These contrast values C_m are reduced in comparison to the ones under plane-wave incidence (see Fig. 5.12). This is of no surprise as the local outcoupling efficiency of the Gaussian beams results from an averaging over a spectrum of plane-waves. In consequence, only a few single plane-waves of this spectrum may exhibit trapping, whereby the remaining plane-waves exhibit local outcoupling efficiency values near to zero. In addition, even after a propagation of 20 dots, the amplitudes of the beams are not perfectly equal as leveling occurs asymptotically toward infinite m. Due to these two reasons, the local outcoupling efficiency of the beams is slightly larger than zero. Nonetheless, contrast values of $C \approx 10^5...10^6$ along the dispersion relations of the leaky eigenmodes are observed (Fig. 5.19b). Now, the phase relation between both beams at $m = 1$ is chosen to

π to ensure that the beams propagate under trapping. This phase selection represents the first electrode. The second electrode is then modeled via a second phase shift at $m > 1$. Plane-wave components, which do not exhibit large contrast values, are dampened by outcoupling and only those components remain which are inherently trapped and exhibit the largest contrast values. In accordance, it is observed, that the contrast values with increasing values of m asymptotically approach the ones under pure plane wave incidence (see Section 5.2). This can be seen by comparing the contrast values for $m = 100$ and $m \to \infty$ in Figs. 5.19c and d with the ones in Fig. 5.12b, respectively.

It is important to recognize that these contrasts have still been evaluated by sweeping a freely choosable phase $2\Delta\Phi_{m-1}$ over the entire range from 0 to 2π. In this experiment, the relative phase is provided by an external electric field. To give an estimate how this link to a physical process affects trapping, the relative phase is approximated by

$$2\Delta\Phi_{m-1} = \frac{8\pi}{\lambda}\frac{\Delta n(E_{m-1})t}{\cos\theta_{int}} \tag{5.53}$$

Hereby, E_{m-1} is assumed as a homogeneous electric field strength between the dots $m-1$ and m. As a matter of course, the true electric field is not homogeneous. Therefore, the following data might slightly differ from the true ones attributed to the tip electrode. Fig. 5.20 shows the values of the normalized local coupling efficiency into the -1$^{\text{st}}$ diffraction order

$$\eta_{m,normalized} = \frac{P_{m,-1,+} + P_{m,-1,-}}{P_{m-1,0,+} + P_{m-1,0,-}} \tag{5.54}$$

as a function of E_{m-1} for $m \to \infty$. The values of $\eta_{m,normalized}$ can be interpreted as a local coupling efficiency into the -1$^{\text{st}}$ diffraction order which is normalized to the power incident on the m^{th} dot instead of to P_{in}. Similar to Fig. 5.13, $\eta_{m,normalized}$ can be tuned between values of 0% and 80% along the entire displayed range of wavelengths. The striking difference to a freely choosable relative phase $2\Delta\Phi_{m-1}$ is the presence of lines of constant relative phases (white dashed lines), which depend on the applied field strength. In other words, $2\Delta\Phi_{m-1}$ is dependent on the wavelength and outcoupling angle and a line of constant relative phase crosses the dispersion relations of the film resonator's leaky eigenmodes. The consequences of this behavior will be discussed later on in Chapter 6. For now, the important point to remember is that linking the phase relation between the two beams to a physical process may alter the occurrence of trapping in comparison to Fig. 5.13. Nonetheless, the observations for Fig. 5.19 imply that the trapping between the two electrodes (Fig. 5.18) can be reproduced by the simulation model over a broad spectral range even when the effects of finite beams and unequal input powers are taken into

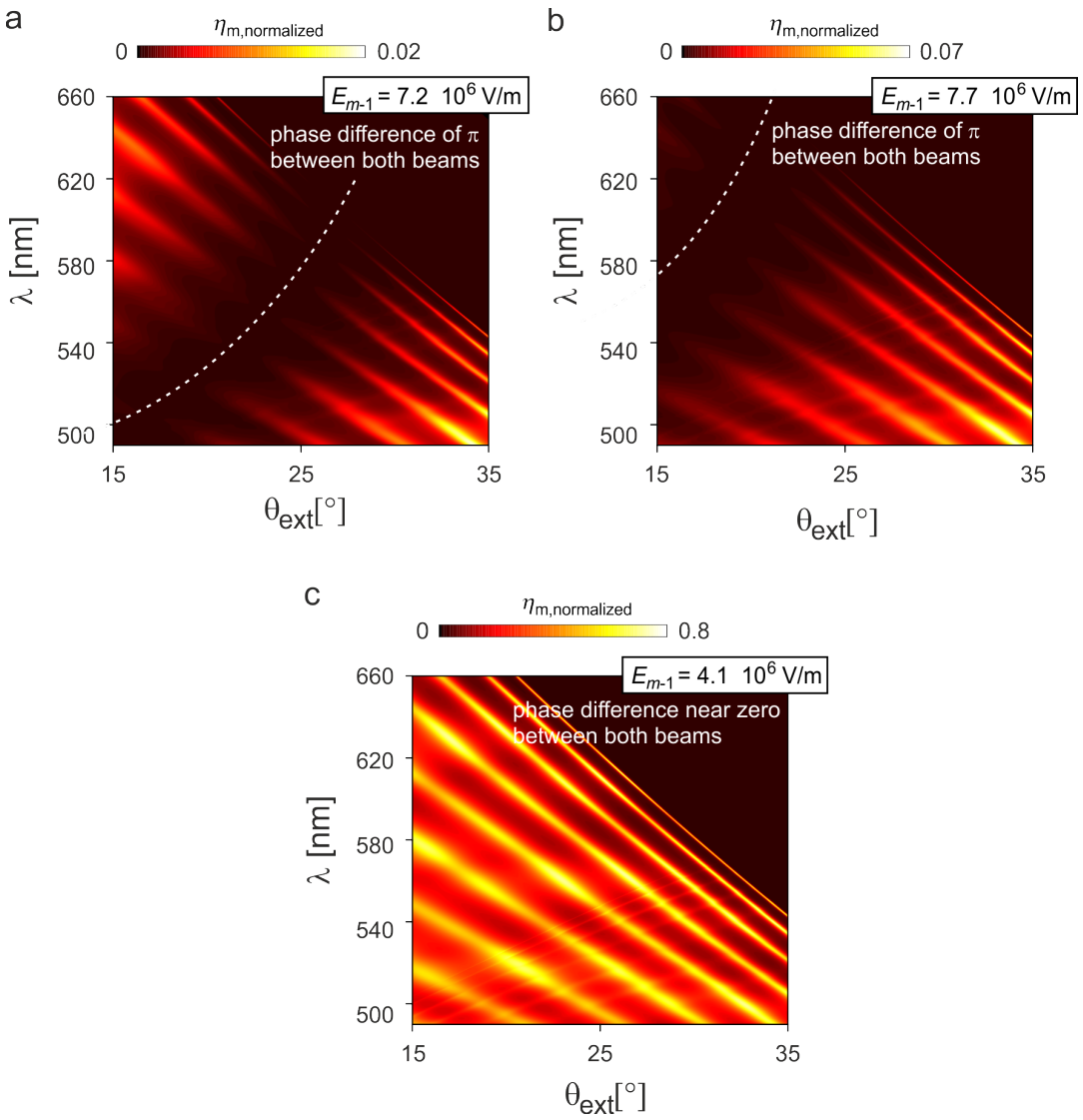

Figure 5.20: a-c) Values of $\eta_{m,normalized}$ for $m \to \infty$ as function of a local external field E_{m-1}.

account. As a matter of course, a more quantitative comparison with the experiment is desired which does not depend on assumptions of the homogeneity of the external electric field.

One simple way to quantitatively compare the simulation model with experimental results is the use of homogeneous electrodes. Such a setup using is displayed in Fig. 5.21.

Here, the electric field in the $LiTaO_3$ wafers can be assumed as homogeneous in good approximation. As the wafers are thick compared to the resonator, they dominate the capacity of the waveguide grating and the phase shift between both beams can be expressed by Eq. 5.53 by setting $E_m = E_g$ (and therefore $2\Delta\Phi_m = 2\Delta\Phi$). Both the validity of Eq. 5.53 for the sample and the homogeneity of the electric field are confirmed by conventional interferometry. Using this setup, various experimental data have been

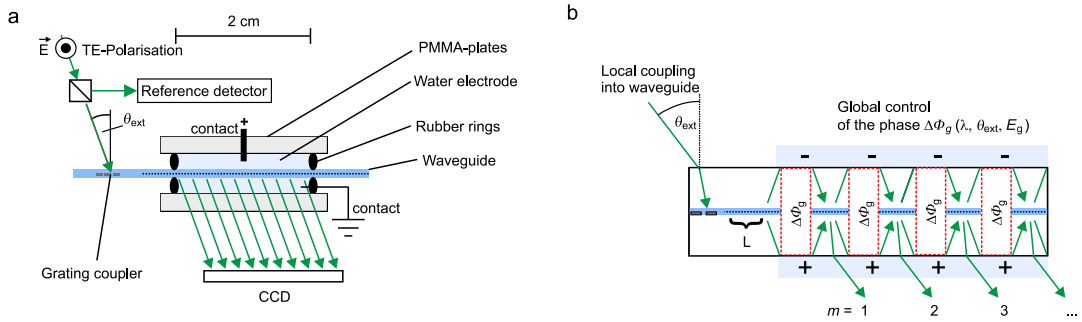

Figure 5.21: a) Sketch of an experimental setup using homogeneous electrodes. b) Corresponding notation of phases and definition of L and m. According to the descriptions in ref. [301]

obtained.

Before these data are compared to the model at hand, the characteristics of η_m attributed to such homogeneous electrode will be presented. Subsequently the effects of global asymmetries and local inhomogeneities will be discussed. Herein, η_m is normalized to its maximum value for each value of m.

The one corresponding to the symmetric waveguide grating (Fig. 5.22a) can be understood as follows. Due to the globally applied field, the phase relation between the beams is altered by the same phase $2\Delta\Phi$. Along $E_g = 0$, the same situation as for $2\Delta\Phi_0 = 0$ in Fig. 5.11 is present. For $E_g \approx 3.9$ kV/mm, the beams are trapped for $m = 1$. Subsequently, the relative phase is shifted by $2\Delta\Phi_m \approx \pi$ again and η_m is maximized. This way, trapping and maximized local outcoupling alternate. Consequently, for both these values of E_g the propagating beams are dampened by local outcoupling and the guided power tends to zero with increasing m. However, at distinct values of E_g, the accumulated phases add up in a way that maxima of η_m are present. These maxima are symmetrically distributed around values of E_g which correspond to a phase shift of 2π.

Global asymmetries mean that the entire waveguide grating is characterized by the same asymmetry of the geometry for every dot. Three cases are considered: first, an asymmetric change of the upper OrmoCore layer from 1900 nm to 1950 nm. Second, an asymmetric grating profile with a surface profile matched to an atomic force micrograph of the transfer-printed binary grating. Third, an asymmetric thickness difference of the wafers corresponding to a phase shift of 0.25λ per dot. These three cases are displayed, along with the initial symmetric waveguide grating, in Fig. 5.22b-d. The graphs show η_m as a function of E_g at $\lambda = 632.8$ nm and $\theta = 42.9°$. An asymmetric change of the bottom Ormocore layer from 1900 nm to 1950 nm induces asymmetric amplitudes of the maxima (Fig. 5.22b).

An asymmetric grating profile with otherwise fixed parameters leads to a formation of

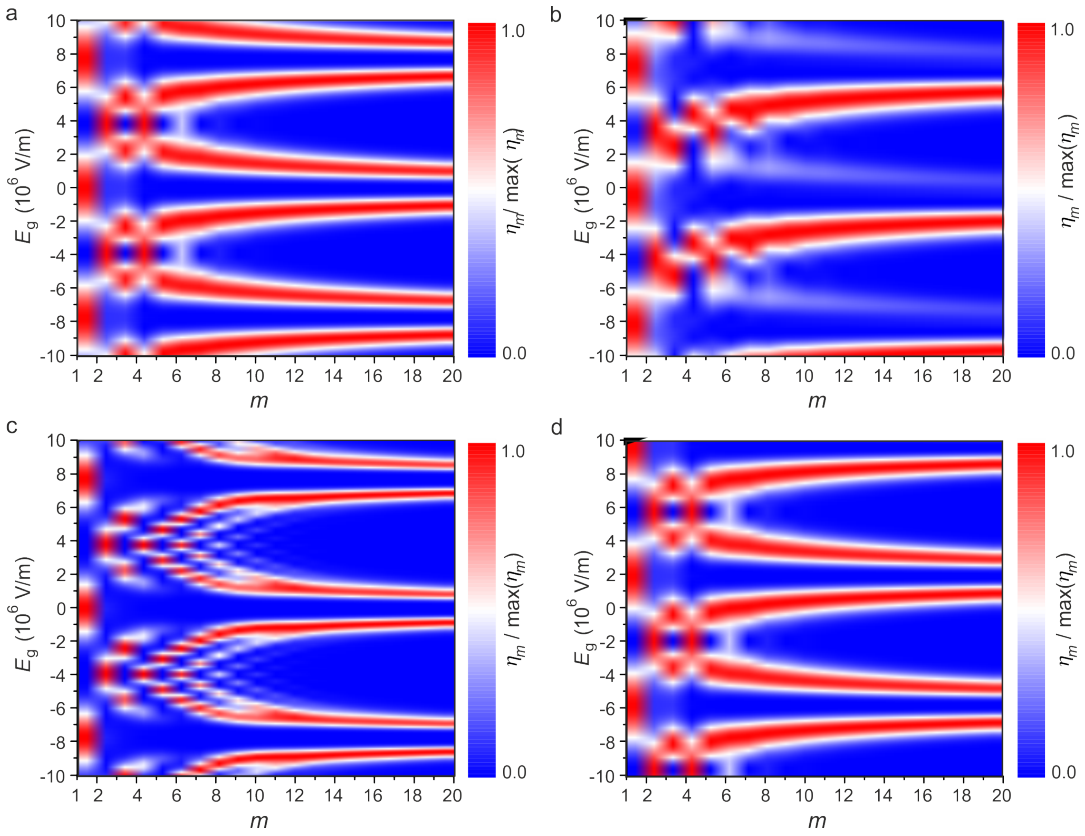

Figure 5.22: Effects of global asymmetries. a) Symmetric waveguide grating as reference. b) Asymmetric OrmoCore layer thicknesses (1950 nm top, 1900 nm bottom). c) Asymmetric grating shape. d) Asymmetric wafer thicknesses.

oscillations with respect to E_g, which are dampened out with increasing values of m (Fig. 5.22c). These oscillations occur as a result of additive phase terms and are a typical sign for strongly asymmetric coupling coefficients due to either non-resonant conditions or other asymmetries. Here, the shift of the excitation angle of the eigenmode dominates this occurrence of oscillations. Concerning an asymmetry induced by unequal thicknesses of the $LiTaO_3$ layers (Fig. 5.22d), a constant shift with respect to E_g is observed in comparison to the characteristics of the symmetric waveguide grating. These cases cover the most important global asymmetries.

Now, the effects of local inhomogeneities are considered (Fig. 5.23). These inhomogeneities are implemented as a local parameter change of the waveguide grating at $m = 10$ with respect to either the OrmoCore layer thicknesses (a), the grating layer thickness (b), the ratio of the beam amplitudes (c), and the wafer thicknesses (d). The corresponding parameters are shown in the caption of the Fig. 5.23. It can be observed that all these effects lead to distinct asymmetric characteristics of η_m.

All these characteristics above are used to fit the simulation model to the experimental data. Herein, it is important to note that the effects of global asymmetries and local inhomogeneities are distinguishable from each other, so that a fit to experimental data

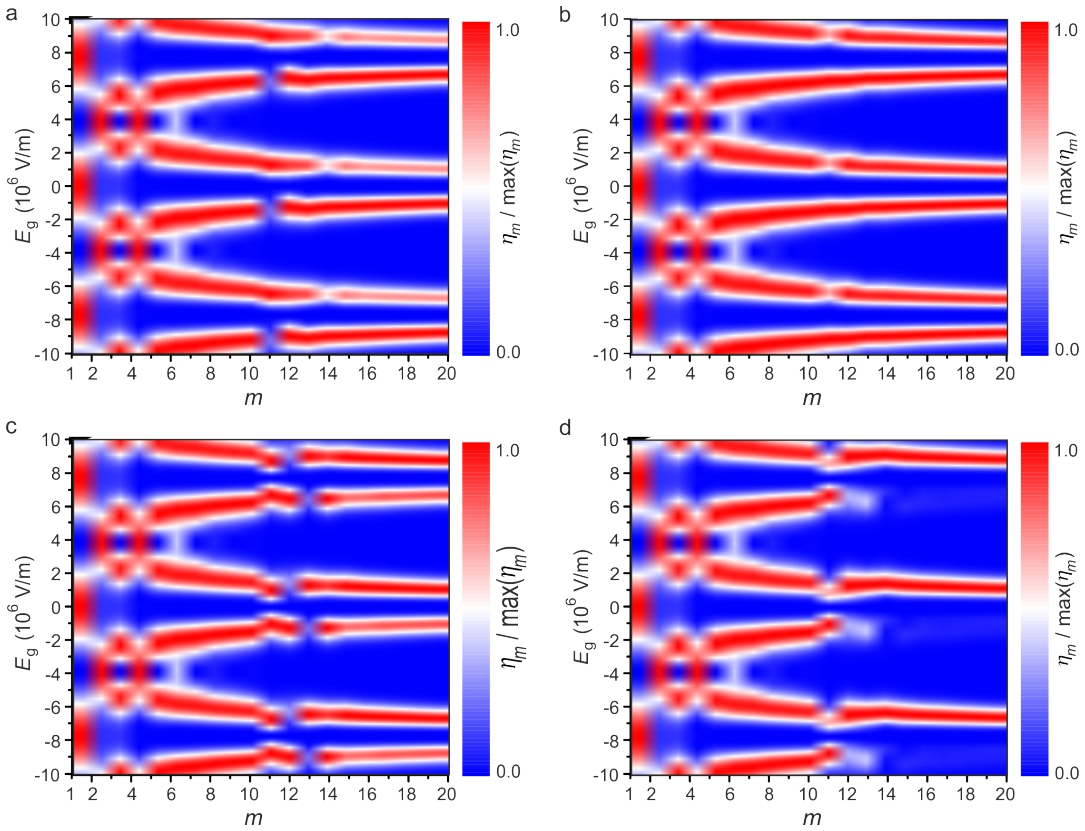

Figure 5.23: Effects of a local inhomogeneity introduced at $m = 10$. a) Inhomogeneity of OrmoCore layer thicknesses (top 1950 nm, bottom 1900 nm) b) Inhomogeneity of grating layer thickness (60 nm instead of 30 nm). c) Inhomogeneity leading to unequal beam amplitudes d) Inhomogeneity of the wafer thicknesses, causing a local phase shift of 0.4λ.

enables an unambiguous assignment of geometry parameters. As a matter of course, only physically reasonable asymmetries or inhomogeneities are introduced to ensure that the simulated values still allow a judgement of the model's validity. In detail, thickness variations were assumed to be below the tolerances of fabrication procedures. The grating geometry was strictly modeled according to AFM data [301]. Concerning the OrmoCore layer thicknesses, the best agreement between the simulation and experimental data is found with values of 1882 nm and 1900 nm (top and bottom). No further global asymmetries are assumed. One local inhomogeneity is assumed at $m = 1$ to match initially unequal input amplitudes and phase relations. Three more inhomogeneities are present at $m = 11$ and 12 as defects are obviously present. Strikingly, no other asymmetries or inhomogeneities are assumed between $m = 1$ and $m = 11$. Therefore, the behavior of η_m within this region exhibits valuable physical information. A comparison between the experimental data and the simulated ones shows excellent agreement and confirms the validity of the simulation model (Fig. 5.24).

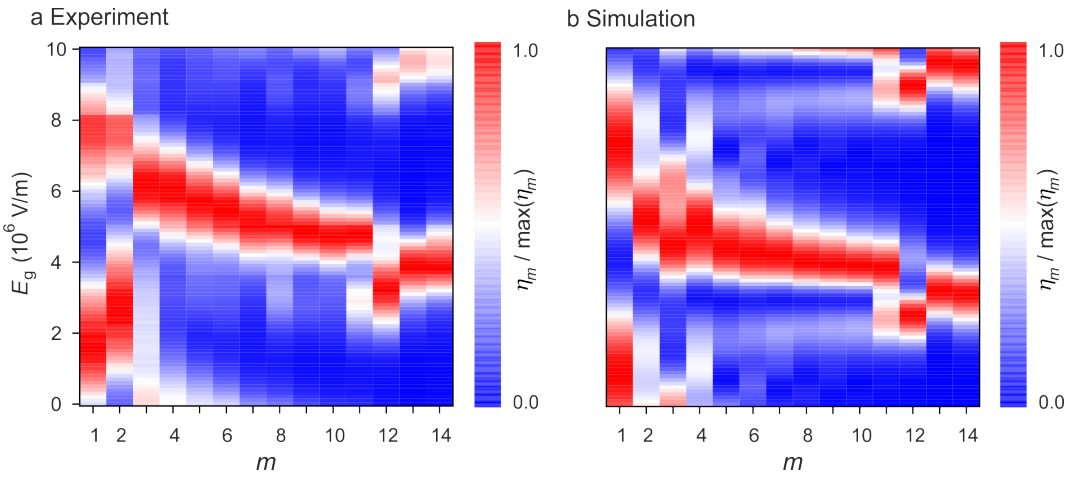

Figure 5.24: Comparison of experimentally obtained values of η_m (a) and simulated values (b) at $\lambda = 632.8$ nm and $\theta_{ext} = 19.65°$. The characteristics of both the measured and simulated data agree well with each other and, thus, confirm the existence of trapping and maximized local outcoupling.

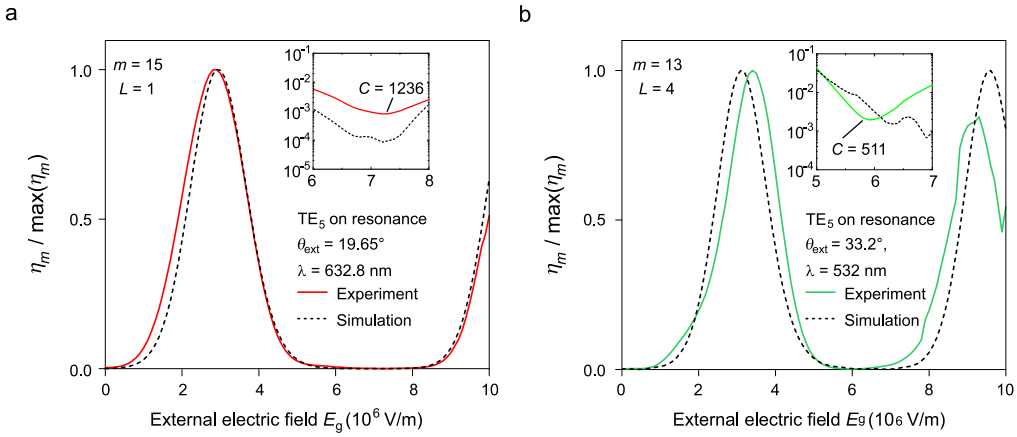

Figure 5.25: Measured and simulated values of η_m for different wavelengths. a) $\lambda = 632.8$ nm and $\theta_{ext} = 19.65°$. b) $\lambda = 532$ nm and $\theta_{ext} = 33.2°$. In both cases, trapping and maximized local outcoupling can be confirmed. The data from subfigure (a) are from ref. [301]

To show that the agreement between the model and the experiment is not only present for one wavelength, different lasers are used. Fig. 5.25 shows a comparison of η_m of for $\lambda = 632.8$ nm at $\theta_{ext} = 19.65°$ and $m = 15$ (Fig. 5.25a), and $\lambda = 532$ nm at $\theta_{ext} = 33.2°$ and $m = 13$ (Fig. 5.25b). Strikingly, large contrast values of 1236 ($\lambda = 632.8$ nm) and 511 ($\lambda = 532$ nm) can be observed. As these wavelengths and angles are in no distinct relation to each other (e.g. a rational number), it is unlikely that these observations are coincidental. Preliminary experiments show that the occurrence of trapping can even be observed for an incoherent broadband light source.

Therefore, it can be concluded that trapping and maximized local outcoupling are indeed present over a broad spectral range for the waveguide grating at hand. Summarizing

their properties with respect to the challenges which have been brought up in Chapter 4, they enable to incouple over a broad range of wavelengths and incident angles. Subsequent to its collection with $L_{prop} \approx 0.3$ mm, light can be trapped ($L_{prop} \approx 3$ m) with the help of local phase changes. In other words, all of these challenges have been successfully addressed. Nonetheless, as these findings are an entirely new concept, their potential consequences for solar concentrators need to be discussed. As this discussion is of subjunctive nature, it can be found in the Outlook of this thesis (see Chapter 6).

Chapter 6

Outlook

Over the course of this thesis, various systems with potential benefits for solar applications have been introduced.

It has been shown that plasmonic systems consisting of AgNP metasurfaces on a silver layer enable simultaneous broadband absorption and heat conductance, rendering them as interesting for solar thermal applications such as water vaporization and thermo-electrics. In addition, it has been demonstrated that the growth of AgNP under light illumination leads to metasurfaces which are adapted to the light source in the form of an engineered k-space. In the future, it is to question how this adaption to light could be used to circumvent the limits of conventional plasmonic systems. Obvious applications could be the use of the k-space engineered metasurfaces for plasmonically enhanced photovoltaics. Assuming that the morphology of the metasurface could be transferred into transparent dielectric media, scattering layers for solar concentrators could be achieved. For example, a stealthy hyperuniform metasurface could potentially be designed in a way that light is only scattered into angles above the critical angle of total internal reflection [233]. Another way to exploit the AgNP metasurfaces could be the following: considering that, subsequent to their growth, the AgNPs could still move on the surface, they might dynamically adapt to a moving light source (e.g. the Sun). This way, a self-tracking plasmonic system might be built. A general drawback of plasmonic systems based on AgNPs is their inherent Ohmic losses.

Concerning thin waveguide gratings consisting of loss-free materials, methods to achieve long propagation lengths with the help of node eigenmodes have been demonstrated. In an exemplary simulation of a waveguide grating, the propagation length (and, thus, the concentration) could be increased by a factor of around 1000 without changing the waveguide's thickness or parameters of the grating layer. Instead, only the geometric symmetry of the waveguide has been exploited, so that the filling factor attributed to node

eigenmodes has been drastically reduced. Moreover, it has been demonstrated that this elongation of the propagation lengths comes along with a drastic increase of the sensitivity to environmental changes, rendering such waveguide gratings as potentially important for sensors and light modulators in the future. For the use of the elongated propagation lengths for solar concentrators, it has been realized that many waveguide gratings would need to be stacked. Preliminary experiments have shown that stacking indeed increases the dynamic acceptance angle, but the necessary number of waveguide gratings leads to an unpractically large fabrication complexity. Moreover, residual outcoupling has been identified as another challenge.

Hybrid BICs have been identified as a way to turn the outcoupling efficiency down to zero. They could be experimentally observed. However, hybrid BICs are of singular nature and zero outcoupling efficiency can only be achieved for one wavelength and one outcoupling angle. Furthermore, Ohmic losses forbid to reach long propagation lengths.

For all these systems, it has been further recognized that their passive nature does not solve the initial problem of Sun-tracking. As a prerequisite for Sun-tracking, it has been identified that a waveguide should be locally switchable between the broadband trapping of light, and the propagation of light over large distances. This way, light could be locally coupled into a waveguide and subsequently guided to a focus point.

These challenges have been tackled using active systems in the regime of the absence of self-interference. Herein, the principle of achieving zero outcoupling efficiency for hybrid BICs has been transferred onto the relative phase between two beams within a waveguide grating. This way, the occurrence of zero outcoupling efficiency to radiation channels is not singular anymore and can be locally affected. Via a simplified theoretical model and the assumption of symmetry, conditions have been derived for which the beams can be locally switched between trapping and perfect local outcoupling. Using an exemplary waveguide grating, the existence of these phenomena has been demonstrated via the proposed model, independent numerical simulations and in experiment. Briefly summarizing these results, light can be locally incoupled, splitted into two beams, and subsequently trapped via controlling the relative phase between the two beams. Strikingly, these phenomena are present for a broad spectral range. In principle, they can be used to maximize the concentration of light with respect to a moving light source, that is, tracking. However, with this knowledge, it is to question which challenges still do remain and how they could be solved.

First of all, the use of homogeneous periodic layers has mainly been introduced to obtain fundamental physical phenomena under controlled and analytically feasible conditions. In fact, a grating diffracts light with via a lateral momentum transfer per diffraction order ν of $k'_{x,\nu}/k_0 = \nu \cdot \lambda/\Lambda$. As a consequence, longer wavelengths are attributed to larger

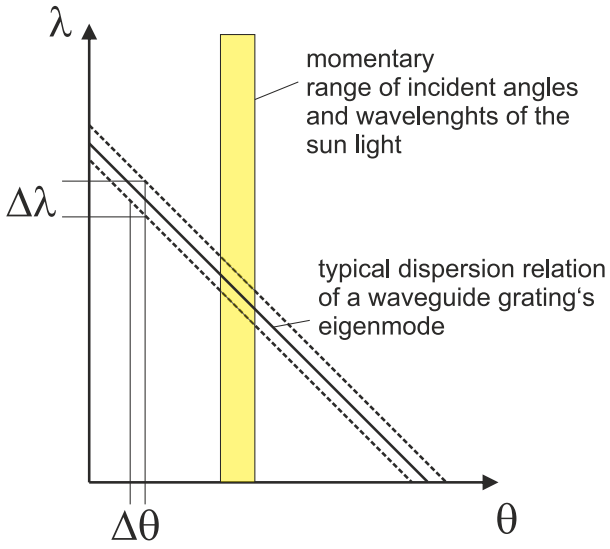

Figure 6.1: The dispersion relation, spectral width $\Delta\lambda$ and acceptance angle $\Delta\theta$ of a waveguide grating's eigenmode vs. the spectral range and angular range attributed to the Sun light. Only a small portion of the Sun light can couple to the eigenmode.

diffraction angles than shorter wavelengths (see Section 2.16). In a waveguide grating, this behavior leads to a typical dispersion relation of an eigenmode as it is displayed in Fig. 6.1. Here, every wavelength is attributed to a different angle of incidence under which the eigenmode can be excited. Therefore, subsequent to the collection of the Sun-light into a waveguide based solar concentrator with an initial structure, the local momentum transfer of a structure must be matched to the light's local spectrum and momentum to enable trapping. Finding an ideal (non-homogeneous) structure is, thus, an important challenge towards solar concentrators based on trapping and perfect coupling. One way to optimize future devices toward solar applications could therefore be the following: the simplest geometries which can be used to match the angular and spectral range attributed to Sun light are, as a matter of course, the ones which act on the zeroth order (e.g. refractive optics, mirrors, etc.). Commonly, these geometries are bulky, so that their use for the method at hand might be hard to realize. Nonetheless, there has been remarkable progress on the field of certain metasurfaces in the recent years. These metasurfaces introduce a phase gradient to bend the direction of the zeroth order. In practice, this means that a thin structured layer acts like a mirror or beam steerer. Recent results have shown that perfect coherence can be achieved for such metasurfaces [312]. Therefore, it might be concluded that trapping and perfect local outcoupling could be realized using metasurfaces to match the Sun's spectrum and range of angles of incidence.

It is further important to question whether the Sun as an incoherent light source can be switched between trapping and perfect coupling. Preliminary experiments could confirm that this is indeed possible, wherein detailed investigation have to be carried out in the future to quantify the local outcoupling efficiency as a function of the wavelength and

angle of incidence.

Using structures which provide large lateral momentum, the average direction of two trapped beams could be locally deflected within a waveguide toward a focal point. This procedure is called 'local deflection' and could be used to support or realize tracking.

It could also be considered to pre-focus light via external optics before it is trapped within a waveguide. As a matter of course, this pre-focusing leads to a larger divergence angle of the two beams within the waveguide. Therefore, the two beams would exhibit self-interference after a short distance of propagation when no appropriate design measures are considered. Such design measures could aim to spectrally split and distribute the light over a phase shifter area (e.g. consisting of a matrix of electrodes), so that there are enough degrees of freedom to enable both trapping and perfect local outcoupling (or local deflection) across the entire spectral and angular range of the incident light. Future studies should aim to investigate different phase shifter areas and light scattering structures to optimize Sun-tracking. Herein, one additional information on trapping has to be given. As photons are Bosons, two pairs of trapped beams do not disturb each other even when their paths cross. This fact has been confirmed via numerical simulations. By applying the same principle on the pre-focused light, this behavior suggests that the conditions for trapping would not be broken even when self-interference becomes present over light's path of propagation. In this sense, the absence of self-interference is only necessary to trap the two beams, but the subsequent introduction of self-interference does not lead to local outcoupling. Future designs of solar concentrators should, thus, take this possibility into account. Nonetheless, this argumentation is, at the current point in time, mostly hypothetical and the behavior of both trapping and perfect local outcoupling under the introduction of self-interference should be rigorously investigated by numerics and experiments. From the logical point of view, the possibility to locally switch between trapping and perfect local outcoupling (or local deflection) might be lost during this process, so that the direction of light should be already set toward a focal point before self-interference sets in.

Another challenge is that the control of the relative phase has been realized via a volume effect (the Pockel's effect) under high voltages. Causing relative phase shifts via other physical effects or miniaturizing the waveguide grating's dimensions (e.g. the thickness) could lead to improved future devices using smaller voltages.

Taking all these arguments above together, trapping and perfect local coupling offer plenty of promising options toward the realization of waveguide based solar concentrators using active Sun-tracking without mechanical parts.

Bibliography

[1] J. Houghton, "Global warming," *Reports on Progress in Physics*, vol. 68, no. 6, pp. 1343–1403, 2005.

[2] C. Folke, S. Polasky, J. Rockström, V. Galaz, F. Westley, M. Lamont, M. Scheffer, H. Österblom, S. R. Carpenter, F. S. Chapin, K. C. Seto, E. U. Weber, B. I. Crona, G. C. Daily, P. Dasgupta, O. Gaffney, L. J. Gordon, H. Hoff, S. A. Levin, J. Lubchenco, W. Steffen, and B. H. Walker, "Our future in the anthropocene biosphere," *Ambio*, vol. 50, no. 4, pp. 834–869, 2021.

[3] M. C. Ruiter, A. Couasnon, M. J. C. Homberg, J. E. Daniell, J. C. Gill, and P. J. Ward, "Why we can no longer ignore consecutive disasters," *Earth's Future*, vol. 8, no. 3, 2020.

[4] M. H. Saier, "Climate change, 2007," *Water, Air, and Soil Pollution*, vol. 181, no. 1, pp. 1–2, 2007.

[5] N. L. Panwar, S. C. Kaushik, and S. Kothari, "Role of renewable energy sources in environmental protection: A review," *Renewable and Sustainable Energy Reviews*, vol. 15, no. 3, pp. 1513–1524, 2011.

[6] N. Kannan and D. Vakeesan, "Solar energy for future world: - a review," *Renewable and Sustainable Energy Reviews*, vol. 62, pp. 1092–1105, 2016.

[7] G. Leach, "The energy transition," *Energy Policy*, vol. 20, no. 2, pp. 116–123, 1992.

[8] R. Falkner, "The paris agreement and the new logic of international climate politics," *International Affairs*, vol. 92, no. 5, pp. 1107–1125, 2016.

[9] P. R. Shukla, J. Skea, R. Slade, A. Al Khourdajie, R. van Diemen, D. McCollum, M. Pathak, S. Some, P. Vyas, R. Fradera, M. Belkacemi, A. Hasija, G. Lisboa, S. Luz, J. Malley, and eds., "Climate change 2022: Mitigation of climate change. contribution of working group iii to the sixth assessment report of the intergovernmental panel on climate change." *IPCC*, 2022.

[10] P. A. Owusu and S. Asumadu-Sarkodie, "A review of renewable energy sources, sustainability issues and climate change mitigation," *Cogent Engineering*, vol. 3, no. 1, 2016.

[11] S. Fawzy, A. I. Osman, J. Doran, and D. W. Rooney, "Strategies for mitigation of climate change: a review," *Environmental Chemistry Letters*, vol. 18, no. 6, pp. 2069–2094, 2020.

[12] F. Bilgili, E. Koçak, Ü. Bulut, and S. Kuşkaya, "Can biomass energy be an efficient policy tool for sustainable development?," *Renewable and Sustainable Energy Reviews*, vol. 71, pp. 830–845, 2017.

[13] V. S. Sikarwar, M. Zhao, P. Clough, J. Yao, X. Zhong, M. Z. Memon, N. Shah, E. J. Anthony, and P. S. Fennell, "An overview of advances in biomass gasification," *Energy & Environmental Science*, vol. 9, no. 10, pp. 2939–2977, 2016.

[14] F. Creutzig, N. H. Ravindranath, G. Berndes, S. Bolwig, R. Bright, F. Cherubini, H. Chum, E. Corbera, M. Delucchi, A. Faaij, J. Fargione, H. Haberl, G. Heath, O. Lucon, R. Plevin, A. Popp, C. Robledo-Abad, S. Rose, P. Smith, A. Stromman, S. Suh, and O. Masera, "Bioenergy and climate change mitigation: an assessment," *GCB Bioenergy*, vol. 7, no. 5, pp. 916–944, 2015.

[15] W. V. Reid, M. K. Ali, and C. B. Field, "The future of bioenergy," *Global change biology*, vol. 26, no. 1, pp. 274–286, 2020.

[16] M. Guo, W. Song, and J. Buhain, "Bioenergy and biofuels: History, status, and perspective," *Renewable and Sustainable Energy Reviews*, vol. 42, pp. 712–725, 2015.

[17] J. Kemper, "Biomass and carbon dioxide capture and storage: A review," *International Journal of Greenhouse Gas Control*, vol. 40, pp. 401–430, 2015.

[18] Y. Kumar, J. Ringenberg, S. S. Depuru, V. K. Devabhaktuni, J. W. Lee, E. Nikolaidis, B. Andersen, and A. Afjeh, "Wind energy: Trends and enabling technologies," *Renewable and Sustainable Energy Reviews*, vol. 53, pp. 209–224, 2016.

[19] P. Veers, K. Dykes, E. Lantz, S. Barth, C. L. Bottasso, O. Carlson, A. Clifton, J. Green, P. Green, H. Holttinen, D. Laird, V. Lehtomäki, J. K. Lundquist, J. Manwell, M. Marquis, C. Meneveau, P. Moriarty, X. Munduate, M. Muskulus, J. Naughton, L. Pao, J. Paquette, J. Peinke, A. Robertson, J. Sanz Rodrigo, A. M. Sempreviva, J. C. Smith, A. Tuohy, and R. Wiser, "Grand challenges in the science of wind energy," *Science*, vol. 366, no. 6464, 2019.

[20] E. F. Moran, M. C. Lopez, N. Moore, N. Müller, and D. W. Hyndman, "Sustainable hydropower in the 21st century," *Proceedings of the National Academy of Sciences of the United States of America*, vol. 115, no. 47, pp. 11891–11898, 2018.

[21] C. Zarfl, A. E. Lumsdon, J. Berlekamp, L. Tydecks, and K. Tockner, "A global boom in hydropower dam construction," *Aquatic Sciences*, vol. 77, no. 1, pp. 161–170, 2015.

[22] E. Barbier, "Geothermal energy technology and current status: an overview," *Renewable and Sustainable Energy Reviews*, vol. 6, no. 1-2, pp. 3–65, 2002.

[23] M. H. Dickson and M. Fanelli, *Geothermal Energy.* Routledge, 2013.

[24] J. W. Lund and A. N. Toth, "Direct utilization of geothermal energy 2020 worldwide review," *Geothermics*, vol. 90, 2021.

[25] A. Anderson and B. Rezaie, "Geothermal technology: Trends and potential role in a sustainable future," *Applied Energy*, vol. 248, pp. 18–34, 2019.

[26] M. Z. Jacobson, M. A. Delucchi, Z. A. Bauer, S. C. Goodman, W. E. Chapman, M. A. Cameron, C. Bozonnat, L. Chobadi, H. A. Clonts, P. Enevoldsen, J. R. Erwin, S. N. Fobi, O. K. Goldstrom, E. M. Hennessy, J. Liu, J. Lo, C. B. Meyer, S. B. Morris, K. R. Moy, P. L. O'Neill, I. Petkov, S. Redfern, R. Schucker, M. A. Sontag, J. Wang, E. Weiner, and A. S. Yachanin, "100% clean and renewable wind, water, and sunlight all-sector energy roadmaps for 139 countries of the world," *Joule*, vol. 1, no. 1, pp. 108–121, 2017.

[27] V. Khare, S. Nema, and P. Baredar, "Solar–wind hybrid renewable energy system: A review," *Renewable and Sustainable Energy Reviews*, vol. 58, pp. 23–33, 2016.

[28] F. Creutzig, P. Agoston, J. C. Goldschmidt, G. Luderer, G. Nemet, and R. C. Pietzcker, "The underestimated potential of solar energy to mitigate climate change," *Nature Energy*, vol. 2, no. 9, 2017.

[29] T. Tsoutsos, N. Frantzeskaki, and V. Gekas, "Environmental impacts from the solar energy technologies," *Energy Policy*, vol. 33, no. 3, pp. 289–296, 2005.

[30] D. Turney and V. Fthenakis, "Environmental impacts from the installation and operation of large-scale solar power plants," *Renewable and Sustainable Energy Reviews*, vol. 15, no. 6, pp. 3261–3270, 2011.

[31] M. K. H. Rabaia, M. A. Abdelkareem, E. T. Sayed, K. Elsaid, K.-J. Chae, T. Wilberforce, and A. G. Olabi, "Environmental impacts of solar energy systems: A review," *The Science of the total environment*, vol. 754, 2021.

[32] K. Ravi Kumar, N. Krishna Chaitanya, and N. Sendhil Kumar, "Solar thermal energy technologies and its applications for process heating and power generation – a review," *Journal of Cleaner Production*, vol. 282, 2021.

[33] M. Thirugnanasambandam, S. Iniyan, and R. Goic, "A review of solar thermal technologies," *Renewable and Sustainable Energy Reviews*, vol. 14, no. 1, pp. 312–322, 2010.

[34] S. A. Kalogirou, "Solar thermal collectors and applications," *Progress in Energy and Combustion Science*, vol. 30, no. 3, pp. 231–295, 2004.

[35] Y. Tian and C. Y. Zhao, "A review of solar collectors and thermal energy storage in solar thermal applications," *Applied Energy*, vol. 104, pp. 538–553, 2013.

[36] B. Xu, P. Li, and C. Chan, "Application of phase change materials for thermal energy storage in concentrated solar thermal power plants: A review to recent developments," *Applied Energy*, vol. 160, pp. 286–307, 2015.

[37] D. Yogi Goswami, "Solar thermal power technology: Present status and ideas for the future," *Energy Sources*, vol. 20, no. 2, pp. 137–145, 1998.

[38] V. Siva Reddy, S. C. Kaushik, K. R. Ranjan, and S. K. Tyagi, "State-of-the-art of solar thermal power plants—a review," *Renewable and Sustainable Energy Reviews*, vol. 27, pp. 258–273, 2013.

[39] O. Behar, "Solar thermal power plants – a review of configurations and performance comparison," *Renewable and Sustainable Energy Reviews*, vol. 92, pp. 608–627, 2018.

[40] O. Behar, A. Khellaf, and K. Mohammedi, "A review of studies on central receiver solar thermal power plants," *Renewable and Sustainable Energy Reviews*, vol. 23, pp. 12–39, 2013.

[41] A. McEvoy, T. Markvart, and L. Castaner, *Practical Handbook of Photovoltaics: Fundamentals and Applications*. Elsevier, 2003.

[42] N. M. Haegel, H. Atwater, T. Barnes, C. Breyer, A. Burrell, Y.-M. Chiang, S. de Wolf, B. Dimmler, D. Feldman, S. Glunz, J. C. Goldschmidt, D. Hochschild, R. Inzunza, I. Kaizuka, B. Kroposki, S. Kurtz, S. Leu, R. Margolis, K. Matsubara, A. Metz, W. K. Metzger, M. Morjaria, S. Niki, S. Nowak, I. M. Peters, S. Philipps, T. Reindl, A. Richter, D. Rose, K. Sakurai, R. Schlatmann, M. Shikano, W. Sinke, R. Sinton, B. J. Stanbery, M. Topic, W. Tumas, Y. Ueda, J. van de Lagemaat, P. Verlinden, M. Vetter, E. Warren, M. Werner, M. Yamaguchi, and A. W. Bett,

"Terawatt-scale photovoltaics: Transform global energy," *Science*, vol. 364, no. 6443, pp. 836–838, 2019.

[43] A. Jäger-Waldau, "Snapshot of photovoltaics—february 2020," *Energies*, vol. 13, no. 4, p. 930, 2020.

[44] E. Kabir, P. Kumar, S. Kumar, A. A. Adelodun, and K.-H. Kim, "Solar energy: Potential and future prospects," *Renewable and Sustainable Energy Reviews*, vol. 82, pp. 894–900, 2018.

[45] K. O. Brinkmann, T. Becker, F. Zimmermann, C. Kreusel, T. Gahlmann, M. Theisen, T. Haeger, S. Olthof, C. Tückmantel, M. Günster, T. Maschwitz, F. Göbelsmann, C. Koch, D. Hertel, P. Caprioglio, F. Peña-Camargo, L. Perdigón-Toro, A. Al-Ashouri, L. Merten, A. Hinderhofer, L. Gomell, S. Zhang, F. Schreiber, S. Albrecht, K. Meerholz, D. Neher, M. Stolterfoht, and T. Riedl, "Perovskite-organic tandem solar cells with indium oxide interconnect," *Nature*, vol. 604, no. 7905, pp. 280–286, 2022.

[46] J.-P. Correa-Baena, M. Saliba, T. Buonassisi, M. Grätzel, A. Abate, W. Tress, and A. Hagfeldt, "Promises and challenges of perovskite solar cells," *Science*, vol. 358, no. 6364, pp. 739–744, 2017.

[47] H. J. Snaith, "Present status and future prospects of perovskite photovoltaics," *Nature Materials*, vol. 17, no. 5, pp. 372–376, 2018.

[48] M. Victoria, N. Haegel, I. M. Peters, R. Sinton, A. Jäger-Waldau, C. del Cañizo, C. Breyer, M. Stocks, A. Blakers, I. Kaizuka, K. Komoto, and A. Smets, "Solar photovoltaics is ready to power a sustainable future," *Joule*, vol. 5, no. 5, pp. 1041–1056, 2021.

[49] D. Gielen, F. Boshell, D. Saygin, M. D. Bazilian, N. Wagner, and R. Gorini, "The role of renewable energy in the global energy transformation," *Energy Strategy Reviews*, vol. 24, pp. 38–50, 2019.

[50] D. Barlev, R. Vidu, and P. Stroeve, "Innovation in concentrated solar power," *Solar Energy Materials and Solar Cells*, vol. 95, no. 10, pp. 2703–2725, 2011.

[51] R. Winston, "Principles of solar concentrators of a novel design," *Solar Energy*, vol. 16, no. 2, pp. 89–95, 1974.

[52] H. L. Zhang, J. Baeyens, J. Degrève, and G. Cacères, "Concentrated solar power plants: Review and design methodology," *Renewable and Sustainable Energy Reviews*, vol. 22, pp. 466–481, 2013.

[53] A. Bejan, *Advanced Engineering Thermodynamics*. John Wiley & Sons, 2016.

[54] L. Yaqi, H. Yaling, and W. Weiwei, "Optimization of solar-powered stirling heat engine with finite-time thermodynamics," *Renewable Energy*, vol. 36, no. 1, pp. 421–427, 2011.

[55] T. M. Pavlović, I. S. Radonjić, D. D. Milosavljević, and L. S. Pantić, "A review of concentrating solar power plants in the world and their potential use in serbia," *Renewable and Sustainable Energy Reviews*, vol. 16, no. 6, pp. 3891–3902, 2012.

[56] H. Cotal, C. Fetzer, J. Boisvert, G. Kinsey, R. King, P. Hebert, H. Yoon, and N. Karam, "Iii–v multijunction solar cells for concentrating photovoltaics," *Energy Environ. Sci.*, vol. 2, no. 2, pp. 174–192, 2009.

[57] P. Pérez-Higueras, E. Muñoz, G. Almonacid, and P. G. Vidal, "High concentrator photovoltaics efficiencies: Present status and forecast," *Renewable and Sustainable Energy Reviews*, vol. 15, no. 4, pp. 1810–1815, 2011.

[58] S. P. Philipps, A. W. Bett, K. Horowitz, and S. Kurtz, "Current status of concentrator photovoltaic (cpv) technology."

[59] I. Luque-Heredia, J.M. Moreno, P.H.Magalhaes, R. Cervantes, G. Quéméré, O. Laurent, "Inspira's cpv sun tracking," in *Concentrator Photovoltaics*, pp. 221–251, Springer, Berlin, Heidelberg, 2007.

[60] M. Green, E. Dunlop, J. Hohl-Ebinger, M. Yoshita, N. Kopidakis, and X. Hao, "Solar cell efficiency tables (version 57)," *Progress in Photovoltaics: Research and Applications*, vol. 29, no. 1, pp. 3–15, 2021.

[61] Z. Wang, Q. Lin, B. Wenger, M. G. Christoforo, Y.-H. Lin, M. T. Klug, M. B. Johnston, L. M. Herz, and H. J. Snaith, "High irradiance performance of metal halide perovskites for concentrator photovoltaics," *Nature Energy*, vol. 3, no. 10, pp. 855–861, 2018.

[62] Y. Zhou, Y. Chen, Q. Zhang, Y. Zhou, M. Tai, K. Koumoto, and H. Lin, "A highly-efficient concentrated perovskite solar cell-thermoelectric generator tandem system," *Journal of Energy Chemistry*, vol. 59, pp. 730–735, 2021.

[63] A. Hasan, J. Sarwar, and A. H. Shah, "Concentrated photovoltaic: A review of thermal aspects, challenges and opportunities," *Renewable and Sustainable Energy Reviews*, vol. 94, pp. 835–852, 2018.

[64] S. Sripadmanabhan Indira, C. A. Vaithilingam, K.-K. Chong, R. Saidur, M. Faizal, S. Abubakar, and S. Paiman, "A review on various configurations of hybrid concentrator photovoltaic and thermoelectric generator system," *Solar Energy*, vol. 201, pp. 122–148, 2020.

[65] A. Radwan, S. Ookawara, and M. Ahmed, "Thermal management of concentrator photovoltaic systems using two-phase flow boiling in double-layer microchannel heat sinks," *Applied Energy*, vol. 241, pp. 404–419, 2019.

[66] G. Smestad, H. Ries, R. Winston, and E. Yablonovitch, "The thermodynamic limits of light concentrators," *Solar Energy Materials*, vol. 21, no. 2-3, pp. 99–111, 1990.

[67] C.-Y. Lee, P.-C. Chou, C.-M. Chiang, and C.-F. Lin, "Sun tracking systems: a review," *Sensors (Basel, Switzerland)*, vol. 9, no. 5, pp. 3875–3890, 2009.

[68] A. Z. Hafez, A. M. Yousef, and N. M. Harag, "Solar tracking systems: Technologies and trackers drive types – a review," *Renewable and Sustainable Energy Reviews*, vol. 91, pp. 754–782, 2018.

[69] P. Heller, *The performance of concentrated solar power (CSP) systems: Analysis, measurement and assessment*. Woodhead Publishing, first edition ed., 2017.

[70] H. Apostoleris, M. Stefancich, and M. Chiesa, *Concentrating Photovoltaics (CPV): The Path Ahead*. Springer International Publishing, 2018.

[71] H. Price, E. Lu¨pfert, D. Kearney, E. Zarza, G. Cohen, R. Gee, and R. Mahoney, "Advances in parabolic trough solar power technology," *Journal of Solar Energy Engineering*, vol. 124, no. 2, pp. 109–125, 2002.

[72] K. S. Reddy, K. R. Kumar, and G. V. Satyanarayana, "Numerical investigation of energy-efficient receiver for solar parabolic trough concentrator," *Heat Transfer Engineering*, vol. 29, no. 11, pp. 961–972, 2008.

[73] K. Lovegrove, G. Burgess, and J. Pye, "A new 500m^2 paraboloidal dish solar concentrator," *Solar Energy*, vol. 85, no. 4, pp. 620–626, 2011.

[74] Y. Shuai, X.-L. Xia, and H.-P. Tan, "Radiation performance of dish solar concentrator/cavity receiver systems," *Solar Energy*, vol. 82, no. 1, pp. 13–21, 2008.

[75] H. Hijazi, O. Mokhiamar, and O. Elsamni, "Mechanical design of a low cost parabolic solar dish concentrator," *Alexandria Engineering Journal*, vol. 55, no. 1, pp. 1–11, 2016.

[76] A. Rabl, "Comparison of solar concentrators," *Solar Energy*, vol. 18, no. 2, pp. 93–111, 1976.

[77] T. Cooper, F. Dähler, G. Ambrosetti, A. Pedretti, and A. Steinfeld, "Performance of compound parabolic concentrators with polygonal apertures," *Solar Energy*, vol. 95, pp. 308–318, 2013.

[78] A.-J. N. Khalifa and S. S. Al-Mutawalli, "Effect of two-axis sun tracking on the performance of compound parabolic concentrators," *Energy Conversion and Management*, vol. 39, no. 10, pp. 1073–1079, 1998.

[79] Y. T. Chen, K. K. Chong, T. P. Bligh, L. C. Chen, J. Yunus, K. S. Kannan, B. H. Lim, C. S. Lim, M. A. Alias, N. Bidin, O. Aliman, S. Salehan, S. Rezan S.A.H, C. M. Tam, and K. K. Tan, "Non-imaging, focusing heliostat," *Solar Energy*, vol. 71, no. 3, pp. 155–164, 2001.

[80] R. Leutz and A. Suzuki, *Nonimaging Fresnel Lenses: Design and Performance of Solar Concentrators*. Springer Science & Business Media, 2001.

[81] R. Leutz, A. Suzuki, A. Akisawa, and T. Kashiwagi, "Design of a nonimaging fresnel lens for solar concentrators," *Solar Energy*, vol. 65, no. 6, pp. 379–387, 1999.

[82] W. T. Xie, Y. J. Dai, R. Z. Wang, and K. Sumathy, "Concentrated solar energy applications using fresnel lenses: A review," *Renewable and Sustainable Energy Reviews*, vol. 15, no. 6, pp. 2588–2606, 2011.

[83] D. R. Mills and G. L. Morrison, "Compact linear fresnel reflector solar thermal powerplants," *Solar Energy*, vol. 68, no. 3, pp. 263–283, 2000.

[84] R. Abbas, J. Muñoz-Antón, M. Valdés, and J. M. Martínez-Val, "High concentration linear fresnel reflectors," *Energy Conversion and Management*, vol. 72, pp. 60–68, 2013.

[85] Y. Yao, Y. Hu, S. Gao, G. Yang, and J. Du, "A multipurpose dual-axis solar tracker with two tracking strategies," *Renewable Energy*, vol. 72, pp. 88–98, 2014.

[86] H. Mousazadeh, A. Keyhani, A. Javadi, H. Mobli, K. Abrinia, and A. Sharifi, "A review of principle and sun-tracking methods for maximizing solar systems output," *Renewable and Sustainable Energy Reviews*, vol. 13, no. 8, pp. 1800–1818, 2009.

[87] İ. Sefa, M. Demirtas, and İ. Çolak, "Application of one-axis sun tracking system," *Energy Conversion and Management*, vol. 50, no. 11, pp. 2709–2718, 2009.

[88] V. Poulek and M. Libra, "New solar tracker," *Solar Energy Materials and Solar Cells*, vol. 51, no. 2, pp. 113–120, 1998.

[89] A. Awasthi, A. K. Shukla, M. M. S.R., C. Dondariya, K. N. Shukla, D. Porwal, and G. Richhariya, "Review on sun tracking technology in solar pv system," *Energy Reports*, vol. 6, pp. 392–405, 2020.

[90] F. Duerr, Y. Meuret, and H. Thienpont, "Tailored free-form optics with movement to integrate tracking in concentrating photovoltaics," *Optics express*, vol. 21, no. S3, pp. A401–A411, 2013.

[91] J. M. Hallas, J. H. Karp, E. J. Tremblay, and J. E. Ford, "Lateral translation micro-tracking of planar micro-optic solar concentrator," in *High and Low Concentrator Systems for Solar Electric Applications V* (L. E. Greene and R. A. Sherif, eds.), vol. 7769 of *SPIE Proceedings*, 2010.

[92] A. Ito, D. Sato, and N. Yamada, "Optical design and demonstration of microtracking cpv module with bi-convex aspheric lens array," *Optics express*, vol. 26, no. 18, pp. A879–A891, 2018.

[93] J. S. Price, X. Sheng, B. M. Meulblok, J. A. Rogers, and N. C. Giebink, "Wide-angle planar microtracking for quasi-static microcell concentrating photovoltaics," *Nature communications*, vol. 6, p. 6223, 2015.

[94] G. S. Brulo, A. J. Grede, A. J. Ren, C. D. Rahn, and N. C. Giebink, "Design of a high-concentration microtracking photovoltaic system," *Journal of Mechanisms and Robotics*, vol. 11, no. 6, 2019.

[95] A. J. Grede, J. S. Price, and N. C. Giebink, "Fundamental and practical limits of planar tracking solar concentrators," *Optics express*, vol. 24, no. 26, pp. A1635–A1646, 2016.

[96] J. S. Price, A. J. Grede, B. Wang, M. V. Lipski, B. Fisher, K.-T. Lee, J. He, G. S. Brulo, X. Ma, S. Burroughs, C. D. Rahn, R. G. Nuzzo, J. A. Rogers, and N. C. Giebink, "High-concentration planar microtracking photovoltaic system exceeding 30% efficiency," *Nature Energy*, vol. 2, no. 8, 2017.

[97] J. H. Karp, E. J. Tremblay, and J. E. Ford, "Planar micro-optic solar concentrator," *Optics express*, vol. 18, no. 2, pp. 1122–1133, 2010.

[98] Y. Liu, R. Huang, and C. K. Madsen, "Two-axis tracking using translation stages for a lens-to-channel waveguide solar concentrator," *Optics express*, vol. 22, no. S6, pp. A1567–A1575, 2014.

[99] P. Xie, H. Lin, Y. Liu, and B. Li, "Total internal reflection-based planar waveguide solar concentrator with symmetric air prisms as couplers," *Optics express*, vol. 22, no. S6, pp. A1389–A1398, 2014.

[100] C. Michel, P. Blain, L. Clermont, F. Languy, C. Lenaerts, K. Fleury-Frenette, M. Décultot, S. Habraken, D. Vandormael, R. Cloots, G. K. V. Thalluri, C. Henrist, P. Colson, and J. Loicq, "Waveguide solar concentrator design with spectrally separated light," *Solar Energy*, vol. 157, pp. 1005–1016, 2017.

[101] Y. Liu, R. Huang, and C. K. Madsen, "Design of a lens-to-channel waveguide system as a solar concentrator structure," *Optics Express*, vol. 22, no. S2, pp. A198–A204, 2014.

[102] S. Bouchard and S. Thibault, "Grin planar waveguide concentrator used with a single axis tracker," *Optics express*, vol. 22, no. S2, pp. A248–A258, 2014.

[103] J. H. Karp, E. J. Tremblay, J. M. Hallas, and J. E. Ford, "Orthogonal and secondary concentration in planar micro-optic solar collectors," *Optics express*, vol. 19, no. S4, pp. A673–A685, 2011.

[104] T.-C. Teng, C.-H. Kuo, and Y.-J. Li, "Planar solar concentrator composed of stacked waveguides with arc-segment structures and movable receiving assemblies," *Optics express*, vol. 28, no. 23, pp. 34362–34377, 2020.

[105] J. M. Hallas, K. A. Baker, J. H. Karp, E. J. Tremblay, and J. E. Ford, "Two-axis solar tracking accomplished through small lateral translations," *Applied optics*, vol. 51, no. 25, pp. 6117–6124, 2012.

[106] S. Bouchard and S. Thibault, "Planar waveguide concentrator used with a seasonal tracker," *Applied optics*, vol. 51, no. 28, pp. 6848–6854, 2012.

[107] W.-C. Shieh and G.-D. Su, "Compact solar concentrator designed by minilens and slab waveguide," in *High and Low Concentrator Systems for Solar Electric Applications VI* (K. VanSant and R. A. Sherif, eds.), SPIE Proceedings, SPIE, 2011.

[108] J. H. Karp and J. E. Ford, "Planar micro-optic solar concentration using multiple imaging lenses into a common slab waveguide," in *High and Low Concentrator Systems for Solar Electric Applications IV* (L. E. Greene, ed.), SPIE Proceedings, SPIE, 2009.

[109] H. Apostoleris, M. Stefancich, and M. Chiesa, "Tracking-integrated systems for concentrating photovoltaics," *Nature Energy*, vol. 1, no. 4, 2016.

[110] A. Lamoureux, K. Lee, M. Shlian, S. R. Forrest, and M. Shtein, "Dynamic kirigami structures for integrated solar tracking," *Nature communications*, vol. 6, 2015.

[111] W. Wang, C. Li, H. Rodrigue, F. Yuan, M.-W. Han, M. Cho, and S.-H. Ahn, "Kirigami/origami-based soft deployable reflector for optical beam steering," *Advanced Functional Materials*, vol. 27, no. 7, 2017.

[112] J. A. Carballo, J. Bonilla, M. Berenguel, J. Fernández-Reche, and G. García, "New approach for solar tracking systems based on computer vision, low cost hardware and deep learning," *Renewable Energy*, vol. 133, pp. 1158–1166, 2019.

[113] T. A. Siddiqui, S. Bharadwaj, and S. Kalyanaraman, "A deep learning approach to solar-irradiance forecasting in sky-videos," in *2019 IEEE Winter Conference on Applications of Computer Vision (WACV)*, pp. 2166–2174, 2019.

[114] N. AL-Rousan, N. A. Mat Isa, and M. K. Mat Desa, "Efficient single and dual axis solar tracking system controllers based on adaptive neural fuzzy inference system," *Journal of King Saud University - Engineering Sciences*, vol. 32, no. 7, pp. 459–469, 2020.

[115] J. C. Sattler, M. Röger, P. Schwarzbözl, R. Buck, A. Macke, C. Raeder, and J. Göttsche, "Review of heliostat calibration and tracking control methods," *Solar Energy*, vol. 207, pp. 110–132, 2020.

[116] L. D. DiDomenico, "Towards doubling solar harvests using wide-angle, broad-band microfluidic beam steering arrays," *Optics Express*, vol. 23, no. 24, p. A1398, 2015.

[117] C. Enrico Clement and S.-Y. Park, "High-performance beam steering using electrowetting-driven liquid prism fabricated by a simple dip-coating method," *Applied Physics Letters*, vol. 108, no. 19, 2016.

[118] V. Zagolla, D. Dominé, E. Tremblay, and C. Moser, "Self-tracking solar concentrator with an acceptance angle of 32°," *Optics express*, vol. 22, no. 7, pp. A1880–A1894, 2014.

[119] V. Zagolla, E. Tremblay, and C. Moser, "Proof of principle demonstration of a self-tracking concentrator," *Optics express*, vol. 22, no. S2, pp. A498–A510, 2014.

[120] E. J. Tremblay, V. Zagolla, D. Loterie, and C. Moser, "Self-tracking planar concentrator using a solar actuated phase-change mechanism," in *Physics, Simulation, and Photonic Engineering of Photovoltaic Devices II*, SPIE Proceedings, SPIE, 2013.

[121] K. A. Baker, J. H. Karp, E. J. Tremblay, J. M. Hallas, and J. E. Ford, "Reactive self-tracking solar concentrators: concept, design, and initial materials characterization," *Applied optics*, vol. 51, no. 8, pp. 1086–1094, 2012.

[122] V. Zagolla, E. Tremblay, and C. Moser, "Efficiency of a micro-bubble reflector based, self-adaptive waveguide solar concentrator," in *Physics, Simulation, and Photonic Engineering of Photovoltaic Devices II*, SPIE Proceedings, SPIE, 2013.

[123] D. J. Griffiths, *Introduction to electrodynamics*. Cambridge University Press, 2017.

[124] J. D. Jackson and R. F. Fox, "Classical electrodynamics, 3rd ed," *American Journal of Physics*, vol. 67, no. 9, pp. 841–842, 1999.

[125] S. Cloude, *An introduction to electromagnetic wave propagation and antennas*. Springer, 1995.

[126] P. C. Clemmow, *The Plane Wave Spectrum Representation of Electromagnetic Fields: International Series of Monographs in Electromagnetic Waves*. Elsevier, 2013.

[127] L. D. Landau, E. M. Lifšic, and L. P. Pitaevskij, *Electrodynamics of continuous media*, vol. 8. Elsevier Butterworth-Heinemann, 2008.

[128] D. Marcuse, *Theory of Dielectric Optical Waveguides*. Elsevier, 2013.

[129] T. Tamir and S. Zhang, "Modal transmission-line theory of multilayered grating structures," *Journal of Lightwave Technology*, vol. 14, no. 5, pp. 914–927, 1996.

[130] I. Shutsko, M. Buchmüller, M. Meudt, and P. Görrn, "Light-controlled fabrication of disordered hyperuniform metasurfaces," *Advanced Materials Technologies*, 2022.

[131] S. A. Maier, *Plasmonics: Fundamentals and applications*. Springer, 2007.

[132] E. D. Palik, *Handbook of Optical Constants of Solids*. s.l.: Elsevier professional, 1. aufl. ed., 1997.

[133] H. Raether, *Surface Plasmons on Smooth and Rough Surfaces and on Gratings*, vol. 111. Springer, 1988.

[134] P. Berini, "Long-range surface plasmon polaritons," *Advances in Optics and Photonics*, vol. 1, no. 3, p. 484, 2009.

[135] Y. Fang and M. Sun, "Nanoplasmonic waveguides: towards applications in integrated nanophotonic circuits," *Light: Science & Applications*, vol. 4, no. 6, 2015.

[136] S. Enoch and N. Bonod, *Plasmonics: From Basics to Advanced Topics*. Springer, 2012.

[137] A. V. Zayats and I. I. Smolyaninov, "Near-field photonics: surface plasmon polaritons and localized surface plasmons," *Journal of Optics A: Pure and Applied Optics*, vol. 5, no. 4, pp. S16–S50, 2003.

[138] K. M. Mayer and J. H. Hafner, "Localized surface plasmon resonance sensors," *Chemical reviews*, vol. 111, no. 6, pp. 3828–3857, 2011.

[139] G. Mie, "Beiträge zur optik trüber medien, speziell kolloidaler metallösungen," *Annalen der Physik*, vol. 330, no. 3, pp. 377–445, 1908.

[140] P. Nordlander, C. Oubre, E. Prodan, K. Li, and M. I. Stockman, "Plasmon hybridization in nanoparticle dimers," *Nano Letters*, vol. 4, no. 5, pp. 899–903, 2004.

[141] H. Wang, D. W. Brandl, P. Nordlander, and N. J. Halas, "Plasmonic nanostructures: artificial molecules," *Accounts of chemical research*, vol. 40, no. 1, pp. 53–62, 2007.

[142] D. F. Swinehart, "The beer-lambert law," *Journal of Chemical Education*, vol. 39, no. 7, p. 333, 1962.

[143] S. T. Peng, T. Tamir, and H. L. Bertoni, "Theory of periodic dielect waveguides," *IEEE Transactions on Microwave Theory and Techniques*, vol. 23, no. 1, pp. 123–133, 1975.

[144] L. Li, "Use of fourier series in the analysis of discontinuous periodic structures," *JOSA A*, vol. 13, no. 9, p. 1870, 1996.

[145] M. G. Moharam and T. K. Gaylord, "Rigorous coupled-wave analysis of planar-grating diffraction," *Journal of the Optical Society of America*, vol. 71, no. 7, p. 811, 1981.

[146] G. D'Aguanno, N. Mattiucci, M. J. Bloemer, D. de Ceglia, M. A. Vincenti, and A. Alù, "Transmission resonances in plasmonic metallic gratings," *Journal of the Optical Society of America B*, vol. 28, no. 2, p. 253, 2011.

[147] J. Chandezon, G. Raoult, and D. Maystre, "A new theoretical method for diffraction gratings and its numerical application," *Journal of Optics*, vol. 11, no. 4, pp. 235–241, 1980.

[148] Klaus-Jürgen Bathe, "Finite element method," in *Wiley Encyclopedia of Computer Science and Engineering*, pp. 1–12, John Wiley & Sons, Ltd, 2008.

[149] A. Taflove, S. C. Hagness, and M. Piket-May, "Computational electromagnetics: The finite-difference time-domain method," in *The Electrical Engineering Handbook*, pp. 629–670, Elsevier, 2005.

[150] A. Alù, D. de Ceglia, G. D'Aguanno, M. A. Vincenti, M. J. Bloemer, and N. Mattiucci, "Transmission resonances in plasmonic metallic gratings," 2011.

[151] S. S. Wang and R. Magnusson, "Theory and applications of guided-mode resonance filters," *Applied optics*, vol. 32, no. 14, pp. 2606–2613, 1993.

[152] M. Nevière, *The Homogeneous Problem.* Springer Berlin Heidelberg, 1980.

[153] K. Seeger, *Semiconductor Physics*. Springer Study Edition Ser, Vienna: Springer Wien, 1973.

[154] K. Sakoda, *Optical Properties of Photonic Crystals*. Springer Science & Business Media, 2004.

[155] S. Joseph, S. Pandey, S. Sarkar, and J. Joseph, "Bound states in the continuum in resonant nanostructures: an overview of engineered materials for tailored applications," *Nanophotonics*, vol. 10, no. 17, pp. 4175–4207, 2021.

[156] C. W. Hsu, B. Zhen, J. Lee, S.-L. Chua, S. G. Johnson, J. D. Joannopoulos, and M. Soljačić, "Observation of trapped light within the radiation continuum," *Nature*, vol. 499, no. 7457, pp. 188–191, 2013.

[157] R. Ulrich, "Efficiency of optical-grating couplers," *Journal of the Optical Society of America*, vol. 63, no. 11, 1973.

[158] T. Tamir and S. T. Peng, "Analysis and design of grating couplers," *Applied Physics*, vol. 14, no. 3, pp. 235–254, 1977.

[159] A. E. Siegman, *Lasers*. University Science Books, 1986.

[160] H. Ma, A.-Y. Jen, and L. R. Dalton, "Polymer-based optical waveguides: Materials, processing, and devices," *Advanced Materials*, vol. 14, no. 19, pp. 1339–1365, 2002.

[161] N. Kooy, K. Mohamed, L. T. Pin, and O. S. Guan, "A review of roll-to-roll nanoimprint lithography," *Nanoscale Research Letters*, vol. 9, no. 1, p. 320, 2014.

[162] J. Park, K. Shin, and C. Lee, "Roll-to-roll coating technology and its applications: A review," *International Journal of Precision Engineering and Manufacturing*, vol. 17, no. 4, pp. 537–550, 2016.

[163] T. Søndergaard, S. M. Novikov, T. Holmgaard, R. L. Eriksen, J. Beermann, Z. Han, K. Pedersen, and S. I. Bozhevolnyi, "Plasmonic black gold by adiabatic nanofocusing and absorption of light in ultra-sharp convex grooves," *Nature communications*, vol. 3, p. 969, 2012.

[164] J. C. Aguirre, S. A. Hawks, A. S. Ferreira, P. Yee, S. Subramaniyan, S. A. Jenekhe, S. H. Tolbert, and B. J. Schwartz, "Sequential processing for organic photovoltaics: Design rules for morphology control by tailored semi-orthogonal solvent blends," *Advanced Energy Materials*, vol. 5, no. 11, 2015.

[165] C. W. Rochester, S. A. Mauger, and A. J. Moulé, "Investigating the morphology of polymer/fullerene layers coated using orthogonal solvents," *The Journal of Physical Chemistry C*, vol. 116, no. 13, pp. 7287–7292, 2012.

[166] A. Bhattacharya, J. W. Rawlins, and P. Ray, *Polymer Grafting and Crosslinking*. John Wiley & Sons, 2008.

[167] A. Schleunitz, J. J. Klein, R. Houbertz, M. Vogler, and G. Gruetzner, "Towards high precision manufacturing of 3d optical components using uv-curable hybrid polymers," in *Optical Interconnects XV* (H. Schröder and R. T. Chen, eds.), SPIE Proceedings, SPIE, 2015.

[168] Binnig, Quate, and Gerber, "Atomic force microscope," *Physical Review Letters*, vol. 56, no. 9, pp. 930–933, 1986.

[169] R. Buestrich, F. Kahlenberg, M. Popall, P. Dannberg, R. Müller-Fiedler, and O. Rösch, "Ormocer®s for optical interconnection technology," *Journal of Sol-Gel Science and Technology*, vol. 20, no. 2, pp. 181–186, 2001.

[170] J. Lawrence and L. Li, "Modification of the wettability characteristics of polymethyl methacrylate (pmma) by means of co2, nd:yag, excimer and high power diode laser radiation," *Materials Science and Engineering: A*, vol. 303, no. 1-2, pp. 142–149, 2001.

[171] J. R. Hntsberger, "Surface energy, wetting and adhesion," *The Journal of Adhesion*, vol. 12, no. 1, pp. 3–12, 1981.

[172] A. Boggs, "A comparative risk assessment of casting solvents for positive photoresist," *Applied Industrial Hygiene*, vol. 4, no. 4, pp. 81–87, 1989.

[173] L. E. Scriven, "Physics and applications of dip coating and spin coating," *MRS Proceedings*, vol. 121, no. 1, pp. 717–729, 1988.

[174] R. G. Larson and T. J. Rehg, "Spin coating," in *Liquid Film Coating*, pp. 709–734, Springer, Dordrecht, 1997.

[175] S. Y. Chou, "Nanoimprint lithography," *Journal of Vacuum Science & Technology B: Microelectronics and Nanometer Structures*, vol. 14, no. 6, p. 4129, 1996.

[176] H. Lan and H. Liu, *UV-nanoimprint lithography: structure, materials and fabrication of flexible molds*, vol. 13. American Scientific Publishers, 2013.

[177] M. OTTO, "Reproducibility and homogeneity in step and repeat uv-nanoimprint lithography," *Microelectronic Engineering*, vol. 73-74, pp. 152–156, 2004.

[178] C. Vieu, F. Carcenac, A. Pépin, Y. Chen, M. Mejias, A. Lebib, L. Manin-Ferlazzo, L. Couraud, and H. Launois, "Electron beam lithography: resolution limits and applications," *Applied Surface Science*, vol. 164, no. 1-4, pp. 111–117, 2000.

[179] H. Jansen, H. Gardeniers, M. de Boer, M. Elwenspoek, and J. Fluitman, "A survey on the reactive ion etching of silicon in microtechnology," *Journal of Micromechanics and Microengineering*, vol. 6, no. 1, pp. 14–28, 1996.

[180] C. Lu and R. H. Lipson, "Interference lithography: a powerful tool for fabricating periodic structures," *Laser & Photonics Reviews*, vol. 4, no. 4, pp. 568–580, 2010.

[181] L. F. Thompson, "An introduction to lithography," in *ACS Symposium Series*, pp. 1–13, Washington, D. C.: American Chemical Society, 1983.

[182] B. Zhang, Q. Wang, N. Shen, and H. Ding, "Experimental investigation and numerical analysis of mechanical ruling for an aluminum-coated diffraction grating," *Journal of Manufacturing Science and Engineering*, vol. 139, no. 2, 2017.

[183] M. Mühlberger, I. Bergmair, A. Klukowska, A. Kolander, H. Leichtfried, E. Platzgummer, H. Loeschner, C. Ebm, G. Grützner, and R. Schöftner, "Uv-nil with working stamps made from ormostamp," *Microelectronic Engineering*, vol. 86, no. 4-6, pp. 691–693, 2009.

[184] C. Steinberg, K. Dhima, D. Blenskens, A. Mayer, S. Wang, M. Papenheim, H.-C. Scheer, J. Zajadacz, and K. Zimmer, "A scalable anti-sticking layer process via controlled evaporation," *Microelectronic Engineering*, vol. 123, pp. 4–8, 2014.

[185] D. M. Mattox, *Handbook of Physical Vapor Deposition (PVD) Processing*. William Andrew, 2010.

[186] T. Jakob, A. Polywka, L. Stegers, T. Riedl, and P. Görrn, "Soft materials for fabrication of nano patterns," *Quantum Matter*, vol. 6, no. 1, pp. 31–36, 2017.

[187] T. Jakob, A. Polywka, L. Stegers, E. Akdeniz, S. Kropp, M. Frorath, S. Trost, T. Schneider, T. Riedl, and P. Görrn, "Transfer printing of electrodes for organic devices: nanoscale versus macroscale continuity," *Applied Physics A*, vol. 120, no. 2, pp. 503–508, 2015.

[188] A. Carlson, A. M. Bowen, Y. Huang, R. G. Nuzzo, and J. A. Rogers, "Transfer printing techniques for materials assembly and micro/nanodevice fabrication," *Advanced Materials*, vol. 24, no. 39, pp. 5284–5318, 2012.

[189] A. Esteves, J. Brokken-Zijp, J. Laven, H. P. Huinink, N. Reuvers, M. P. Van, and G. de With, "Influence of cross-linker concentration on the cross-linking of pdms and the network structures formed," *Polymer*, vol. 50, no. 16, pp. 3955–3966, 2009.

[190] M. Meudt, T. Jakob, A. Polywka, L. Stegers, S. Kropp, S. Runke, M. Zang, M. Clemens, and P. Görrn, "Plasmonic black metasurface by transfer printing," *Advanced Materials Technologies*, vol. 3, no. 11, 2018.

[191] B. Tollens, "Ueber ammon-alkalische Silberlösung als Reagens auf Aldehyd," *Berichte der deutschen chemischen Gesellschaft*, vol. 15, no. 2, pp. 1635–1639, 1882.

[192] S. S. Djokić and P. L. Cavallotti, "Electroless deposition: Theory and applications," in *Electrodeposition*, pp. 251–289, Springer, New York, NY, 2010.

[193] J. W. P. Schmelzer, ed., *Nucleation Theory and Applications*. Wiley VHC, 2005.

[194] A. Polywka, C. Tückmantel, and P. Görrn, "Light controlled assembly of silver nanoparticles," *Scientific reports*, vol. 7, 2017.

[195] E. Teague, F. E. Scire, S. M. Baker, and S. W. Jensen, "Three-dimensional stylus profilometry," *Wear*, vol. 83, no. 1, pp. 1–12, 1982.

[196] J. I. Goldstein, D. E. Newbury, J. R. Michael, N. W. Ritchie, J. H. J. Scott, and D. C. Joy, *Scanning Electron Microscopy and X-Ray Microanalysis*. Springer, 2017.

[197] I. V. Nemtsev, I. A. Tambasov, A. A. Ivanenko, and V. Y. Zyryanov, "Angle-resolved reflection spectroscopy of high-quality pmma opal crystal," *Photonics and Nanostructures - Fundamentals and Applications*, vol. 28, pp. 37–44, 2018.

[198] J. Homola, S. S. Yee, and G. Gauglitz, "Surface plasmon resonance sensors: review," *Sensors and Actuators B: Chemical*, vol. 54, no. 1-2, pp. 3–15, 1999.

[199] A. Yeniay, R. Gao, K. Takayama, and A. F. Garito, "Ultra-low-loss polymer waveguides," *Journal of Lightwave Technology*, vol. 22, no. 1, pp. 154–158, 2004.

[200] J. C. Mullikin, L. J. van Vliet, H. Netten, F. R. Boddeke, G. van der Feltz, and I. T. Young, "Methods for ccd camera characterization," in *Image Acquisition and Scientific Imaging Systems* (H. C. Titus and A. Waks, eds.), SPIE Proceedings, pp. 73–84, SPIE, 1994.

[201] N. Daldosso, M. Melchiorri, L. Pavesi, G. Pucker, F. Gourbilleau, S. Chausserie, A. Belarouci, X. Portier, and C. Dufour, "Optical losses and absorption cross-section of silicon nanocrystals," *Journal of Luminescence*, vol. 121, no. 2, pp. 344–348, 2006.

[202] M. I. Reja, J. Akhtar, M. N. Malik, S. Ahmed, J. Islam, and A. Iqbal, "A comparative analysis of the characterization methods for submicron silicon waveguide propagation loss," in *2015 2nd International Conference on Electrical Information and Communication Technologies (EICT)*, pp. 347–352, IEEE, 12/10/2015 - 12/12/2015.

[203] M. Meudt, C. Bogiadzi, K. Wrobel, and P. Görrn, "Hybrid photonic–plasmonic bound states in continuum for enhanced light manipulation," *Advanced Optical Materials*, vol. 8, no. 20, 2020.

[204] C. C. Teng, "Precision measurements of the optical attenuation profile along the propagation path in thin-film waveguides," *Applied optics*, vol. 32, no. 7, pp. 1051–1054, 1993.

[205] F. M. Menger and A. M. Sanchez, "Spectroscopy with the polarizable solvent diiodomethane," *Chemical Communications*, no. 2, pp. 199–200, 1997.

[206] K.-D. Chen, Y.-F. Lin, and C.-H. Tu, "Densities, viscosities, refractive indexes, and surface tensions for mixtures of ethanol, benzyl acetate, and benzyl alcohol," *Journal of Chemical & Engineering Data*, vol. 57, no. 4, pp. 1118–1127, 2012.

[207] B. J. Lee, K. Park, T. Walsh, and L. Xu, "Radiative heat transfer analysis in plasmonic nanofluids for direct solar thermal absorption," *Journal of Solar Energy Engineering*, vol. 134, no. 2, 2012.

[208] M. Imtiaz Hussain, C. Ménézo, and J.-T. Kim, "Advances in solar thermal harvesting technology based on surface solar absorption collectors: A review," *Solar Energy Materials and Solar Cells*, vol. 187, pp. 123–139, 2018.

[209] M. Jonson and G. D. Mahan, "Mott's formula for the thermopower and the wiedemann-franz law," *Physical Review B*, vol. 21, no. 10, pp. 4223–4229, 1980.

[210] M. K. Hedayati, M. Javaherirahim, B. Mozooni, R. Abdelaziz, A. Tavassolizadeh, V. S. K. Chakravadhanula, V. Zaporojtchenko, T. Strunkus, F. Faupel, and M. Elbahri, "Design of a perfect black absorber at visible frequencies using plasmonic metamaterials," *Advanced Materials*, vol. 23, no. 45, pp. 5410–5414, 2011.

[211] L. Zhou, Y. Tan, D. Ji, B. Zhu, P. Zhang, J. Xu, Q. Gan, Z. Yu, and J. Zhu, "Self-assembly of highly efficient, broadband plasmonic absorbers for solar steam generation," *Science advances*, vol. 2, no. 4, 2016.

[212] J. Hao, J. Wang, X. Liu, W. J. Padilla, L. Zhou, and M. Qiu, "High performance optical absorber based on a plasmonic metamaterial," *Applied Physics Letters*, vol. 96, no. 25, 2010.

[213] Y. Cui, J. Xu, K. Hung Fung, Y. Jin, A. Kumar, S. He, and N. X. Fang, "A thin film broadband absorber based on multi-sized nanoantennas," *Applied Physics Letters*, vol. 99, no. 25, 2011.

[214] M. G. Nielsen, A. Pors, O. Albrektsen, and S. I. Bozhevolnyi, "Efficient absorption of visible radiation by gap plasmon resonators," *Optics express*, vol. 20, no. 12, pp. 13311–13319, 2012.

[215] M. Yan, J. Dai, and M. Qiu, "Lithography-free broadband visible light absorber based on a mono-layer of gold nanoparticles," *Journal of Optics*, vol. 16, no. 2, 2014.

[216] Z. Liu, G. Liu, G. Fu, X. Liu, and Y. Wang, "Multi-band light perfect absorption by a metal layer-coupled dielectric metamaterial," *Optics express*, vol. 24, no. 5, pp. 5020–5025, 2016.

[217] G.-C. Li, Q. Zhang, S. A. Maier, and D. Lei, "Plasmonic particle-on-film nanocavities: a versatile platform for plasmon-enhanced spectroscopy and photochemistry," *Nanophotonics*, vol. 7, no. 12, pp. 1865–1889, 2018.

[218] J. J. Mock, R. T. Hill, A. Degiron, S. Zauscher, A. Chilkoti, and D. R. Smith, "Distance-dependent plasmon resonant coupling between a gold nanoparticle and gold film," *Nano Letters*, vol. 8, no. 8, pp. 2245–2252, 2008.

[219] K. S. Kunz and R. J. Luebbers, *The Finite Difference Time Domain Method for Electromagnetics*. CRC Press, 1993.

[220] A. L. Giermann and C. V. Thompson, "Solid-state dewetting for ordered arrays of crystallographically oriented metal particles," *Applied Physics Letters*, vol. 86, no. 12, 2005.

[221] C. V. Thompson, "Solid-state dewetting of thin films," *Annual Review of Materials Research*, vol. 42, no. 1, pp. 399–434, 2012.

[222] M. Born and E. Wolf, *Principles of Optics: Electromagnetic Theory of Propagation, Interference and Diffraction of Light*. Elsevier, 2013.

[223] N. Yamamoto, S. Ohtani, and F. J. García de Abajo, "Gap and mie plasmons in individual silver nanospheres near a silver surface," *Nano Letters*, vol. 11, no. 1, pp. 91–95, 2011.

[224] A. Isihara, *Statistical Physics*. Academic Press, 2013.

[225] A. A. High, R. C. Devlin, A. Dibos, M. Polking, D. S. Wild, J. Perczel, N. P. de Leon, M. D. Lukin, and H. Park, "Visible-frequency hyperbolic metasurface," *Nature*, vol. 522, no. 7555, pp. 192–196, 2015.

[226] P. Shekhar, J. Atkinson, and Z. Jacob, "Hyperbolic metamaterials: fundamentals and applications," *Nano convergence*, vol. 1, no. 1, p. 14, 2014.

[227] L. P. Mosteller and F. Wooten, "Optical properties and reflectance of uniaxial absorbing crystals*," *Journal of the Optical Society of America*, vol. 58, no. 4, p. 511, 1968.

[228] P. C. Logofatu, "Reflectance and transmittance of a uniaxial thin film with the optic axis perpendicular to the surface," in *ROMOPTO 2012: Tenth Conference on Optics: Micro- to Nanophotonics III* (V. I. Vlad, ed.), SPIE Proceedings, SPIE, 2013.

[229] I. Shutsko, M. Buchmüller, M. Meudt, and P. Görrn, "Plasmon–induced disorder engineering for robust optical sensors," *Advanced Optical Materials*, 2022.

[230] Y. A. Krutyakov, A. A. Kudrinskiy, A. Y. Olenin, and G. V. Lisichkin, "Synthesis and properties of silver nanoparticles: advances and prospects," *Russian Chemical Reviews*, vol. 77, no. 3, pp. 233–257, 2008.

[231] S. Yu, C.-W. Qiu, Y. Chong, S. Torquato, and N. Park, "Engineered disorder in photonics," *Nature Reviews Materials*, vol. 6, no. 3, pp. 226–243, 2021.

[232] J. S. Lim, "Two-dimensional signal and image processing," *Englewood Cliffs*, 1990.

[233] P. M. Piechulla, B. Fuhrmann, E. Slivina, C. Rockstuhl, R. B. Wehrspohn, and A. N. Sprafke, "Tailored light scattering through hyperuniform disorder in self–organized arrays of high–index nanodisks," *Advanced Optical Materials*, vol. 9, no. 17, 2021.

[234] B. D. Thackray, V. G. Kravets, F. Schedin, G. Auton, P. A. Thomas, and A. N. Grigorenko, "Narrow collective plasmon resonances in nanostructure arrays observed at normal light incidence for simplified sensing in asymmetric air and water environments," *ACS Photonics*, vol. 1, no. 11, pp. 1116–1126, 2014.

[235] S. Torquato, "Hyperuniformity and its generalizations," *Physical review. E*, vol. 94, no. 2-1, 2016.

[236] D. Chen, E. Lomba, and S. Torquato, "Binary mixtures of charged colloids: a potential route to synthesize disordered hyperuniform materials," *Physical chemistry chemical physics : PCCP*, vol. 20, no. 26, pp. 17557–17562, 2018.

[237] Z. Ma and S. Torquato, "Hyperuniformity of generalized random organization models," *Physical review. E*, vol. 99, no. 2-1, 2019.

[238] W. Man, M. Florescu, K. Matsuyama, P. Yadak, G. Nahal, S. Hashemizad, E. Williamson, P. Steinhardt, S. Torquato, and P. Chaikin, "Photonic band gap in isotropic hyperuniform disordered solids with low dielectric contrast," *Optics Express*, vol. 21, no. 17, pp. 19972–19981, 2013.

[239] E. C. Garnett, B. Ehrler, A. Polman, and E. Alarcon-Llado, "Photonics for photovoltaics: Advances and opportunities," *ACS Photonics*, vol. 8, no. 1, pp. 61–70, 2021.

[240] D. Taillaert, P. Bienstman, and R. Baets, "Compact efficient broadband grating coupler for silicon-on-insulator waveguides," *Optics Letters*, vol. 29, no. 23, pp. 2749–2751, 2004.

[241] M. L. Dakss, L. Kuhn, P. F. Heidrich, and B. A. Scott, "Grating coupler for efficient excitation of optical guided waves in thin films," *Applied Physics Letters*, vol. 16, no. 12, pp. 523–525, 1970.

[242] A. Mekis, S. Gloeckner, G. Masini, A. Narasimha, T. Pinguet, S. Sahni, and P. de Dobbelaere, "A grating-coupler-enabled cmos photonics platform," *IEEE Journal of Selected Topics in Quantum Electronics*, vol. 17, no. 3, pp. 597–608, 2011.

[243] S. Ura, J. Inoue, K. Kintaka, and Y. Awatsuji, "Proposal of small-aperture guided-mode resonance filter," in *2011 13th International Conference on Transparent Optical Networks*, IEEE, 2011.

[244] S. S. Wang and R. Magnusson, "Design of waveguide-grating filters with symmetrical line shapes and low sidebands," *Optics Letters*, vol. 19, no. 12, pp. 919–921, 1994.

[245] K. Kintaka, T. Majima, J. Inoue, K. Hatanaka, J. Nishii, and S. Ura, "Cavity-resonator-integrated guided-mode resonance filter for aperture miniaturization," *Optics Express*, vol. 20, no. 2, pp. 1444–1449, 2012.

[246] S. T. Thurman and G. M. Morris, "Controlling the spectral response in guided-mode resonance filter design," *Applied optics*, vol. 42, no. 16, pp. 3225–3233, 2003.

[247] S. S. Wang and R. Magnusson, "Multilayer waveguide-grating filters," *Applied optics*, vol. 34, no. 14, pp. 2414–2420, 1995.

[248] D. C. Flanders, H. Kogelnik, R. V. Schmidt, and C. V. Shank, "Grating filters for thin–film optical waveguides," *Applied Physics Letters*, vol. 24, no. 4, pp. 194–196, 1974.

[249] M. Meudt, A. Henkel, M. Buchmüller, and P. Görrn, "A theoretical description of node-aligned resonant waveguide gratings," *Optics*, vol. 3, no. 1, pp. 60–69, 2022.

[250] P. Görrn, T. Rabe, T. Riedl, and W. Kowalsky, "Loss reduction in fully contacted organic laser waveguides using TE2 modes," *Applied Physics Letters*, vol. 91, no. 4, 2007.

[251] P. Görrn, "Waveguide, method of projecting light from a waveguide, and display," US Patent 10739623B2, 2018.

[252] P. Görrn, "Method of concentrating light and light concentrator," US Patent 10558027B2, 2014.

[253] P. Görrn and M. Meudt, "Light concentrator," International Patent WO202119962A1, 2021.

[254] F. Kehl and S. Follonier, "Self-referenced waveguide grating sensor," *Optics Letters*, vol. 41, no. 7, pp. 1447–1450, 2016.

[255] F. Song, J. Xiao, A. J. Xie, and S.-W. Seo, "Polymer waveguide grating sensor integrated with a thin-film photodetector," *Journal of optics (2010)*, vol. 16, no. 1111, 2014.

[256] N. Zaytseva, W. Miller, V. Goral, J. Hepburn, and Y. Fang, "Microfluidic resonant waveguide grating biosensor system for whole cell sensing," *Applied Physics Letters*, vol. 98, no. 16, 2011.

[257] A. M. Ferrie, Q. Wu, and Y. Fang, "Resonant waveguide grating imager for live cell sensing," *Applied Physics Letters*, vol. 97, no. 22, 2010.

[258] P. Nellen, K. Tiefenthaler, and W. Lukosz, "Integrated optical input grating couplers as biochemical sensors," *Sensors and Actuators*, vol. 15, no. 3, pp. 285–295, 1988.

[259] D. Clerc and W. Lukosz, "Integrated optical output grating coupler as biochemical sensor," *Sensors and Actuators B: Chemical*, vol. 19, no. 1-3, pp. 581–586, 1994.

[260] J. Vörös, J. Ramsden, G. Csúcs, I. Szendrő, S. de Paul, M. Textor, and N. Spencer, "Optical grating coupler biosensors," *Biomaterials*, vol. 23, no. 17, pp. 3699–3710, 2002.

[261] Q. Wang, D. Zhang, Y. Huang, Z. Ni, J. Chen, Y. Zhong, and S. Zhuang, "Type of tunable guided-mode resonance filter based on electro-optic characteristic of polymer-dispersed liquid crystal," *Optics Letters*, vol. 35, no. 8, pp. 1236–1238, 2010.

[262] A. Forouzmand and H. Mosallaei, "Electro-optical amplitude and phase modulators based on tunable guided-mode resonance effect," *ACS Photonics*, vol. 6, no. 11, pp. 2860–2869, 2019.

[263] A. Kodigala, T. Lepetit, Q. Gu, B. Bahari, Y. Fainman, and B. Kanté, "Lasing action from photonic bound states in continuum," *Nature*, vol. 541, no. 7636, pp. 196–199, 2017.

[264] S. I. Azzam, K. Chaudhuri, A. Lagutchev, Z. Jacob, Y. L. Kim, V. M. Shalaev, A. Boltasseva, and A. V. Kildishev, "Single and multi–mode directional lasing from arrays of dielectric nanoresonators," *Laser & Photonics Reviews*, vol. 15, no. 3, 2021.

[265] M. Wu, S. T. Ha, S. Shendre, E. G. Durmusoglu, W.-K. Koh, D. R. Abujetas, J. A. Sánchez-Gil, R. Paniagua-Domínguez, H. V. Demir, and A. I. Kuznetsov, "Room-temperature lasing in colloidal nanoplatelets via mie-resonant bound states in the continuum," *Nano Letters*, vol. 20, no. 8, pp. 6005–6011, 2020.

[266] G. Huang, S. R. Curt, K. Wang, and C. N. Markides, "Challenges and opportunities for nanomaterials in spectral splitting for high-performance hybrid solar photovoltaic-thermal applications: A review," *Nano Materials Science*, vol. 2, no. 3, pp. 183–203, 2020.

[267] L. Carletti, K. Koshelev, C. de Angelis, and Y. Kivshar, "Giant nonlinear response at the nanoscale driven by bound states in the continuum," *Physical review letters*, vol. 121, no. 3, 2018.

[268] L. Carletti, S. S. Kruk, A. A. Bogdanov, C. de Angelis, and Y. Kivshar, "High-harmonic generation at the nanoscale boosted by bound states in the continuum," *Physical Review Research*, vol. 1, no. 2, 2019.

[269] K. Fan, I. V. Shadrivov, and W. J. Padilla, "Dynamic bound states in the continuum," *Optica*, vol. 6, no. 2, p. 169, 2019.

[270] M. M. Salary and H. Mosallaei, "Tunable all-dielectric metasurfaces for phase-only modulation of transmitted light based on quasi-bound states in the continuum," *ACS Photonics*, vol. 7, no. 7, pp. 1813–1829, 2020.

[271] S. Han, L. Cong, Y. K. Srivastava, B. Qiang, M. V. Rybin, A. Kumar, R. Jain, W. X. Lim, V. G. Achanta, S. S. Prabhu, Q. J. Wang, Y. S. Kivshar, and R. Singh, "All-dielectric active terahertz photonics driven by bound states in the continuum," *Advanced Materials*, vol. 31, no. 37, 2019.

[272] C. W. Hsu, B. Zhen, A. D. Stone, J. D. Joannopoulos, and M. Soljačić, "Bound states in the continuum," *Nature Reviews Materials*, vol. 1, no. 9, 2016.

[273] H. M. Doeleman, F. Monticone, W. den Hollander, A. Alù, and A. F. Koenderink, "Experimental observation of a polarization vortex at an optical bound state in the continuum," *Nature Photonics*, vol. 12, no. 7, pp. 397–401, 2018.

[274] E. N. Bulgakov and D. N. Maksimov, "Avoided crossings and bound states in the continuum in low-contrast dielectric gratings," *Physical Review A*, vol. 98, no. 5, 2018.

[275] B. Zhen, C. W. Hsu, L. Lu, A. D. Stone, and M. Soljačić, "Topological nature of optical bound states in the continuum," *Physical review letters*, vol. 113, no. 25, 2014.

[276] S. I. Azzam, V. M. Shalaev, A. Boltasseva, and A. V. Kildishev, "Formation of bound states in the continuum in hybrid plasmonic-photonic systems," *Physical review letters*, vol. 121, no. 25, 2018.

[277] S.-G. Lee, S.-H. Kim, and C.-S. Kee, "Bound states in the continuum (bic) accompanied by avoided crossings in leaky-mode photonic lattices," *Nanophotonics*, vol. 9, no. 14, pp. 4373–4380, 2020.

[278] D. C. Marinica, A. G. Borisov, and S. V. Shabanov, "Bound states in the continuum in photonics," *Physical Review Letters*, vol. 100, no. 18, 2008.

[279] Friedrich and Wintgen, "Interfering resonances and bound states in the continuum," *Physical review. A, General physics*, vol. 32, no. 6, pp. 3231–3242, 1985.

[280] E. N. Bulgakov, D. N. Maksimov, P. N. Semina, and S. A. Skorobogatov, "Propagating bound states in the continuum in dielectric gratings," *Journal of the Optical Society of America B*, vol. 35, no. 6, 2018.

[281] D. A. Bykov, E. A. Bezus, and L. L. Doskolovich, "Coupled-wave formalism for bound states in the continuum in guided-mode resonant gratings," *Physical Review A*, vol. 99, no. 6, 2019.

[282] W. Suh, Z. Wang, and S. Fan, "Temporal coupled-mode theory and the presence of non-orthogonal modes in lossless multimode cavities," *IEEE Journal of Quantum Electronics*, vol. 40, no. 10, pp. 1511–1518, 2004.

[283] A. A. Wereszczak and C. E. Anderson, "Borofloat and starphire float glasses: A comparison," *International Journal of Applied Glass Science*, vol. 5, no. 4, pp. 334–344, 2014.

[284] N. C. Panoiu and R. M. Osgood, "Enhanced optical absorption for photovoltaics via excitation of waveguide and plasmon-polariton modes," *Optics Letters*, vol. 32, no. 19, pp. 2825–2827, 2007.

[285] Y. Xu, P. Bai, X. Zhou, Y. Akimov, C. E. Png, L.-K. Ang, W. Knoll, and L. Wu, "Optical refractive index sensors with plasmonic and photonic structures: Promising and inconvenient truth," *Advanced Optical Materials*, vol. 7, no. 9, 2019.

[286] Z. Liu, M. Yu, S. Huang, X. Liu, Y. Wang, M. Liu, P. Pan, and G. Liu, "Enhancing refractive index sensing capability with hybrid plasmonic–photonic absorbers," *Journal of Materials Chemistry C*, vol. 3, no. 17, pp. 4222–4226, 2015.

[287] A. A. Rifat, G. A. Mahdiraji, Y. M. Sua, R. Ahmed, Y. G. Shee, and F. R. M. Adikan, "Highly sensitive multi-core flat fiber surface plasmon resonance refractive index sensor," *Optics Express*, vol. 24, no. 3, pp. 2485–2495, 2016.

[288] F. Bahrami, M. Maisonneuve, M. Meunier, J. S. Aitchison, and M. Mojahedi, "An improved refractive index sensor based on genetic optimization of plasmon waveguide resonance," *Optics Express*, vol. 21, no. 18, pp. 20863–20872, 2013.

[289] C. Haffner, D. Chelladurai, Y. Fedoryshyn, A. Josten, B. Baeuerle, W. Heni, T. Watanabe, T. Cui, B. Cheng, S. Saha, D. L. Elder, L. R. Dalton, A. Boltasseva, V. M. Shalaev, N. Kinsey, and J. Leuthold, "Low-loss plasmon-assisted electro-optic modulator," *Nature*, vol. 556, no. 7702, pp. 483–486, 2018.

[290] Z. Yu and S. Fan, "Extraordinarily high spectral sensitivity in refractive index sensors using multiple optical modes," *Optics Express*, vol. 19, no. 11, pp. 10029–10040, 2011.

[291] X. Chen, K. Zhou, L. Zhang, and I. Bennion, "Simultaneous measurement of temperature and external refractive index by use of a hybrid grating in d fiber with enhanced sensitivity by hf etching," *Applied optics*, vol. 44, no. 2, pp. 178–182, 2005.

[292] E. A. Velichko and A. I. Nosich, "Refractive-index sensitivities of hybrid surface-plasmon resonances for a core-shell circular silver nanotube sensor," *Optics Letters*, vol. 38, no. 23, pp. 4978–4981, 2013.

[293] L. Zhou, X. Sun, X. Li, and J. Chen, "Miniature microring resonator sensor based on a hybrid plasmonic waveguide," *Sensors*, vol. 11, no. 7, pp. 6856–6867, 2011.

[294] S. Singh, S. K. Mishra, and B. D. Gupta, "Sensitivity enhancement of a surface plasmon resonance based fibre optic refractive index sensor utilizing an additional layer of oxides," *Sensors and Actuators A: Physical*, vol. 193, pp. 136–140, 2013.

[295] T. Lepetit, E. Akmansoy, J.-P. Ganne, and J.-M. Lourtioz, "Resonance continuum coupling in high-permittivity dielectric metamaterials," *Physical Review B*, vol. 82, no. 19, 2010.

[296] K. Koshelev, S. Lepeshov, M. Liu, A. Bogdanov, and Y. Kivshar, "Asymmetric metasurfaces with high-q resonances governed by bound states in the continuum," *Physical review letters*, vol. 121, no. 19, 2018.

[297] Z. F. Sadrieva, I. S. Sinev, K. L. Koshelev, A. Samusev, I. V. Iorsh, O. Takayama, R. Malureanu, A. A. Bogdanov, and A. V. Lavrinenko, "Transition from optical bound states in the continuum to leaky resonances: Role of substrate and roughness," *ACS Photonics*, vol. 4, no. 4, pp. 723–727, 2017.

[298] S. Romano, G. Zito, S. Torino, G. Calafiore, E. Penzo, G. Coppola, S. Cabrini, I. Rendina, and V. Mocella, "Label-free sensing of ultralow-weight molecules with all-dielectric metasurfaces supporting bound states in the continuum," *Photonics Research*, vol. 6, no. 7, p. 726, 2018.

[299] J. Wang, J. Kühne, T. Karamanos, C. Rockstuhl, S. A. Maier, and A. Tittl, "All–dielectric crescent metasurface sensor driven by bound states in the continuum," *Advanced Functional Materials*, vol. 31, no. 46, 2021.

[300] Y. Liu, W. Zhou, and Y. Sun, "Optical refractive index sensing based on high-q bound states in the continuum in free-space coupled photonic crystal slabs," *Sensors*, vol. 17, no. 8, 2017.

[301] A. Henkel, M. Meudt, M. Buchmüller, and P. Görrn, "Electrically switchable broadband photonic bound states in the continuum," ArXiV pre-print 2102.01686, 2021.

[302] P. Görrn, "Wellenleiteranordnung und Verfahren zur Ablenkung wenigstens eines Lichtstrahls bzw. Lichtstrahlpaares," Deutsche Patentanmeldung Nr. 102021127637.3, 2021.

[303] Z. Zhang, M. Kang, X. Zhang, X. Feng, Y. Xu, X. Chen, H. Zhang, Q. Xu, Z. Tian, W. Zhang, A. Krasnok, J. Han, and A. Alù, "Coherent perfect diffraction in metagratings," *Advanced Materials*, vol. 32, no. 36, 2020.

[304] D. G. Baranov, A. Krasnok, T. Shegai, A. Alù, and Y. Chong, "Coherent perfect absorbers: linear control of light with light," *Nature Reviews Materials*, vol. 2, no. 12, pp. 1–14, 2017.

[305] Y. D. Chong, L. Ge, H. Cao, and A. D. Stone, "Coherent perfect absorbers: time-reversed lasers," *Physical review letters*, vol. 105, no. 5, 2010.

[306] W. Wan, Y. Chong, L. Ge, H. Noh, A. D. Stone, and H. Cao, "Time-reversed lasing and interferometric control of absorption," *Science*, vol. 331, no. 6019, pp. 889–892, 2011.

[307] J. Shi, X. Fang, E. T. F. Rogers, E. Plum, K. F. MacDonald, and N. I. Zheludev, "Coherent control of snell's law at metasurfaces," *Optics Express*, vol. 22, no. 17, pp. 21051–21060, 2014.

[308] M. Pu, Q. Feng, M. Wang, C. Hu, C. Huang, X. Ma, Z. Zhao, C. Wang, and X. Luo, "Ultrathin broadband nearly perfect absorber with symmetrical coherent illumination," *Optics Express*, vol. 20, no. 3, pp. 2246–2254, 2012.

[309] J. W. Yoon, G. M. Koh, S. H. Song, and R. Magnusson, "Measurement and modeling of a complete optical absorption and scattering by coherent surface plasmon-polariton excitation using a silver thin-film grating," *Physical review letters*, vol. 109, no. 25, 2012.

[310] M. Kang, F. Liu, T.-F. Li, Q.-H. Guo, J. Li, and J. Chen, "Polarization-independent coherent perfect absorption by a dipole-like metasurface," *Optics Letters*, vol. 38, no. 16, pp. 3086–3088, 2013.

[311] S. Zanotto, F. P. Mezzapesa, F. Bianco, G. Biasiol, L. Baldacci, M. S. Vitiello, L. Sorba, R. Colombelli, and A. Tredicucci, "Perfect energy-feeding into strongly coupled systems and interferometric control of polariton absorption," *Nature Physics*, vol. 10, no. 11, pp. 830–834, 2014.

[312] M. Kang, H.-T. Wang, and W. Zhu, "Wavefront manipulation with a dipolar metasurface under coherent control," *Journal of Applied Physics*, vol. 122, no. 1, 2017.

[313] G. Lifante, *Integrated photonics: Fundamentals*. J. Wiley, 2010.

[314] W. Bogaerts, D. Pérez, J. Capmany, D. A. B. Miller, J. Poon, D. Englund, F. Morichetti, and A. Melloni, "Programmable photonic circuits," *Nature*, vol. 586, no. 7828, pp. 207–216, 2020.

[315] D. Marpaung, J. Yao, and J. Capmany, "Integrated microwave photonics," *Nature Photonics*, vol. 13, no. 2, pp. 80–90, 2019.

[316] P. Cheben, R. Halir, J. H. Schmid, H. A. Atwater, and D. R. Smith, "Subwavelength integrated photonics," *Nature*, vol. 560, no. 7720, pp. 565–572, 2018.

[317] C. Sun, M. T. Wade, Y. Lee, J. S. Orcutt, L. Alloatti, M. S. Georgas, A. S. Waterman, J. M. Shainline, R. R. Avizienis, S. Lin, B. R. Moss, R. Kumar, F. Pavanello, A. H. Atabaki, H. M. Cook, A. J. Ou, J. C. Leu, Y.-H. Chen, K. Asanović, R. J. Ram, M. A. Popović, and V. M. Stojanović, "Single-chip microprocessor that communicates directly using light," *Nature*, vol. 528, no. 7583, pp. 534–538, 2015.

[318] D. N. Hutchison, J. Sun, J. K. Doylend, R. Kumar, J. Heck, W. Kim, C. T. Phare, A. Feshali, and H. Rong, "High-resolution aliasing-free optical beam steering," *Optica*, vol. 3, no. 8, p. 887, 2016.

[319] L. Midolo, A. Schliesser, and A. Fiore, "Nano-opto-electro-mechanical systems," *Nature Nanotechnology*, vol. 13, no. 1, pp. 11–18, 2018.

[320] T. J. Seok, N. Quack, S. Han, R. S. Muller, and M. C. Wu, "Large-scale broadband digital silicon photonic switches with vertical adiabatic couplers," *Optica*, vol. 3, no. 1, p. 64, 2016.

[321] T. Bifano, "Mems deformable mirrors," *Nature Photonics*, vol. 5, no. 1, pp. 21–23, 2011.

[322] T. Cui, B. Bai, and H.-B. Sun, "Tunable metasurfaces based on active materials," *Advanced Functional Materials*, vol. 29, no. 10, 2019.

[323] Y.-W. Huang, H. W. H. Lee, R. Sokhoyan, R. A. Pala, K. Thyagarajan, S. Han, D. P. Tsai, and H. A. Atwater, "Gate-tunable conducting oxide metasurfaces," *Nano Letters*, vol. 16, no. 9, pp. 5319–5325, 2016.

[324] A. K. Srivastava, V. G. Chigrinov, and H. S. Kwok, "Ferroelectric liquid crystals: Excellent tool for modern displays and photonics," *Journal of the Society for Information Display*, vol. 23, no. 6, pp. 253–272, 2015.

[325] P. Yeh and C. Gu, *Optics of liquid crystal displays.* J. Wiley, 2010.

[326] P. G. de Gennes and J. Prost, *The physics of liquid crystals.* Oxford University Press, 1995.

[327] F. Fan, A. K. Srivastava, V. G. Chigrinov, and H. S. Kwok, "Switchable liquid crystal grating with sub millisecond response," *Applied Physics Letters*, vol. 100, no. 11, 2012.

[328] D. E. Smalley, Q. Y. J. Smithwick, V. M. Bove, J. Barabas, and S. Jolly, "Anisotropic leaky-mode modulator for holographic video displays," *Nature*, vol. 498, no. 7454, pp. 313–317, 2013.

[329] S.-D. Wu, T. K. Gaylord, E. N. Glytsis, and Y.-M. Wu, "Three-dimensional converging-diverging gaussian beam diffraction by a volume grating," *Journal of the Optical Society of America. A, Optics, image science, and vision*, vol. 22, no. 7, pp. 1293–1303, 2005.

Erklärung der selbstständigen Verfassung der Dissertation

Ich, Maik Meudt (geb. Wolter), versichere an Eides statt, dass ich die vorliegende Dissertation einschließlich beigefügter Abbildungen, Skizzen, Darstellungen, etc. selbständig verfasst und keine anderen als die angegebenen Hilfsmittel benutzt habe. Die Stellen der Arbeit, die dem Wortlaut oder dem Sinne nach anderen Werken entnommen sind, wurden in jedem einzelnen Fall unter Angabe der Quellen und nach den üblichen Regeln wissenschaftlichen Zitierens deutlich als Entlehnung kenntlich gemacht.

Wuppertal,_____

Ort, Datum, Unterschrift